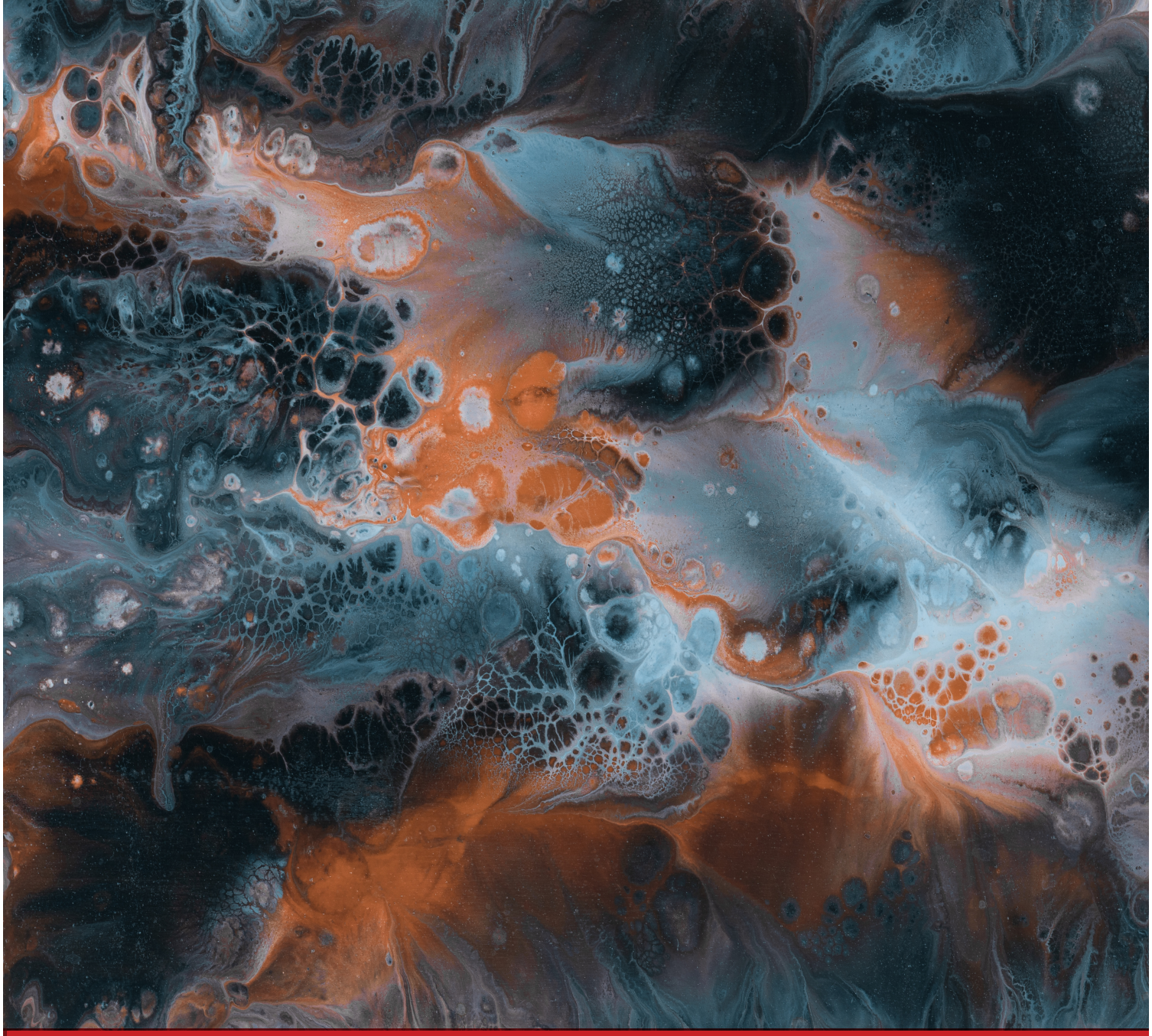

High-end application of basic oxygen furnace steel slag as sustainable building materials

Air granulation , Reactivity, Leachability,& Application as a binder

M. Jawad Ahmed

Bouwstenen 373

HIGH-END APPLICATION OF BASIC OXYGEN FURNACE STEEL SLAG AS SUSTAINABLE BUILDING MATERIALS

Air granulation, Reactivity, Leachability, & Application as a binder

Muhammad Jawad Ahmed

This project is done under the financial support of the Netherlands Organisation for Scientific Research (NWO) with project number 10023338. This projects is partially managed by the Netherlands Materials Innovation Institute (M2i) with project number S81.6.15565b.

CIP-DATA LIBRARY TECHNISCHE UNIVERSITEIT EINDHOVEN

High-end application of basic oxygen furnace steel slag as sustainable building materials - Air granulation, Reactivity, Leachability, & Application as a binder by Muhammad Jawad Ahmed
ISBN: 978-90-386-5848-3
Bouwstenen 373
NUR 955

PhD Thesis, Eindhoven University of Technology, the Netherlands
Cover design: iStock license number: 1286908316 (purchased) Printed by: www.proefschriftmaken.nl

HIGH-END APPLICATION OF BASIC OXYGEN FURNACE STEEL SLAG AS SUSTAINABLE BUILDING MATERIALS

Air granulation, Reactivity, Leachability, & Application as a binder

PROEFSCHRIFT

ter verkrijging van de graad van doctor aan de Technische Universiteit Eindhoven, op gezag van de rector magnificus prof.dr. S.K. Lenaerts, voor een commissie aangewezen door het College voor Promoties, in het openbaar te verdedigen op woensdag 22 November 2023 om 16:00 uur

door

MUHAMMAD JAWAD AHMED

geboren te Gujranwala, Pakistan

Dit proefschrift is goedgekeurd door de promotoren en de samenstelling van de promotiecommissie is als volgt:

Voorzitter:	prof. dr. ir. A.S.J. Suiker
Promotor:	prof. dr. ir. H.J.H. Brouwers
Copromotor 1:	assistant prof. dr. dipl. min. K. Schollbach
Leden:	prof. dr. L. M. Ottosen (Technical University of Denmark)
	prof. dr. C. Cheeseman (Imperial College London)
	assistant prof. dr. J. Yliniemi (University of Oulu)
	prof. dr. E.J.M. Hensen
	prof. dr. S.R. van der Laan

Het onderzoek of ontwerp dat in dit proefschrift wordt beschreven is uitgevoerd in overeenstemming met de TU/e Gedragscode Wetenschapsbeoefening.

In loving memory of my father
(1952 - 1997)

PREFACE

This thesis presents the work as part of the NWO and M2i project titled "High-end application of converter steel slag as sustainable building materials". My doctoral journey started on 1st September 2018 when I joined the Building Materials group as a Ph.D. student under the supervision of prof. dr. ir. H.J.H. Brouwers. Firstly, I want to present my cordial gratitude to my supervisor and 1st promoter prof. dr. ir. H.J.H. Brouwers who provided me with this opportunity in the first place. During my doctoral journey, you are the only person who rescued me from the toughest moments when I was twice so close to quitting. I am grateful to you for having faith in my abilities. This thesis would not have been possible without your kind guidance, assistance, and leadership.

I am also thankful for my co-promoter and daily supervisor assistant prof. dr. Katrin Schollbach for her invaluable guidance, support, and hours of scientific deliberation which you have invested to make this thesis possible. I am thankful that you have provided me with a lot of research freedom to choose my research direction and guidance for its ample execution. I would also like to thank prof. dr. Sieger van der Laan for the provision of materials, practical analysis from the TATA Steel lab, and guidance. I would also like to thank associate prof. Qinglian Yu and, assistant prof. dr. Florent Gauvin for his contribution to part of my thesis.

I extend my gratitude to the members of the promotion committee prof. dr. Lisbeth M. Ottosen from the Technical University of Denmark, prof. dr. Chris Cheeseman from Imperial College London, assistant prof. dr. Juho Yliniemi from the University of Oulu, prof. dr. Emile Hensen and prof. dr. Sieger van der Laan for reviewing my work and providing me comments for improvement. I am also grateful to the industrial and user committee members whose active participation was instrumental in defining the research trajectory. The user committee members included prof. dr. Sieger van der Laan (TATA Steel), dr. Ir. Viktoria Savran (Material innovation, M2i), dr. M. Hunger (ENCI), Ir. H. van den Broek (Hess), Mr. M. van Eerde (Kijlstra Betonmortel), Mr. Berto Dekker (V.d. Bosch Beton), Ir. M. van Kempen (Blue Phoenix group). I am especially thankful to TATA Steel for providing me with materials for the research.

The genesis of this thesis requires laborious laboratory work which would not be possible without the help of lab staff. I especially want to pay my heartfelt gratitude to ing. A.C.A. Delsing and Mr. H.L.W. Smulders who always accommodated me for the experiments even under tough corona circumstances. I would like to pay special thanks to the floor secretaries Nathaly, Leontine, Astrid, and Manon who always efficiently take care of bureaucratic matters and keep the working environment conducive for me. Without your assistance, this work was not possible.

I met many talented and amazing people in the building materials research group. I enjoyed their companionship and learned a lot from their experience. I would especially like to thank Qadeer, Veronica, Anna, Winnie, Kinga, and Jonathan with whom I shared my best moments. I always enjoy their company, discussions, and conference trips. I would also like to thank my former colleagues Yuri, Perry, Kate, Azee, Marc, Gang, Tao,

Peipeng, Cao, Zhengyao, Yuxuan, and Shaohu. I would also like to show my gratitude to my present colleagues who are multitalented and brilliant researcher namely Iris, Alex, Charles, Hoss, Leila, Felix, Naomi, Ricardo, Xuan, Zhihan, Marina, Helong, Darou, Fan, Jia, Beatrice, Zixing, Smantha, Yanjie, Yan, Ceren, Nataliya, and Shashank. It has been an absolute pleasure working with all of you and enjoyed every moment of it. During my doctoral study, I had an opportunity to supervise the final internship of three students from Fontys and Universite Clermont Auvergne. I want to pay my special thanks to Remco Cuijpers, Kim Lambrechts, and Sterenn Durand for your due diligence and hard work as well as for contributing to my project. During this internship, I have learned a lot from you and hopefully, you have learned something from me.

On this journey, I have got to know very special people Waqas Khan (Chota bhi) and Ariqa Chaudhary who have become family to me. I have always been a great admirer of your positive attitude toward life goals and wish you great success in every walk of life. My Ph.D. journey started in Finland where I made many lasting friends Ali Raza, Shahid Khan (Doctor), Shahid Khan (Professor), and Abuzar Nasim Kiani (John Shelby). I am thankful to you for providing me with emotional, intellectual, and brotherly support in the ebbs and flow of my life. Though it was more an "ebb" than flow, I always commend your friendship with me.

Before mentioning my family members, I would like to say a big cordial thanks to Qadeer Alam for his selfless support, and untiring guidance as well as for motivating me to excel. I am fortunate enough to know you. If someone asks me the definition of a "true friend". I will answer it with your name. Moreover, I would also like to express my gratitude for assisting me in the conversion of my thesis into LaTeX, and thoroughly enjoyed your witty comments on my research.

Lastly, I would like to mention my mother (Naseem Akhter), a beacon of strength and warmth who guided me through life's journey in tears and joy. I also cannot express how grateful I am for my siblings (Asad Bhai, Zagum Bhai, Allama Waqas, Shehbaz Ahmed (my interior ministry), and my sweet sister (Saeeda). Infinite love for nieces (Arfa and Khadija) and nephew (Abdullah)- my heart beats with you. You are the light that brightens up my path and a source of unwavering strength.

This thesis is a testament to my scientific journey, a path of knowledge and endless toil. Without the kind support of all, this odyssey would not embrace its grace. I am eagerly waiting for what the future holds for me with great optimism.

Muhammad Jawad Ahmed
November 2023

SUMMARY

Basic oxygen furnace (BOF) slag, also known as Lindz-Donawitz (LD) slag is a byproduct of the steelmaking process. The recycling and reusing of BOF slag as cementitious material carries the challenges of low reactivity of dicalcium silicate (C_2S) phases, potential leaching of heavy metals (Cr and V), and low reactivity with binders in general. To address these challenges, this thesis provides insight into the air granulation of BOF slag, hydration studies, leaching behaviour as well as the possible substitution in ordinary Portland cement (OPC) and belite calcium sulfoaluminate cement (BCSA). The fundamental insight into the synthesis, hydration, and immobilization of heavy metals (Cr and V) in C_2S, as well as possible chemical activation for an understanding of BOF slag reactivity, is also the focus of this study.

The first Chapter provides insight into the background, motivation, and outline of this dissertation. The main emphasis on the importance of a systematic understanding of the chemical and mineralogical composition, C_2S reactivity, and leachability for efficient BOF slag recycling is explained. Subsequently, the second Chapter deals with a detailed explanation of the physical, chemical, and analytical methods employed throughout the execution of this study.

In the third Chapter, the air granulation of BOF slag is discussed. Air granulation can be a promising way to increase the reactivity of BOF slag and enable recycling as a cement replacement. For this reason, BOF slag was air granulated and separated into different fractions (0.5-0.25 mm, 1-0.5 mm, 2-1 mm, 4-2 mm) to study the influence of size and therefore cooling speed on its mineralogy. The results showed that the main minerals in air granulated BOF slag are the same as in industrially cooled slag, but that additional perovskite is formed, which has not been reported before. All fractions contained large phenocrysts of C_2S and (Mg, Fe)O surrounded by a dense matrix containing the other minerals. The three largest slag fractions are very similar to each other in chemical composition and microstructure, while the smallest fraction (0.5-0.25 mm) contains a higher content of (Mg, Fe)O even though the starting composition was the same. The leaching of chromium and vanadium is greatly increased compared to standard cooled BOF slag indicating that air granulation results in greater dissolution of BOF slag despite generating very little amorphous content.

The fourth Chapter deals with the sol-gel synthesis of dicalcium silicate. The predominant phase in BOF slag is dicalcium silicate, comprising 35-50% of the slag. Therefore, the synthesis of dicalcium silicate (C_2S) via sol-gel (acid-catalyzed) process including the aqueous route, non-aqueous route, and the Pechini method is reported. The attention has been focused on determining the crystalline polymorphs, amorphous content as well and impurities. Intermediate dried gels have been investigated via thermal analysis to monitor changes in the gel structures and precursors at low temperatures. The synthetic parameters including calcination time and temperature, Ca/Si molar ratio and mode of cooling have been optimized to get pure β-C_2S with low amorphous content. The dependency of $\beta \rightarrow \gamma$ C_2S polymorphic transformation on mean crystallite size (D_{cryst}) is studied. Overall, the Pechini method exhibits the most

promising results for the purity and tuning of β-C_2S polymorph. Moreover, the non-aqueous and aqueous routes require calcining the dried gel at a temperature higher than 1200 °C due to the presence of CaO precursors as $CaCO_3$. The theoretical calculations of amorphous content have revealed that the change in the stoichiometry from 2.0 to 1.7 Ca/Si ratio is not a viable solution to improve the C_2S product yield.

Chapter 5 deals with the synthesis of Cr and V doped dicalcium silicate under varying sintering conditions, reactivity, and leaching behaviour. It is shown that C_2S can incorporate Cr (VI) and V (V) consequently leading to the stabilization of α′- and β-C_2S. Instead, Cr (II, III) and V < (V) tend not to substitute in C_2S. Despite reactive polymorphs (α′- and β-C_2S) stability due to Cr (VI) and V (V) incorporation, the early age (48-72 h) C_2S reactivity is drastically reduced due to Cr (VI) and V (V) incorporation. Moreover, one batch leaching test revealed that the V (V) leaching is inversely proportional to aqueous Ca^{2+} ion concentration at pH > 12 while Cr leaching is sensitive to its oxidation state, and dissolution of C_2S. Even though C_2S can incorporate Cr (VI) and V (V) ions, the final leaching is governed by the immobilization potential of C-S-H gel, pH as well as types of calcium chromate and vanadate complexes.

In Chapter 6, the focus lies on the hydration rate of dicalcium silicate under sodium-based chemical activators. This study analyses the effect of fixed moles (0.8M) Na^+ bearing OH^-, SO_4^{2-}, and CO_3^{2-} anions on β-dicalcium silicate (C_2S) hydration at ambient conditions. These anions were chosen because it is mostly used as an alkali-based chemical activator for C_2S. Therefore, β-C_2S synthesized via the Pechini method and the effect of varying water-to-solid ratio alongside chemical activation on the β-C_2S reactivity. The findings showed that carbonate increased the early hydration by 55% at the early stage which has been attributed to the simultaneous precipitation of C-S-H and calcite. But at a later stage, no hydration activity is attributed to the lack of transportable calcium ions between the solid surface and solution as confirmed by in-situ pH as well as conductivity measurements. The significant effect of sulphate ions was observed at later ages 14-28 days due to the dissolution of calcium sulphate at high pH promoting calcium silicate hydrate precipitation. The hydroxide ion exhibited no significant increase in hydration at any stage due to the early precipitation of portlandite and high solution pH. Overall, the β-C_2S reactivity in water exhibited the highest degree of hydration at 67% upon curing 28 days.

Chapter 7 deals with the in-depth hydration and leaching behaviour of air granulated BOF slag. The air granulated slag exhibited higher early-age (4 days) hydration than standard-cooled BOF slag. The hydration of the slag leads to the formation of hydration products such as C-S-H, hydrogarnet, and hydrotalcite (sjoegrenite). Moreover, the slag degree of hydration (DOH) reaches up to 41% after 28 days of curing. The formation of slag hydration products is controlled by the dissolution of SiO_2 and Fe_2O_3 bearing phases such as larnite and brownmillerite phases. The 2-1- and 4-2-mm slag fractions of 28 days hydrated slag sample immobilize the V up to 88% and 91% respectively. The 28-day hydrated 2-1 mm slag fraction immobilizes Cr up to 61% due to high DOH (41%) while the hydrated 4-2 mm slag fraction decreases Cr leaching up to 42%.

The eighth Chapter aims to understand the potential of air granulated BOF slag as a binder in mortars. The slag was substituted in OPC at replacement levels of 5, 20, 35 and 50%. The mechanical performance of the cement-slag composites is correlated with the hydration behaviour through thermal, mineralogical, and microstructural analysis. The

findings show that the granulation improved the grindability, reactivity, and compressive strength till 28 days. The 5% slag exhibited the synergy of mechanical performance while 35% performed better than quartz (an inert filler). The performance decline upon 20-50% replacements is attributed to the absence of brownmillerite reactivity of the slag. Overall, the granulation did not improve the cement-slag composite performance significantly till 90 days.

Chapter 9 focuses on valorizing the air granulated BOF slag with ye´elimite-based cement. Basic oxygen furnace (BOF) slag as a binder causes a negative effect on OPC performance upon exceeding the limit of 5% replacement. At the same time, a high-volume slag utilization is desired to benefit slag recycling as supplementary cementitious materials. Therefore, this study aims to optimize the air granulated BOF slag substitution potential in belite calcium sulfoaluminate cement (BCSA) by investigating the hydration products in standard mortar. Especially, the reactivity of BCSA-slag binder is correlated with workability and mechanical performance alongside volumetric stability. As a result, the 10-30% slag replacement delays the final setting time by inhibiting the ettringite formation leading to a decrease in mechanical performance till 28 days. At later ages (28-180), the 30-50% substitution exhibited the synergy of mechanical performance, which is attributed to the hydrogarnet, C-S-H, and strätlingite formation. Moreover, all BCSA-slag mortars exhibited heavy metals' leaching and drying shrinkage below the permissible limit.

In the final chapter 10, the summary of conclusions and recommendations for future work is precised. This research provides a detailed insight about the viability of air granulation of BOF slag, speciation of Cr and V in slag as well as in C_2S alongside leachability for fitness of the material for efficient recycling in building materials. Moreover, the hydration rate of sodium-based activators is discussed which emphases the importance of understanding C_2S reactivity. Overall, air granulation of BOF slag exhibited good grindability, high early-stage reactivity, immobilization of heavy metals as well as synergy of mechanical performance upon replacement in OPC (5%) and BCSA (30-50%). These characteristics of air granulated BOF slag will provide a fresh prospect for efficient recycling of the material.

CONTENTS

LIST OF FIGURES

LIST OF TABLES

CEMENT CHEMISTRY NOTATIONS

The cement chemistry notation used throughout the dissertation are stated below for a quick reference.

A	Al_2O_3
$\bar{C}$	CO_2
C	CaO
C_2A	$2CaO \cdot Al_2O_3$
CS	$CaO \cdot SiO_2$
C_3S	$3CaO \cdot SiO_2$
C_2S	$2CaO \cdot SiO_2$
$C_2(F,A)$	$2CaO \cdot Fe_2O_3 \cdot Al_2O_3$
$C_4A_3\ \bar{S}$	$4CaO \cdot 3Al_2O_3 \cdot SO_3$
F	Fe_2O_3
H	H_2O
K	K_2O
N	N_2O
$\bar{S}$	SO_3
S	SiO_2
T	TiO_2

ACRONYMS

BOF	Basic Oxygen furnace
BCSA	Belite calcium sulfoaluminate cement
BET	Brunauer–Emmett–Teller
EDX	Energy Dispersive X-ray spectroscopy
FTIR	Fourier transform Infrared Spectroscopy
GC	Gas chromatography
IBC	"Isoleren-Beheersen-Controleren" in Dutch
IC	Ion Chromatography
ICP	Inductively Coupled Plasma
ICSD	Inorganic Crystal Structure Database
L/S	Liquid-to-solid ratio
LOI	Loss on Ignition
OPC	Ordinary Portland Cement
PARC	PhAse Recognition and Characterization
PSD	Particle Size Distribution
PTE	Potentially Toxic Elements
SCM	Supplementary Cementitious Materials
SI	Spectral Imaging
SEM	Scanning Electron Microscopy
SQD	Soil Quality Decree
SSA	Specific Surface Area
TGA	Thermogravimteric Analysis
W/S	Water-to-Solid ratio
XPS	X-ray Photoelectron Spectroscopy
XRD	X-ray Diffraction
XRF	X-ray Fluorescence Spectroscopy

1 INTRODUCTION

1.1 BACKGROUND AND MOTIVATIONS

The steel industry produces approximately 2 Gt of steel annually worldwide. The annual global steel production increased from 0.2 Gt of crude steel to 1.8 Gt between 1950 and 2018. It is estimated that steel demand will increase from 1.6 Gt in 2020 to 2.5 Gt of crude steel by 2100 globally. Most of the steel is manufactured from the integrated routes as shown in Figure 1.1 [1–4]. In the steel-making process, the iron ores are reduced to molten iron by using coke as a reducing agent in the blast furnace first. Then, the molten iron from the blast furnace is poured into a basic oxygen furnace containing scrap metals.

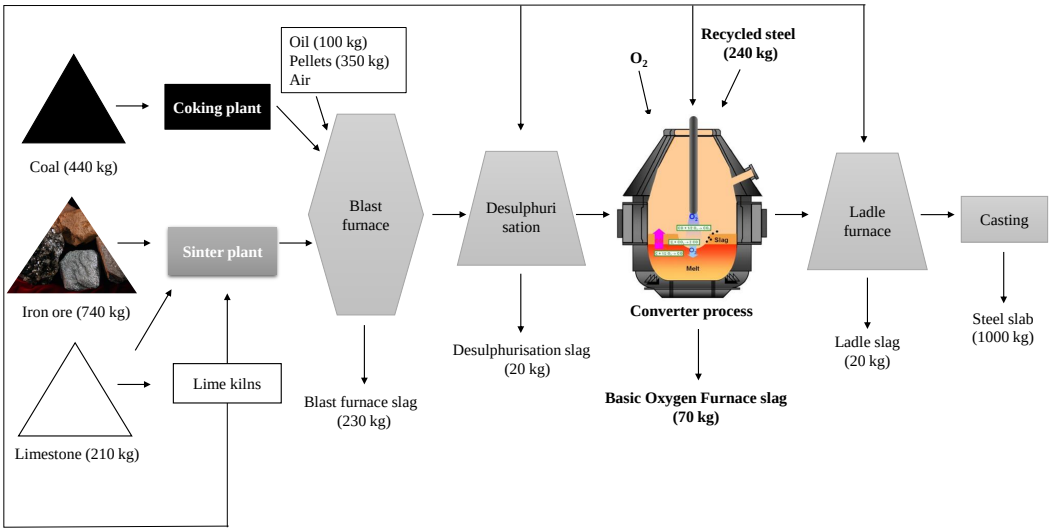

Figure 1.1: Schematic of steel production with the rough estimation of raw materials and byproduct streams in the parentheses. The arrows represent the flow of the steel-making process and the addition of raw materials at every step. Sulphur is an unwanted impurity in the steel and is removed by a process known as "desulphurisation". Overall, the slag rate and subsequent steel production steps vary with the production sites [1].

Subsequently, pure oxygen is blown into the furnace to oxidize carbon in molten iron to produce low-carbon steel. In the process, burnt dolomite is added to remove impurities from molten iron and crude steel leading to the formation of slags (a melt usually covering the surface of the molten metals). The slag from the basic oxygen furnace is called converter steel slag or Basic Oxygen Furnace (BOF) slag. The slag formation process is controlled by the reactions of hot metal oxidation products, SiO_2, MnO, P_2O_5, and FeO/Fe_2O_3 the fluxes, lime, and doloma (CaO-MgO) forming basic slag constituents [5]. The slags contain large amounts of calcium silicate alongside other compounds and can be recycled in various applications. But a significant portion of the

slag is either stockpiled or land filled due to increasingly tight environmental regulations [2].

The BOF route accounts for 70% of total steel production globally [6]. Around 70-110 kg of BOF slag is produced per ton of steel generation [7]. In Europe, the total production of steel furnace slag was 0.02 Gt in 2018 [8]. Out of all steel furnace slags, the BOF slag accounts for 52.3% of the total steel furnace slags in Europe as shown in Figure 1.2 [8, 9]. A small portion of BOF slag is recycled with added value in many countries while a high percentage is stockpiled or recycled at a significant rate, particularly in the Netherlands at the TATA steel facility. The residual steel slag is recycled in low-end applications in the construction industry such as aggregates [10, 11]. Considering the rate at which natural resources are being depleted, and the tremendous quantity of steel slag available, it is of great importance to take advantage of the material's properties and recycle steel slag as an efficient building material to reduce its environmental impact [12].

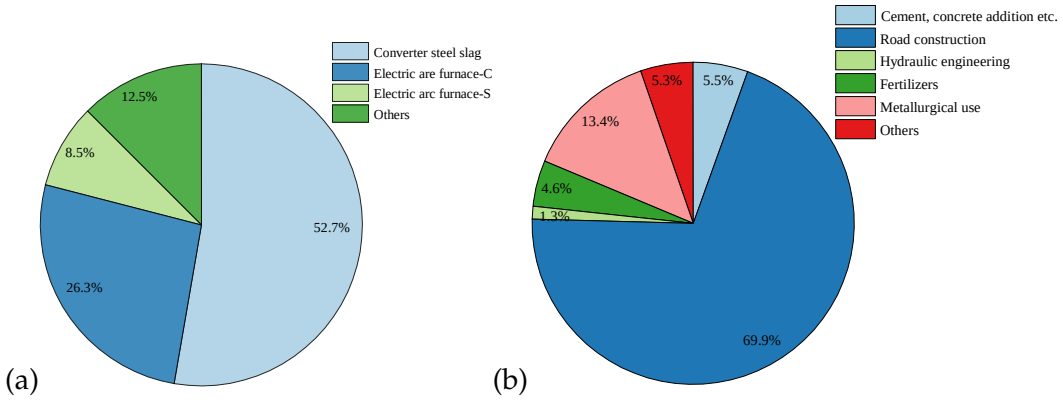

Figure 1.2: Steel furnace slag production and overall usage in Europe. The percentage is based on the data obtained from the Netherlands, Belgium, Bosnia-Herzegovina, Bulgaria, Czech Republic, France, Finland, Greece, Germany, Italy (partly), Luxembourg, Netherlands, Poland, Portugal, Romania, Slovak Republic, Slovenia, Sweden, Spain, and the United Kingdom [8].

The recycling and reuse of BOF slag carry many challenges [13, 14]. Several strategies have been reported to improve the BOF slag valorization, such as mineral modification, carbonation, weathering, mechanical and alkali-activation as well as high-temperature curing [15–18]. In particular, efforts are made to valorize BOF slag as fine aggregates for the development of geopolymer-based materials (high-end application) by mixing it with other waste streams such as fly ash, mine tailings, and blast furnace slag [19–24]. Moreover, the maximum 5% replacement as an alternative to blast furnace slag in cement production exhibited a promise for high-end application [6, 25]. However, no profound economical application has been reported yet. BOF slag contains dicalcium silicate (35-45 wt. %) and brownmillerite (20-30 wt. %) mineralogically, similar in phase composition to ordinary Portland cement (OPC) [26]. This makes BOF slag an ideal candidate for the replacement of clinker, and this approach can reduce the part of the limestone up to 160 kg/t as well as reduction in energy consumption up to 11.4 kg/t of clinker production [27]. Several technical problems, such as the intensification of clinkering reactions due to steel slag addition, discourage this application. However, the overall low reactivity of the BOF slag compared to Portland cement has hindered its

widespread use as supplementary cementitious material [28]. Due to the high strength and abrasion resistance of the BOF slags, it has found some use as aggregate in asphalt [10, 29, 30]. Other suggested uses include the production of fertilizer [31], the production of building materials via carbonation [32], or the recovery of vanadium via leaching [33]. However, the first two applications are only suitable for converter slag that contains no or very little vanadium and chromium due to concerns about leaching [34], while vanadium recovery is only feasible for slags containing sufficient vanadium.

1.1.1 *Chemical and mineral composition of BOF slag*

The average chemical oxide composition of the BOF slag has been shown in Table 1.1 [35, 36]. The oxide composition is variable, but converter slag tends to be very rich in CaO and Fe_2O_3 (30-50 wt. %), with lower amounts of SiO_2 and MgO (10 to 20 wt. %). Components such as MnO, Al_2O_3, P_2O_5, and TiO_2 are present as minor oxides (2-5 wt. %). The slag can contain V_2O_5 and Cr_2O_3 depending on the iron ore and recycled steel residues [26, 37].

Table 1.1: The average oxide composition of BOF slag.

Chemical Oxide	CaO	SiO_2	Al_2O_3	Fe_2O_3	MgO
BOF slag (wt. %)	38-46	10-15	1-3	20-30	7-9

The main mineral phases in the slag are α'-C_2S (α'-Ca_2SiO_4) βC_2S, (β-Ca_2SiO_4),(Fe, Mg)O and C_2(A, F) ($Ca_2(Al, Fe)_2O_5$) as presented in cement chemistry notation (1.1) [38]. Additionally, the magnetite (Fe_3O_4), alite (Ca_3SiO_5), free lime (CaO), and merwinite ($Ca_3Mg(SiO_4)_2$) can be present depending on the varying quality of the converter steel production [39, 40].

Table 1.2: The mineral composition of BOF slag.

Phase	Name	Content (wt. %)
Ca_2SiO_3	Hatrurite	0-5
α', β -Ca_2SiO_4	Larnite	35-45
$Ca_2(Fe, Al)_2O_5$	Brownmillerite/Srebrodolskite (solid solution)	20-25
CaO	Lime	0-10
(Fe, Mg)O	Magnesio-wüstite (solid solution)	20-30

1.1.2 *Dicalcium silicate (C_2S)*

C_2S is also a minor component of Portland cement clinker (5-10 wt. %) and is becoming more relevant due to the increasing use of alternative binders (belite clinkers contain between 40-60 wt. % belite mineralogically) [41, 42]. It is currently being investigated as a solution to reduce the CO_2 emissions of the cement industry as well as building materials that contain C_2S such as BOF steel slag [34, 43–46]. Therefore, it is important to understand the formation and hydraulic properties of C_2S which is complicated by the existence of five crystalline polymorphs (Figure 1.3) [47, 48]. The most common modification in the materials is β-C_2S. The thermodynamically stable polymorph at room temperature is γ-C_2S, which is highly undesirable in Portland cement due to the low hydraulic activity. The transition from α (orthorhombic) to β (monoclinic) is reversible while the transformation from β (monoclinic) to γ (orthorhombic) causes the irreversible disintegration of the beta phase due to microcracks because of a 14% increase in lattice volume in a phenomenon known as dusting. The C_2S reactivity, in general, depends on the polymorph, foreign ion substitution, and crystallite size. It is possible to stabilize polymorphs other than γ-C_2S at room temperature by the incorporation of dopants such as Al^{3+}, B^{3+}, P^{5+}, S^{6+}, Fe^{3+}, and K^{1+} [49]. The general order of reactivity of different polymorphs of C_2S is as follows [50, 51]:
Amorphous C_2S> α-C_2S> β-C_2S> γ-C_2S

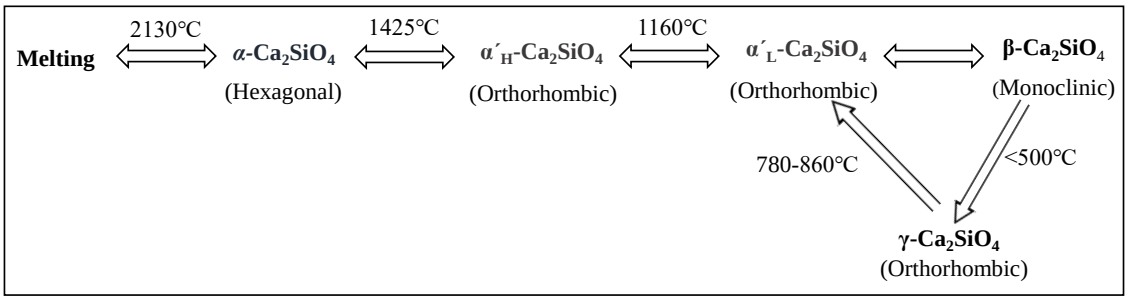

Figure 1.3: Different polymorphs of dicalcium silicate (C_2S) and their transition temperatures [44, 48].

1.1.3 *Activation of C_2S*

The main drawback that restricts the application of BOF is the low reactivity of β-C_2S leading to slow strength development [52]. The material admixture especially NaOH, KOH, C-S-H seeds, and commercial oxide nanoparticles, etc. is reported to accelerate the hydration of belite cement where the excess cumulative heat release is attributed to the β-C_2S reactivity [43, 47, 53]. Thus, a systematic understanding of the β-C_2S hydration rate via chemical activation is a prerequisite for its technical application.

1.1.4 *Immobilization of Cr and V in C_2S*

Cr and V are among the most hazardous heavy metals within the BOF slag [54]. The presence of V and Cr in BOF steel slag, its toxicity, and the potential mobility in leachate

have attained significant attention due to environmental implications. The leaching of several elements with permissible limits has been shown in the Table 1.3.

Table 1.3: The permissible emission limit of inorganic elements in three different types of building materials according to the Dutch soil quality decree (SQD).

Parameter	Shaped[1] E_{64} (mg/m^2)	Non-shaped[2] (mg/kg of dry mass)	IBC building materials[3] (mg/kg of dry mass)
Antimony (Sb)	8.7	0.32	0.7
Arsenic (As)	260	0.9	2
Barium (Ba)	1,500	22	100
Cadmium (Cd)	3.8	0.04	0.06
Chrome (Cr)	120	0.63	7
Cobalt (Co)	60	0.54	2.4
Copper (Cu)	98	0.9	10
Mercury (Hg)	1.4	0.02	0.08
Lead (Pb)	400	2.3	8.3
Molybdenum (Mo)	144	1	15
Nickel (Ni)	81	0.44	2.1
Selenium (Se)	4.8	0.15	3
Tin (Sn)	50	0.4	2.3
Vanadium (V)	320 [4]	1.8 [4]	20
Zinc (Zn)	800	4.5	14
Bromide (Br)	670 [5]	20 [5]	34
Chloride (Cl)	110,000 [5]	616 [4, 5]	8,800
Fluoride (F)	2,500 [5]	55 [5]	1,500
Sulfate (SO_4)	165,000 [5]	2,430 [5]	20,000

[1] Building materials have a minimum volume of 50 cm^3 and stable shape under normal conditions.
[2] Building materials are used freely such as aggregates.
[3] Building materials can only be used when isolation, management,
and control are applied (IBC stands for "Isoleren-Beheersen-Controleren" in Dutch).
[4] Building materials are used in large surface water bodies and for chloride of 1070 mg/kg dry matter (unformed).
[5] Direct contacts with seawater or brackish water with a naturally occurring chloride content of more than 5,000 mg/l:
a) no maximum emission values for chloride and bromide, and
b) the maximum emission values for fluoride and sulphate included in the table multiplied by a factor of 4.

V and Cr can get incorporated into the C_2S and therefore their mobility, as well as toxicity, depending on the chemical nature of the host matrix (redox potential, solubility, reactivity, etc.), oxidation state, and substitutable vacancy in the crystal lattice (Ca or Si-site) [53]. The aliovalent nature of Cr and V, and their tendency to occupy the Ca or Si site in C_2S dictates the enrichment mechanism in the host matrix and leaching behaviour [55–58]. Therefore, a good knowledge of V and Cr substitution in C_2S under varying

sintering (oxidizing and reducing) conditions is required to understand their chemical and environmental impact.

1.2 RESEARCH AIM AND STRATEGY

The technical aspects of basic oxygen furnace (BOF) slag as building material are extensively reported in the literature. But the material understanding especially the mineral composition, its correlation with reactivity, and speciation of heavy metals are often overlooked. These properties are highlighted under the effect of mechano-chemical activation, mineral modification, and varying cooling conditions. Overall, there is insufficient information available about the contribution of the slag's minerals specifically dicalcium silicate in the immobilization of potentially toxic elements (PTEs; Cr and V), its correlation with reactivity, and leaching behaviour. These properties become more relevant when BOF slag is subjected to a change in cooling method from standard cooling to air granulation and its potential application as supplementary cementitious material (SCM). It is important to mention here that no study has been reported on the systematic utilization of air granulated BOF slag from the in-depth characterization of material composition to the application as a binder. This project aims to develop an understanding of the effect of air granulation on the BOF slag, reactivity, and leaching behaviour of slag. BOF slag reactivity as well as Cr and V speciation is further investigated by ex-situ synthesis of the C_2S slag phase which accounts for 35-45 wt. % of the whole slag. Moreover, the mineralogy, reactivity, and application of air granulated BOF slag as a binder in different types of cement (OPC and BCSA) is investigated to utilize slag as supplementary cementitious material (SCM). The BOF slag application as a cementitious material will not only bring low costs of manufacturing to final products, but it will also assist in reducing the quantity of landfilled materials leading to efficient use of natural resources. For efficient recycling of BOF slag, a fundamental understanding of the slag is imperative.

The work of the thesis can be divided primarily into three distinct sections.

1. The first section deals with the impact of air granulation on the BOF slag mineralogy and leaching with an emphasis on the synthesis of β-C_2S via varying sol-gel methods, ex-situ mimicking of the slag's C_2S phases, immobilization of Cr and V on Si-site of C_2S, reactivity and leaching mechanism.

2. The second section describes the impact sodium oxide activation mechanism of β-C_2S with special reference to anions (OH^-, SO_4^{2-}, and CO_3^{2-}) to understand the hydration rate. Moreover, a detailed insight into the air granulated BOF hydration and immobilization of heavy metals to understand an efficient strategy for recycling.

3. The third/last section concerns the high-end application of air granulated BOF as a binder in OPC and BCSA types of cement with special emphasis on substitution optimization in mortar mix design.

This thesis provides detailed information about the impact of air granulation on mineralogy, reactivity, and leaching of BOF slag. The fundamental understanding of the

dicalcium silicate synthesis, its immobilization of Cr and V, associated reactivity as well as leaching behaviour. The detailed hydration of C_2S has been explored. Moreover, the substitutional potential of BOF slag as a binder has been optimized in OPC. Additionally, the high slag volume replacement in BCSA is explored to valorize slag as a building product.

1.3 OUTLINE OF THE THESIS

The main body and connection of the thesis are shown in Figure 1.4. The whole body of the work has been classified into three sections. The summary of every chapter is as follows.

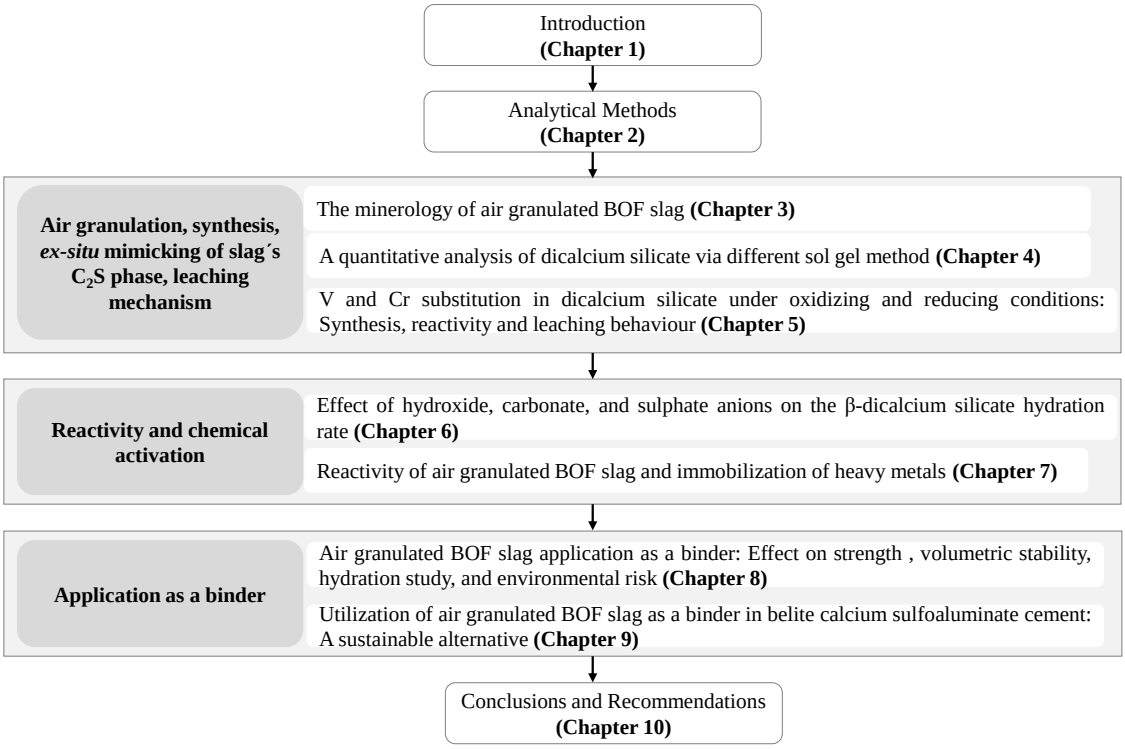

Figure 1.4: Outline of the thesis with the classification of the chapters.

Chapter 2 describes the air granulation of BOF slag that has been used alongside characterization as well as analytical methods employed to investigate the material.

Chapter 3 deals with the impact of air granulation on the mineralogy of the BOF slag. The quantification associated with crystalline and amorphous content of every slag fraction with special emphasis on the influence of size and cooling speed on its mineralogy e.g., α', β-C_2S. Moreover, the leaching of Cr and V is quantified concerning its localization in mineral phases.

Chapter 4 summarizes the synthesis of β-C_2S via Pechini, non-aqueous, and aqueous methods. The attention has been focused on comprehending the number of crystalline polymorphs, amorphous as well as residual and complementary forming phases. The intermediate dried gels have been investigated via thermal analysis to monitor changes in the gel structures and precursors at low temperatures. The synthetic parameters

including calcination time and temperature, Ca/Si molar ratio and mode of cooling have been optimized to get pure β-C_2S with low amorphous content.

Chapter 5 explains the ex-situ mimicking of the slag´s C_2S phase via doping Cr and V on Si-site in C_2S under oxidizing and reducing sintering conditions. The C_2S polymorphs stability, the effect of varying calcination conditions on heavy metals (Cr, V) incorporation as well as the oxidation state, and microstructure along with early age hydration is reported along with early age (48-72 h) hydration and the leaching behaviour.

Chapter 6 describes the effect of fixed (0.8M) Na^+ balanced by either (OH^-, SO_4^{2-}, and CO_3^{2-} anions on β-dicalcium silicate (C_2S) reactivity is investigated. The exothermic reaction of varying water-to-solid ratios and chemical activation is monitored. The order of hydration product formation and degree of hydration (DOH) is correlated with the anionic effect. Furthermore, the heat release is correlated with the concentration of hydroxyl ions alongside the ionic strength of the hydrating media at an early stage (1-5 days) to understand the β-C_2S dissolution-precipitation reaction events.

Chapter 7 is based on the continuation of the previous one about the characterization of the air granulation of BOF slag using the same air granulated slag. The two size fractions from 4-2- and 2-1-mm air granulated BOF slag were chosen as they yield 90% of air granulation of the BOF slag. The hydration (1-28 days) is investigated with special emphasis on slag reactivity, degree of hydration, and tendency to immobilize heavy metals (Cr and V) in hydration products.

Chapter 8 deals with the optimization of the substitutional potential of the air granulated BOF slag in OPC. The workability, mechanical performance, dimension stability, and environmental risk of 5, 20, 35, and 50% replacement clusters of OPC with slag as well as quartz powder were analysed over time. In addition to that, the cement-slag paste sample having the same mortar substitution factor was evaluated to understand the hydration behaviour for the novel binder application. Finally, the correlation between the chemically bound water of cement-slag pastes and the strength development of mortars as well as the potential leaching of heavy metals were reported.

Chapter 9 describes the high-volume slag utilization desired to benefit slag recycling as supplementary cementitious materials. For this purpose, the replacement of 10, 20, 30, 40, and 50% BCSA cement by the slag in mortars is chosen to optimize the substitutional potential. The effect of the BCSA-slag cluster's reactivity on workability, mechanical performance, and drying shrinkage over time is studied to understand the novel binder application. Moreover, the potential leaching of heavy metals especially V and Cr is evaluated to assess the environmental risk.

Chapter 10 provides some conclusions derived from the thesis. Moreover, the recommendation for further study.

2 MATERIALS AND METHODS

2.1 MATERIALS

2.1.1 *Air granulated BOF slag*

BOF slag is taken from regular production at Tata Steel Europe in Ijmuiden. The slag granulation was achieved by pouring it in front of a strong air fan. The tap temperature of the slag at the converter furnace was 1592 °C, and the batch size was 40 tonnes. It is known that approximately 40 °C drops occur in temperature at tapping. Further cooling of the slag can be considered negligible during transportation to the slag yard since it develops a self-insulating freeze lining against the slag pot (TATA proprietary reports). The slag temperature at granulation can, therefore, be expected to have been around 1550 °C. A batch of 36 tonnes of slag was granulated while 4 tonnes of freeze-on remained in the slag pot. As the exact cooling rate during granulation is unknown but predominantly depends on granule size. Consequently, the larger slag granules get cool slower than the smaller ones.

2.1.2 *Dicalcium silicate powder*

C_2S powder was synthesized in the lab through the different sol-gel methods exclusively the Pechini method, the aqueous and non-aqueous route. For this purpose, the calcium and silica oxide precursors were mixed in a stochiometric ratio (2:1) until stated otherwise [59]. A detailed information is provided in the section 4.3.

2.1.3 *Types of cement*

For ordinary Portland cement (OPC), the CEM-I 42.5 N (ENCI Heidelberg cement) was chosen as a binder replacement for air granulated BOF slag. Belite calcium sulfoaluminate (BCSA) cement is supplied by Vicat cement.

2.2 ANALYTICAL AND CHARACTERIZATION METHOD

2.2.1 *Representative sampling*

A representative sample was taken from every fraction of granulated BOF slag. For this purpose, a large-capacity static sample splitter was used equipped with adjustable chute bars and openings. The sieved sample was poured evenly into the hopper followed by passing through the gate release hopper. The divided powder sample was collected in two boxes. The process was repeated until a consistent distribution was achieved.

2.2.2 *Conventional sieving*

The received slag was sieved between 0.25 and 8 mm using a vibratory sieve shaker (Restch; AS 450 Basic) as shown in Figure 2.1. The same sieved batch was used for the mortar study in this whole thesis.

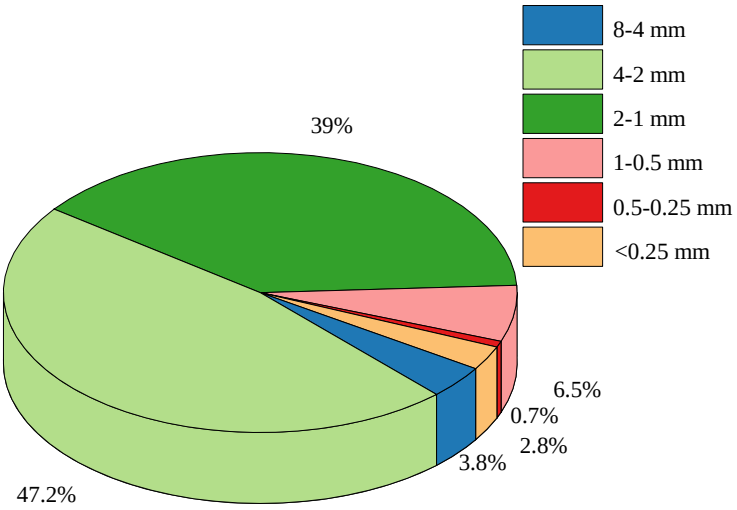

Figure 2.1: Air granulated BOF slag granulation yield.

2.2.3 *Mechanical grinding*

The air granulated BOF slag was then dried in an oven at 100 °C before grinding. The slag is grounded by using a disk mill (Retsch RS 300 XL) as well as a planetary ball mill (Pulverisette 5, Fritsch). Representative aliquots of 1 kg (0.25-8 mm) were added to a grinding jar of disk mill for 20-30 minutes at a constant speed of 912 per minute.

2.2.4 *Specific density and surface area*

The specific density of the milled and hydrated slag is tested by a Helium pycnometer (AccuPyc II 1340). To understand the impact of specific surface area (SSA) on the hydration kinetics, the nitrogen adsorption (Tristar II 3020 V1.03 series micrometer) at 77K was measured using BET (Brunauer-Emmett-Teller) methods.

2.2.5 *Particle size distribution*

The particle size distribution (PSD) was determined using Mastersizer 2000 from Malvern with Hydro 2000S wet unit and the powder sample was dispersed in isopropanol.

2.2.6 *Isothermal calorimetric analysis*

Isothermal heat conduction calorimetric measurements were conducted in TAM AIR isothermal calorimetric device at 20 ± 0.5 °C. Pre-determined amounts of the powders

were added to the vials. After acclimatization of the materials and hydration media to room temperature, the sample was mixed ex-situ. After the designated time, the hydration was stopped by the solvent exchange method (immersing in isopropanol followed by diethyl ether washing) [60].

2.2.7 *Thermal gravimetric analysis*

The thermal analysis was done on the samples using a Jupiter STA 49 F1 Netzsch instrument. The sample was heated from 40 to 1000 °C at the rate of 15 K/min under an air/N_2 environment.

2.2.8 *X-ray fluorescence*

Before XRF analysis, mass change was measured via heating slag samples at 1000 °C for 2 hours to calculate the loss on ignition (LOI). For the preparation of fused beads, the residue from the LOI was mixed with borate flux by keeping the sample to flux ratio (1:12) respectively, a mixture of 67% Li_2BO_7 and 33% $LiBO_2$ (Claisse). Moreover, 150 µL of 4 M LiBr was added to the mix as a non-wetting agent. The mixture was placed in a borate fluxer oven (classisse leNeo) for 24 mins at 1065 °C. The chemical oxide composition of the powder sample was determined with X-ray fluorescence (XRF; PANalytical Epsilon 3, standardless) using fused beads.

2.2.9 *X-ray diffraction*

X-ray powder diffractograms were acquired using a Bruker D2 and D4 diffractometer with an X-ray Co radiation X-ray source. The instrument has a fixed/variable divergence slit with an opening of 0.5° and 0.04 rad Soller slits. Reflections were measured between 5° and 90° 2 Theta (θ) with a step size of 0.02°. All samples for qualitative and quantitative analysis were prepared via back-loading. The mineral phases were identified with X'Pert Highscore Plus 2.2 employing the ICDD PDF-2 database. For QXRD (quantitative X-ray diffraction), the 10 wt. % Si was added to the hydrated samples. The samples were homogeneously mixed utilizing a McCrone micronizing mill. Quantification was done with TOPAS 4.2 software from Bruker. All crystal structures for quantification were obtained from the ICSD database. The error values given in the results are calculated by TOPAS.

2.2.10 *Average crystallite size*

The quantification and determination of the crystallite size of the synthesized product was measured by using TOPAS 4.2 Bruker software using fundamental peak fitting parameters. TOPAS applies peak shape (Lorenzt/Gaussian convolution-Voigt profile) to calculate crystallite size rather than FWHM (Full width at half maximum) at a given angle (Scherrer equation). LVol-IB was used to calculate FWHM and Integral breadth to get volume-weighted mean crystallite sizes. The value of dimensionless shape factor (K=constant) was 0.89 in TOPAS 4.2 Bruker software.

2.2.11 *X-ray photoelectron spectroscopy*

The XPS measurements are carried out with a Thermo Scientific K-Alpha, equipped with a monochromatic small-spot X-ray source and a 180° double-focusing hemispherical analyzer with a 128-channel detector. Spectra were obtained using an aluminum anode (Al Kα = 1486.6 eV) operating at 72 W and a spot size of 400 μm. Survey scans were measured at a constant pass energy of 200 eV and region scans at 50 eV. The background pressure was 2 x 10^{-9} mbar and during measurement 3 x 10^{-7} mbar Argon because of the charge compensation dual-beam source. The quantification was performed by using CasaXPS (version 2.3.23rev 1.2 k) software.

2.2.12 *Fourier transform infrared spectroscopy*

The IR spectra were measured with a Fourier transform infrared spectrometer (FT-IR) from Perkin Elmer Frontier FTIR. The spectrometer was equipped with the diffuse reflectance device Gladi. ATR. Sixty scans are acquired with optical retardation of 0.25 cm and a resolution of 4 cm^{-1} from 400 to 4000 cm^{-1}.

2.2.13 *Scanning electron microscopy*

Scanning Electron Microscopy (SEM) was performed using a Phenom Pro-X scanning electron microscope. The sample was prepared by spreading the powder on conductive carbon adhesive tapes followed by coating with gold employing Quorum 150 TS plus sputter coater. Micrographs were recorded using a backscattered electron detector (BSE) at 15 kV with a spot of four.

2.2.14 *Large area phase mapping*

The sieved slag granules and hydrated samples were embedded in resin (Struers EpoFix), cut, polished using alcohol-based diamond suspensions, and then coated with carbon before acquiring spectral imaging (SI) data sets for large area phase mapping. A JEOL JSM-7001F SEM equipped with two 30 mm^2 SDD detectors (Thermo Fisher Scientific) and NORAN-System 7 hardware with NSS.3.3 software was used, with an accelerating voltage of 15 kV and a beam current of 6.2 nA. One SI field consisted of a data set of 512 x 384 data points, with a data point size of 1 μm. To get representative data, several SI fields were measured, and their total area was 30.2 (4-2 mm), 16.7 (2-1 mm), 17.8 (1-0.5 mm), and 9.7 mm^2 (0.25-0.5 mm). The SI image sets were analyzed and stitched together using PhAse Recognition and Characterization (PARC) software developed by Tata Steel [26, 61]. PARC groups SI data points according to their composition determined with EDX and generates a phase map, phase amounts in area%, as well as the average composition of these phases. The chemical composition given here is the average of all SI fields analyzed, the error is the standard deviation between fields. To determine the size of the phenocrysts (C_2S and Mg-wüstite) in the air granulated BOF slag phase maps, Image J [62] was used. Areas smaller than 10 μm^2 were removed from further evaluation to avoid artifacts that can occur because the resolution of the EDX is only about 1 μm^2 and does not return accurate values for very small grains. The grains were then sorted

into size bins, normalized by the total area of the BOF slag granules measured for each size fraction, and recalculated to an equivalent diameter assuming a spherical shape for each grain. No stereological correction was applied to the data.

2.2.15 *Flowability and setting time*

The flow table was performed to measure the flowability of fresh paste according to EN 1015-3:2004. The water-to-binder (w/b) ratio was kept constant, and flow was adjusted with a superplasticizer (Sika ViscoFlow®-37 con. 32% SP-Polycarboxylate ether). The setting time is measured according to NF EN 196-3 with a Vicat needle.

2.2.16 *Drying shrinkage and mass loss*

The drying shrinkage and the drying mass loss were measured according to DIN 52450 to determine the long-term stability. For this purpose, the specimens were cured in an acclimatized room at 21 ± 2 °C and relative humidity of 60 ± 5% RH, where the measurement was carried out for the time being till a further change in values became constant.

2.2.17 *Mechanical performance*

The compressive and flexural strength of the mortar specimens were evaluated after 1, 3, 7, 28, 90, and 180 days. After casting, the specimen surface was covered with a thin film to prevent water evaporation besides carbonation and placed for curing under standard conditions (21 ± 3 °C, 95 ± 3% relative humidity). The compressive, as well as flexural strength, were measured at a speed of 2400 and 50 N/s respectively. The average of three specimens was calculated to evaluate the reproducibility of results.

2.2.18 *Leaching analysis*

One batch leaching test was performed on the sample according to EN 12457-2 using deionized water with a liquid-to-solid ratio of 10. The leaching test (EN 12457-2:2002 E) is applied for the characterization of granular material below 4 mm. Moreover, the one-batch leaching test provides comparable results with the column leaching test. The mixture was placed in plastic bottles and shaken continuously for 24 h at 21 ± 2 °C. After the experiment, the liquids were filtered through a 0.2 µm Polyether sulfone membrane and stored at 5 °C after acidifying with nitric acid (65% supra pure) to prevent precipitation. Before acidification, the pH was measured. Ion chromatography (IC) was employed to determine Ca, using a device from Thermo Fischer (Dionex ICS-1100). ICP-OES spectrometer (Spectroblue FMX36) was used for quantitative analysis of the leachate.

3 THE MINERALOGY OF AIR GRANULATED BASIC OXYGEN FURNACE SLAG

ABSTRACT

A fast cooling of BOF slag by air granulation would be a promising way to increase the reactivity of the slag generating amorphous phases. Therefore, air granulated BOF slag is characterized extensively. In this study, BOF slag was separated into different fractions (0.5-0.25 mm, 1-0.5 mm, 2-1 mm, 4-2 mm) after air granulation to study the effect of particle size and associated cooling speed on its mineralogy. The air granulated slag fractions were characterized using X-ray fluorescence, quantitative X-ray diffraction, large area phase mapping based on scanning electron microscopy, and energy-dispersive X-ray spectroscopy as well as leaching behaviour. The findings show that the main minerals in the air granulated slag are not significantly different from industrially cooled slag except for perovskite phase. All the fractions contained large phenocrysts of dicalcium silicate and Mg-wüstite surrounded by a dense matrix of other minerals. The three largest fractions (4-0.5 mm) exhibited the same oxide composition alongside microstructure, while the smallest fraction (0.5-0.25 mm) contains a relatively higher content of Mg-wüstite while having the same starting chemical composition. A negligible free lime content close to the detection limit 0.1 ± 0.1 wt. % of XRD in all size fractions was observed. The leaching of chromium and vanadium is increased significantly as compared to standard cooled BOF slag indicating that air granulation results in the greater dissolution of phases containing these elements despite low amorphous content.

Major part of this chapter is published elsewhere: K. Schollbach, M.J. Ahmed, S.R. van der Laan, The mineralogy of air granulated converter slag, Int. J. Ceram. Eng. Sci. 3 (2021) 21–36.

3.1 INTRODUCTION

The sustainability goals set by the Netherlands to reduce the use of raw materials 50% by the year 2030, emphasizes the importance of the efficient slag recycling [63]. One strategy to enhance the reactivity of BOF for an application in cement, is fast cooling through granulation to prevent crystallization [64]. This technique is already used to produce amorphous blast furnace slag that has excellent properties as a pozzolanic material in Portland cement [65]. Air granulation specifically is also a promising way to recover heat from the BOF slag that has a temperature between 1250 and 1700 °C when it is removed from the converter [66]. It could also help to stabilize C_3S, which is more reactive than C_2S [67]. The current industrial practice is to pour the liquid slag into pits and cool it using water. But the bulk of the slag still cools very slowly using this method (up to 24 h), and the resulting slag is reported to be almost completely crystalline [26, 68].

A few studies have investigated the influence of cooling speed on the BOF slag mineralogy using different approaches. For example, Choi and Jung [69] re-melted the BOF slag under an argon atmosphere and then cooled it at speeds between 10-50 °C/min starting from temperatures between 1600 and 1110 °C. They concluded that these conditions did not generate significant amounts of amorphous phase because the slag crystallizes very rapidly. Gautier et al. [69] compared water granulated, industrially cooled, and intentionally slow cooled BOF slag with each other. They found that the slow cooling promoted the formation of C_2S and MgO, while fast cooling resulted in the formation of C_3S that later converted to free lime and C_2S. The cooling speed also significantly influenced the crystallite size of the mineral phases. The connection between cooling speed and leaching properties was investigated by Tossavainen et al. [70], who compared water granulated and air-cooled with industrially produced converter slag. The results show a clear decrease in Ca, Fe, and Si leaching with increasing cooling speed. Overall, the literature is limited and to the best of the authors' knowledge there is no information available about air granulated BOF slag and a quantitative investigation of the influence of fast cooling on the BOF slag mineralogy is still missing.

This study investigates air granulated BOF slag sieved into different size fractions (4-2 mm, 2-1 mm, 1-0.5 mm, 0.5-0.25 mm) to gain information about the influence of the cooling speed. The chemical bulk composition was measured with XRF, while the mineralogical composition was determined using quantitative XRD, SEM/EDX based large area phase mapping using PARC (Phase Recognition and Characterization) software was employed to determine microstructure, phase amounts, and average compositions. One batch leaching test was carried out to determine the environmental impact and reactivity of the granulated slag. The results for the different slag sizes were compared with each other to gain insight into the state of BOF slag before granulation, its crystallization behavior, and the influence of the cooling speed, which forms the basis for understanding converter slag reactivity. In turn, this could enable the recycling of large amounts of BOF slag as a cement replacement material and reduce the CO_2 emissions of the building materials industry.

3.2 MATERIALS

BOF slag from regular production at Tata Steel Europe in IJmuiden was granulated at Harsco Metals Holland B.V. in a make-shift experimental facility by pouring it in front of a strong air fan (see section 2.1.1). The granulated slag was sieved in the lab and divided into the following size fractions: >4 mm (3.8 wt. %), 4-2 mm (47.2 wt. %), 2-1 mm (39 wt. %), 1-0.5 mm (6.5 wt. %), 0.5-0.25 mm (0.7 wt. %) and <0.25 mm (2.8 wt. %) (Figure 2.1. The fraction >4 mm consisted of welded smaller granules and was not investigated further. The fraction <0.25 mm was also excluded from further analysis, due to XRD measurements showing very high amounts of contamination that were likely introduced while collecting the granules from the slag yard. The fraction 0.5-0.25 mm also contained some contaminants such as blast furnace slag. Their influence on the analysis is discussed in the results. The complete mineralogical composition of all fractions is given in Table A.1 in the Appendix A.

3.3 RESULTS AND DISCUSSION

3.3.1 *Bulk chemical and mineralogical composition*

The mineralogical composition of the air granulated BOF slag size fractions is given in Table 3.1. The standard converter slag phases C_2S, (Fe,Mg)O, and srebrodolskite ($Ca_2(Fe,Al)_2O_5$) [26, 71] were detected. C_2S is present as the α'_H and β polymorphs in all granulated slag fractions, which is commonly the case in the industrially cooled BOF slag [26]. In addition, several new phases were identified: perovskite $CaTiO_3$, pseudobrookite Fe^2TiO_5, rutile TiO_2, titanite $CaTiSiO_5$, protoenstatite $(Mg,Fe)SiO_3$, and naquite FeSi. There were also phases present, especially in the smallest fraction, that are not BOF slag minerals, e.g., quartz SiO_2, calcite $CaCO_3$, or corundum Al_2O_3. The presence of corundum is an artefact of the sample preparation with the McCrone XRD mill (Retsch), using corundum grinding elements. The other phases likely became mixed with the granulated slag while collecting the granules in the slag yard. Calcite and vaterite are also weathering products of BOF slag. To compare the fractions with each other the contamination phases were removed, and the rest recalculated to 100 wt. % as shown in Table 3.1 and Figure 3.1 show the results, the original quantification including contaminants is given in Table A.1, Appendix A. It is worth mentioning here that the slag contains almost no free lime.

The three largest granulated slag fractions are very similar. The overall C_2S content is the same (41 to 44 wt. %), but the β-C_2S content in the granulated converter slag increases with increasing granulated slag size fraction, while the α'_H-C_2S decreases (from 28 to 22 wt. %). This is likely an effect of the slower cooling of the larger slag fractions, which allows for the transformation of more α'_H-C_2S, which is stable at higher temperatures, into β-C_2S. Only γ-C_2S is stable at room temperature, but the other high-temperature polymorphs can be stabilized by rapid cooling and the incorporation of minor ions [72, 73]. The srebrodolskite ($Ca_2(Fe,Al)_2O_5$) content increases with increasing fraction size, while the perovskite ($CaTiO_3$) content decreases. The srebrodolskite ($A_2B_2O_5$) structure can be regarded as an anion-deficient analogue of perovskite (ABO_3) and a solid solution between both minerals exists [74] that can be

described by the exchange mechanism $Fe^{3+}(B)+0.5(O) \leftrightarrows Ti^{4+}(B)+0.5O^{2-}(O)$ in conjunction with the simplified endmember components $Ca(A)Fe(B)O_{2.5}$ and $Ca(A)Ti(B)O_3$. The larger slag fractions cool slower, which gives srebrodolskite more time to form. This also fits with the observation that the sum of srebrodolskite and perovskite stays roughly the same in the three largest fractions (32 to 35 wt. %). The amorphous content of the three largest granulated slag fractions is low overall and follows no clear trend.

Table 3.1: Mineralogical composition of granulated BOF slag without contaminants is quantified by QXRD. The error values are calculated by TOPAS.

Phase	**Formula**	**4-2 mm**	**2-1 mm**	**1-0.5 mm**	**0.5-0.25 mm**
Larnite, β-C_2S	Ca_2SiO_4	22 ± 0.5	19.4 ± 0.5	14.5 ± 0.5	8.1 ± 0.7
α´$_H$-C_2S	Ca_2SiO_4	21.9 ± 0.9	22 ± 0.9	27.6 ± 1.0	25 ± 1.6
Mg-Wuestite	(Fe,Mg)O	15.5 ± 1.2	15.4 ± 0.9	15.5 ± 0.8	13.5 ± 0.4
Srebrodolskite	$Ca_2(Fe,Al)_2O_5$	25.2 ± 0.3	22 ± 0.3	21.7 ± 0.3	16.5 ± 0.5
Perovskite	$CaTiO_3$	7.9 ± 0.2	10.3 ± 0.2	13.1 ± 0.2	11.1 ± 0.3
Magnetite	Fe_3O_4	2.6 ± 0.1	2.1 ± 0.1	2.9 ± 0.1	8.7 ± 0.3
Pseudobrookite	Fe_2TiO_5	0.3 ± 0.1	0.3 ± 0.1	0.3 ± 0.1	0.1 ± 0.1
Lime	CaO	0.1 ± 0.1		0.1 ± 0.1	
Protoenstatite	$Mg_2Si_2O_6$	1.3 ± 0.1	0.7 ± 0.2		
Naquite	FeSi	0.7 ± 0.1	0.5 ± 0.1	0.6 ± 0.1	0.4 ± 0.1
Titanite	$CaTiSiO_5$				0.6 ± 0.1
Rutile	TiO_2	0.4 ± 0.1	0.4 ± 0.1	0.5 ± 0.1	
Amorphous		2.1 ±1.8	7 ± 1.5	3.1 ± 1.8	15.9 ± 1.4
$Ca_2(Fe,Al)_2O_5$ + $CaTiO_3$		33.1	32.3	34.8	27.6

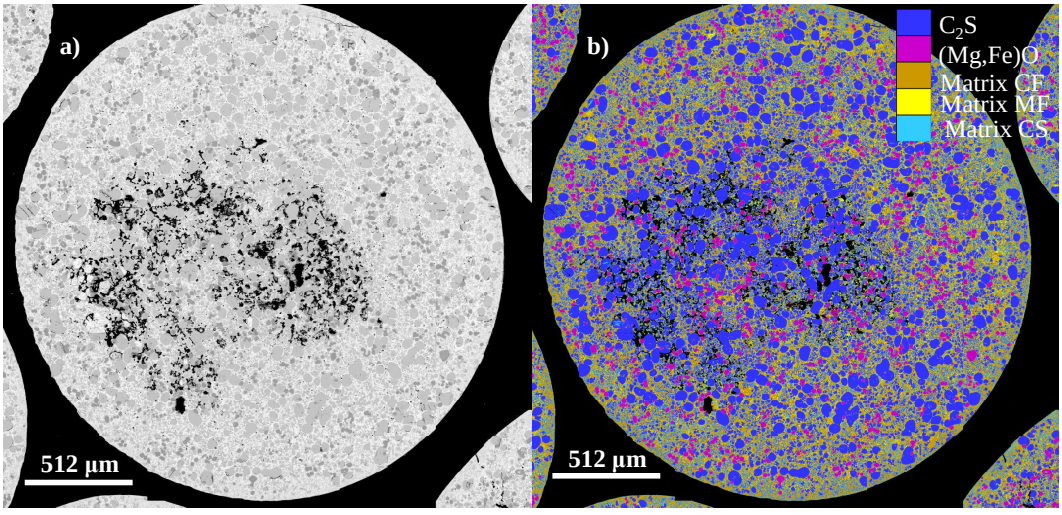

Figure 3.1: Air granulated converter slag 4-2 mm a) SEM greyscale image b) EDX based phase map.

The smallest granulated slag fraction (<0.25 mm) contains a noticeably lower amount of β-C_2S, while the amorphous content is much higher than in the other fractions (15.5 wt. %). This could indicate that the amorphous phase is generated during air granulation, however, this value is not reliable because the sample is contaminated with blast furnace slag, which is amorphous (Figure 3.2). The high content of magnetite (Fe_3O_4) indicates that this fraction is more oxidized than the larger ones due to the higher surface area that encounters air during cooling. Iwasaki [38] discusses the effect of oxidation on BOF slag and also mentions the formation of magnetite as well as a srebrodolskite/perovskite solid solution. No C_3S and practically no free lime (CaO) was detected in the samples. The absence of these phases could simply be a matter of an inappropriate chemical composition of the slag for crystallization of these phases. However 1-2 wt. % free-lime commonly forms in BOF slags at near-solidus conditions [75, 76], which may have been avoided with the rapid fractional crystallization occurring during air granulation.

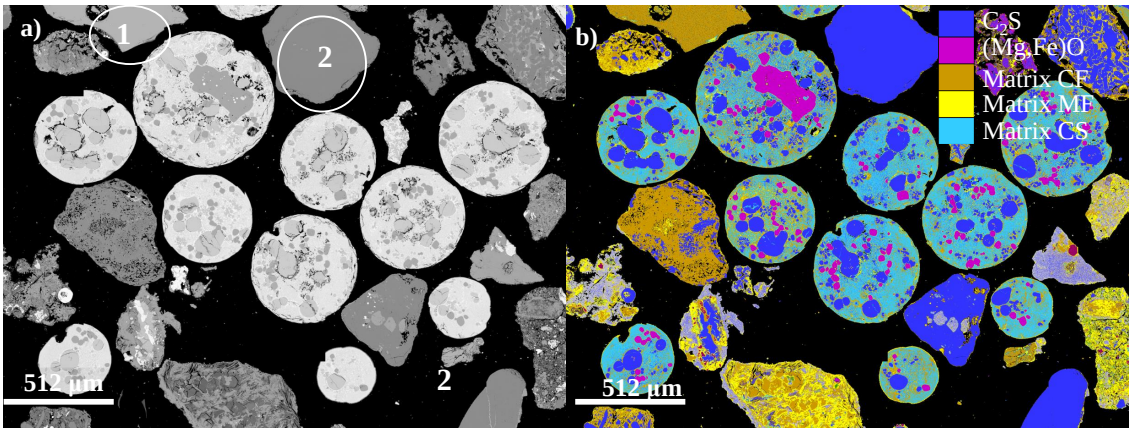

Figure 3.2: Air granulated converter slag 0.5-0.25 mm surrounded by other grains a) SEM greyscale image 1- blast furnace slag 2- quartz b) EDX based phase map.

The oxide composition of all air granulated BOF slag fractions is given in Table 3.2. The two largest fractions show a small gain on ignition due to the oxidation of Fe^{2+} to Fe^{3+}, while the two smallest fractions lost weight, mainly due to the decomposition of calcite [60]. Around 2/3 of the total iron content in the slag is Fe^{2+}, the rest is present as Fe^{3+}. Table 3.2 only shows the amount of Fe_2O_3 because fused beads were made for the XRF analysis, and the process oxidizes all Fe^{2+} to Fe^{3+}. Chemically the 4-2 , 2-1, and 1-0.5 mm fractions of air granulated BOF slag are very similar and well within the range of industrially cooled BOF slag reported in the literature [26, 68, 70]. The 0.5-0.25 mm fraction however shows a much higher Al_2O_3 and SiO_2 content, while CaO and MgO are lower. The SiO_2 content is likely influenced by the 8.9 wt. % quartz contained in the sample (Table A.1), while the deviating Al_2O_3, CaO, and MgO contents are caused by the presence of amorphous contaminants such as blast furnace slag (Figure 3.1).

3.3.2 *Microstructure and mineralogy determined by large area phase mapping*

To study the influence of rapid cooling on the microstructure and composition of the mineral phases large area SEM/EDX phase mapping was carried out using PARC. The

results for the 4-2 and the 0.5-0.25 mm fractions are given in Figure 3.1, Figure 3.2, respectively. The phase maps of the other two fractions are shown in the Appendix (Figures A.1 & A.2). Granules of the same size developed strikingly similar crystallization microstructures and only one representative granule is described here in detail to highlight the characteristic features of its size fraction. All granulated slag fractions contained large crystals of C_2S and (Mg,Fe)O that are embedded in a fine-grained matrix that is a mix of different minerals with a size below the EDX resolution of 1 µm. Similar observations were made by other researchers [69, 70].

Table 3.2: Chemical bulk composition of air granulated BOF slag size fraction measured with XRF.

Fraction	MgO	Al_2O_3	SiO_2	P_2O_5	CaO	TiO_2	V_2O_5	Cr_2O_3	MnO	Fe_2O_3	LOI	*GOI
4-2 mm	8.9	2.0	15.5	1.5	45.6	1.5	0.6	0.2	4.2	20.5		0.8
2-1 mm	8.8	2.1	15.4	1.5	45.3	1.5	0.6	0.2	4.2	20.6		0.5
1-0.5 mm	8.5	2.9	15.3	1.5	44.0	1.5	0.6	0.2	4.1	21.1	0.2	
0.5-0.25 mm	5.8	7.9	19.9	1.0	30.4	1.2	0.4	0.2	2.7	24.9	5.6	

*GOI= Gain on ignition due to conversion of ferrous oxide into ferric oxide

Based on variation in Ca – Si composition the matrix was divided into 3 groups using a density plot (Figure 3.3). These groups were named Matrix CF (CaFe), CS (CaSi), and MF (MgFe) according to the major elements present. Very small amounts of CaO and (Ca,Mg)O phase were also detected. The area% of each phase is given in Figure 3.5a, the average chemical composition of the major phases in Figure 3.4 and Figure 3.5 (b, c, d). The results are free from the influence of contaminants because only SI fields containing BOF slag grains were analyzed.

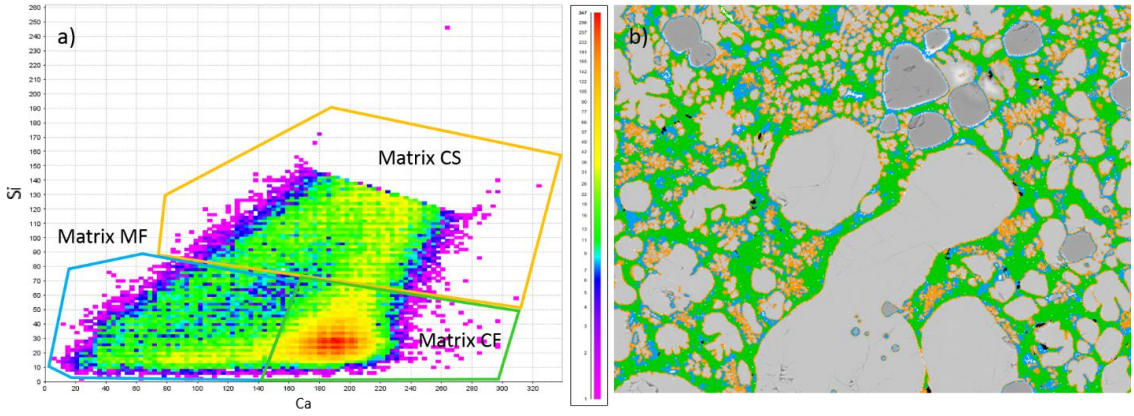

Figure 3.3: a) PARC density plot for all data points belonging to the matrix phase and their division into 3 matrix parts. The intensity of the Ca Kα peak is plotted against the intensity of Si Kα, the colour indicates the density of overlapping data points. b) Corresponding areas in a SI data field of air granulated BOF slag.

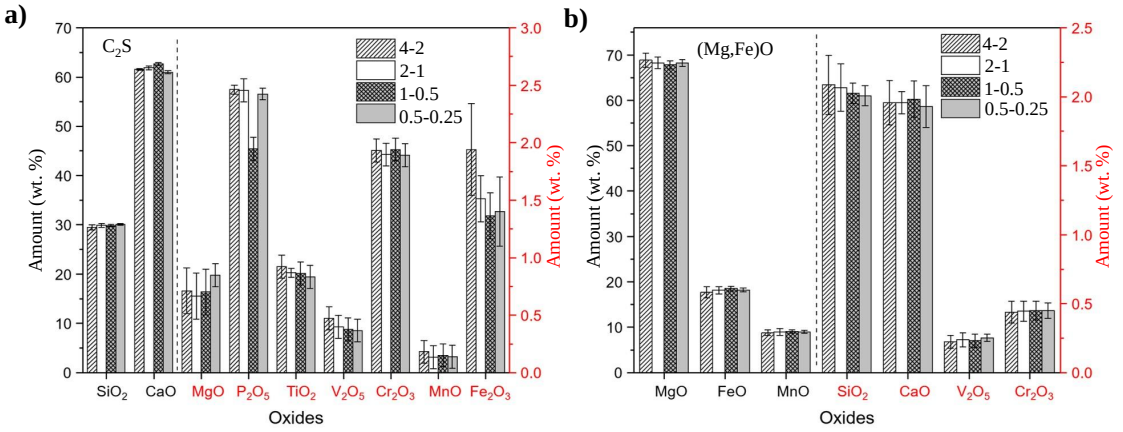

Figure 3.4: Average composition of a) C_2S and b) (Mg,Fe)O phenocrysts related to the grain size of the air granulated converter slag. Note the difference in scale for major and minor oxides.

a)

	Fraction	C_2S	(Mg,Fe)O	CaO	(Mg,Ca)O	Matrix		
						CF	MF	CS
Area%	2-4mm	43.9	6.7	0.5	0.3	27	9.2	12.5
	1-2mm	40.5	6.2	0.5	0.3	24.5	8.7	19.2
	0.5-1mm	29	6.7	0.4	0.5	23.8	11.5	28.1
	0.25-0.5mm	21.1	10.3	0.4	0.4	16.2	6.5	45
wt. %	2-4mm	39.5	7.9	0.6	0.4	28.0	12.5	11.2
	1-2mm	36.7	7.3	0.6	0.4	25.6	12.0	17.4
	0.5-1mm	26.1	7.9	0.5	0.6	24.7	15.1	25.3
	0.25-0.5mm	19.5	12.4	0.5	0.5	17.2	8.4	41.6
	Density (g/cm³)	3.3	4.2	3.3	3.4	3.8	4.3	3.3

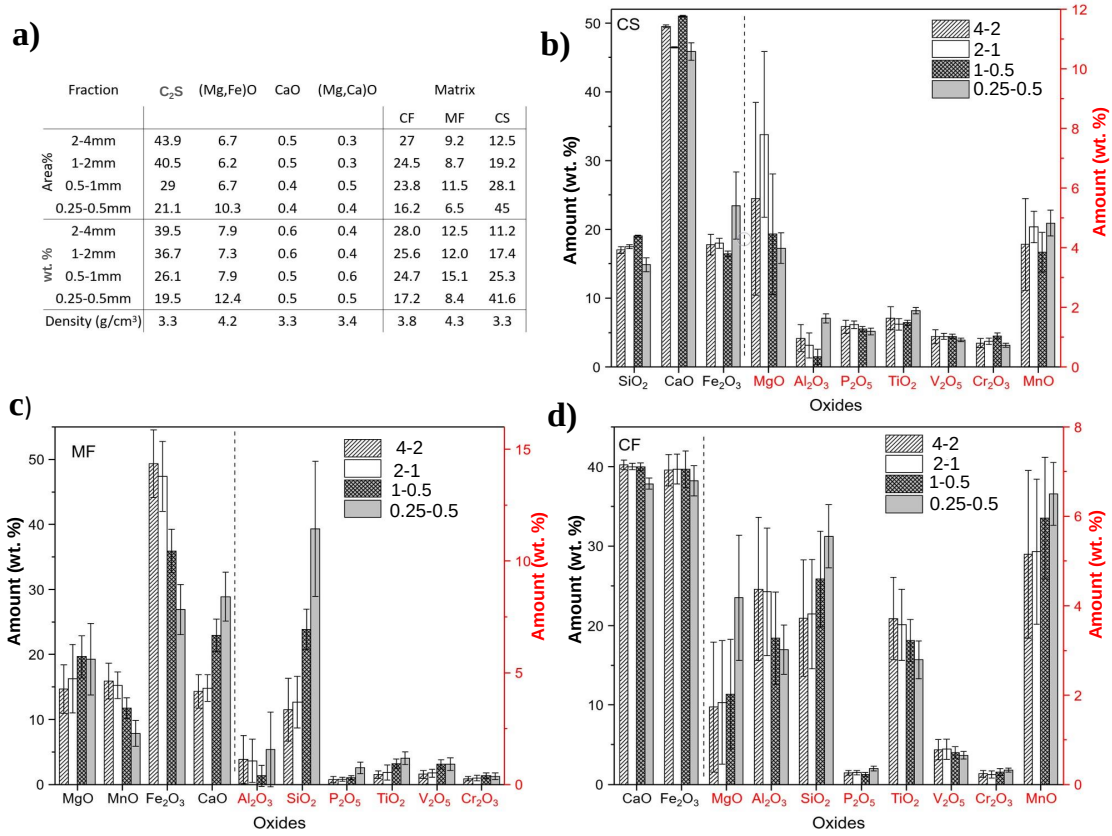

Figure 3.5: Results of PARC analysis a) Phases in air granulated converter slag in area% and wt. % including the densities used for conversion from area% into wt. % b) Composition of the CS matrix part c) Composition of the MF matrix part d) Composition of the CF matrix part. Note the difference in scale for major and minor oxides.

There is a clear correlation between slag size fraction and phase content in area%. The largest fraction (4-2 mm) contained the highest amount of C_2S and the lowest total

amount of matrix phase, while the opposite was true for the smallest fraction (0.5-0.25 mm). The 0.5-0.25 mm fraction also contained the largest amount of the calcium and silica-rich Matrix CS, which reduced with increasing size fraction (Figure 3.5a). This is a clear indication that lower cooling speeds allow for the growth of C_2S out of this matrix part. This is also corroborated by the microstructure itself (Figure 3.6). In the 0.5-0.25 mm fraction, the C_2S is present as large, round phenocrysts. They form in the liquid slag before granulation at temperatures of around 1550 °C [69] and can be regarded as equilibrium crystallization. In the larger slag fractions, the C_2S shows leaf-like shapes that are formed during granulation and can be regarded as quench crystallization because they form after the equilibrium C_2S during cooling. These shapes are likely connected, three-dimensional structures in the slag. It should be noted that PARC cannot differentiate between C_2S polymorphs, because their chemistry is the same.

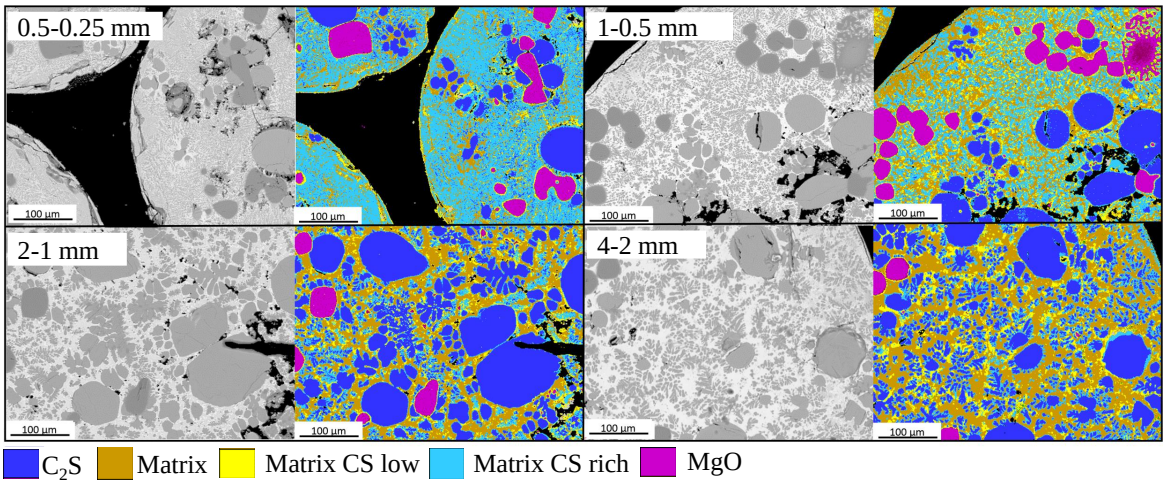

Figure 3.6: Formation of C_2S out of the CS rich matrix with increasing air granulated BOF slag size fraction/decreasing cooling speed. The C_2S present in the 0.5-0.25 mm fraction is the equilibrium C_2S formed before granulation. The quench C_2S forming during cooling shows a leaf-like structure.

The composition of C_2S (Figure 3.4) changes with increasing slag size fraction and becomes more iron rich. The V_2O_5 and TiO_2 contents also increase slightly, because the quench C_2S incorporates more minor ions as the composition of the liquid slag changes during cooling [77]. We are aware that the Cr_2O_3 content in the C_2S is higher than the true value by about an order of magnitude due to the Si + Ca sum peak in the C_2S spectrum overlapping with the Cr Kα emission line. No C_3S was formed based on the microstructure of the granulated slag. C_3S forms at higher temperatures than C_2S as well-defined euhedral crystals but requires a more calcic slag composition. These C_3S crystal shapes are preserved during cooling even if the C_3S itself converts to C_2S and CaO [26, 78].

Most equilibrium C_2S phenocrysts in the smallest granulated slag fraction have a diameter of around 9 µm (Figure 3.7 (a)). It can be assumed that this is very close to the average size the phenocrysts had in the liquid slag before cooling, because the smallest fraction cools so quickly that there is little time for further (quench) C_2S to form. With increasing fraction size many small grains (around 2 µm in diameter) appear due to the formation of quench C_2S in leaf-like shapes. At the same time, the number of very large

(15-30 μm) C_2S phenocrysts increases slightly. This shows that C_2S continues crystallizing and growing during cooling. The bigger granulated slag fractions cool slower and allow more time for the leaf-like patterns to form. This quench C_2S also grows on the equilibrium phenocrysts increasing their average size. According to the XRD results, the α'-C_2S content changes very little in the different granulated slag sizes. However, the β-C_2S content increases with increasing droplet size, which indicates that the quench C_2S in the leaf-like patterns is largely β-C_2S. The exact cooling rate of the granulated slag fractions is unknown, but the amount of quench C_2S is similar to that observed by Gautier et al. [69], who used water quenching and estimates a cooling time of 3-5 seconds. It is likely that water quenching is less effective for rapid cooling of converter slag than for blast furnace slag due to its self-insulating properties. The cooling speeds of air and water granulation could therefore be in a similar range.

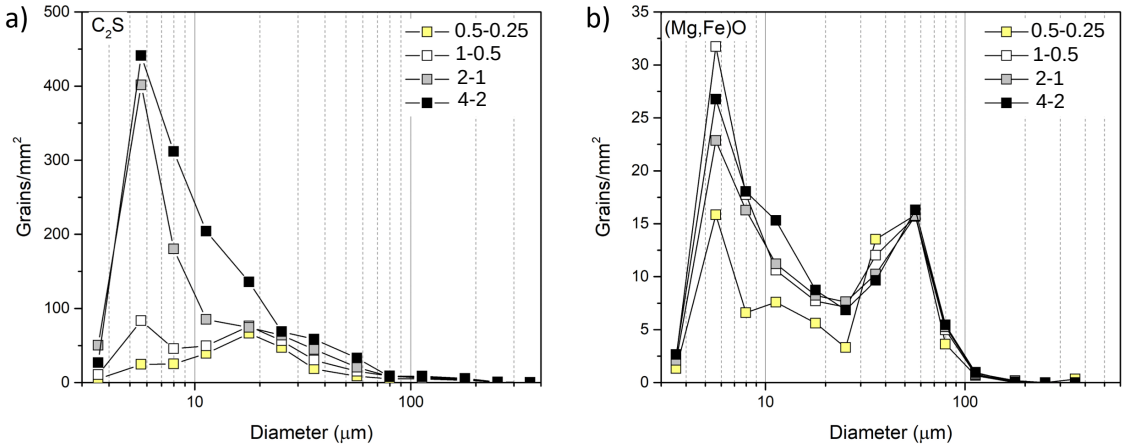

Figure 3.7: Size distribution of a) C_2S and b) (Mg,Fe)O crystals in air granulated BOF slag. The diameter is calculated from the grain area assuming perfect circular shape. The number of grains is normalized by the total area measured.

(Mg,Fe)O is the other phenocryst phase present in the air granulated BOF slag. Calculations with FactSage (a software suite for thermodynamic calculations) show that it starts crystallizing at around 1840 °C for this slag composition. Some C_2S phenocrysts in the samples contained (Mg,Fe)O inclusions showing that it forms at higher temperatures than the C_2S (Figure 3.6, 1-0.5 mm). This order of crystallization was also found by other researchers [69]. The (Mg,Fe)O content in the 3 largest granulated BOF slag fractions was between 6.2 and 6.7 area%, while the 0.5-0.25 mm fraction contained 10.3 area% (Figure 3.4a). There is a clear correlation between the size fraction and phenocryst size distribution (Figure 3.7b).

The smallest granulated slag fraction (0.5-0.25 mm) shows a bimodal distribution with maxima at around 3 and 25 μm. This may be due to the fact that some of the (Mg,Fe)O is present as small inclusions in the C_2S, which are prevented from further growth during cooling of the slag. With increasing droplet size the first maximum increases in intensity showing that new, small (Mg,Fe)O is formed with decreasing cooling speed. However, the size of the largest (Mg,Fe)O phenocrysts remains largely unchanged. The amount of matrix decreases with increasing droplet size and decreasing cooling speed from around 68 area% (0.5-0.25 mm) to 49 area% (4-2 mm). As discussed previously, the Matrix CS

part forms C_2S but does not change its average composition with changing cooling speed (Figure 3.5b). There is also a clear increase in the amount of Matrix CF with slower cooling. This matrix part is rich in CaO and Fe_2O_3 (Figure 3.5d) and contains the majority of Al_2O_3 and TiO_2 present in the slag. Based on the composition this PARC phase contains the srebrodolskite ($Ca_2(Fe,Al)O_5$) detected in XRD together with the other TiO2 bearing phases (Table 3.1, Figure 3.2). Srebrodolskite ($Ca_2(Fe,Al)O_5$) is the last phase to form during standard cooling of BOF slag, as can be seen from the texture of industrially cooled slag. More Matrix CF is generated the slower the granulated slag cools, while its average composition changes only slightly. With increasing size, it becomes richer in Al_2O_3 and TiO_2, while the MgO, SiO_2, and MnO content decreases.

The amount of MF matrix (6.5-11.5 area%) shows no clear correlation with the slag fraction size but has the greatest variation in composition. The iron and manganese content decreases with decreasing slag size, while the CaO, SiO_2, and MgO contents increase. Based on this trend it can be assumed that (Mg,Fe)O grows out of this matrix phase during cooling. The formation of new (Mg,Fe)O can also be seen in the phenocryst size distribution (Figure 3.7b). BOF steel slag is generated in batches and can be quite variable in composition, depending on the quality of steel produced. However, the general crystallization behaviors described here are expected to apply to other slag compositions as well, especially those that contain little free lime, even if the phase proportions may be different.

3.3.3 *Influence of granulation on phase distribution and chemical bulk composition*

It is possible to calculate the chemical bulk composition of each granulated BOF slag fraction out of the PARC data if the phases are converted from area% into wt. % using their densities (Figure 3.5a). For C_2S and (Mg,Fe)O the appropriate density can be taken directly from the Rietveld refinement results. They are 3.3 and 4.3 g/cm^3 respectively. Assigning a density to the three matrix phases is less straightforward because they are a mix of different minerals. However, it is clear that the Matrix CS phase reacts to C_2S during cooling, the Matrix MF phase contains mostly (Mg,Fe)O, and that the Matrix CF phase is very rich in srebrodsolskite ($Ca_2(Fe,Al)O_5$). For this reason, they can be assigned the densities of C_2S, (Mg,Fe)O and srebrodolskite (3.8 g/cm^3 based on Rietveld refinement), respectively. The phase composition in wt. % can be seen in Figure 3.5 and the calculated bulk composition in Table 3.3.

Table 3.3: Chemical bulk composition of air granulated converter slag size fractions determined via PARC. All results are given in wt. %.

Size	MgO	Al_2O_3	SiO_2	P_2O_5	CaO	TiO_2	V_2O_5	Cr_2O_3	MnO	Fe_2O_3
4-2 mm	8.7	1.5	15.2	1.2	43.4	1.7	0.6	1.0	4.7	21.7
2-1 mm	9.1	1.4	15.6	1.2	43.4	1.6	0.6	1.0	4.7	21.1
1-0.5 mm	10.2	1.0	15.0	0.9	43.1	1.5	0.7	0.9	5.0	21.5
0.5-0.25 mm	12.6	1.3	14.2	1.1	40.5	1.5	0.7	0.8	4.9	21.5

For the three biggest fractions the measured XRF bulk composition (Table 3.2) matches the calculated bulk composition very well, but there is a big difference for the 0.5-0.25 mm fraction due to the contamination with other minerals. It is also clear that the Cr_2O_3 content is overestimated by an order of magnitude in the calculated

composition for reasons explained before. But this does not influence the other oxide amounts in any significant way.

This calculated chemical bulk composition has the advantage of being free from contaminant influence because non-slag phases can be excluded from phase mapping with PARC, even if they are amorphous. It also shows that the deviating bulk composition of the 0.5-0.25 mm granulated slag fraction is not just an effect of contamination. This is unexpected because all slag fractions were derived from the same converter slag batch. The likely explanation is an uneven distribution of the C_2S and (Mg,Fe)O phenocrysts in the different droplets, which affects their bulk composition. To visualize if accumulation/depletion of phenocrysts is the cause of the compositional differences, variation diagrams have been constructed in which the element-oxide components are plotted against CaO (Figure 3.8). In these diagrams, the bulk composition of each converter slag fraction is represented as well as the compositions of the (Mg,Fe)O and C_2S phenocrysts (Figure 3.4). Element oxides that lie on a straight line indicate a compositional relationship derived by the addition or subtraction of C_2S and (Mg,Fe)O phenocrysts respectively. Relative proportions of each phase can be calculated with a lever-rule approach. Oxide (Mg,Fe)O/Oxide C_2S are the oxide concentrations in the (Mg,Fe)O and C_2S phenocrysts as determined with PARC (Figure 3.4).

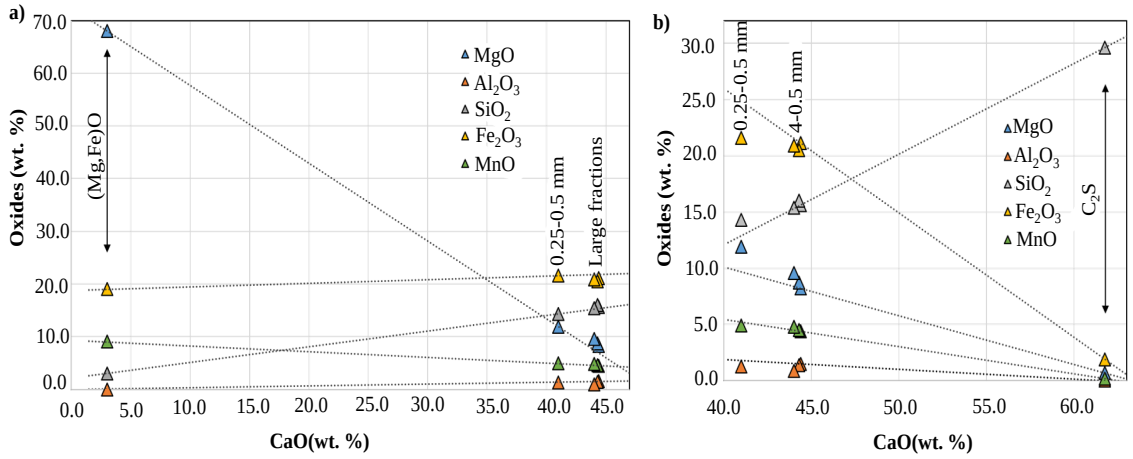

Figure 3.8: Variation diagram a) addition of (Mg,Fe)O b) addition of C_2S to air granulated BOF slag.

The variation diagrams show that the composition of the three largest granulated slag fractions is consistent with the composition of the smallest slag fraction (0.5-0.25 mm) containing more (Mg,Fe)O (in the range of 5 to 10 wt. %). If C_2S is added to the 0.5-0.25 mm fraction instead, the Fe_2O_3 and SiO_2 concentrations of the larger slag fraction are relatively far outside the range. This means the different composition of the smallest slag fraction is likely caused by an enrichment of (Mg,Fe)O phenocrysts and not by a lack of C_2S. The reason for this is unclear, but may be connected to the bimodal size distribution of the (Mg,Fe)O or the granulation process itself.

3.3.4 *Vanadium and chromium leaching*

The environmental properties of the BOF slag were measured using the one batch leaching test and the results are shown in Table 3.4 along with the pH of the leachate. Chromium and Vanadium are the only elements above the legal limit defined in the Dutch soil quality decree for all fractions and much higher than observed for normal industrially cooled slag.

Table 3.4: Leaching data ICP analysis of the one batch leaching test and pH of the leachate. The legal limit is the limit set by the Dutch soil quality decree for unbound material. Left measured value, right values corrected for contaminants. All results in mg per kg of dry solid sample.

		Measured values				**Corrected values**			
	pH	**11**	**10.8**	**10.9**	**9.6**				
Element*	**Legal limit**	**4-2 mm**	**2-1 mm**	**1-0.5 mm**	**0.5-0.25 mm**	**4-2 mm**	**2-1 mm**	**1-0.5 mm**	**0.5-0.25 mm**
Sb	0.32	0.19	0.19	0.17	0.18	0.20	0.19	0.18	0.23
As	0.9	0.21	0.22	0.15	0.15	0.22	0.22	0.16	0.19
Ba	22	0.11	0.02	0.02	0.11	0.11	0.02	0.02	0.14
Cr	0.63	1.7	1.83	1.91	2.42	1.75	1.86	1.98	3.05
Mo	1	0.14	0.14	0.002	0.011	0.14	0.14	0.00	0.01
V	1.8	11.49	10.84	11.43	8.84	11.83	11.03	11.82	11.13
Zn	4.5	0.06	0.06	0.07	0.08	0.06	0.06	0.07	0.10

*Cu, Co, Hg, Ni, Se, Cd, Pb, and Sn was below the detection limit.

This is likely the result of an increased solubility of the slag due to air granulation, which releases chromium and vanadium. Vanadium leaching decreases with decreasing slag size, while chromium leaching increases. However, these leaching results are also influenced by the presence of contaminants such as quartz and calcite. These contaminant phases do not contain V and Cr as effectively reduce the amount of slag in the sample as well as the pH. The 0.5-0.25 mm fraction contains the highest amount of contaminants and has the lowest pH (9.6). But since the amount of crystalline contaminants is known from XRD (Table A.1 in appendix A) an attempt can be made to correct the leaching values (Table 3.4). In these corrected values the vanadium leaching turns out very similar for all granulated slag droplet fractions (11.03 to 11.83 mg/kg ds), while the Cr leaching still increases with decreasing slag size fraction (from 1.75 to 3.05 mg/kg ds). Table 3.5 shows how much of the total V_2O_5 and Cr_2O_3 present in the slag this represents. It also shows the distribution of both oxides between C_2S, MgO, and the matrix. The total leachable amount of V_2O_5 reduces slightly with decreasing slag size. At the same time, we also see a decrease of the V_2O_5 bound in C_2S as the result of a lower C_2S content in the smaller

granules. It is likely that both, C_2S and the matrix, leach V_2O_5, but that C_2S contributes more. The high leaching of vanadium therefore indicates an increased solubility of C_2S in water compared to industrially cooled slag. If this is the case, it can be expected that C_2S hydrates when used as a cement replacement material and could show similar properties to belite cement [47].

Table 3.5: Total amount of V_2O_5 (from PARC bulk composition) and Cr_2O_3 (from XRF bulk composition) in granulated converter slag, the amount leachable from the slag, and the distribution of these oxides between the host phases C_2S, matrix and (Mg,Fe)O (from PARC).

V_2O_5						**Cr_2O_3**					
	Total	**Leachable**	**C_2S**	**Matrix**	**MgO**		**Total**	**Leachable**	**C_2S**	**Matrix**	**MgO**
Size	(wt.%)	(%)	(%)	(%)	(%)	Size	(wt. %)	(%)	(%)	(%)	(%)
4-2 mm	0.60	0.70	31.4	66.1	2.5	4-2 mm	0.18	0.26	77.6	19.5	2.9
2-1 mm	0.61	0.65	24.2	73.2	2.5	2-1 mm	0.18	0.27	71.8	25.3	3.0
1-0.5 mm	0.68	0.62	15.0	82.3	2.6	1-0.5	0.17	0.29	55.1	41.3	3.6
0.5-0.25 mm	0.66	0.60	11.4	84.0	4.6	0.5-0.25 mm	0.15	0.45	46.6	46.8	6.6

The leachable amount of the total Cr_2O_3 content in the slag fractions clearly increases with decreasing slag size from 0.26% to 0.45%. As discussed before the content of Cr_2O_3 in C_2S is systematically overestimated, but the trend in the distribution between the 3 phases shown in Table 3.5 is still useful and seems to indicate that the matrix is contributing the majority of leached Cr_2O_3.

3.4 CONCLUSIONS AND OUTLOOK

Air granulated converter slag was divided into four different size fractions (0.5-0.25, 1-0.5 , 2-1- and-4-2 mm) to study the influence of granule size and therefore cooling speed on the mineralogy of BOF slag. The three largest fractions are very similar in chemical and mineralogical composition, with a total Ca_2SiO_4 (C_2S) content of 41-44 wt. % and very little amorphous phase. The smallest granulated BOF slag fraction (0.5-0.25 mm) is markedly different in composition. It contains less Ca_2SiO4 and shows the highest amorphous content (15.5 wt. %), which may be caused in part by contamination with blast furnace slag. This fraction is the most oxidized and contains large amounts of magnetite (Fe_3O_4). The chemical bulk composition also shows it contains more MgO and less CaO and SiO_2. All granulated slag fractions contain phenocrysts of Mg-wüstite ((Fe,Mg)O) and C_2S that are embedded in a finely grained matrix that formed during cooling. No individual mineral phases can be discerned in the matrix due to their small size (<1 μm). The smallest slag fraction contains 5-10% more (Fe,Mg)O phenocrysts, which is also responsible for the difference in bulk composition. However, the starting composition was the same for all fractions. Further investigation is required to understand this phenomenon. The fine-grained matrix of the granulated slag can be

divided into three types based on the composition: Ca/Si-rich, Ca/Fe-rich, and Mg/Fe-rich. The amount of Ca/Si-rich matrix reduces with decreasing cooling speed/ increasing granule size and forms quench Ca_2SiO_4 in the form of leaf-like patterns. The Ca/Fe rich matrix type contains the majority of Al_2O_3 and TiO_2 alongside the srebrodolskite and perovskite. The Mg/Fe rich matrix has a highly variable composition, containing less MnO and Fe_2O_3 with decreasing slag size and is assumed to be the source of additional Mg-wüstite that forms during cooling. All slag fractions leach more Cr and V than industrially cooled BOF slag and surpass the legal limit defined by the Dutch soil quality decree. The V leaching is very similar for all fractions, while the Cr leaching increases with decreasing slag size. The main sources of these elements are C_2S and the matrix phase. The increased V and Cr leaching indicate that granulated BOF slag is more soluble in water than industrially cooled slag. The results show that it is not possible to create amorphous BOF slag using air granulation. But even if sufficiently rapid cooling is applied, around 30 wt. % of the slag would remain crystalline, due to the formation of solid Ca_2SiO_4 and Mg-wüstite before cooling. However, the air-granulation may have suppressed the near-solidus crystallization of free-lime. The absence of free lime would circumvent the problem of volume expansion caused by its hydration. The leaching results indicate a higher solubility of C_2S in water and therefore the potential for a higher hydraulic reactivity. Further research into the cementitious properties is currently ongoing, but it seems that an application as a partial cement replacement has great potential and could make it possible to recycle all steel slag in the future. It may also solve the problematic leaching of V and Cr, as the hydration products of cement have a high binding capacity for heavy metals.

4

A QUANTITATIVE ANALYSIS OF DICALCIUM SILICATE SYNTHESIZED VIA DIFFERENT SOL-GEL METHODS

ABSTRACT

In this chapter, the synthesis of dicalcium silicate (C_2S) via the sol-gel (acid-catalyzed) process including aqueous route, non-aqueous route, and the Pechini method is reported. Before replicating the slag´s C_2S in ex-situ environment, it is important to understand the efficacy of the synthesis method. Therefore, the composition of C_2S (α', β, and γ) polymorphs, by-products, and amorphous content is established by employing QXRD (quantitative X-ray diffraction) studies. The attention has been focused to comprehend assay-amorphous relationships of C_2S yield. Intermediate dried gels have been investigated via thermal analysis to monitor changes in the gel structures as well as precursors at low temperatures. The synthetic parameters including calcination time and temperature, Ca/Si molar ratio and mode of cooling have been optimized to get pure β-C_2S with low amorphous content. The dependency of β to γ-C_2S polymorphic transformation on mean crystallite size ($D_{crystallite}$) is studied. Overall, the Pechini method exhibits the most promising results for the purity and stabilization of β-C_2S polymorph. Moreover, the non-aqueous and aqueous routes require calcining the dried gel at a temperature higher than 1200 °C due to the carbonation of CaO leads to solid state reaction partially. Moreover, the altering stoichiometry from 2.0 to 1.7 Ca/Si ratio is not a viable solution to improve the C_2S product yield as unreacted silica hides as amorphous content in QXRD measurement.

Major part of this chapter is published elsewhere: M.J. Ahmed, K. Schollbach, S.R. van der Laan, M.V.A Florea, H.J.H. Brouwers, A quantitative analysis of dicalcium silicate synthesized via different sol-gel methods, Mater. Des. 213 (2022) 110329.

4.1 INTRODUCTION

Dicalcium silicate (C_2S) is an important natural mineral known as larnite or belite. It is a monoclinic (β) polymorph of C_2S and exhibits interesting properties such as non-toxic bioactivity, high energy storage capacity as well as flame and thermal resistance [79–81]. It is used in various applications such as white light-emitting diodes (LEDs), high-density energy storage and energy production, environmental remediation, and biomedical engineering [43, 82–84].

C_2S can be synthesized by various traditional (solid-state or fusion) processes and alternatives such as self-combustion or solution combustion synthesis, hydrothermal synthesis, aerosol flame, spray pyrolysis, or the sol-gel process [85–93]. The sol-gel methods are widely used and based on the gelation of colloidal particles, hydrolysis, polycondensation of nitrates or alkoxides, and hypercritical drying of gel [94]. The resulting product is dried and heated at atmospheric temperature. The sol-gel methods have the advantage of synthesizing β-C_2S that has a high specific surface area (up to 26.5-27 m^2/g) and is stable at room temperature without using any additional chemical stabilizers/dopants. The synthesis temperatures also tend to be lower compared to solid-state synthesis [89, 95–97]. The stability of β-C_2S synthesized via the sol-gel method has been attributed to the small particle size (1-3 μm) that prevents a transformation into γ-C_2S [97].

Qualitative X-ray powder diffraction (XRD) is the standard analytical tool for identifying C_2S polymorphs [98]. However, diffractograms are typically complex with an overlap of the diffraction peaks of α, β, and γ-C_2S. If the reaction is incomplete, other phases such as wollastonite, quartz or free lime can also be present, making analysis even more complex. So, it is often not possible to identify all impurities or C_2S polymorphs, especially if their content is very low. Moreover, the method allows no insight into the amorphous content meaning it is frequently ignored [99]. However, the amorphous C_2S tends to be the most reactive part of the sample, so its content should be known to reliably design materials for cementitious applications.

Quantitative XRD (QXRD, Rietveld method) can solve these problems, especially if an internal standard is applied to determine the amorphous content. It can also be used to derive additional information about a sample, such as crystallite size, which is an important parameter that can determine the stability of C_2S polymorphs. However this method is rarely applied [49, 87, 90, 94, 95, 100] and to the best of the author's knowledge, not detailed QXRD including amorphous content determination exists of C_2S synthesized via sol-gel (aqueous, non-aqueous, and the Pechini) methods [49, 101–103].

Before replicating the slag´s C_2S in ex-situ environment, it is important to understand the efficacy of the synthesis method. Therefore, the aim of this chapter is to study the content of C_2S (α', β, γ) polymorphs quantitatively including amorphous phase and minor phases synthesized via three different sol-gel (acid-catalyzed) methods including the Pechini, non-aqueous, and aqueous route. The three methods are compared to see which sol-gel route provides high β-C_2S polymorph yield with low amorphous content [43, 83, 104]. The different calcination temperatures and durations are compared, as well as changing the Ca/Si stoichiometry [93, 105]. The calcination temperatures and times have been chosen to get a clear insight into the relationship between amorphous content, secondary phases, and total C_2S content [49, 87, 95, 106, 107]. Moreover, the importance

of compacting the intermediate dried gel before calcination is shown by comparing loose powder and pressed pellets. The sol-gel reactions such as polyesterification, silica nanoparticle polymerization as well as the transformation of calcium oxide precursors into hydroxide and carbonate are investigated via TG, DTG and DTA analysis. Moreover, the correlation between mean crystallite size (D_{cryst}) and the β to γ-C_2S transformation is investigated.

4.2 MATERIALS

$Ca(NO_3)_2.4H_2O$ (Sigma-Aldrich CAS: 13477-34-4 ⩾ 99.0%), colloidal SiO_2 (30 wt. % Ludox® AM Sigma-Aldrich), colloidal SiO_2 (40 wt. % Ludox® AM Sigma-Aldrich), CH_3CO_2H glacial (Sigma-Aldrich CAS: 64-19-7), $Si(OC_2H_5)_4$ (Sigma-Aldrich CAS: 78-10-4, ⩾ 99.0), $C_6H_8O_7.H_2O$ (VWR, Analytical grade, CAS: 5949-29-1), HNO_3 (Sigma-Aldrich, CAS: 7697-37-2, ⩾ 65%)and C_2H_5OH (Sigma-Aldrich CAS: 64-17-5) were used as received. The reagents were added in the stoichiometric ratios corresponding to the synthesis of C_2S unless indicated otherwise.

The molar ratio, calcination temperature, and time, as well as reaction parameters, have been summarized in Table 4.1 and are based on previously reported synthesis [49, 93].

Table 4.1: Sol-gel synthesis routes and reaction parameters.

Method	Molar ratio	Reagent	Temperature (°C)	Time (h)	Cooling
Pechini	2	40 wt. % silica sol. (particle size = 20.0-24.0 nm), $Ca(NO_3)_2.4H_2O$, 85% resin content	700-1400	1-3	1, 2
Non-aqueous	2	Tetraethyl orthosilicate, $Ca(NO_3)_2.4H_2O$, Ethanol	1000-1200	5-8	1
Aqueous	1.7, 2	30 wt. % silica sol. (particle size=<150 μm), $Ca(NO_3)_2.4H_2O$	1000-1200	5-8	1

1 = cooled in the furnace after switching off the heating (Figure 4.1); **2 =** cooled in the furnace followed by a sample is removed at 542 °C and then air quenched.

4.3 METHODS

4.3.1 *Pechini method*

The $Ca(NO_3)_2.4H_2O$ and colloidal silica (40 wt. % suspensions in water) were employed as a cation source of Ca and Si at a 2:1 molar ratio. The citric acid monohydrate was chosen as a source of α-hydroxy acid to chelate with Ca^{2+}, and ethylene glycol to construct a gel through esterification. The resin content (Rc) was fixed to 85%, as it gives the best results according to the literature [49]. The Rc can be adjusted with the Eq.4.1

$$RC = \frac{m_{resin}}{m_{resin} + m_{oxides}} . 100 \tag{4.1}$$

m_{oxide} = theoretical yield based on the starting amount of CaO and SiO_2, m_{resin} = the mass of organic precursors

The $Ca(NO_3)_2.4H_2O$ was dissolved in distilled water followed by the addition of citric acid monohydrate. The colloidal silica suspension was added after that already dissolved

in ethylene glycol. Then a few drops of nitric acid were added to achieve a pH < 2 to avoid flocculation. The resin content was composed of 60 wt. % citric acid monohydrate and 40 wt. % ethylene-glycol. The mixture was heated to 80 °C to obtain a gel by evaporating water for 6-8 h. Then the gel was charred at 250 °C in an oven for 4-5 h. The resultant xerogel was finely ground into powder and calcined at the desired temperature in an alumina crucible at a heating rate of 5 °C/min [102]. The sample was cooled naturally in a furnace. The rate of furnace cooling showed in Figure 4.1. At calcination temperature 1400 °C, the cooling condition was modified in such a way that one sample was removed from the furnace at 542 °C and air-quenched below the aforementioned temperature.

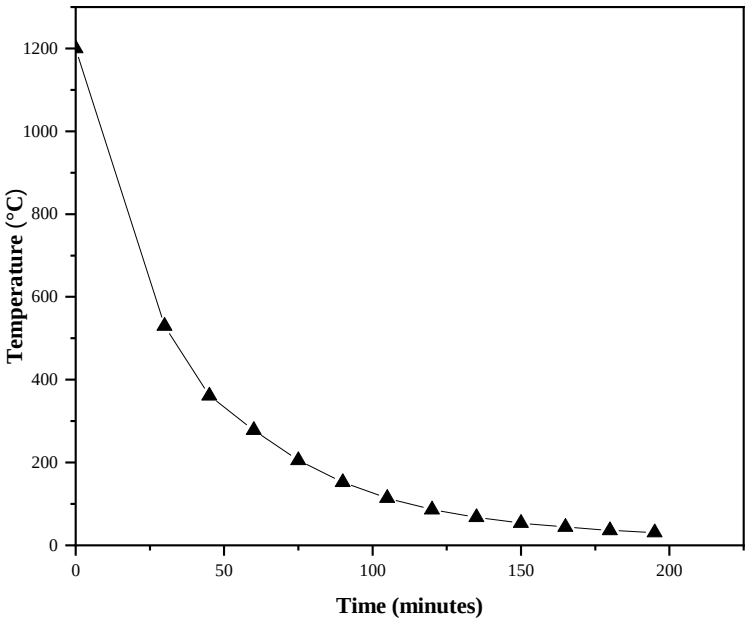

Figure 4.1: The rate of furnace cooling employed for sol-gel (acid-catalysed) synthesis (cooling Method 1).

4.3.2 *Non-aqueous method*

The TEOS (tetraethyl orthosilicate) and $Ca(NO_3)_2.4H_2O$ were employed as a source of Si and Ca, respectively, with a 1:2 molar ratio. The following steps were executed; 1) TEOS was mixed with ethanol (molar ratio C_2H_5OH: TEOS = 1.5) separately, 2) $Ca(NO_3)_2.4H_2O$ was dissolved in a minimum amount of ethanol. Then both solutions were mixed followed by the dropwise- addition of glacial acetic acid to reach a pH < 2-3. The sample was left overnight, and a translucent gel was obtained. The gel was dried, ground, pressed into a pellet, and calcined at the desired temperatures using a heating rate of 5°C/min [93, 97]. The sample was cooled according to Method 1 (Table 4.1: Sol-gel synthesis routes and reaction parameters. and Figure 4.1).

4.3.3 *Aqueous method*

The $Ca(NO_3)_2.4H_2O$ and colloidal silica (30 wt. % suspensions in water) were employed as a source of Ca and Si respectively in a 2:1 molar ratio. The $Ca(NO_3)_2.4H_2O$ was dissolved

in water to complete dissolution followed by the addition of colloidal silica while the solution was stirring. Then a few drops of nitric acid were added to get a pH $\leqslant$ 2-3. The sample was heated for 4-6 hours at 70 °C and a translucent gel was obtained. The gel was stored for 24 hours at 38 °C in the oven. The gel was then dried, ground, and calcined at the desired temperature with a heating rate of 5 °C/min [86, 97]. The sample was cooled according to Method 1 (Table 4.1 and Figure 4.1). The information about characterization methods is presented in Chapter 2.

4.4 RESULTS AND DISCUSSIONS

4.4.1 *C_2S synthesis via the Pechini method*

The intermediate, amorphous gel produced with the Pechini method was charred at 250 °C, and then TG/DSC was analyzed to determine the lowest calcination temperature for C_2S synthesis (Figure 4.2 (a, b)). The decomposition of the dried gel can be broadly divided into three main steps. The first mas-loss step from 40 to 250 °C can be attributed to the loss of water physisorbed on the surface of the dried gel. The second strong exothermic step (250-600 °C) can be assigned to the resin breakdown and residual carbon combustion. The mass loss step around 251-350 °C can be attributed to the polymer fragmentation, formed by polyesterification of citric acid and ethylene glycol. The mass loss step around 405-445 °C may occur due to the decomposition of the carboxylic group, carbonates, and nitrates. The exothermic peak of polymer fragmentation may overlap with the endothermic process of decomposition of nitrates and carbonates in DTA analysis. The third slight exothermic step (600-700 °C) is attributed to the crystallization of C_2S. The TG signal becomes stable at around 650 to 700 °C. So, 700 °C was chosen as the lowest calcination temperature [98].

The C_2S synthesized via the Pechini method has been investigated after heating the precursor to temperatures in the range of 700-1400 °C and a calcination time of 1-3 hours with cooling Method 1 unless stated otherwise. The XRD diffractograms without internal standard (silicon) are shown in Figure 4.3. And the results of QXRD are shown in Table 4.2.

At 700 °C, the α'-C_2S (22.5 wt. %) polymorph and amorphous content (68.3 wt. %) were the major phases with minor amounts of β-C_2S (9.2 wt. %) present. The particles calcined at 700 °C appeared spherical, porous, and highly agglomerated (Figure 4.7 (a)), which is in line with the literature [108]. By increasing the calcination temperature to 800 °C, the dominant crystalline phase became β-C_2S (27.5 wt. %) alongside α'-C_2S (19.4 wt. %) and amorphous content (53.1 wt. %). The high amorphous content at 700-800 °C C_2S points out that the (α' and β) polymorphs matrix is poorly crystalline.

When the calcination temperature was raised to 900 °C, the α'-C_2S completely transformed to β-C_2S (83.0 wt. %). The amount of amorphous content decreased from 53.1 to 16.8 wt. % while only β-C_2S crystallized out of the amorphous matrix. A further increase in calcination temperature to 1000 °C led to only a small increase in β-C_2S (83.7 wt. %). At 1100 °C, γ-C_2S (2.9 wt. %) started to appear, which increased slightly (3.7 wt. %) at 1200 °C. The γ-C_2S formation was observed at a calcination temperature of 1300 °C with natural furnace cooling (cooling Method 1) in earlier studies [103]. Overall, β-C_2S was the dominant product in the range of 900-1200 °C. The sequence of phase

development was consistent with previous studies [102]. Minor amounts of wollastonite, quartz, grossular, and CaNaAlO were also observed during the synthesis. The quartz and wollastonite are likely due to incomplete conversion of reactants, while the impurity phases of grossular and CaNaAlO may form due to trace amounts of aluminum and sodium in the reagent or the corundum from the crucible [103].

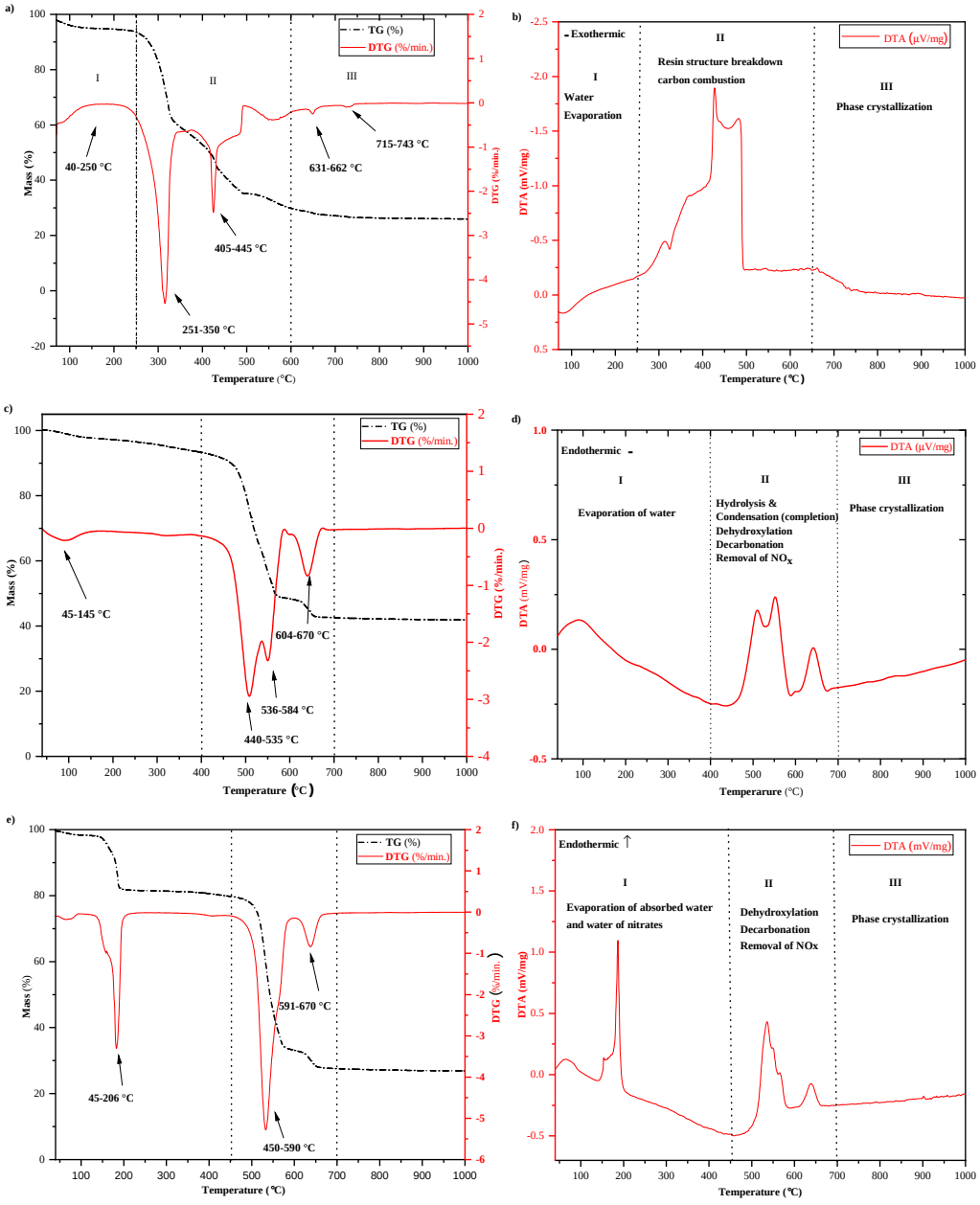

Figure 4.2: Thermal analysis of intermediate dried gels from all sol-gel routes (a) TG and DTG (b) DTA analysis of the dried gel synthesized from the Pechini method pre-charred at 250 °C (c) TG and DTG (d) DTA analysis of the dried gel synthesized via non-aqueous route and pre-dried at 150 °C (e) TG and DTG (f) DTA analysis of the dried gel synthesized via aqueous route and pre-dried at 150 °C.

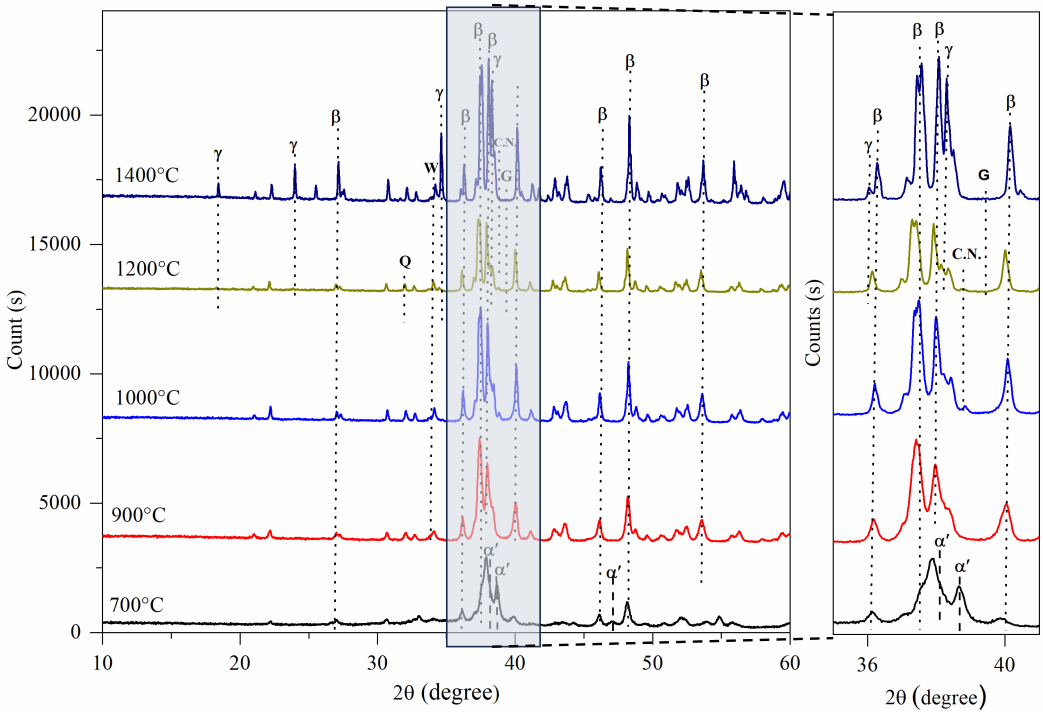

Figure 4.3: XRD pattern of the dried gel obtained with the Pechini method after heating to different temperatures. The crystalline phases are labelled as α' = α'-C_2S, β = β-C_2S, γ = γ-C_2S, W = wollastonite-2M, C.N = Calcium sodium Aluminum oxide, G = grossular, Q = quartz.

Table 4.2: QXRD of the C_2S synthesized via Pechini method with error values.

Temperature (°C)	**700**	**800**	**900**	**1000**	**1100**	**1200**	**1400**	**1400**	***1400**
Calcination time (h)	3	3	1	1	1	1	1	1	1
Cooling method	1	1	1	1	1	1	1	2	2
α'-C_2S (wt. %)	22.5 ± 0.9	19.4 ± 0.7							
β-C_2S (wt. %)	9.2 ± 0.8	27.5 ± 0.6	83.0 ± 0.2	83.7 ± 0.3	85.2 ± 0.3	86.4 ± 0.3	76.1 ± 0.3	92.4 ± 0.3	92.0 ± 0.3
γ-C_2S (wt. %)					2.9 ± 0.2	3.7 ± 0.2	23.4 ± 0.2	5.7 ± 0.2	6.1 ± 0.2
Wollastonite-2M (wt. %)			0.2 ± 0.1		0.3 ± 0.2				
Quartz low (wt. %)						0.8 ± 0.1			
Grossular (wt. %)					0.7 ± 0.1	0.6 ± 0.1	0.6 ± 0.1	0.3 ± 0.1	0.4 ± 0.1
CaNaAlO (wt. %)				0.3 ± 0.1		0.4 ± 0.1			
XRD-amorphous (wt. %)	68.3 ± 1.6	53.1 ± 1.0	16.8 ± 1.0	15.9 ± 1.4	10.9 ± 1.3	8.0 ± 1.3		1.6 ± 1.5	1.5 ± 1.4

At 1400 °C, the amount of γ-C_2S reached 23.4 wt. % in the sample cooled via Method 1. The γ-C_2S is not formed at 1400°C, because it is a low-temperature modification. Instead, it is formed out of β-C_2S during cooling. The phenomenon of β to γ-C_2S transformation is dependent upon particle size [103, 105, 107]. With increasing calcination temperature, the crystallite size of the C_2S increases due to sintering effects. Then internal strain is generated inside the β-C_2S crystals during cooling. This strain becomes larger with increasing crystallite size and will result in the transformation of β-C_2S into γ-C_2S, once a critical crystallite size is achieved. The β-destabilization can be restricted by increasing the cooling speed (physical stabilization) above the γ-stability field temperature or by incorporating impurities into the crystal structure (chemical stabilization) [105]. The calcined sample at 1400 °C cooled down via Method 2 decreased in γ-C_2S from 23.4 wt. % to 5.7 wt. % with 92.0 wt. % β-C_2S [107]. The metastable β-C_2S achieved at 1400 °C with cooling Method 2 was analyzed 8 weeks later and no conversion into γ-C_2S had taken place. The average crystallite size ($D_{crystallite}$) growth at increasing calcination temperature and its correlation with C_2S polymorphic transformation is discussed in Section 4.4.4.

A few representative FTIR spectra have been taken to investigate bonding systems (Figure 4.6 (a)). In the case of the Pechini method, the strong and broadband regions at 896 cm^{-1} and 509 cm^{-1} are attributed to (α'_H-C_2S (orthorhombic). The band at 997 cm^{-1} can be attributed to β-C_2S. At 900-1000 °C, the new bands 503 cm^{-1}, 540 cm^{-1} in the SiO_2-bending region and 847 cm^{-1}, 865 cm^{-1}, 895 cm^{-1}, 992 and 1016 cm^{-1} in the SiO_2-stretching region clearly indicates the presence of β-C_2S. As the calcination temperature is elevated higher than 1000 °C, a new band appears at 497 cm^{-1} in the SiO_2-bending region indicating the presence of γ-C_2S. The strong band regions at 519 cm^{-1}, 541 cm^{-1}, 841 cm^{-1}, 893, and 991 cm^{-1} indicate the strong presence of β-C_2S. The FTIR studies of C_2S synthesized via the Pechini method exhibited complete agreement with previous studies [107, 109, 110].

4.4.2 *C_2S synthesis via the non-aqueous route*

The thermal events of intermediate gel dried at 150 °C were analyzed via TG and DSC as shown in Figure 4.2 (c, d). The first endothermic mass loss step occurs due to the loss of physisorbed water on the dried gel sample. The second strong endothermic event is comprised of the three mass loss steps. The mass loss of around 440-535 °C occurs due to the removal of by-products (H_2O and C_2H_5OH) upon completion of TEOS hydrolysis and condensation. The mass loss around 536-584 °C may be assigned to dehydroxylation of portlandite ($Ca(OH)_2$) and decomposition of nitrates. The mass loss around 604-670 °C likely occurs due to the removal of carbon dioxide from calcite ($CaCO_3$). The third slight exothermic event with no mass loss is attributed to the phase crystallization out of the amorphous matrix [111]. It is clear from the thermal event analysis that in the first step, the water evaporates to form xerogel, and calcium nitrates precipitate onto the surface of the network. In the next step, the calcium nitrate breaks down into the calcium oxide to react with the silica network to form dicalcium silicate. The surface and internal silanol groups may convert into the strained siloxane bridges in thermally induced condensation of hydroxylated silica surface below 500 °C. The strained siloxane bridges are converted into stable siloxane groups at a temperature higher than 500 °C. The presence of calcite

visible around 600-700 °C as a calcium source delays the supply of calcium oxide for the reaction. Moreover, stable siloxane bridges react at a much slower rate than strained siloxane bridges. Conclusively, the presence of calcite as a calcium source requires a high calcination temperature for the complete conversion of reactants into a product.

For the C_2S synthesis via the non-aqueous route, the precursors were calcined in the temperature range of 1000-1200 °C and a calcination time from 5 to 8 hours was chosen [97]. The XRD patterns without internal standards are shown in Figure 4.4 and the results of QXRD are shown in Table 4.3.

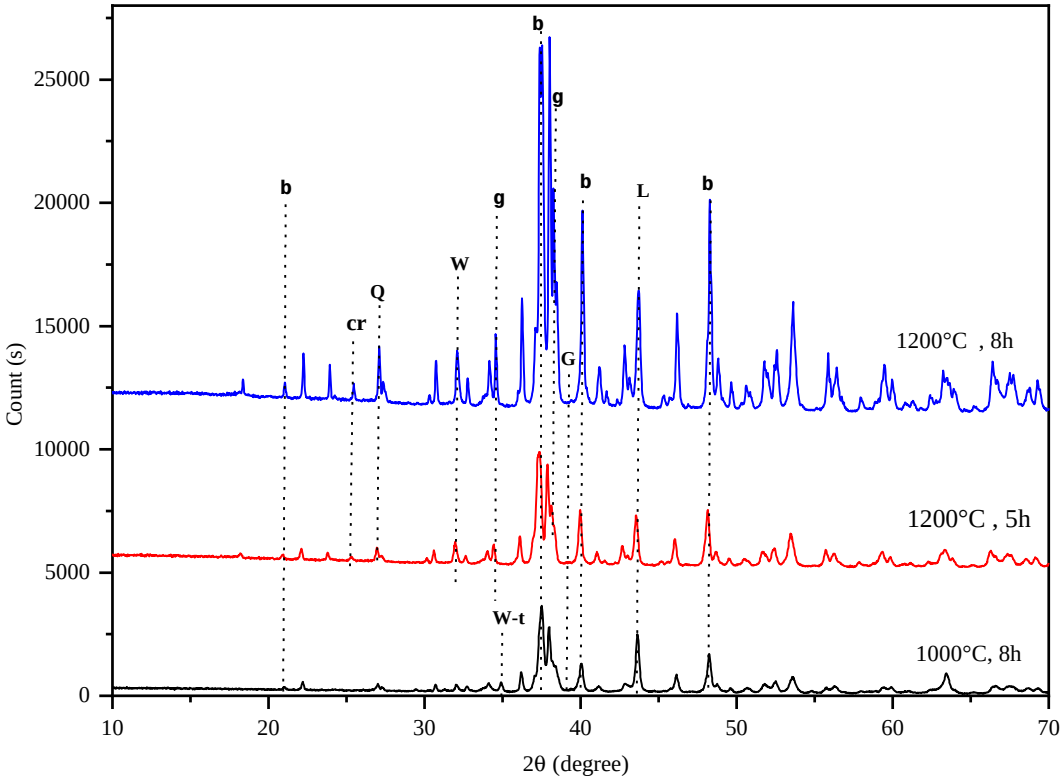

Figure 4.4: XRD pattern of C_2S synthesized via non-aqueous route. The crystalline phases are labelled as β = β-C_2S, γ = γ-C_2S, W = wollastonite-2M, W-t = wollastonite-triclinic L = lime, G = grossular, Cr = cristobalite, Q = quartz.

When the intermediate dried-gel was fired at 1000 °C for 8 h, the major phase was β-C_2S (73.4 wt. %) with wollastonite (5.1 wt. %), unreacted lime (7.6 wt. %), and (12.3 wt. %) XRD amorphous content. An SEM micrograph of C_2S synthesized at 1000 °C is shown in Figure 4.7 (b) and shows the same morphology reported in other studies [102]. The presence of free-lime and wollastonite indicates that the conversion of reactants was incomplete [87]. Therefore, the calcination temperature was elevated to 1200 °C for 5 h, and γ-C_2S (4.5 wt. %) appeared alongside β-C_2S (81.3 wt. %) with a clear decrease in wollastonite (1.7 wt. %) and free-lime (4.9 wt. %) as well as a decrease of the amorphous content to 5.7 wt. %. A further increase of the calcination time from 5 to 8 h at 1200 °C yielded more γ-C_2S (16.7 wt. %) and a decrease in β-C_2S (from 81.3 to 75.1 wt. %). The 3.8 wt. % of amorphous content at 1200 °C for 8 h calcination suggested that most of the C_2S matrix was crystalline. However, it was successful in further decreasing the lime (2.7 wt. %) and wollastonite (0.6 wt. %)

content. A small amount of quartz and cristobalite was also visible, as the remaining, unreacted SiO_2 in the amorphous content started to crystallize. It seems clear that the content of these two phases is only reducing due to solid state sintering reactions taking place at elevated temperatures as well as longer reaction times. Moreover, the wollastonite and lime crystallize directly out of the amorphous phase showing an incomplete reaction. It can be explained based on the thermal events of precursors' transformation during calcination. Firstly, the presence of calcium carbonate during thermal events delays the reaction with the silica network (Figure 4.2 (c, d)). Secondly, the formation of Si-O-Si bonds traditionally takes place at high temperatures while the condensation reaction between the -OH group begins at room temperature. However, many of Si-O-Si bonds are not stable even at a temperature higher than 1000 °C to achieve bonding energy close to bulk fracture energy [112]. Conclusively, the incomplete polycondensation reaction of Si-O-Si bonding is completed via high-temperature calcination (act as a solid-state synthesis partially).

Table 4.3: QXRD of the product synthesized by a non-aqueous route of the sol-gel method with error values.

Temperature (°C)	**1000**	**1200**	**1200**	**1200**
Calcination time (h)	8	5	8	5
Sintered sample morphology	Pressed pellet	Pressed pellet	Pressed pellet	Powder
β-C_2S (wt. %)	73.4 ± 0.6	81.3 ± 0.3	75.1±0.3	53.1±0.2
γ-C_2S (wt. %)		4.5 ± 0.2	16.7±0.2	11.1±0.1
Wollastonite-triclinic (wt. %)	5.1 ± 0.7			
Wollastonite-2M (wt. %)		1.7 ± 0.1	0.6±0.1	0.2±0.1
Pseudo-wollastonite (wt. %)				4.1±0.2
Lime (wt. %)	7.6 ± 0.1	4.9 ±0.1	2.7±0.1	3.2±0.1
Grossular (wt. %)	0.6 ± 0.2	0.6±0.1	0.1±0.06	1.0±0.1
Quartz (wt. %)		0.2±0.03	0.2±0.03	0.1±0.02
Cristobalite (wt. %)		1.1±0.07	0.8±0.07	
XRD-amorphous (wt. %)	12.9 ± 1.2	5.7 ±1.5	3.8±1.6	26.8±0.6

An interesting phenomenon was observed when the dried-gel intermediate was calcined in the form of loose powder at 1200 °C for 5 h as opposed to the standard pressed pellet. The QXRD showed higher XRD-amorphous content (26.8 wt. %), γ-C_2S (11.1 wt. %) than the pressed pellet results (XRD-amorphous = 3.8 wt. %, γ-C_2S = 4.5 wt. %) as the energy of the constrained particle is different from the isolated particle. That is why the pressing of the pellet likely contributes toward the matrix constraint for particle growth and stabilizes more β-C_2S [105]. Considering the results, all the intermediate dried-gel samples synthesized via non-aqueous and aqueous routes are pressed into a pellet before calcination to obtain optimal results.

The transmittance pattern at the 1459-1460 cm^{-1} and 3639 cm^{-1} can be attributed to the calcium carbonates and hydroxide synthesized via the non-aqueous route due to partial carbonation of free lime (Figure 4.6 (b)). The bands in the region 992-998 cm^{-1}, 896 cm^{-1},

840-870 cm^{-1} corresponds to β-C_2S, and the broadening of peaks can be attributed to the formation of γ-C_2S at 1200 °C for 8 h calcined sample [97].

4.4.3 *C_2S synthesis via aqueous route*

The thermal events of intermediate gel dried at 150 °C via aqueous route exhibited the mass loss events such as removal of water of nitrates and physisorbed water followed by the decomposition of nitrates, dehydroxylation of silica network and calcium hydroxide as well as the removal of carbon dioxide from calcium carbonate respectively (Figure 4.2).

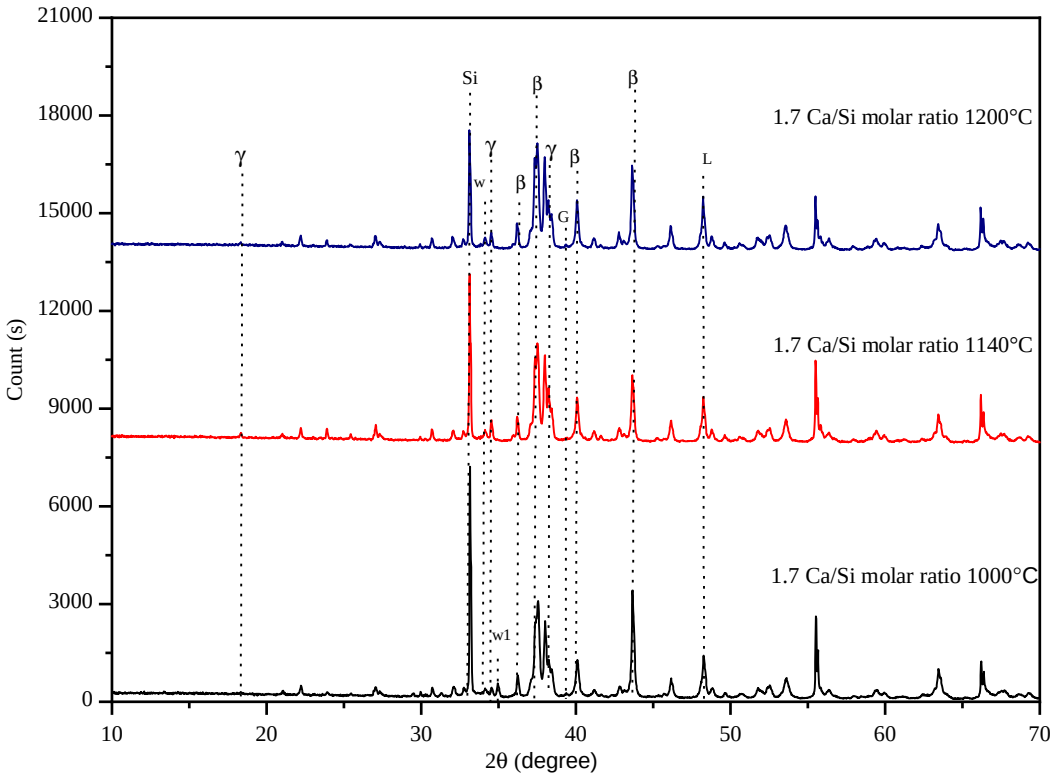

Figure 4.5: XRD pattern of C_2S synthesized via an aqueous route of the sol-gel method. The crystalline phases are labelled as Si = as internal standard β = β-C_2S, W = wollastonite-2M, L = lime, G = grossular, γ = γ-C_2S, W1 = wollastonite-1A.

The initial Ca/Si molar ratio was 2 and the sample was calcined at 1200 °C for 5 h. The major phase was β-C_2S (77.6 wt. %) alongside γ-C_2S (6.6 wt. %) and a low amount of XRD-amorphous (3.7 wt. %) phase (Table 4.4). The amount of CaO was rather higher with 9.1 wt. % than with the non-aqueous route (4.9 wt. %). Minor phases like quartz (0.1 wt. %) and cristobalite (0.8 wt. %) were also observed. The high CaO amount indicated an incomplete reaction between the calcium and silica precursors similar to the non-aqueous synthesis route. However, the lime content was much higher and the amorphous content lower, which seems the point to a problem with the stoichiometry instead (Table 4.5). To test this hypothesis as well as to avoid unreacted free lime, the Ca/Si ratio was adjusted from 2.0 to 1.7 was adjusted as reported in a few studies [93, 105]. The intermediate

dried gel with a 1.7 Ca/Si starting molar ratio was fired at 1000 °C, 1140 °C, and 1200 °C respectively.

Table 4.4: QXRD of the product synthesized by aqueous route with error values.

Temperature (°C)	**1000**	**1140**	**1200**	**1200**
Calcination time (h)	8	5	5	5
Ca/Si molar ratio (mol)	1.7	1.7	1.7	2
β-C_2S (wt. %)	46.1 ± 0.3	74.3 ± 0.3	78.7 ± 0.3	77.6 ± 0.9
γ-C_2S (wt. %)	2.8 ± 0.2	11.6 ± 0.2	7.8 ± 0.2	6.6 ± 0.3
Lime (wt. %)	6.1 ± 0.2	7.8 ± 0.1	8.7 ± 0.1	9.1 ± 0.2
Grossular (wt. %)	0.5 ± 0.2	1.0 ± 0.2	1.0 ± 0.2	2.0 ± 0.3
Quartz (wt. %)		0.04 ± 0.02	0.04 ± 0.02	0.1 ± 0.05
Cristobalite (wt. %)				0.8 ± 0.2
Wollastonite-2M (wt. %)		0.7 ± 0.2	0.6 ± 0.2	
Wollastonite-1A (wt. %)	3.1± 0.2			
XRD amorphous (wt. %)	41.3 ± 1.2	4.6 ± 1.2	3.2 ± 1.3	3.7 ± 2.3

The results clearly show that a reduction in the starting CaO content was not successful in reducing the free lime content after calcination. To make sure that the results are not due to an incorrect quantification, the theoretical composition of the amorphous content was calculated via subtracting all the mineral phases determined with QXRD from the bulk composition (Table 4.5). If the difference is positive that means the QXRD results are at least theoretically possible. This calculation was done for two samples, one with a Ca/Si ratio of 2 and the other with a Ca/Si ratio of 1.7, both calcined at 1200 °C for 5 h.

Table 4.5: Theoretical amorphous content composition of samples synthesized via the aqueous route. Both samples were sintered at 1200 °C for 5 h. The theoretical amorphous oxide composition is the difference between the starting composition and the oxides contained in the crystalline phases.

Ca/Si molar ratio	**2**			**1.7**		
	QXRD (wt. %)	CaO (mol. %)	SiO_2 (mol. %)	QXRD (wt. %)	CaO (mol. %)	SiO_2 (mol. %)
Starting Composition		66.7	33.3		63	37
Total C_2S	84.2	56.2	28	86.5	54.5	32
Lime	9.1	9.1		8.7	8.7	
Grossular	2	0.9	0.9	1	0.4	0.4
Quartz	0.1		0.1			
Cristobalite	0.8		0.8			
Wollastonite-2M				0.6	0.4	0.2
Total		66.2	29.8		64	32.6
Amorphous	3.7	0.6	3.5	3.2	-1	4.3

The theoretical composition of the amorphous content for the Ca/Si = 2 sample is CaO = 0.6 mol. % and SiO_2 = 3.5 mol. %, showing that a lot of the SiO_2 remains XRD-amorphous while the CaO tends to crystallize. In the Ca/Si = 1.7 sample, the theoretical composition of the amorphous content is CaO = -1 mol. %, SiO_2 = 4.3 mol. %. The CaO content is negative which is not possible for a real phase. Considering the error of QXRD, it can be assumed that the real CaO content in the amorphous phase is around 0 mol. %, and thus it consists entirely of amorphous SiO_2. Conclusively, the change in stoichiometry (2.0 to 1.7 Ca/Si molar ratio) is not a viable solution to convert more reactants into β-C_2S.

The TG/DSC analysis of the pre-dried intermediate at 150 °C offers an explanation for this phenomenon (Figure 4.2 (c, d, e, f)). It clearly shows that the formation of calcium carbonate and the incomplete Si-O-Si network are the inherent issues of the aqueous and non-aqueous routes of sol-gel synthesis. Conclusively, the part of the calcium tends to react with the amorphous silica during high temperature sintering and long calcination time. This explains the gradual decrease of free lime and wollastonite when the calcination temperature is raised from 1000 to 1200 °C. Moreover, the alkoxide-assisted Si-O-Si network as in the case of the non-aqueous route tends to react with calcium precursors more efficiently than an aqueous route (Table 4.3 and Table 4.4).

The FTIR studies of the aqueous route (1.7 Ca/Si molar ratio at 1140 °C), the broadening of vibration peaks indicated the change in the symmetry order from β (monoclinic) to γ (orthorhombic) showing the presence of γ-C_2S (Figure 4.6 (b)). All this information exhibited a compromise with previously reported FTIR studies [107].

4.4.4 *Effect of calcination temperature on C_2S mean crystallite size (D_{cryst})*

The idea of mean crystallite size ($D_{cryst.}$) helps to understand the C_2S polymorphic transformation at varying calcination temperatures because it is the main factor for the stabilization of β-C_2S without any chemical stabilizer [107]. In the case of the Pechini method, the $D_{cryst.}$ increases as the calcination temperature are raised from 700 °C to 1400 °C (Figure 4.8).

The (D_{cryst}) size can be determined for each C_2S polymorph as part of the QXRD and as such is taken directly from TOPAS. At 700-800 °C, a (D_{cryst}) size < 27 nm was observed for the α′- C_2S polymorph and would be one of the reasons for the high-temperature polymorph stabilization. From 700 to 1400 °C, the crystallite size of β-C_2S increases from 27 nm to as big 102 nm in the case of cooling Method 1. The γ-C_2S started to appear with a (D_{cryst}) of about 59 nm alongside β-C_2S 83 nm at 1100 °C. In the previous studies, the critical particle size 5-10 μm was reported for β-C_2S stabilization [105, 107]. In the present studies, the (D_{cryst}) is considered which is much smaller than the reported critical particle size. Therefore, the critical (D_{cryst}) for β-C_2S stabilization at room temperature seems to be below 83 nm in the case of Pechini synthesis. At 1400 °C, the (D_{cryst}) for β-C_2S can grow to a size of 102 nm approximately at which internal strain generated during cooling may induce γ-C_2S formation (23.4 wt. %) in a naturally cooled sample in a furnace (cooling Method 1). When the sample was cooled with Method 2 (Pechini method), the resultant β-C_2S (D_{cryst}) becomes slightly higher 105 nm than the (D_{cryst}) of γ-C_2S cooled via Method 1. This observation points out that the faster cooling could prevents the larger

γ-C_2S crystal transforming into the γ-C_2S and leading to an increase in the overall mean crystallite size [107].

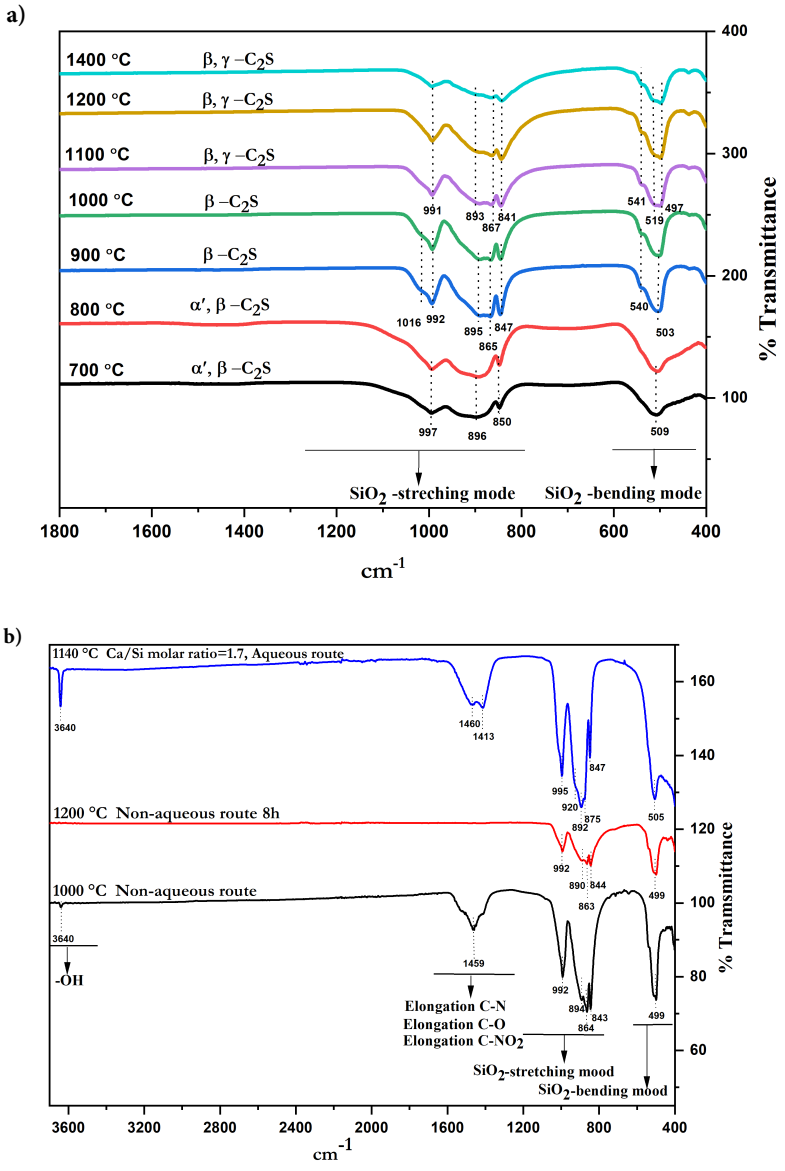

Figure 4.6: FTIR spectra of C_2S synthesized via Pechini method. b) FTIR spectra of C_2S synthesized via non-aqueous and aqueous routes.

In the case of the non-aqueous and aqueous route of the sol-gel method (Figure 4.9 (a, b)), the calculated D_{cryst} of β and γ-C_2S polymorph lies in the range of 36-78 and 91-170 (min. to the max.) nm respectively. The D_{cryst} also increases with the calcination temperature and time. It can be concluded that the different route (aqueous, non-aqueous, and the Pechini method) of sol-gel synthesis results their own critical mean crystallite size for the β to γ transformation which depends on synthetic route, starting precursors, calcination temperature, and time as well as cooling conditions and matrix composition

(Ca to Si molar ratio). The critical D_{cryst} for the β-C_2S stabilization can only be defined in consideration of the aforementioned parameters.

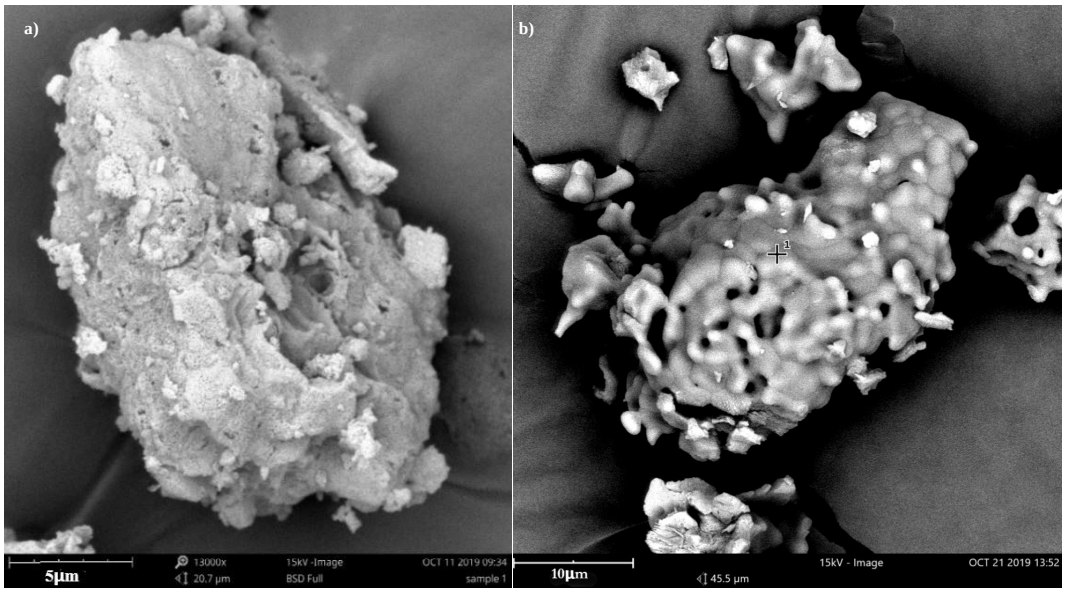

Figure 4.7: SEM micrograph of C_2S synthesized via (a) the Pechini method calcined at 700 °C (b) non-aqueous route at 1000 °C.

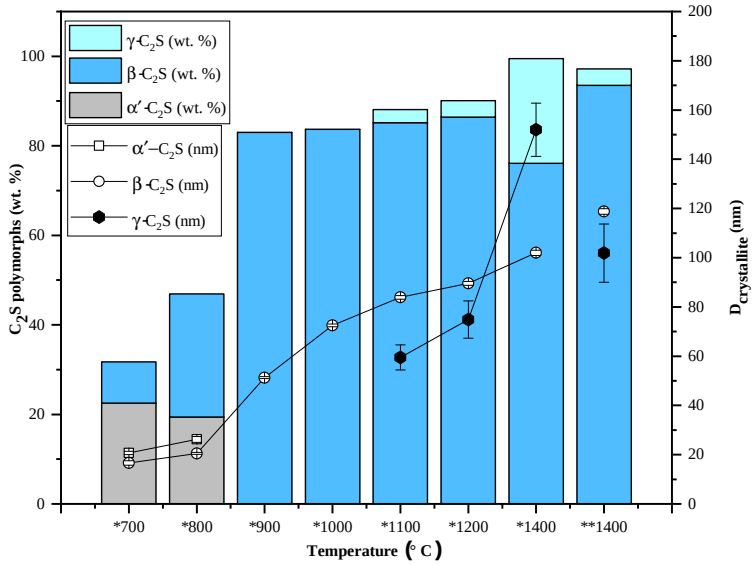

Figure 4.8: Correlation between temperature (°C), mean crystallite size D_{cryst} (nm) and polymorphic transition of C_2S (α′, β, γ) synthesized by the Pechini method (∗=the sample is cooled according to Method 1), (∗∗=the sample is cooled down via Method 2).

In the case of the non-aqueous and aqueous route of the sol-gel method (Figure 4.9 (a, b)), the calculated D_{cryst} of β and γ-C_2S polymorph lies in the range of 36-78 and 91-170 (min. to the max.) nm respectively. The D_{cryst} also increases with the calcination temperature and time. It can be concluded that the different route (aqueous,

non-aqueous, and the Pechini method) of sol-gel synthesis results their own critical mean crystallite size for the β to γ transformation which depends on synthetic route, starting precursors, calcination temperature, and time as well as cooling conditions and matrix composition (Ca to Si molar ratio). The critical D_{cryst} for the β-C_2S stabilization can only be defined in consideration of the aforementioned parameters.

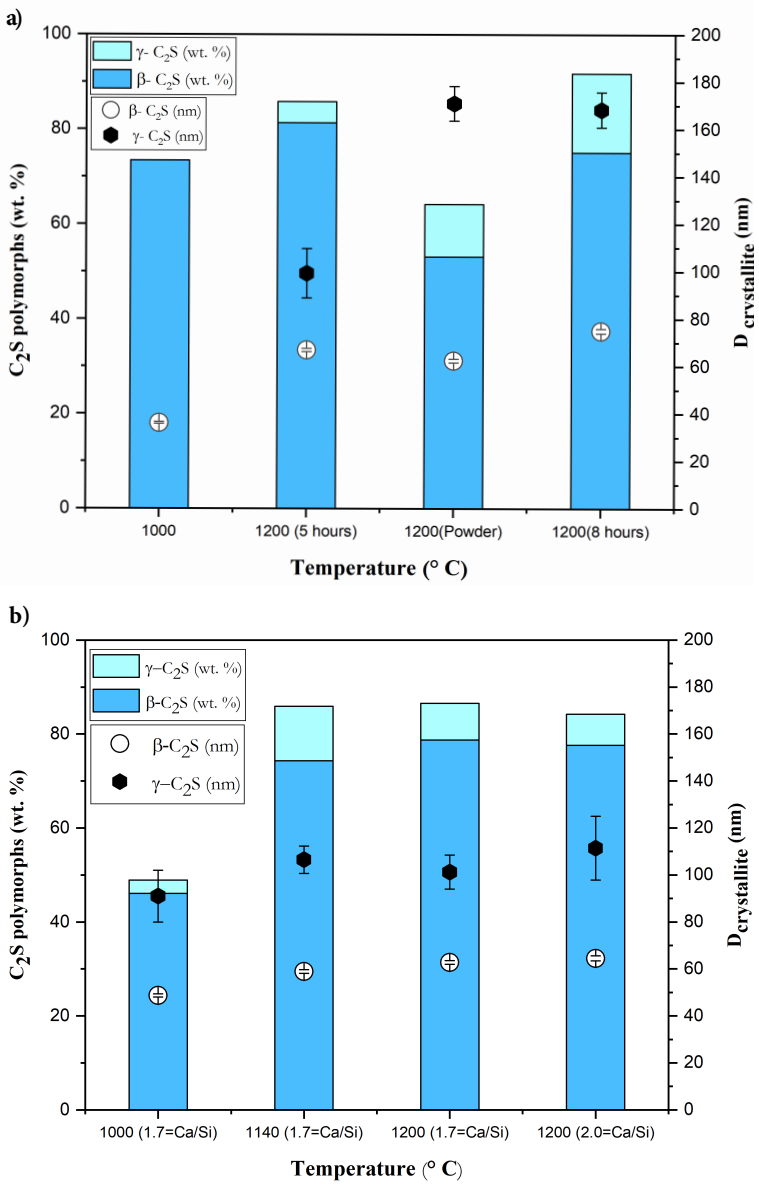

Figure 4.9: a) Correlation of calcination temperature with D_{cryst} size (nm) of β and γ-C_2S polymorphs synthesized via non-aqueous route. b) Correlation of calcination temperature with D_{cryst} size (nm) of β and γ-C_2S polymorphs synthesized via aqueous route.

4.5 SUMMARY AND CONCLUSION

The synthesis of C_2S was investigated via the sol-gel (acid-catalyzed) method including the aqueous route, non-aqueous route, and the Pechini method. The Pechini method was

found to be the best method for pure C_2S synthesis and tuning of desired polymorphs at low calcination temperature. This can easily be attributed to the efficient calcium polymer network as an intermediate, avoiding the formation of calcium hydroxide and calcium carbonate that only tends to react with the silica network at high temperatures.

The non-aqueous route of the sol-gel method exhibited the second most promising results to synthesize a high amount of β-C_2S (81.3 wt. %) with low lime (2.7 wt. %) and amorphous (3.8 wt. %) content at 1200 °C calcined for 5 h. The insight about by-products such as quartz, cristobalite, wollastonite, and lime can easily be overlooked via standard XRD analysis due to high peak overlapping. The presence of these phases is due to the formation of calcium carbonate and amorphous silica during calcination leads to an inherent problem of the non-aqueous route.

The aqueous route of a sol-gel method was found to be the least promising method of sol-gel synthesis. The lack of alkoxide assisted Si-O-Si efficient network and formation of calcium carbonate promotes the high amount of unreacted CaO and silica phases after synthesis. The calculation of QXRD and theoretical composition of amorphous content concluded that any change in the stoichiometry of Ca and Si precursors lower than 2 would lead to unreacted silica and calcium oxide hiding as XRD amorphous content rather than facilitation of pure β-C_2S synthesis. That's why the change in stoichiometry is not recommended.

The D_{cryst} (mean crystallite size) for β to γ transformation depends on the thermal history (calcination temperature and time, mode of cooling), route of sol-gel (Pechini, non-aqueous and aqueous) synthesis, and matrix (calcium or silica-rich) composition. Considering all these parameters, the critical D_{cryst} for β-C_2S stabilization was recorded below 83 nm approximately in the case of Pechini method synthesis.

In summary, the present work provides a detailed understanding of the advantages and disadvantages of the different sol-gel methods. This study shows the importance of considering the amorphous content, as it can mask impurities/secondary phases in the synthesized samples. This information will assist to better design the ex-situ mimicking of slag C_2S phase and provide an insight into their potential impact on the leaching and reactivity.

5

VANADIUM AND CHROMIUM SUBSTITUTION IN DICALCIUM SILICATE UNDER OXIDIZING AND REDUCING CONDITIONS; SYNTHESIS, REACTIVITY, AND LEACHING STUDIES

ABSTRACT

Dicalcium silicate (C_2S) is known to incorporate potentially hazardous metals (Cr and V) in a belite-rich cementitious system. The effect of the electrovalence nature of V and Cr on C_2S polymorphs' (α', β, γ) stability under oxidizing and reducing conditions as well as their reactivity are systematically investigated via analyzing oxidation states, phase composition, bonding system, and microstructure quantitatively. It is shown that C_2S can incorporate Cr (VI) and V (V) consequently leading to the stabilization of α', β-C_2S. Instead, Cr (II, III) and V < (V) tend not to substitute in C_2S. Despite stabilizing the reactive polymorphs (α', β-C_2S), the early age (48-72 h) C_2S reactivity is drastically reduced due to Cr (VI) and V (V) incorporation. Moreover, one batch leaching test revealed that the V (V) leaching is inversely proportional to aqueous Ca^{2+} ions at pH > 12 while Cr leaching is sensitive to its oxidation state, and dissolution of C_2S. Even though C_2S can incorporate Cr (VI) and V (V) ions, the final leaching is governed by the immobilization potential of C-S-H gel, pH as well as types of calcium chromate and vanadate complexes.

Major part of this chapter is published elsewhere: M.J. Ahmed, R. Cuijpers, K. Schollbach, S.R. van der Laan, M. Van Wijngaarden-Kroft, T. Verhoeven, H.J.H. Brouwers, V and Cr substitution in dicalcium silicate under oxidizing and reducing conditions – Synthesis, reactivity, and leaching behavior studies, J. Hazard. Mater. 442 (2023) 130032.

5.1 INTRODUCTION

Ordinary Portland cement (OPC) is one of the most used artificial materials in the world. Cement manufacturing requires high energy and resource consumption leading to significant CO_2 footprints [44, 113]. Substantial efforts have been made in developing alternative raw materials and adjusting clinker composition to address the challenges for the sustainable development of the cement industry [43, 114–119]. Industrial by-products such as iron and steel-making slag, electroplating sludge, and metal surface galvanic sludge are being investigated as alternative raw materials for clinker production [37, 120, 121]. However, these materials contain potentially toxic elements (PTEs) such as Cr, V, Vi, As, etc. and their content is strictly regulated by European environmental legislation [122, 123]. Therefore, the leaching of PTEs hinders the potential use of these materials for a sustainable future [124, 125].

Dicalcium silicate (C_2S) is a major constituent of basic oxygen furnace (BOF) slag, belite-based clinker, and a minor constituent of OPC [126, 127]. Cr and V are among the most abundant PTEs within the BOF slag [54]. The presence of V and Cr in BOF steel slag, its toxicity, and the potential mobility in leachate have attained significant attention due to environmental implications. V and Cr can get incorporated into the C_2S and therefore their mobility, as well as toxicity depend on the chemical nature of the host matrix (redox potential, solubility, reactivity, etc.), oxidation state, and substitutable vacancy in the crystal lattice (Ca or Si-site) [48]. The aliovalent nature of Cr and V, and their potential to occupy either the Ca or Si site in C_2S dictates the enrichment mechanism in the host matrix and leaching behaviour [55–58]. Therefore, a good knowledge of V and Cr substitution in C_2S under varying sintering (oxidizing and reducing) conditions is required to understand their chemical and environmental impact.

C_2S exists in several polymorphs such as x, α, α'_L, α'_H, β, and γ [128]. The stable γ-polymorph at room temperature is well known for its lower reactivity as compared to other C_2S polymorphs (x, α, α'_L, α'_H, β) [95, 114–117, 122]. The incorporation of Cr and V chemically stabilizes α' or β-C_2S which can affect its reactivity [100]. The substitution of an ion on Ca or Si-site in C_2S can be predicted using the structure difference factor (D) which is based on the radius, electrovalence, and electronegativity of the substituent. The D factor indicates that the heavy metal ions with an oxidation state > (II) mostly occupy the Si-site in C_2S [44]. The incorporation and replacement of SiO_4^{4-} in C_2S by smaller ions of higher negative valency (e.g., BO_4^{5-}) is effective in the stabilization of β-C_2S [129]. If an RO_4 ion is substitutionally accepted in the C_2S lattice for SiO_4^{4-}, a further reorganization is required to preserve the charge neutrality of the total system [130–132]. The substitution of anionic position (SiO_4^{4-}) is difficult to study in stochiometric mixes. Alternatively, the substitution of Cr and V in C_2S can be observed by creating a vacancy on the Si-site when reactants are in a non-stochiometric ratio [133]. It has also been recognized that the oxidation state of Cr and V is controlled by the oxygen (pO_2) partial pressure or sintering atmosphere. The use of reducing sintering conditions is one of the methods to prevent the formation of a high oxidation state of Cr (VI) and V(V) [134, 135].

A few studies have been conducted to investigate the doping behaviour of V and Cr in C_2S [56, 115, 136, 137]. However, there is not much information available for V substitution on Si-site in C_2S. For example, at which oxidation state Cr and V prefer to substitute on the Si-site in C_2S is an important question. This also holds for the

maximum amount of substitution of Cr and V on the Si-site in C_2S under certain oxidizing and reducing conditions. In this regard, the systematic understanding of the Cr and V occupation on the Si-site in C_2S under well-defined calcination (oxidizing and reducing) conditions, the oxidation state, impact on reactivity, and environmental impact is necessary for the valorization. Such analytical studies would help to understand the aliovalent Cr, V distribution in C_2S, and its correlation with leaching behaviour in Cr, V bearing C_2S phases in belite-based binders, slags as well as sludges.

This chapter investigates the oxidation state of V and Cr substituted on Si-site in C_2S quantitively under oxidizing (air) and reducing (20% CO/80% CO_2) sintering conditions. The effect of Cr and V doping on C_2S polymorphs is correlated with their oxidation states quantitively by using X-ray photoelectron spectroscopy (XPS), QXRD (Quantitative X-ray diffraction), FTIR (Fourier transform Infrared spectroscopy), and SEM-EDX (scanning electron microscopy-energy dispersive X-ray analysis). Furthermore, the early-stage hydration is studied via isothermal calorimetry and thermal gravimetric analysis (TGA) to understand the effect of Cr and V substitution on C_2S reactivity by considering the important factors such as lime, water to solid ratio (w/s), type of C_2S polymorphs, and specific surface area (SSA). Lastly, the Cr and V mobility in aqueous solution is correlated with substitution on Si-site in C_2S, oxidation state, the extent of the C_2S dissolution as well as phase composition by using ICP-OES (inductively coupled plasma-optical emissions spectroscopy), and IC (ion chromatography).

5.2 MATERIALS

$Ca(NO_3)_2.4H_2O$ (Sigma-Aldrich CAS: 13477-34-4 $\geqslant$ 99.0%), $Cr(III)(NO_3)_3.9H_2O$ (Sigma-Aldrich CAS: 7789-02-8, 99.0%), $V(IV)O(C_5H_7O_2)_2$ (Sigma-Aldrich CAS: 3153-62-2, $\geqslant$ 98.0%), $Si(OC_2H_5)_4$ (Sigma-Aldrich CAS: 78-10-4, $\geqslant$ 99.0%), HNO_3 (Sigma-Aldrich, CAS:7697-37-2, $\geqslant$ 65%) and C_2H_5OH (Sigma-Aldrich CAS:64-17-5) were used as received. The reagents were added in the stoichiometric ratios corresponding to the synthesis of C_2S unless indicated otherwise.

The chemical composition, sample labeling, calcination temperature, and time are summarized in Table 5.1. To avoid confusion between the Oxygen "O" symbol and sample labeling, the "O" is hyphenated (-O) in this chapter.

Table 5.1: Sol-gel synthetic parameters as calcined at 1200 °C for 8 h under oxidizing and reducing conditions.

Chemical Composition of the System	**Calcination condition**	**Short description**
Ca_2SiO_4	Oxidizing	Ref. (-O)
Ca_2SiO_4	Reducing	Ref. (R)
$Ca_2Si_{(1-x)}Cr_xO_4$ (X=5, 10, 15)	Oxidizing	Cr(5, 10, 15)-O
$Ca_2Si_{(1-x)}V_xO_4$ (X=5, 10, 15)	Oxidizing	V(5, 10, 15)-O
$Ca_2Si_{(1-x)}Cr_xO_4$ (X=2, 4, 6, 8, 10, 15)	Reducing (20% CO/80% CO_2)	Cr(2, 4, 6, 8, 10, 15)R
$Ca_2Si_{(1-x)}V_xO_4$ (X=2, 4, 6, 8, 10, 15)	Reducing (20% CO/80% CO_2)	V(2, 4, 6, 8, 10, 15)R

5.3 METHODS

5.3.1 *Non-aqueous method*

The TEOS (tetraethyl orthosilicate) and $Ca(NO_3)_2.4H_2O$ (calcium nitrate tetrahydrate) were employed as a source of Si and Ca at molar ratio. TEOS was mixed with ethanol at a molar ratio of 1:5 separately. After this, the $Ca(NO_3)_2.4H_2O$, $Cr(III)(NO_3)_3.9H_2O$, and $V(IV)O(C_5H_7O_2)_2$ were dissolved in a minimum amount of ethanol. Then both solutions were mixed followed by the dropwise addition of HNO_3 to reach a pH between 2 and 3. The samples were left overnight, and a translucent gel was obtained. The gel was dried at 150 °C to obtain the intermediate product, which was then ground, pressed into a pellet, placed in the oven at room temperature, and calcined at 1200 °C for 8 h using a heating rate of 5 °C/min. For oxidizing conditions, the sample is heated in a Nabertherm high-temperature furnace HTCT (LC011H6SN) under a standard air atmosphere. After heating the sample to the desired temperature, it is cooled naturally in the furnace. The rate of furnace cooling is adapted from the oxidizing furnace as shown in Figure 5.1 (b) and is also used for synthesis under reducing conditions to rule out the different cooling rate effects on the end product [138].

For the reducing condition calcination, the furnace was heated to 1200 °C in the heated zone. The dried intermediate gel was weighed and placed on a ceramic (Corundum) disk in the cold part, on the bottom, of the furnace, as shown in Figure 5.1 (a).

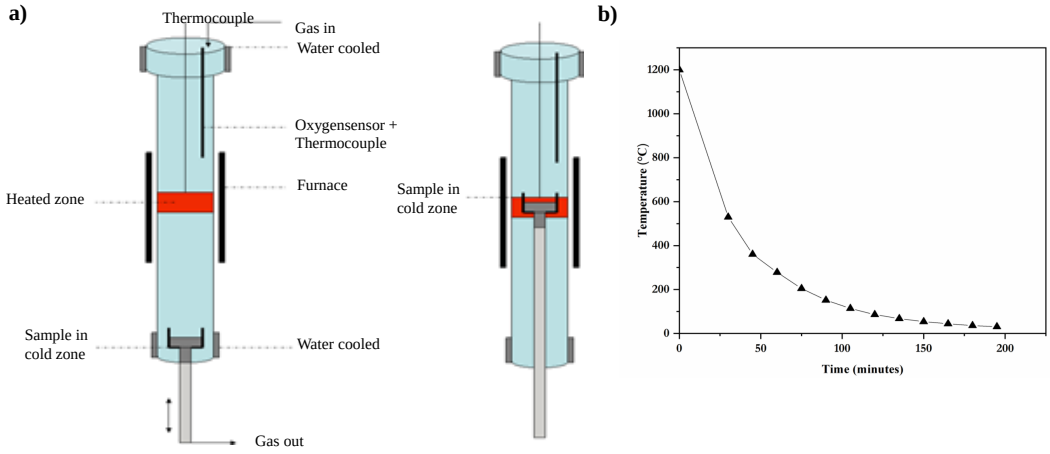

Figure 5.1: The heating furnace (a) the Gero furnace used for calcination under reducing conditions (20% CO/80% CO_2) (b) furnace cooling rate.

The sample was first heated to 700 °C at 5 °C/min. under the oxidizing condition to complete the hydrolysis of $Si(OC_2H_5)_4$ through condensation reaction and remove all the carbon (see appendix B Figure B.1-thermal gravimetric analysis). The furnace was flushed with Argon gas with a high flow rate to remove the oxygen. After the gas flow was changed to a reducing gas mixture (2 l/min. 20% CO/80% CO_2). The sample was then lowered into the heated zone, with a speed that corresponds to a heating rate of 5 °C/min. The sample stayed at 1200 °C for 8 h. The furnace was again flushed with Argon gas before the removal of the sample. The rate of furnace cooling for oxidizing and reducing conditions is shown in Figure 5.1 (b). To reduce the influence of the particle

size distribution (PSD) on the hydration kinetics, the synthesized powder was sieved to narrow the size distribution to 20-40 µm as shown in Figure 5.2 (a and b). The specific surface area (SSA) was determined via PSD estimation as shown in Table 5.2.

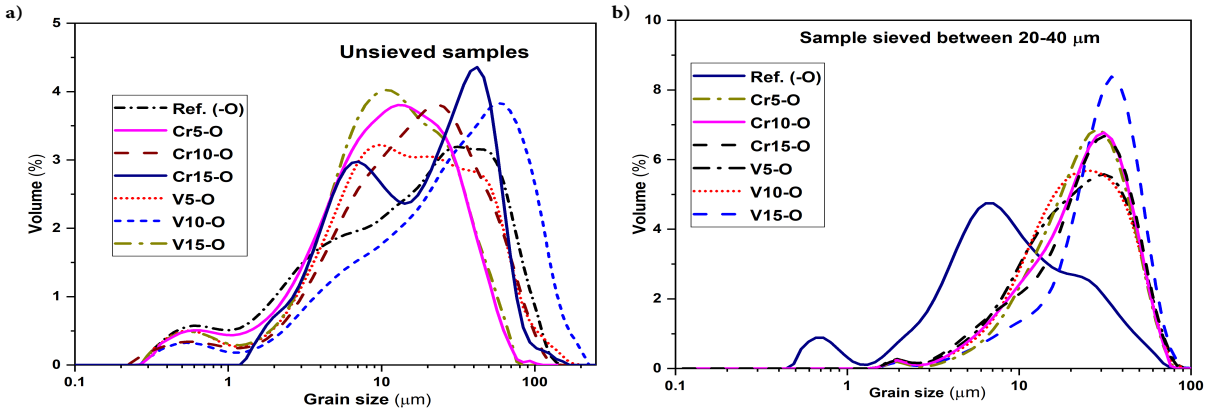

Figure 5.2: Cr and V doped C_2S under oxidizing conditions (a) non-sieved sample (b) sample sieved between 20-40 µm.

Table 5.2: The specific surface area (SSA) of the samples.

	unit	Ref. (-O)	Cr5-O	Cr10-O	Cr15-O	V5-O	V10-O	V15-O
SSA (Sieved 20-40 µm)	m^2/g	3.8	2.1	2.1	2.1	1.8	1.8	1.6
SSA	m^2/g	2.9	4.6	4.3	5.3	5.5	4.4	2.9

The sample was first heated to 700 °C at 5 °C/min. under the oxidizing condition to complete the hydrolysis of $Si(OC_2H_5)_4$ through condensation reaction and remove all the carbon (see appendix B Figure B.1-thermal gravimetric analysis). The furnace was flushed with Argon gas with a high flow rate to remove the oxygen. After the gas flow was changed to a reducing gas mixture (2 l/min. 20% CO/80% CO_2). The sample was then lowered into the heated zone, with a speed that corresponds to a heating rate of 5 °C/min. The sample stayed at 1200 °C for 8 h. The furnace was again flushed with Argon gas before the removal of the sample. The rate of furnace cooling for oxidizing and reducing conditions is shown in Figure 5.1 (b). To reduce the influence of the particle size distribution (PSD) on the hydration kinetics, the synthesized powder was sieved to narrow the size distribution to 20-40 µm as shown in Figure 5.2 (a and b). The specific surface area (SSA) was determined via PSD estimation as shown in Table 5.2.

5.4 RESULTS AND DISCUSSION

5.4.1 *Characterization of the synthesized product*

5.4.1.1 *Cr doped C_2S*

The QXRD of the Cr-doped C_2S under oxidizing and reducing conditions is given in Table 5.3. The results showed that the replacement of silicon with chromium prevents the

formation of γ-C_2S because only the Ref. (-O) contains this polymorph (16.7 wt. %) (see appendix B Figure B.2 for XRD pattern and peak assignment). The Cr5-O sample exhibits a substantial increase in the amount of β-C_2S from 75.1 to 87.8 wt. % and stabilization of α'-C_2S (5.3 wt. %) compared to the Ref. (-O) sample.

As the replacement level increases from Cr5-O to Cr15-O, the α' increases from 5.3 to 43.3 wt. % with a decreasing amount of β-C_2S from 87.8 to 24.5 wt. % which indicates the incorporation of Cr in C_2S. The stabilization of high-temperature polymorph α'-C_2S at room temperature is usually associated with the exsolution of impurity ions such as Na_2O, K_2O, etc. [131] and Cr_2O_3 could contribute in the same manner. The impurity ion hinders the transformation of α' to γ-C_2S during the cooling process. Consequently, the metastable α'-C_2S persists around 675-750 °C, and upon further cooling, to room temperature, it partially collapses to β-C_2S [139]. In addition to high-temperature polymorphs (α' and β) of C_2S, other chromium-bearing phases formed such as Cr_2O_3, the chromium analogue to silicocarnotite ($Ca_5Cr_{3-x}Si_xO_{12}$) [140] as well as minor phases such as lime, calcite, cristobalite, and quartz. Moreover, the amorphous content increases from 2.5 to 26.4 wt. % with an increasing amount of Cr replacing Si in samples.

To understand the maximum Cr-substitution on the Si-site, a theoretical Cr distribution between C_2S + amorphous content and the rest of Cr-bearing phases such as Cr_2O_3, chromium analogue to silicocarnotite, etc. was calculated as shown in Table 5.4. The distribution of Cr has been calculated by considering the starting stoichiometric composition and the QXRD of the samples. The amount of Cr in Cr-bearing crystalline phases is calculated. For the chromium analogue, the silicocarnotite composition ($Ca_5Cr_{1.82}Si_{1.176}O_{12}$) was assumed based on XRD phase information. If this amount of Cr is subtracted from the total amount of Cr in the system. It follows that the remaining amount is incorporated into the C_2S, the amorphous content, or both. However, it is not possible to differentiate if the Cr is evenly distributed between C_2S polymorphs and amorphous content. As the amount of total Cr increases from 3.3 to 5 wt. % (Cr10-O and Cr15-O respectively), a marginal increase of Cr from 2.5 to 2.6 wt. % is calculated for C_2S + amorphous phase. Therefore, 2.6 wt. % seems to be the maximum that can be incorporated into the C_2S + amorphous phase. For amounts higher than 2.6 wt. % Cr seems to crystallize as separate Cr phases such as Cr_2O_3 or the Cr analogue of silicocarnotite. The comparison between the Cr concentration in C_2S + amorphous content and QXRD analysis of the Cr5-O sample indicates that approximately a maximum of 1.4 wt. % (4.1 mol. %) Cr can be substituted in C_2S theoretically (Table 5.3 and Table 5.4). The Cr5-O contains an amorphous content as low as 3.5 ± 1.5 wt. % which indicates the Cr is mostly incorporated into α' and β-C_2S.

Under the reducing (20% CO/80% CO_2) condition (Table 5.3), the reference sample (Ref. (R) exhibits a lower total amount of β/γ-C_2S (70.4 and 1.4 wt. %) with higher amorphous content (17.0 wt. %) than the Ref. (-O) sample calcined under oxidizing conditions. The presence of high amounts of free lime (7.2 wt. %) along with wollastonite (1.2 wt. %) and quartz + cristobalite (1.7 wt. %) indicates the incomplete reaction of the precursors. It would originate due to a little hindrance in a sintering reaction between incomplete Si-O-Si network, wollastonite, and calcium oxide due to reducing condition.

Table 5.3: QXRD of the chromium-doped C_2S synthesized via the sol-gel process under oxidizing and reducing (20% CO/80% CO_2) conditions at 1200 °C for 8 h.

Phases (wt. %)	**Ref. (-O)**	**Cr5-O**	**Cr10-O**	**Cr15-O**	**Ref. (R)**	**Cr2R**	**Cr4R**	**Cr6R**	**Cr8R**	**Cr10R**	**Cr15R**
α′-C_2S		5.3 ± 0.2	23.1 ± 0.3	43.3 ± 0.6							
β-C_2S	75.1 ± 0.3	87.8 ± 0.3	46.9 ± 0.4	24.5 ± 0.6	70.4 ± 0.8	61.2 ± 0.3	64.1 ± 0.3	61.9 ± 0.2	71.02 ± 0.3	59.2 ± 0.2	58.3 ± 0.3
γ-C_2S	16.7 ± 0.2				1.4 ± 0.3						
Lime	2.7 ± 0.1	1.2 ± 0.06	0.7 ± 0.08	0.6 ± 0.1	7.2 ± 0.2	7.5 ± 0.1	5.6 ± 0.1	7.9 ± 0.1	10.2 ± 0.1	6.7 ± 0.1	10.1 ± 0.1
Calcite		0.7 ± 0.1	0.8 ± 0.1	1.5 ± 0.2	0.4 ± 0.1	1.0 ± 0.1	1.1 ± 0.1	1.1 ± 0.1	1.3 ± 0.1	1 ± 0.1	1.6 ± 0.2
(Para)Wollastonite	0.2 ± 0.1				1.2 ± 0.3	8.7 ± 0.2	13.4 ± 0.0.2	8.2 ± 0.2	9.0 ± 0.2	11.2 ± 0.1	5.6 ± 0.4
Cr_2O_3		0.3 ± 0.06	0.7 ± 0.1	1.3 ± 0.2							
$CaCr_2(III)O_4$						0.6 ± 0.1	0.6 ± 0.1	1.2 ± 0.1	1.6 ± 0.1	1.7 ± 0.1	1.8 ± 0.1
$CaCrSi_4O_{10}$			0.7 ± 0.2								
$Ca_5Cr_{1.82}Si_{1.176}O_{12}$				2.3 ± 0.4							
Quartz+Cristobalite	1.0 ± 0.07	1.1 ± 0.08	0.7 ± 0.1	0.8 ± 0.1	1.7 ± 0.5	0.9 ± 0.07	1.2 ± 0.08	0.9 ± 0.1	1 ± 0.04	1 ± 0.06	0.8 ± 0.08
Grossular	0.6 ± 0.2	0.1 ± 0.09			0.8 ± 0.2						
XRD amorphous	3.8 ± 1.6	3.5 ± 1.5	26.4 ± 1.2	25.8 ± 2.1	17.0 ± 3.5	20.2 ± 0.8	14.1 ± 1.0	19 ± 0.7	6.0 ± 1.1	19.3 ± 0.8	21.7 ± 1.0

The complete conversion of reactants into C_2S in sol-gel synthesis partially requires a sintering reaction between the CaO and Si-O-Si network at high temperatures under oxidizing conditions as discussed in Chapter 4 [138].

Table 5.4: Theoretical composition calculation of vanadium and chromium distributed among different mineral phases synthesized under oxidizing conditions. The theoretical composition is the difference between the starting amount of heavy elements (Cr, V) and the oxides contained in the C_2S + amorphous as well as Cr/V-bearing phases.

Sample	Total substitution (wt. %)	Cr or V in C_2S + Amorphous phases (wt. %)	Cr or V in Chromium and Vanadium phases (wt. %)
Cr5-O	1.7	1.4	0.3
Cr10-O	3.3	2.5	0.8
Cr15-O	5	2.6	2.4
V5-O	1.7	1.3	0.4
V10-O	3.3	2.3	1
V15-O	5	3.1	1.9

As the Si was replaced with 2, 4, 6, 8, 10, 15 mol. % Cr under reducing conditions, the β-C_2S (ranging from 58.3 to 71.0 wt. %) was the only C_2S polymorph that formed during cooling. Moreover, a considerable amount of lime (5.6-10.2 wt. %), (Para)wollastonite (5.6 to 13.4 wt. %) was observed alongside $CaCr_2(III)O_4$ (0.6-1.8 wt. %) and high amorphous (6.0-21.7 wt. %) content. The high amount of unreacted lime and wollastonite phases point to an imbalanced Ca and Si stoichiometry with a lack of Si available for C_2S synthesis. The stabilization of only β-C_2S, the imbalanced stoichiometry, and high amorphous content under reducing conditions indicate that no Cr was incorporated into C_2S. This could happen due to a change in the Cr oxidation state in reducing conditions as the addition of Cr on the Si-site in C_2S is highly dependent on the oxidation state and geometry of the Cr ion [136].

FTIR has been chosen to investigate bond systems as shown in Figure 5.3 (a, b). Usually, the β-C_2S has a characteristic absorption band in the range of 990-998 cm^{-1} and 860 cm^{-1} due to silica stretching. The intensity of this band decreased, and the broadband appeared indicating the presence of α′-C_2S with an increasing amount of Cr dopant in Cr5-O, Cr10-O, and Cr15-O, as shown in Figure 5.3 (a). The carbonation of the sample arising from exposure to air can result in the band at 1490 cm^{-1}, caused by the asymmetric stretching of carbonate (CO_3^{2-}) ions. The small sharp peak at 3650 cm^{-1} depicts the presence of calcium hydroxide originating due to lime reaction with moisture. In reducing conditions, the broadening of the band around 890 cm^{-1} can be attributed to wollastonite as shown in Figure 5.3 (b) [110].

To understand the Cr occupancy on the Si-site in C_2S, the oxidation state of Cr ions has been measured quantitatively in the Cr5-O, Cr6R, Cr10-O, Cr10R, Cr15-O, and Cr15R samples due to approximately the same starting Ca/Si (2.2) molar ratio of the precursors as shown in Figure 5.4. The binding energies of Ca 2p ($2p_{3/2}$: 347 eV) and Si 2p ($2p_{3/2}$: 101 eV) agrees with previously reported C_2S values (see XPS elemental analysis, appendix B Table B.2 [130, 141, 142]. The separation between Si 2p and Ca 2p binding energies ($\delta_{Ca\text{-}Si}$) was calculated as 245.7 eV which is slightly lower than the 246.07 eV value reported for β-C_2S (see Table B.3 in appendix B) [141].

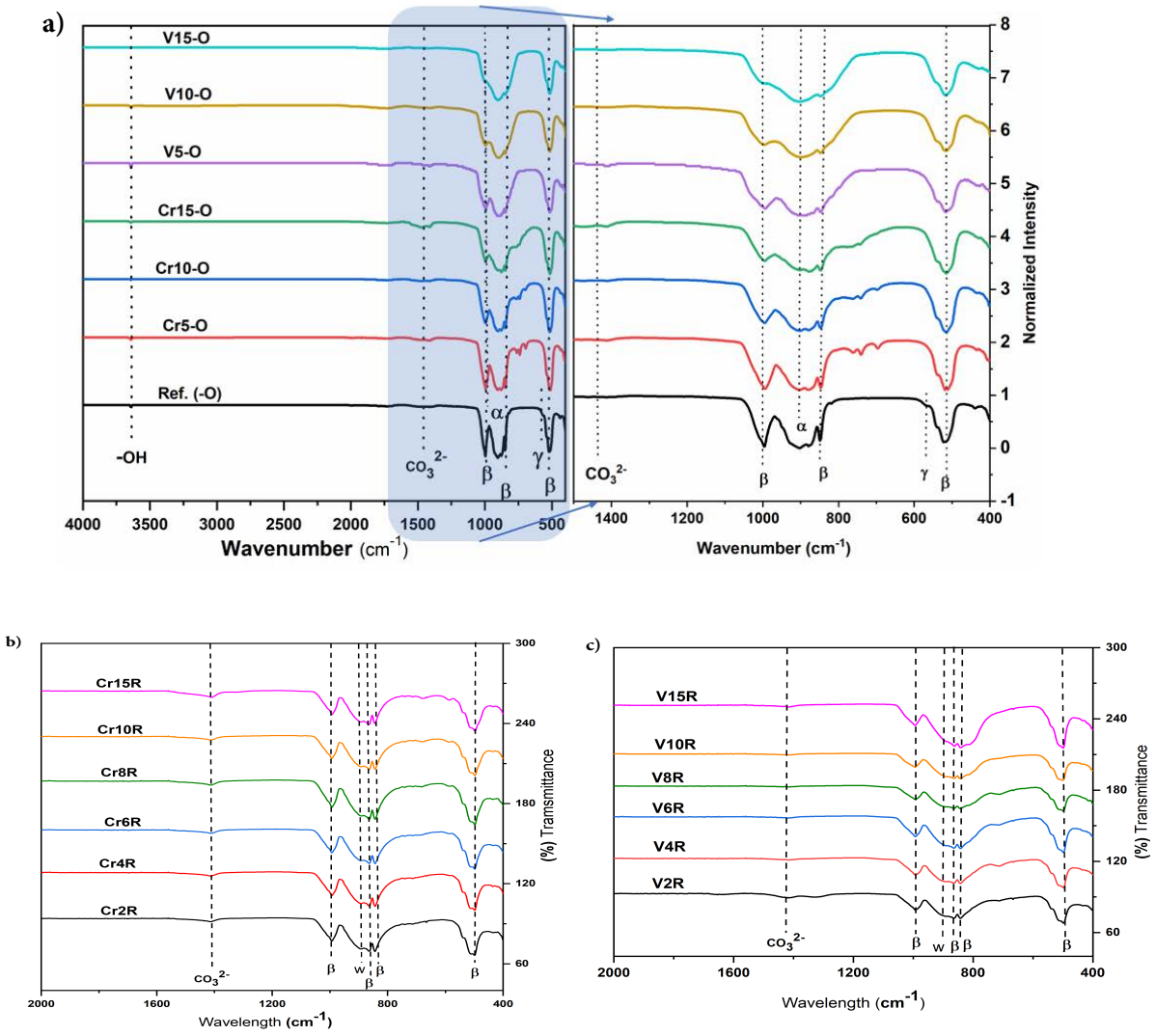

Figure 5.3: FTIR analysis Cr and V doped C_2S (a) oxidizing conditions (b) Cr doped C_2S under reducing conditions (c) V doped under reducing conditions.

Under oxidizing conditions, a Cr $2p_{3/2}$ peak at binding energy 579.6 eV is assigned as Cr (VI) which indicates the incorporation of Cr in C_2S. The Cr $2p_{3/2}$ peaks at binding energy 576.6 and 578.1 eV are assigned to Cr (III) which is predominant in the Cr5-O, Cr10-O, and Cr15-O samples. The shift in binding energy from 576.6 to 578.1 eV indicates the presence of Cr (III) in two different sites and orientations [143, 144]. No Cr (IV) was observed. It is worth mentioning here that the Cr was added as Cr (III) for the synthesis of C_2S. The results indicate that as the amount of Cr increases in the samples, a specific amount of Cr (VI) can be incorporated in C_2S on the Si-site which is approximately the same in all the samples as shown in Figure 5.4 (c). However, most of the chromium stayed as Cr (III) either in the form of Cr2O3 (576.6 eV) or bound in a different phase as the shift 578.1 eV indicates in the measurement. This is most likely the amorphous phase that was observed via QXRD. However, the α'-C_2S stabilization due to the increasing amount of Cr in the samples cannot only be associated with Cr incorporation in C_2S as the amount of Cr (VI) is approximately the same in Cr10-O, and Cr15-O samples (Figure 5.4 (c), Table

5.3 and Table 5.4). Some other factors are also contributing to the Cr (VI) incorporation in C_2S. This observation is sufficiently compelling for further characterization of material to understand the phenomenon of α'-C_2S stabilization.

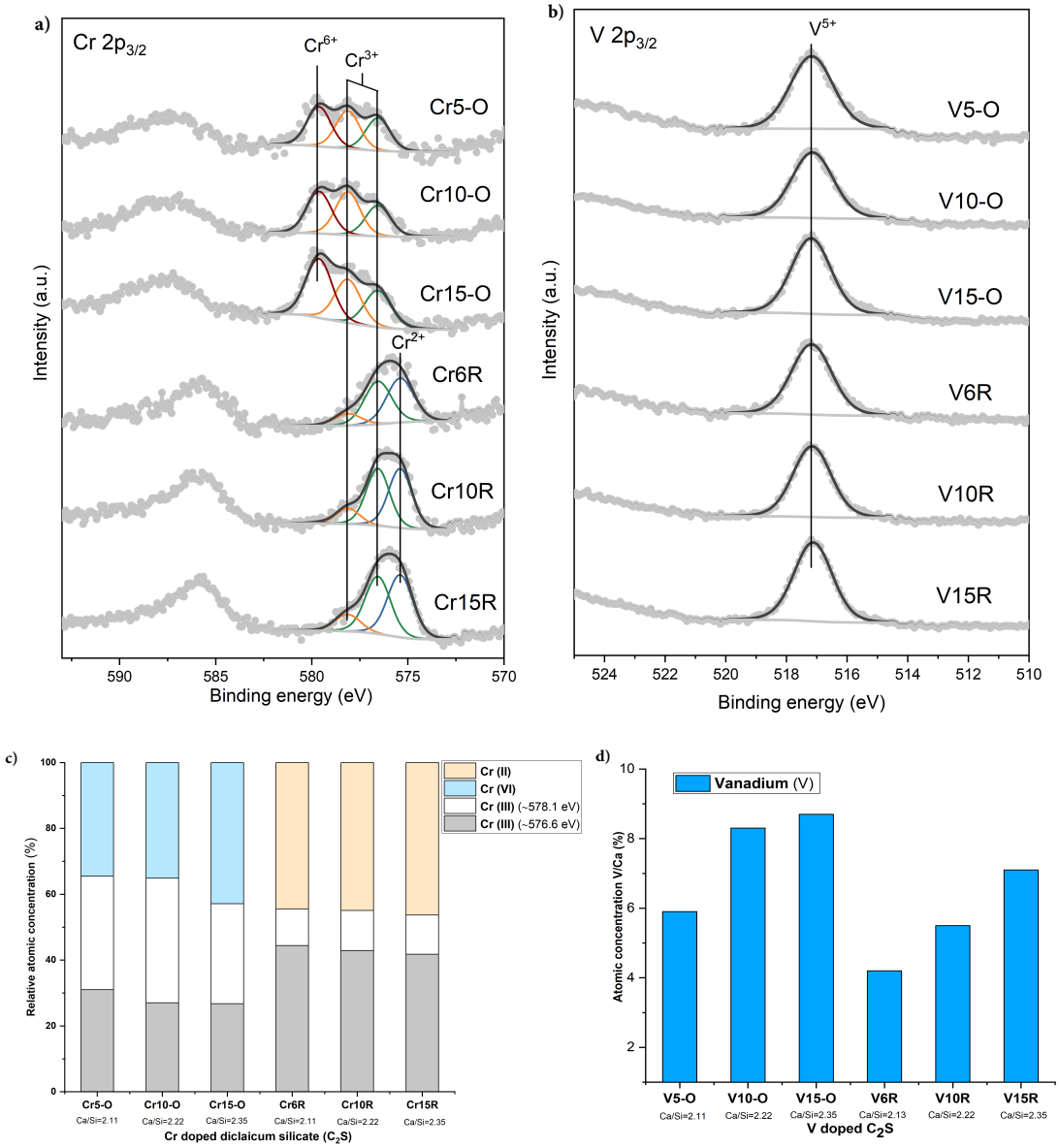

Figure 5.4: XPS analysis of Cr and V doped C_2S (a) Cr $2p_{3/2}$ scan of Cr doped C_2S (b) V $2p_{3/2}$ scan of V doped C_2S (c) relative percentage oxidation sate of Cr doped C_2S under oxidizing and reducing condition (d) relative Ca/V ratio of V doped C_2S under oxidizing and reducing condition.

Under reducing conditions, the samples only contained Cr (II) and (III) oxidation states as shown in Figure 5.4 (a, c). The Cr $2p_{3/2}$ binding energy peak at 575.4 eV is assigned as Cr (II) [145]. This observation alone explains a large amount of free lime and (Para)wollastonite phases. Cr (II) and (III) exist in octahedral geometry and tend not to substitute on the Si-site in C_2S leading to a silica deficit, which creates (Para)/wollastonite and free lime instead (Table 5.3) [56].

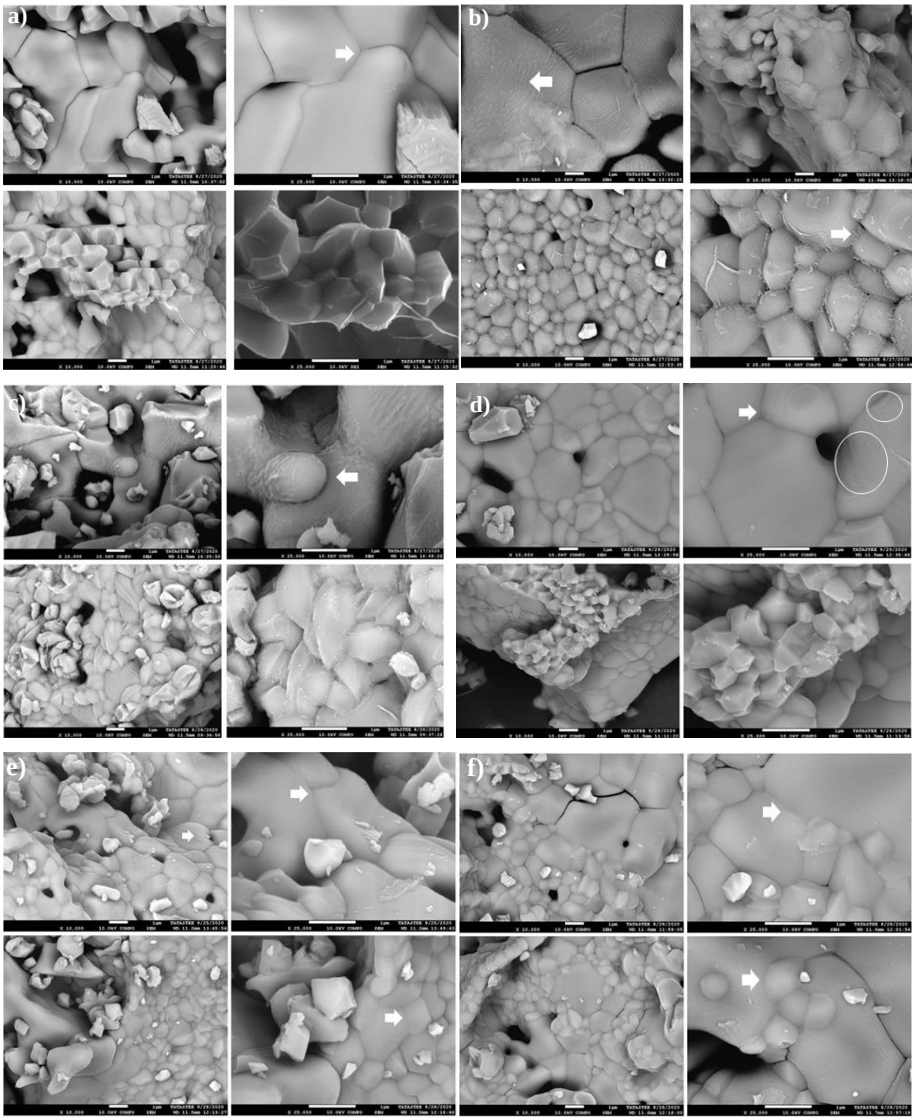

Figure 5.5: SEM (Scanning electron microscopy) analysis of Cr and V doped C_2S under oxidizing conditions (a) Cr5-O (b) Cr10-O (c) Cr15-O (d) V5-O (e) V10-O (f) V15-O. "white arrow" indicates the grain boundaries and "circle" indicates the sign of surface relief.

SEM-BS (backscattered image) images were taken of Cr5-O, Cr10-O, and Cr15-O as shown in Figure 5.5 (a, b, c) to gain information about the microstructure. The two different kinds of grains were recognized; smooth grains, as well as grains covered with a glassy layer. The Cr-doped C_2S also exhibited small and large grains with lamellar morphology as previously reported for the incorporation of other ions [146]. The Cr5-O sample exhibited smooth grain with conspicuous grain boundaries (Figure 5.5a). As the amount of Cr increased in Cr10-O, the individual grain surface was covered with a glassy layer as well, and the grain boundary phase precipitated between the striae (Figure 5.5b). As the Cr amount further increased in Cr15-O, the more grains were covered with a glassy layer as shown in Figure 5.5 (c). It would happen due to the formation of the C_2S-Cr_2O_3 glass phase as the Cr amount increases from 5-15 mol. % in the samples. This glassy phase fits with the fact that an increasing amount of amorphous content is detected with the increasing replacement of Si with Cr (Table 5.3).

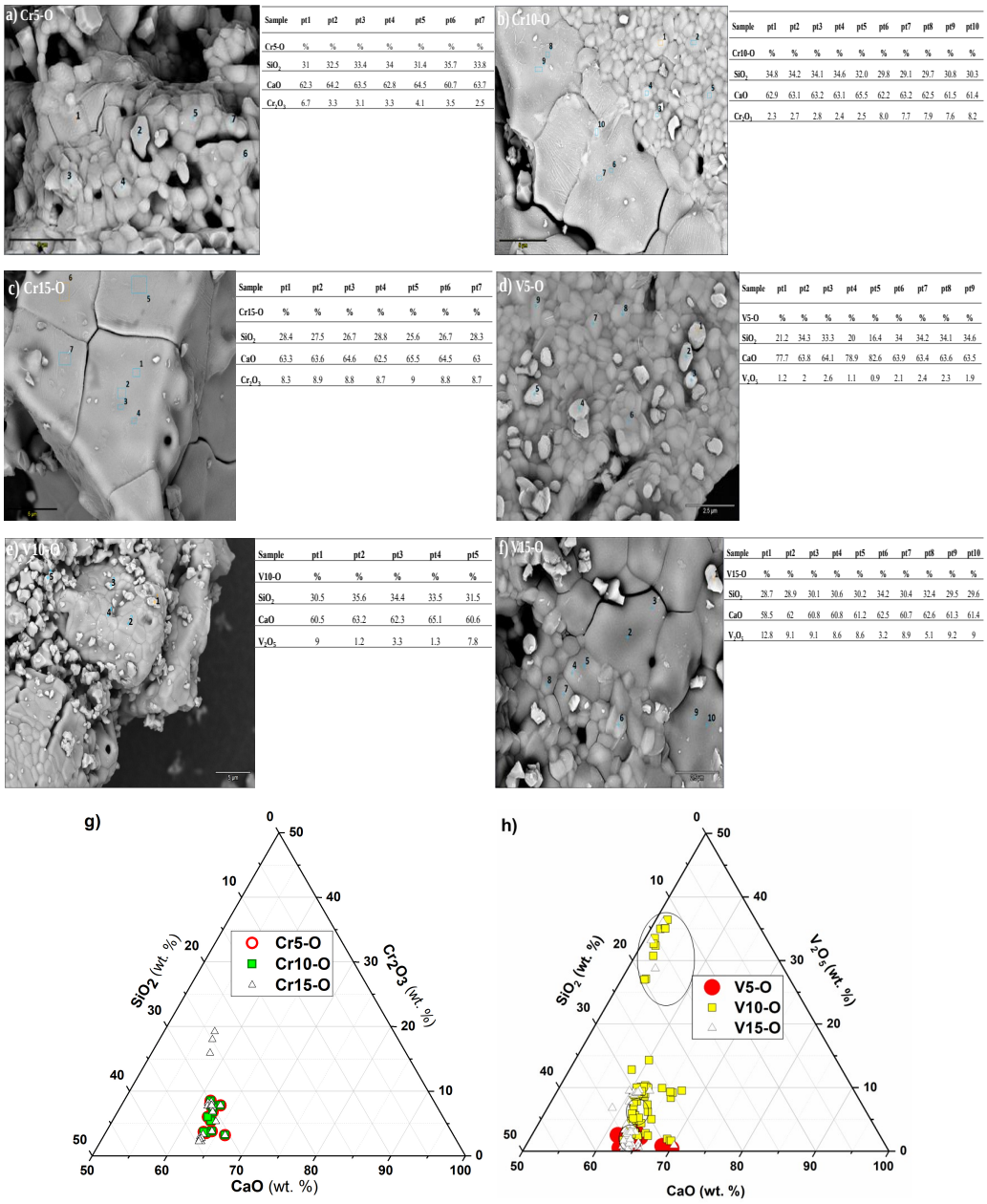

Figure 5.6: EDX (Energy dispersive X-ray) analysis of Cr and V doped C_2S under oxidizing conditions-the oxide composition of varying spot positions (a) Cr5-O (b) Cr10-O (c) Cr15-O (d) V5-O (e) V10-O (f) V15-O (g) oxide composition of Cr (5, 10, 15) -O (h) oxide composition of V (5, 10, 15) -O.

The stabilization of α'-C_2S in the Cr10-O and Cr15-O samples cannot be attributed to a change in average crystallite size as the small crystallite size favours the formation of α'/β-polymorphs over γ-C_2S (Figure B.3 in apppendix B) and average crystallite size does not change with an increasing amount of Cr. Moreover, the α'-C_2S stabilization due to the increasing amount of Cr cannot only be associated with Cr incorporation in C_2S as the amount of Cr (VI) is approximately the same in Cr10-O, and Cr15-O samples (Table 5.3 and Table 5.4, Figure 5.5a). It would rather change due to the matrix constraint (coverage of individual C_2S grain with glass layer) which prevents the $\alpha' \rightarrow \beta$ transformation. The free

energy of an isolated particle may be considerably different from that of a constrained particle. The glassy layer constraining the C_2S grains restricts the growth of the mean particle size to below a critical size that would cause the transformation from $\alpha \rightarrow \beta \rightarrow \gamma$ otherwise [105, 107]. Therefore, the matrix constraint is one of the main reasons behind the stabilization of α'-C_2S with an increasing amount of Cr in the sample.

In addition to SEM BS imaging, EDX spot analysis was performed on the samples to determine the composition. An example of the spots measured is shown in Figure 5.6 (a, b, c). All measured spots of the synthesized Cr5-O, Cr10-O, and Cr15-O have been plotted in the oxide composition diagram shown in Figure 5.6 (g). It is worth mentioning here that the resolution is 1 μm, therefore it is difficult to measure the small features like the glassy layer separately because analysis always includes the underlying phase. However, the amount of Cr increases as the amount of Cr increases in the sample, and the highest amount was observed in the glass layer of the Cr15-O sample. The oxide composition diagram indicated that there is not much difference in the composition of Cr5-O and Cr10-O samples. But in the Cr15-O sample, the distinction between Cr-bearing C_2S phases and Cr-enriched phases became conspicuous which was also observed in the XRD sample (Table 5.3).

5.4.1.2 *V doped C_2S*

The QXRD of V-doped C_2S under oxidizing and reducing conditions is shown in Table 5.5. The replacement of V on the Si-site under oxidizing condition (V5-O) prevents the formation of γ-C_2S (16.7 wt. %) that is observed in the reference sample (see Figure B.2 in appendix B for XRD pattern and peak assignment). Sample V5-O exhibited the stabilization of α'-C_2S (8.3 wt. %) and β-C_2S (71.8 wt. %) alongside minor phases such as free-lime, calcite, quartz, cristobalite, and higher amorphous content (15.4 wt. %) than the reference sample (3.8 wt. %). As the amount of V increased in V10-O, and V15-O samples, the more α'-C_2S (27.0 and 27.1 wt. % respectively) stabilized pointing to the incorporation of V on the Si-site. The β-C_2S amount decreased from 71.8 to 29.9 wt. % at the same time with an increasing amount of amorphous content (from 15.4 to 36.2 wt. %). Additionally, some minor vanadium-bearing crystalline phases like VO_2 and CaV_2O_4 alongside some calcite, quartz, and cristobalite were observed. The theoretical distribution of V is calculated between C_2S + amorphous phases and V-bearing phases as shown in Table 5.4. The amount of V increases from 1.3 to 3.1 wt. % incorporated in C_2S + amorphous phases with an increasing amount of V in the sample. Considering the amount of amorphous content (15.4 ± 1.7 wt. %) and vanadium-bearing crystalline phase in V5-O, it is difficult to predict the maximum substitution of V on Si- site in C_2S theoretically.

Under reducing conditions, the V-doped C_2S exhibits only the β-C_2S polymorph as shown in Table 5.2. This indicates that vanadium is not incorporated into the C_2S as similar behaviour was observed in the case of Cr doping under reducing conditions. The V2R sample contains 72.1 wt. % β-C_2S and 9.4 wt. % lime as observed in Ref. (R) but a higher amount of (Para)wollastonite (12.4 wt. %).

Table 5.5: QXRD of the Vanadium doped C_2S synthesized via the sol-gel process under oxidizing and reducing (20% CO/80% CO_2) conditions at 1200 °C for 8 h.

Phases (wt. %)	**Ref. (-O)**	**V5-O**	**V10-O**	**V15-O**	**Ref. (R)**	**V2R**	**V4R**	**V6R**	**V8R**	**V10R**	**V15R**
α′-C_2S		8.3 ± 0.3	27.0 ± 0.4	27.1 ± 4.8							
β-C_2S	75.1 ± 0.3	71.8 ± 0.5	46.3 ± 0.4	29.9 ± 4.3	70.4 ± 0.8	72.1 ± 0.3	60.3 ± 0.3	60.3 ± 0.3	58.9 ± 0.4	67.2 ± 0.9	58.0 ± 0.5
γ-C_2S	16.7 ± 0.2				1.4 ± 0.3						
Lime	2.7 ± 0.1	2.6 ± 0.08	0.1 ± 0.06	1.6 ± 0.3	7.2 ± 0.2	9.4 ± 0.1	5.0 ± 0.1	5.9 ± 0.1	7.7 ± 0.1	5.5 ± 0.1	4.2 ± 0.1
Calcite		0.3 ± 0.1	1.4 ± 0.2	1.6 ± 0.3	0.4 ± 0.1	0.9 ± 0.1	0.4 ± 0.1	0.7 ± 0.1	0.7 ± 0.2	0.9 ± 0.2	1.7 ± 0.2
(Para)Wollastonite	0.2 ± 0.1				1.2 ± 0.3	12.4 ± 0.2	10.3 ± 0.2	7.9 ± 0.2	8.8 ± 0.2	6.5 ± 0.3	6.4 ± 0.3
Quartz + Cristobalite	1.0 ± 0.1	1.2 ± 0.1	0.6 ± 0.1	0.6 ± 0.1	1.7 ± 0.5	1.5 ± 0.1	1.3 ± 0.1	1.0 ± 0.1	0.8 ± 0.1	0.8 ± 0.03	1.5 ± 0.1
VO_2		0.4 ± 0.08	0.9 ± 0.2	1.0 ± 0.2		0.3 ± 0.1	0.1 ± 0.1		0.1 ± 0.1		
V_5O_9			0.1 ± 0.3					0.7 ± 0.1	0.7 ± 0.2	1.2 ± 1.0	1.8 ± 0.2
CaV_2O_4				0.9 ± 0.3							
$CaVO_3$								0.5 ± 0.2	0.6 ± 0.2	0.3 ± 0.3	0.4 ± 0.3
CaV_3O_7								0.8 ± 0.1	0.7 ± 0.2	0.8 ± 0.2	1.2 ± 0.2
$Ca(VO)Si_4O_{10}$											0.3 ± 0.1
Grossular	0.6 ± 0.2	0.2 ± 0.1	1.5 ± 0.2	0.8 ± 0.4	0.8 ± 0.2					0.3 ± 0.2	
XRD amorphous	3.8 ± 1.6	15.4 ± 1.7	22.2 ± 1.9	35.2 ± 8.3	17.0 ± 3.5	2.9 ± 1.1	22.5 ± 0.9	21.9 ± 1.0	21.2 ± 1.2	16.7 ± 1.7	24.5 ± 1.2

As the amount of V replacement increases under reducing conditions (V4R, V6R, V8R, V10R, V15R), new V-bearing crystalline phases such as V_5O_9, $CaVO_3$, CaV_3O_7, $Ca(VO)Si_4O_{10}$ are observed alongside a high amount of β-C_2S (58.0-67.2 wt. %), (Para)wollastonite (6.4-10.3 wt. %) and lime (4.2-7.7 wt. %). The high amount of (Para)wollastonite and lime indicates that the Ca to Si stoichiometry is imbalanced.

Consequently, vanadium is unable to substitute on the Si-site in C_2S under reducing conditions due to a geometrical or oxidation state mismatch between the vacancy (Si-site) and the substituent. This leads to the Si deficit and promotes the (Para)wollastonite formation. Such behaviour was observed in Cr under reducing conditions.

XPS analysis was performed to get better insight into the oxidation state of the V5-O, V6R, V10-O, V10R, V15-O, and V15R samples as shown in Figure 5.4. The V $2p_{3/2}$ peak at binding energy 517.2 eV is assigned as V (V) as shown in Figure 5.4 (b) (see appendix B, Table B.2 XPS elemental analysis) [147, 148]. The V/Ca atomic concentration (%) is calculated to make a direct comparison between all the measurements as shown in Figure 5.4 (d). Moreover, Ca is taken as the denominator because the amount of Ca does not change in all the V-doped C_2S samples. Only V (V) is found in V5-O, V10-O, and V15-O samples as well as the C_2S samples calcined under reducing conditions (V6R, V10R, V15R) (Figure 5.4 (b, d). An oxidation state lower than V(V) was not observed. Possibly, the V5R, V10R, and V15R samples fully oxidize to V(V) on cooling because the vanadium (II-IV) oxide is highly sensitive to air oxidation [148]. The stabilization of α′-C_2S with the increasing amount of V indicates the occupation of the Si-site by V(V) due to V_2O_5 substituting as the foreign ion (Table 5.5). Usually, the impurity ions such as V(V) in the present case can only be incorporated as foreign ions at high clinkering temperatures [139]. The absence of α′-C_2S and the presence of a high amount of (Para)wollastonite in V6R, V10R, and V15R indicates that the V was not available as V(V) at high temperatures under reducing conditions. Therefore, it was not substituted on the Si-site in C_2S.

The presence of vanadium species also complicates the assignment of peaks in FTIR. A representative FTIR spectrum has been chosen to investigate bond systems as shown in Figure 5.3 (a, c). Usually, the β-C_2S has a characteristic absorption band in the range of 990-998 cm^{-1} and 860 cm^{-1} due to SiO_2-stretching. However, the characteristic V-O-V asymmetric stretch vibrations, as well as V-O-V octahedral bending, lie in the region of 1010-1040 and 840-860 cm^{-1} [149, 150]. These two bands´ shoulders are superimposed on a broad peak around 900 cm^{-1} in the stretching region. The α′-C_2S also has a strong and broad characteristic absorption at 895 cm^{-1}. This causes peak broadening in the samples with a higher concentration of α′-C_2S as the amount of the dopant increases in the V5-O, V10-O, and V15-O as shown in Figure 5.3 (a). Moreover, the broadening of the shoulder around 990-1035 cm^{-1} can be attributed to V=O isolated double bonds [151]. The α′- and β-C_2S polymorphs both showed a strong absorption around 520 cm^{-1} with a faint shoulder at 540 cm^{-1} in the SiO_2-bending region. In the mixture in which both phases are present, the polymorph-specific absorptions are indistinguishable. The slight carbonation of the sample arising from exposure to air can result in the band at 1490 cm^{-1}, caused by the asymmetric stretching of carbonate (CO_3^{2-}) ions. The small sharp peak at 3650 cm^{-1} can point out the presence of free lime in the sample that was slightly hydrated in the air.

The C_2S sample calcined under reducing conditions (V2R, V4R, V6R, V8R, V10R, and V15R) feature β-C_2S as a dominant phase. But the broadening of signal around 840-860, 890, and 990-1040 cm^{-1} can also be attributed to the presence of wollastonite and

vanadium-bearing phases in the samples. All these findings showed a good agreement with QXRD and previous reports [152].

An extensive SEM-EDX analysis was performed to get an insight into the microstructure and composition of the V-doped C_2S under oxidizing conditions. Sample V5-O exhibited twin domains with distinct grain boundaries and lamellae characteristics (Figure 5.5d) like the Cr-containing samples. Additionally, a sign of surface relief perpendicular to the twin domain can also be observed which is the characteristic deformation evolved during the $\alpha' \rightarrow \beta$ transition due to the doping of foreign ions in C_2S [153]. As the amount of V increases in V10-O and V15-O, more grain is covered with a glassy layer indicating the presence of V -bearing amorphous phases (Figure 5.5 (e, f)). Moreover, the distinct grain boundaries also start to disappear indicating the precipitation of new phases after the formation of C_2S. Therefore, the increase in the amorphous content and V-bearing crystalline phases was observed in V10-O and V15-O samples as it matches with the QXRD observation (Table 5.5).

The oxide composition of V5-O, V10-O, and V15-O samples was measured with EDX on random spots including the precipitate at grain boundaries, smooth grain, and grain covered with a glass layer. A few of the spot data from backscattered images are shown as an example in Figure 5.6 (d, e, f). It was observed that the V5-O sample gave a slightly higher average V2O5 concentration in the middle of smooth grains. At high Si replacement with V, the V10-O and V15-O samples exhibited a vanadium concentration as high as 36% in the smooth grains while the average was 1-2% in the single grains covered with a glass layer. Moreover, the V15-O sample showed the highest V_2O_5 concentration ranges from 5-10% in the grains covered with a glass layer. All these data points are not coverable in Figure 5.6 (d, e, f) and therefore, are plotted in the form of an oxide composition diagram as shown in Figure 5.6 (h). The higher concentration of vanadium in the grains up to 36% than a stoichiometric oxide composition of the mineral phases in the V5-O, V10-O, and V15-O samples would possibly be observed due to the relatively small average crystallite size of α' and β-C_2S which leads to an overestimation of the vanadium concentration (Table 5.5) (see average crystallite size in Figure B.3 in appendix B). That's why the oxide composition diagram exhibits some outliers which leads to the wide range of the composition.

The replacement of Si with V in the C_2S matrix leads to the formation of three types of phase composition such as primary C_2S, V-rich C_2S, and high V-bearing phases as encircled in Figure 5.6 (h). In the V10-O and V15-O samples, the vanadium started to enrich in separate phases which would be the reason for the high amorphous content (Table 5.5).

5.4.2 *Hydration studies of Cr and V doped C_2S*

Cr and V doped C_2S under oxidizing conditions (Cr5-O, Cr10-O, Cr15-O, V5-O, V10-O, V15-O) were measured via isothermal calorimetry to determine the hydration rate. The heat flow curves were normalized to the mass of the solid and are presented in Figure 5.7. The C_2S reactivity is highly sensitive to the specific surface area, lime (CaO) content, water-to-solid ratio (w/s), and the type of C_2S (α', β, γ) polymorph [95, 154]. Therefore, the samples were sieved to between 20-40 μm, and different w/s ratios were investigated. Usually, the increase in the w/s ratio enhances the degree of dissolution

of C_2S [155]. However, the Ref. (-O) sample does not show any significant increase or decrease in the heat release with varying w/s ratio. Instead, a constant cumulative heat 56 J/g C_2S is observed with increasing w/s from 0.5 to 1.0 as shown in Figure 5.7 (b, f). All Cr and V-containing samples show almost no heat release in the first 48 hours, except for an initial strong heat flow for the first twenty minutes that might be attributed to the dissolution of C_2S phases [156]. A similar pattern of early heat release was observed in all the samples with varying water-to-solid ratios (inset of Figure 5.7 (a, c, e). To exclude the possible baseline disturbances in the first 20-30 minutes due to the opening of the calorimeter ampoule, a weighed amount of water was measured alongside all samples and was labeled as H_2O. This way it can be ensured that the exothermic peaks during the first 20-30 minutes of hydration are indeed coming from the sample as shown in Figure 5.7 (a, b). The samples were hydrated for 20 minutes and were further investigated via thermal gravimetric analysis after stopping the hydration. It is concluded that the initial peak originated from the formation of portlandite due to free lime dissolution as shown in Figure 5.7 (g, h). That is why, the contribution of heat signal due to free lime reaction is removed from the cumulative heat release of all the samples. As a result, the Ref. (-O) sample exhibited the highest cumulative heat release (56 J/g), while a nominal 1-7 J/g cumulative heat of hydration was observed in all the Cr and V doped C_2S with varying water to solid ratio. It is known that the presence of lime decreases the dissolution of C_2S, and the Ref. (-O) (2.7 wt. %) contains the highest amount of free lime (Table 5.3 and Table 5.5) [155] but it is also the most reactive. The incorporation of minor ions such as potassium or boron into C_2S is reported to improve hydration activity due to the stabilization of high-temperature polymorphs (α' and β-C_2S) [43, 156, 157]. However, Cr and V-containing samples exhibited minimal reactivity. Even having α' (5-9 wt. %) and β-C_2S (71-88 wt. %) in the Cr5-O and V5-O sample as compared to Ref. (-O) β (75 wt. %) γ-C_2S (17 wt. %), the early stage (48-72 h) C_2S reactivity is not improved.

As the dissolution of solids is a surface phenomenon, the rate of dissolution is dependent on the total surface area of the dissolving solid as shown in the general rate law expression (Eq. 5.1).

$$Rate = k \cdot S_{react}(t) \cdot f(\Delta G) \tag{5.1}$$

k = rate constant (s^{-1})
S_{react} = reactive surface area (m^2/g)
f = unknow priori function for free enthalpy
ΔG = Gibbs free energy change (kJ/mol)

The specific surface area (SSA) of the sieved sample Ref. (-O) (3.8 m^2/g) contains the highest available surface for the reaction (Table 5.2). Therefore, the lower reactivity of Cr5-O and V5-O samples than the Ref. (-O) can also be attributed to the less available surface for the reaction with water [158]. Persuasively, the early age (48-72 h) of C_2S reactivity is more dependent on the available SSA than lime, w/s ratio, and the type of C_2S polymorph.

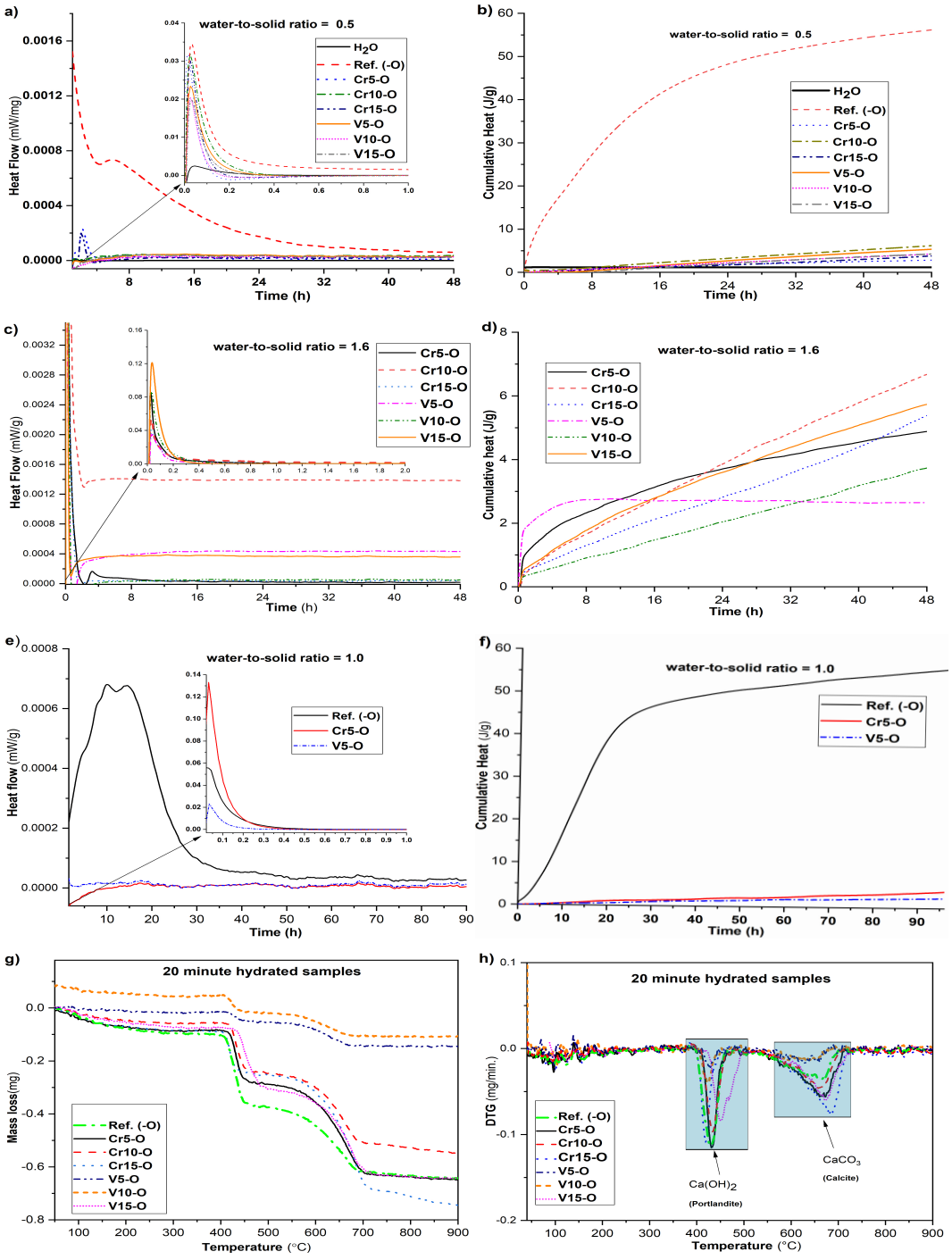

Figure 5.7: Heat release of the chromium and vanadium doped C_2S under oxidizing conditions sieved between 20 and 40 µm. with water to solid ratio (a) 0.5 (c) 1.0 (e) 1.6. Cumulative heat release in J/g of the (b) 0.5 (d) 1.0 (e) 1.6. TG curve of the synthesized C_2S samples showing the mass loss in function of temperature (e) mass loss of Cr and V doped C_2S samples under oxidizing conditions in first 20 minutes of hydration (f) DTG curve of the synthesized C_2S samples showing the mass loss per minute in function of temperature.

5.4.3 *Leaching behaviour*

The leaching of Cr and V doped C_2S under varying (oxidizing and reducing) calcination conditions depends on the oxidation state of Cr and V, its substitution amounts, pH, type of mineral phase as well as the kinetic equilibrium between varying oxides of chromate and vanadate. Calcium chromate is soluble at > 20 g/L in the water while calcium vanadate is insoluble at room temperature. The synthesized samples contain C_2S ($K_{sp} = 9.17 \times 10^{-6}$), and free lime (CaO) ($Ksp = 4.3 \times 10^{-6}$) that upon hydration can increase the pH of the leachate as shown in the following Eqs. 5.2 & 5.3 [158].

$$CaO + H_2O \longrightarrow Ca(OH)_{2(aq)} \rightleftharpoons Ca^{2+} + 2\,OH^{-} (pH = 12.46) \tag{5.2}$$

$$Ca_2SiO_4 + 2\,H_2O \rightleftharpoons 2\,Ca^{2+} + H_2SiO_4{}^{2-} + 2\,OH^{-} (pH = 10 - 12.5) \tag{5.3}$$

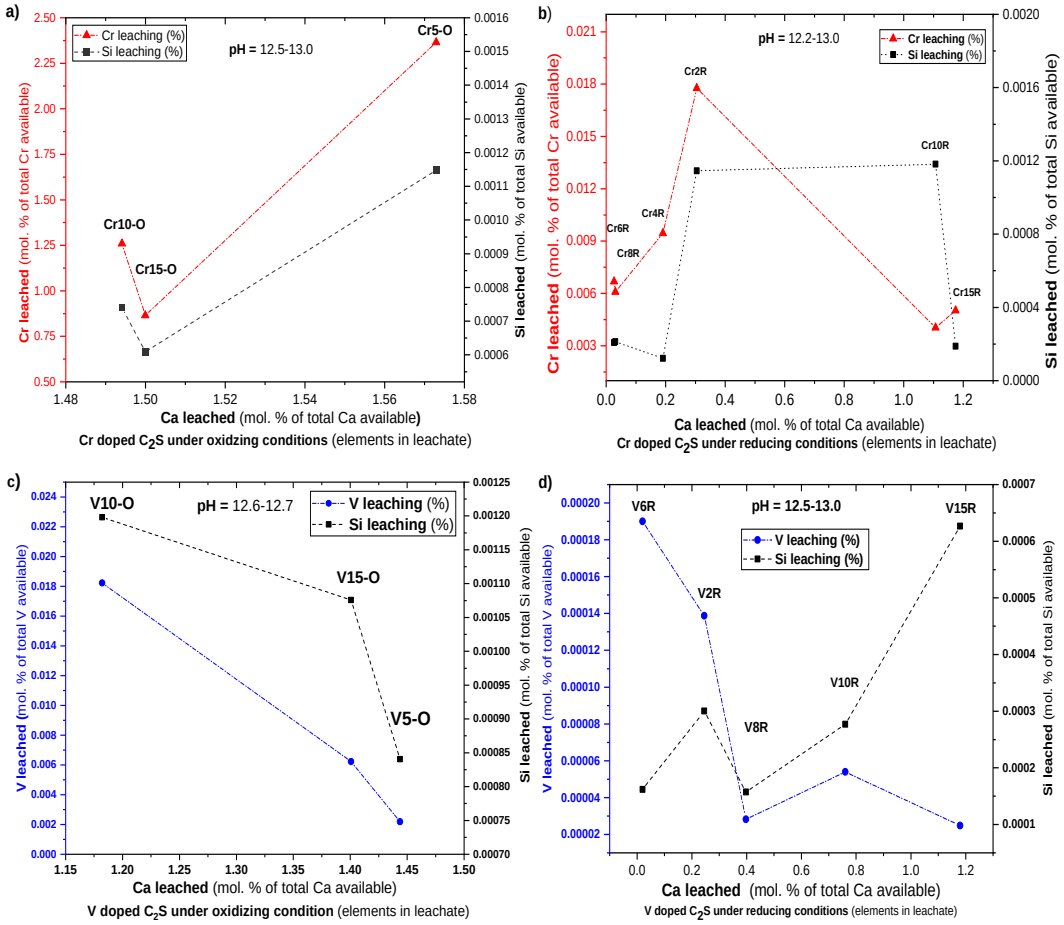

Figure 5.8: One batch leaching analysis (w/s = 10) of Cr and V doped C_2S, the amount Si, Cr and V has been plotted as a function of Ca (%) leaching and pH range mentioned on the graph (a) Cr doped C_2S under oxidizing conditions (b) Cr doped C_2S under reducing conditions (c) V doped under oxidizing conditions (d) V doped under reducing conditions.

The pH of the Cr5-O, Cr10-O, and Cr15-O samples after placement in water for 24 h at a liquid/solid ratio of 10 was found to be in the range of 12.5-13.0. The Cr5-O sample exhibited the highest percentage of Cr, Si, and Ca leaching as compared to Cr10-O and Cr15-O samples as shown in Figure 5.8 (a). The Cr leaching is directly proportional to Si leaching in all the samples synthesized under oxidizing conditions while the aqueous Ca^{2+} concentration varies slightly in Cr10-O and Cr15-O samples. At pH > 12.0, the dominant species of chromate ion is CrO_4^{2-}. The solubility product (K_{sp}) value of $CaCrO_4$ is 5.1×10^{-6}, and the chemical reaction between Ca^{2+} and CrO_4^{2-} has been shown in Eq. (5.4).

$$Ca^{2+} + CrO_4^{2-} \rightleftharpoons CaCrO_4 (pH => 12) \tag{5.4}$$

The part of Cr (VI) can be immobilized by the formation of the low solubility chromium complex. The behaviour can be understood with the help of the Cr distribution in mineral phases and amorphous content in Cr5-O, Cr10-O, and Cr15-O samples. In Cr5-O, the Cr (VI) can substitute on the Si-site in C_2S as shown in Section 5.4.1.1. The highest Cr leaching from the Cr5-O sample can be attributed to the high dissolution of C_2S phases as the associated Si leaching supports the idea. As the replacement of Cr increases in Cr10-O and Cr15-O, more individual grains are covered with a glass layer which restricts the dissolution of C_2S (Figure 5.5 (a, b, c) (see Table B.4 for QXRD of leachate residues and Table B.5 for IC/ICP data in appendix B).

The Ca and Cr leaching in the samples produced under reducing conditions decreased as compared to the values for samples calcined under oxidizing conditions as shown in Figure 5.8 (b). The Cr2R sample exhibited the highest Cr leaching value while other Cr (4-15) R samples showed a clear decrease. This can be attributed to the increasing stabilization of Cr (II and III) upon incremental addition of Cr to the samples (Table 5.3), which does not occupy the Si-site in C_2S, the Cr (VI) leaching is directly proportional to the degree of C_2S dissolution.

It is shown in Section 5.4.1.2 that the V(V) tends to substitute on the Si-site in C_2S under oxidizing conditions (V5-O, V10-O, V15-O). Upon dissolution, the type of calcium vanadate precipitates depends on the pH of the leachate. $Ca(VO_3)_2$ forms around pH 5-8 while Ca_2V2O_7, as well as $Ca_3(VO_4)_2$, are the dominant precipitates in the range of pH 9-10.6 and 10.6-13 respectively [159]. The pH of the V5-O, V10-O, and V15-O samples was found in the range of 12.6-12.7, the dominant calcium vanadate would be $Ca_3(VO_4)_2$ ($\log K_{sp}$ = -17.97) as shown in Eq. (5.5).

$$3\,Ca^{2+} + 2\,VO_4^{2-} \rightleftharpoons Ca_3(VO_2)_4 (pH => 12) \tag{5.5}$$

The percentage of Si and V leaching from V5-O, V10-O, and V15-O is shown in Figure 5.8 (c). It can be observed that the maximum V concentration in the leachate is inversely proportional to the aqueous Ca^{2+} concentration. It seems that the percentage of V leaching is controlled by the percentage of aqueous Ca^{2+} in the leachate. The sample V10-O exhibited the highest percentage of V (0.018%) leaching but the lowest percentage of Ca^{2+} (1.16%) leaching, while the V15-O contains the highest amount of V in the C_2S matrix phases. This can be understood by considering the source of Ca^{2+} in the leachate. The V10-O sample contains the lowest amount of free lime (0.1 wt. %) as one of the active sources of aqueous Ca^{2+}. While the V15-O sample exhibited high free lime (1.6 wt. %) and calcite (1.6 wt. %). The presence of dissolved CO_2 in the solution (leads to the formation of $CaCO_3$ ($K_{sp} = 3.36 \times 10^{-9}$)) provides a sink for calcium in the leachate due to

the lower solubility of calcium carbonate than calcium hydroxide. Moreover, the aqueous Ca^{2+} concentration develops from C_2S dissolution results in vanadate concentration either at or very close to the solubility limit of $Ca_3(VO_4)_2$ which limits the concentration of vanadate in solution. Conclusively, the amount of V leaching is independent of the starting amount of V in the C_2S matrix. It depends on the active aqueous Ca^{2+} source in the solution, the type of calcium vanadate complex, and pH. The amount of Si leaching is directly proportional to the V concentration in the leachate which is indicated by the degree of dissolution of C_2S phases and active occupation of V_2O_5 on the Si-site. The dissolution of C_2S leads to the formation of Ca-Si-H which can also actively uptake some parts of V_2O_5 on tetrahedral Si-sites [159].

In reducing conditions, overall calcium, silicon, and vanadium concentration decrease as compared to oxidizing condition samples as shown in Figure 5.8 (b). As we have seen above, the leaching of vanadium is controlled by the active calcium source in the leachate. The vanadium leaching is inversely proportional to calcium concentration in the leachate. The reduced sample contains a high amount of free lime (4.2-9.4 wt. %) that would limit the solubility of $Ca_3(VO_4)_2$ like the sample under oxidizing conditions.

5.5 CONCLUSIONS AND OUTLOOK

The Cr (0-15 mol. %) and V (0-15 mol. %) incorporation on the Si-site in C_2S was investigated using sol-gel synthesis under oxidizing and reducing (20% CO/80% CO_2) conditions. The C_2S polymorphs stability, the effect of varying calcination conditions on heavy metals (Cr, V) incorporation as well as the oxidation state, and microstructure were studied along with early age (48-72 h) hydration at different water-to-solid ratios and the leaching behaviour. The important findings are as follows:

C_2S can incorporate Cr (VI) and V(V) on the Si-site in C_2S under air-oxidizing conditions. This led to the stabilization of the high-temperature polymorphs α' and β-C_2S as shown in the Cr5-O and V5-O samples. A Cr and V content higher than 5 mol. % started to stabilize in heavy metal (Cr and V) bearing amorphous phases due to the substitution limit. The stabilization of α'-C_2S in Cr-containing samples can be attributed to matrix constraint induced by the formation of a glassy layer covering individual C_2S particles. In addition to that, the twin domains were observed in the V5-O sample which is the characteristic deformation that evolves during the $\alpha' \rightarrow \beta$ transition due to doping of foreign ions in C_2S. A constant amount of Cr (VI) can be substituted on the Si-site in C_2S which is independent of the starting amount of Cr in the sample. A maximum of 4.1 mol. % Cr can be substituted on the Si-site in C_2S theoretically while it was difficult to predict the maximum substitution of V due to high amorphous content in the sample. The remaining chromium oxide forms separate Cr (III) phases in the most stable oxidation state.

Cr and V oxide tend not to incorporate on the Si-site in C_2S under reducing conditions (20% CO/80% CO_2) due to oxidation state mismatch. The Cr was present as (II) and (III) oxidation states in samples Cr2R-Cr15R samples which led to the formation of high amounts of CaO and (Para)wollastonite due to a calcium to silica ratio of less than 2. The V2R-V15R samples also contained calcium vanadate phases with high amorphous content (2.9-24.5 wt. %), (Para)wollastonite (6.4-12.4 wt. %), and lime (4.2-9.4 wt. %) indicating a similar Si deficit. The incorrect stoichiometry shows that V and Cr were not available in a favourable oxidation state to be incorporated in C_2S at high temperatures.

The incorporation of V and Cr into C_2S stabilizes the reactive α', β-C_2S but drastically reduces the early-stage hydration activity of C_2S compared to the Ref. (-O) sample. Even though the reference sample contains a significant amount of γ which is non-reactive as well as free lime it also reduces the solubility of C_2S. The specific surface area for the reference is higher than for the doped samples making it reactive at early age hydration. The V (V) and Cr (VI) substituted on the Si-site in C_2S exhibited higher mobility than the Cr (II)(III) containing C_2S samples. The Cr leaching is sensitive to the oxidation state as well as the Cr-bearing amorphous phases in the sample. Despite being present in the mobile Cr (VI) oxidation state, the coverage of Cr grains with a glass layer decreases the dissolution degree of the solid and the leaching of Cr. Conclusively, once Cr (VI) is substituted on the Si-site in C_2S, the Cr leaching is directly proportional to the degree of C_2S phase dissolution. The vanadium leaching is controlled by the active source of aqueous Ca^{2+} which is independent of the starting amount of V in the sample. The V leaching is inversely proportional to the aqueous Ca^{2+} in the leachate due to the formation of $Ca_3(VO_4)_2$ at pH > 12. The directly proportional relationship between V and Si leaching in the V5O, V10O, and V15O samples shows that the V_2O_5 was released from the Si site of C_2S. The Si leaching from V2R, V4R, V6R, V8R, V10R, and V15R samples was independent of V leaching indicating the source of V_2O_5 is not the Si-site of C_2S.

This information provides an insight into the oxidation state, speciation, and leaching mechanism of Cr as well as V from C_2S. it has been explained in Chapter 3 that the air granulated BOF slag leaches a significant amount of Cr and V which requires an understanding of the speciation and leachability of heavy metals (especially Cr and V) in a C_2S environment. So, this knowledge can assist in controlling the leaching of Cr and V from the slag.

6

EFFECT OF HYDROXIDE, CARBONATE, AND SULPHATE ANIONS ON THE β-DICALCIUM SILICATE HYDRATION RATE

ABSTRACT

The effect of fixed (0.8M) Na^+ balanced by either OH^-, SO_4^{2-}, and CO_3^{2-} anions on β-dicalcium silicate (C_2S) reactivity is investigated. The exothermic reaction of varying water-to-solid ratios and chemical activation is monitored. Subsequently, the hydration products are characterized via FTIR, TG/DTG, QXRD, and SEM analysis. The findings showed that the carbonate ions expedited the reactivity up to 55% at 1-7 days due to the simultaneous precipitation of calcium silicate hydrate (C-S-H) and calcite. At 7-28 days, the lack of transportable cations between the solid surface and solution impeded further hydration, as confirmed by in-situ pH and conductivity measurements. The sulphate ions accelerated the reactivity only upon calcium sulphate dissolution at high pH. The hydroxide ions decelerated the hydration due to the earlier precipitation of portlandite than C-S-H. Overall, the β-C_2S reaction with water exhibited the highest hydration degree (67%) after 28 days of hydration. It is envisioned that the chemically activated β-C_2S reaction's product which tends to precipitate earlier than the C-S-H would limit the C_2S hydration activity. Overall, the β-C_2S reaction with water exhibited the highest hydration degree (67%) after 28 days of hydration.

Major part of this chapter is published elsewhere: M.J. Ahmed, K. Lambrechts, X. Ling, K. Schollbach, H.J.H. Brouwers, Effect of hydroxide, carbonate, and sulphate anions on the β-dicalcium silicate hydration rate, Cem. Concr. Res. 173 (2023) 107302.

6.1 INTRODUCTION

Dicalcium silicate (C_2S) is an important constituent of belite clinker (40-60 wt. %), belite calcium sulfoaluminate cement (25-50 wt. %), basic Oxygen furnace steel slag (30-50 wt. %), and ordinary Portland cement (OPC, 10-15 wt. %), where it exists in the form of β-C_2S polymorph, stabilized at room temperature due to presence of impurities [43, 80, 160–162]. Belite-rich binders offer sustainable growth by lowering the enthalpy of formation (for alite and belite are 1810 kJ/kg, 1350 kJ/kg, respectively), the kiln operating temperature (1200-1350 °C) and the associated CO_2 emissions [163]. However, the main drawback that restricts the application of belite cement is the low reactivity of β-C_2S leading to slow strength development owing to not fulfilling the current standards [52]. The material admixture especially NaOH, KOH, C-S-H seeds, and commercial oxide nanoparticles, etc. is reported to accelerate the hydration of belite cement where the excess cumulative heat release is attributed to the β-C_2S reactivity [43, 53, 163]. Thus, a systematic understanding of the β-C_2S hydration via chemical activation is a prerequisite for its technical application.

Several strategies have been reported to improve the C_2S hydration by mechanical grinding, mineralizers, or dopants (NaF, SO_3, B_2O_3, etc.) and chemical activators such as alkali oxides, salts as well as calcium silicate hydrate (C-S-H) seeds [164–167]. Chemical activation particularly NaOH, KOH, Na_2CO_3, and K_2CO_3, etc. is acknowledged to accelerate the C_2S hydration due to the interaction of calcium silicate hydrate (C-S-H) with soluble alkali oxides [52, 168–171]. β-C_2S reactivity in NaOH and KOH hydration mediums is reported to increase both the hydration degree alongside associated early strength development [52, 168, 172][13,17,18]. Especially, a high concentration of 5 M KOH could significantly accelerate the β-C_2S reactivity, while it was demonstrated that low concentrations of NaOH slow down the dissolution of β-C_2S [52, 173]. The improved hydraulic properties of β-C_2S in the KOH environment are attributed to the larger ionic radius and electronegativity of potassium cation compared to sodium ion [172, 174]. These differences in ionic properties would give different interactions with the C-S-H formation and associated mechanical properties. Moreover, the addition of carbonate solutions was reported to shorten the induction period alongside improved hydraulic activity of C_2S, especially at low $NaHCO_3$ concentrations which were more effective than KOH [172]. Subsequently, a 0.28M Na_2SO_4-activated C_2S exhibited a better 28-day mechanical strength than Na_2CO_3 without significant change in hydraulic activity [175, 176]. The emphasis of these studies lies more on the role of cation interaction (Na^+, K^+) with C-S-H, especially the Ca/Si ratio, C-(Na/K)-S-H, and the degree of silicate chain polymerization. But the presence of anions equally impacts the reaction kinetics, particularly the C-S-H dissolution-precipitation reaction.

Very few studies have investigated the effect of the anions on tuning the β-C_2S reactivity. Especially information about the β-C_2S dissolution-precipitation as well as its correlation with solution ionic strength and hydration degree over time is missing. In addition to that, the non-systematic concentrations of the activators reported in the literature make it difficult to compare the effect of cations and anions in the hydration process [167, 172, 177, 178]. If undersaturation is the leading cause of the C_2S dissolution, then the anions also play a vital role in dictating the C-S-H precipitation alongside cations [179] as it has been ignored often. Therefore, a systematic approach is desired to

understand the contribution of anions, pH, and ionic strength to comprehend the hydration rate at ambient conditions. To the author´s best knowledge, there is no systematic study reported where the amount of activator is adjusted to have fixed moles of sodium cations containing hydroxide, carbonate, and sulphate anions for β-C_2S chemical activation.

For this purpose, pure β-C_2S was synthesized at 1200 °C via the Pechini method. The synthesis method and calcination condition are chosen to attain lime-free C_2S. To study the effect of anions on β-C_2S activation, the molarity of sodium ion is fixed to 0.8 M to have comparable Na^+ concentration in all samples. The effect of dissolution degree on the β-C_2S reactivity is investigated to promote the forward direction dissolution reaction at ambient conditions by using the water to the solid (w/s) ratios between 0.5 and 1.6. Moreover, the order of hydration product formation and degree of hydration (DOH) is correlated with the anionic effect via the bonding system, and thermal, mineralogical, and microstructural analysis over 28 days of hydration. Finally, the heat release is correlated with the concentration of hydroxyl ions alongside the ionic strength of the hydrating media at an early stage (1-5 days) via in-situ pH and conductivity measurements to understand the β-C_2S dissolution-precipitation reaction events.

6.2 MATERIALS

$Ca(NO_3)_2{\cdot}4H_2O$ (Sigma-Aldrich, CAS: 13477-34-4), colloidal SiO_2 (40 wt.%, LUDOX® AS-40, Sigma-Aldrich, CAS: 7631-86-9), TEOS/$Si(OC_2H_5)_4$ (Sigma-Aldrich, CAS: 78-10-4), Citric acid monohydrate (VWR, CAS: 5949-29-1), ethylene glycol (VWR, CAS: 107-21-1), 65% HNO_3 (Sigma-Aldrich, CAS: 7697-37-2), ethanol (Sigma-Aldrich, CAS: 64-17-5) were used as received. The reagents were added in the stoichiometric ratios 2:1 Ca/Si corresponding to the synthesis of C_2S. Dicalcium silicate has been synthesized via the Pechini method by calcining intermediate charred gel at 1200 °C (Table 6.1). A detailed synthesis method can be studied in Chapter 4 [138]. Alkali salts NaOH (Merck, CAS: 1310-73-2), Na_2CO_3 (Sigma-Aldrich CAS: 497-19-8), and Na_2SO_4 (Merck, CAS: 7757-82-6) were dissolved in deionized water (DI). The resulting solutions are directly used as hydration media in this study. Moreover, the $CaCO_3$ from Sigma-Aldrich (CAS: 471-43-1, $\geqslant$ 99.0%) is used to study the filler effect.

6.2.1 *Methods*

6.2.1.1 *Hydration studies*

A fixed molar concentration of sodium cations such as 0.8M NaOH, 0.4M Na_2CO_3, and 0.4M Na_2SO_4 is used as alkali activators for β-C_2S. Isothermal heat conduction calorimetric measurements were conducted in TAM AIR isothermal calorimetric device at 20 ± 0.5 °C for 14 days. Pre-determined amounts of the C_2S were added to the vials. After acclimatization of the materials and hydration media to room temperature, the sample was mixed ex- situ. After the designated time, the hydration was stopped by solvent exchange method (immersing in isopropanol followed by diethyl ether washing) and samples are labelled as shown in Table 6.1

Table 6.1: Sample labelling of the hydration mediums at 20 ± 0.5 °C and 60% relative humidity.

Hydration mediums	**C_2S + water**	**C_2S + 0.8 M NaOH solution**	**C_2S + 0.4M Na_2CO_3 solution**	**C_2S + 0.4M Na_2SO_4 solution**
Sample label	Reference	0.8M NaOH	0.4M Na_2CO_3	0.4M Na_2SO_4
pH	7.2	13.2	11.3	6.9

In-situ pH and conductivity measurements of the hydrating samples were executed in a climate-controlled room, which is kept at 20 ± 0.5 °C with 60% humidity. After acclimatization of the solutions the conductivity probe, the Greisinger GMH 3431, and the Voltcraft PE-03 pH probe were calibrated. The hydration media was stirred by hand upon insertion of probes and data logging with a 7.5-minute interval was started. To prevent water evaporation the beaker was sealed with parafilm and tape. The pH and conductivity measurements were performed with a 1.6 w/s ratio. As the excess water increased the volume, ensured the probes were in full contact with the system. The starting pH values of the alkali activators are presented in Table 6.1.

6.3 RESULTS AND DISCUSSION

6.3.1 *Hydration behaviour in varying water-to-solid (w/s) ratio*

The QXRD analysis of synthesized sample exhibited high crystallinity (91 wt. %) with low amount of XRD-amorphous (9 wt. %). C_2S synthesized by Pechini method contains a high amount of beta polymorph 83 wt. % with no free lime alongside 8 wt. % γ-C_2S (Table 6.2, see Figure B.4 for Rietveld refinement fit).

Table 6.2: QXRD of the C_2S synthesized at 1200 °C via the Pechini method with error values and specific surface area (SSA).

Mineral Phases	**β-C_2S**	**γ-C_2S**	**Quartz**	**Wollastonite 2-M**	**XRD-amorphous**
Amount (wt. %)	82.7 ± 0.2	8.0 ± 0.1	0.9 ± 0.1	0.1 ± 0.07	8.4 ± 1.2
BET-SSA (m^2/g)			0.85		

The 14 days hydration behaviour of β-C_2S with water and 0.8 moles of Na^+ activators was monitored via isothermal calorimetry as shown in Figure 6.1. The heat flow is normalized by the mass of the sample. Two different w/s ratios (1.6 and 0.5) were investigated to understand the effect of dissolution degree on β-C_2S reactivity. The results for a w/s ratio of 1.6 indicated that the reference sample exhibited no significant exothermic heat of hydration. However, around 96 h, a clear increase in the heat flow indicated C-S-H precipitation [180]. A heat flow pattern just like the reference was observed for 0.8M NaOH as well as 0.4M Na_2SO_4 samples. The addition of the same moles of sodium activator did not alter the exothermic heat of C_2S hydration till 96 h except for the 0.4M Na_2CO_3 sample. The exothermic heat pattern has conspicuous features of dissolution as well as an induction period followed by an acceleration and deceleration period featured in the 0.4M Na_2CO_3 sample. After 48 h, no further

exothermic heat of hydration was observed in the sodium carbonate sample till 14 days. Decreasing the w/s ratio from 1.6 to 0.5 resulted in shortening the induction period from 22 to 10 h in the 0.4M Na_2CO_3 samples indicating that a low dissolution degree is observed to reach equilibrium till 14 days. Moreover, the 0.5 w/s ratio decreases the overall C_2S exothermic heat flow in the reference sample without significant a change in the 0.8M NaOH sample (Figure 6.1 (a)).

The 14 days cumulative heat flow exhibited an increase of 45 and 78%, respectively, upon increasing the 0.5 to 1.6 w/s ratio in the reference as well as the 0.4M Na_2CO_3 sample. But the overall cumulative heat of hydration is practically the same for sodium hydroxide activator in all w/s ratios (Figure 6.1(b)). These observations indicated that the C_2S dissolution is dependent on the w/s ratio to achieve the solubility equilibrium. The increase in cumulative heat of hydration (42-62 J/g, 18-36 J/g) and induction period (10-22 h) upon increasing the w/s (from 0.5 to 1.6) ratio in reference and 0.4M Na_2CO_3 sample, respectively, emphasizes the strong dependence of the C_2S dissolution rate on the local ion concentration of OH^- and CO_3^{2-} at the C_2S-grain surface interface [158, 181]. Contrary to the previous study [178, 182], the 0.4M Na_2CO_3 sample does not exhibit a higher exothermic heat of hydration than the reference sample. The variations in the results can be attributed to the significant difference ($\Delta E_{activation}$ = 20-22 kJ/mol) in activation energy with varying β-C_2S surface area [95]. Consequently, the activation energy impacts the hydration process in the rate-controlling step.

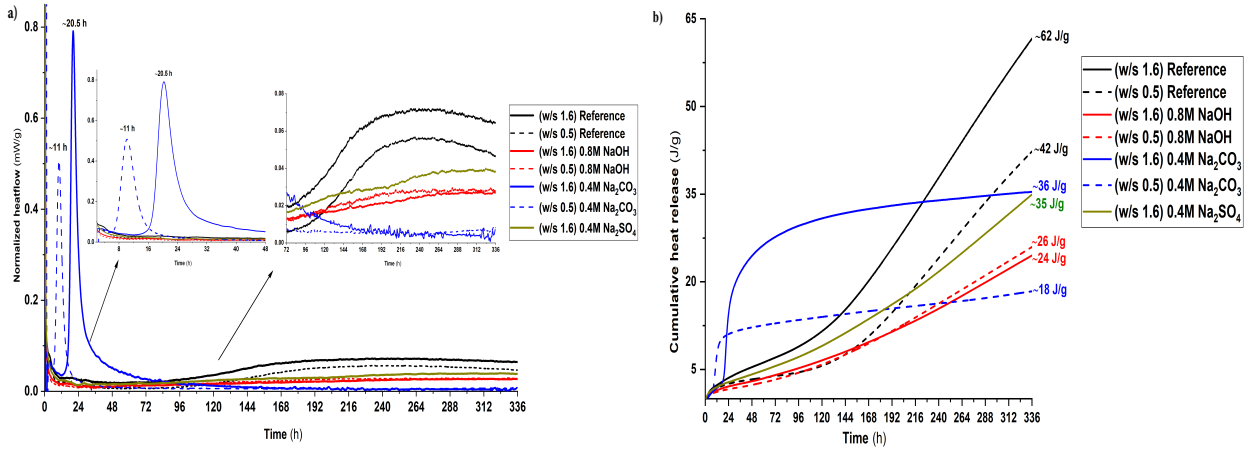

Figure 6.1: Exothermic heat curve of C_2S, hydrated in water-to-solid (w/s) ratio of 1.6 and 0.5 a) normalized heat flow b) cumulative heat of hydration.

At low w/s ratio, the distance from the equilibrium is not high enough and the solution reaches the solubility equilibrium during dissolution [180]. But in the presence of a hydroxide-rich medium such as the 0.8M NaOH sample, the change in w/s ratio does not impact the cumulative hydration heat (26 J/g) indicating a very slow dissolution of C_2S. The relatively higher hydroxide concentration close to the surface restricts further silicate dissolution due to strong deprotonation at high pH [183]. The dissolution of C_2S will move in the forward direction only upon precipitation of calcium hydroxide such as:

$$Ca_2SiO_{4\,hydroxylated-surface} \rightleftharpoons 2\,Ca^{2+} + H_4SiO_4 + 4\,OH^- \tag{6.1}$$

$$H_4SiO_4 + OH^- \rightleftharpoons H_3SiO_4^- + H_2O \tag{6.2}$$

$$H_3SiO_4^- + H_2O \rightleftharpoons H_2SiO_4^{2-} + H_2O \tag{6.3}$$

The calorimetric studies indicated that the 1.6 w/s enhances the dissolution degree of C_2S. For this reason, it was adopted for the remaining experiments. Among 0.8M Na^+ activators in a 1.6 w/s ratio, 0.4M Na_2CO_3 exhibited higher reactivity within 24 h while showing 41% lower cumulative hydration heat than reference after 14 days of hydration. Moreover, the 0.4M Na_2SO_4 sample exhibited the same overall cumulative hydration heat (36 J/g) as the 0.4M Na_2CO_3 sample at a w/s ratio of 1.6 but showed a steady increase in the heat of hydration after the first 24h which was not the case for the carbonate sample. As the standard enthalpy of formation (Δ_fH^θ) suggests a more favorable reaction for calcium sulphate ($CaSO_4$, Δ_fH^θ = -1434 kJ/mol) precipitation than calcium carbonate ($CaCO_3$, Δ_fH^θ = -1208 kJ/mol) formation [184]. However, the precipitation of the hydration products seems to be controlled by some other factors such as C_2S dissolution-precipitation equilibrium, ionic strength, and pH of the hydration medium [185]. These observations require further insights as provided in the next sections.

6.3.2 *Characterization and order of hydration product formation*

As mentioned above, the exothermic heat signals are very low in intensity and different anions particularly SO_4^{2-}, CO_3^{2-}, OH^- etc. can precipitate as calcium sulphate, calcium carbonate, and calcium hydroxide respectively. To understand the events of exothermic hydration reactions, FTIR analysis has been performed on the hydrated sample after 7, 14, and 28 days (see peak assignment Figure B.5 (a, b, c) in appendix B) as shown in Table 6.3

All samples exhibited similar band positions mostly originating from the β-C_2S vibrations. They have narrow band splitting in the range of 800-1200 cm^{-1} corresponding to the Si-O bonds asymmetric and symmetric stretching vibrations of Si-O bands, a band around 496, 535 cm^{-1} associated to Si-O-Si bending vibrations, and 450-455 cm^{-1} vibration pointing deformation of SiO_4 tetrahedra. The interaction with air cannot be avoided in the sample, thereby, the bands around 1400-1500 cm^{-1}, and 1640-1650 cm^{-1} are assigned to an asymmetric stretch of CO_3^{2-} and H-O-H bending vibrations of molecular H_2O respectively. The broad band centered around 3300 cm^{-1} is due to stretching vibrations of hydroxyl groups in H_2O with varying degrees of hydrogen bond strengths [186–188].

After 7 days of curing, the distinct band of C-S-H Q^1 (815 cm^{-1}) is only observed in the 0.4M Na_2CO_3 with a distinct carbonate band (713 cm^{-1}) indicating the precipitation of calcium carbonate as a by-product. But mid-IR bands centred 3300 cm^{-1} exhibited the strongly ordered hydrogen-bonded samples observed in all the hydrated samples [189]. These bands suggest the presence of C-S-H in all samples, but the not distinct band for C-S-H can be assigned. After 14 days of curing, the distinct C-S-H Q^2 (940-950 cm^{-1}) bands alongside Q^1-type hydration products appear in all the hydrated samples. The relative intensity of the Q^2 (940-950 cm^{-1}) type bands increased in all the hydrated samples upon 28 days of curing which confirms the polymerization of the silicate chain [171]. Furthermore, the distinct bands 636, 616 cm^{-1} and centred around 1100 cm^{-1} indicate the precipitation of gypsum in the 0.4M Na_2SO_4 sample [190].

Table 6.3: General assignments of bands in FTIR fingerprint region.

Band Position (cm^{-1})	Assigned to	Signal evolution concerning sample curing age (days)			
		Reference	0.8M NaOH	0.4M Na_2CO_3	0.4M Na_2SO_4
~3643	ν OH [$Ca(OH)_2$]	14, 28	14, 28	14, 28	14, 28
~3360-3315, 2970	ν OH (H_2O)	7, 14, 28	7, 14, 28	7, 14, 28	7, 14, 28
~1640-1650	δ OH (H_2O)	7, 14, 28	7, 14, 28	7, 14, 28	7, 14, 28
~1415-1490	ν_3 CO (CO_3^{2-})	7, 14, 28	7, 14, 28	7, 14, 28	7, 14, 28
~1380-1390, ~1305-1340	δ C-H (aliphatic structure)	14, 28	14, 28	14, 28	14, 28
~1125-1165	ν Si-O	14, 28	14, 28	14, 28	14, 28
~1100-1110	ν_3 SO (SO_4^{2-})	-	-	-	7, 14, 28
~992	ν_3 Si-O-Si (β-C_2S)	7, 14, 28	7, 14, 28	7, 14, 28	7, 14, 28
~940-950	ν Si-O (C-S-H) Q^2	14, 28	14, 28	14, 28	14, 28
~897, 885, 863, 844	ν_3 Si-O-Si ((γ/β-C_2S)	7, 14, 28	7, 14, 28	7, 14, 28	7, 14, 28
~815	ν Si-O (C-S-H) Q^1	14, 28	14, 28	7, 14, 28	14, 28
~713	ν_4 CO (CO_3^{2-})	-	-	7, 14, 28	-
~636, 616	ν_4 SO (SO_4^{2-})	-	-	-	7, 14, 28
~537, 495, 436	ν_4 Si-O-Si (γ/β-C_2S)	7, 14, 28	7, 14, 28	7, 14, 28	7, 14, 28
~450-455	δ Si-O (SiO_4 Td)	14, 28	14, 28	7, 14, 28	14, 28

Through FTIR analysis, the exothermic reaction observed via calorimetry can be interpreted. At the early stage (0-72 h), the 0.4M Na_2CO_3 sample exhibited Q^1-type hydration products alongside calcium carbonate. After 3 to 14 days, no exothermic heat event is observed but the silicate polymerization happens, and the Q^2-type hydration product is confirmed. In reference, to 0.8M NaOH and 0.4M Na_2SO_4 samples, the hydration reaction proceeds over time by C-S-H precipitation as well as polymerization as a slow and continuous process. The type of hydration products is further confirmed by the DTG (see Figure B.6 in appendix B for percentage mass loss events). The mass loss events 50-220 °C is attributed to dehydration of C-S-H (also gypsum in case of 0.4M Na_2SO4 (Table 6.3)), 430-510 °C corresponds to dehydration of calcium hydroxide alongside 550-800 °C decarbonation of calcium carbonate (Figure 6.2 (a, b, c)) [191][42]. All samples hydrated at 7 days exhibited the formation of C-S-H with the highest amount of bound water in 0.4 M Na_2CO_3 sample which confirms the calorimetric results. Upon

curing for 14 and 28 days, the C-S-H content was increasing, showing the samples were continuously hydrating except for 0.4 M Na_2CO_3. The reference sample exhibited the highest mass loss associated with C-S-H after 28 days of cured sample (Figure 6.2 (c)).

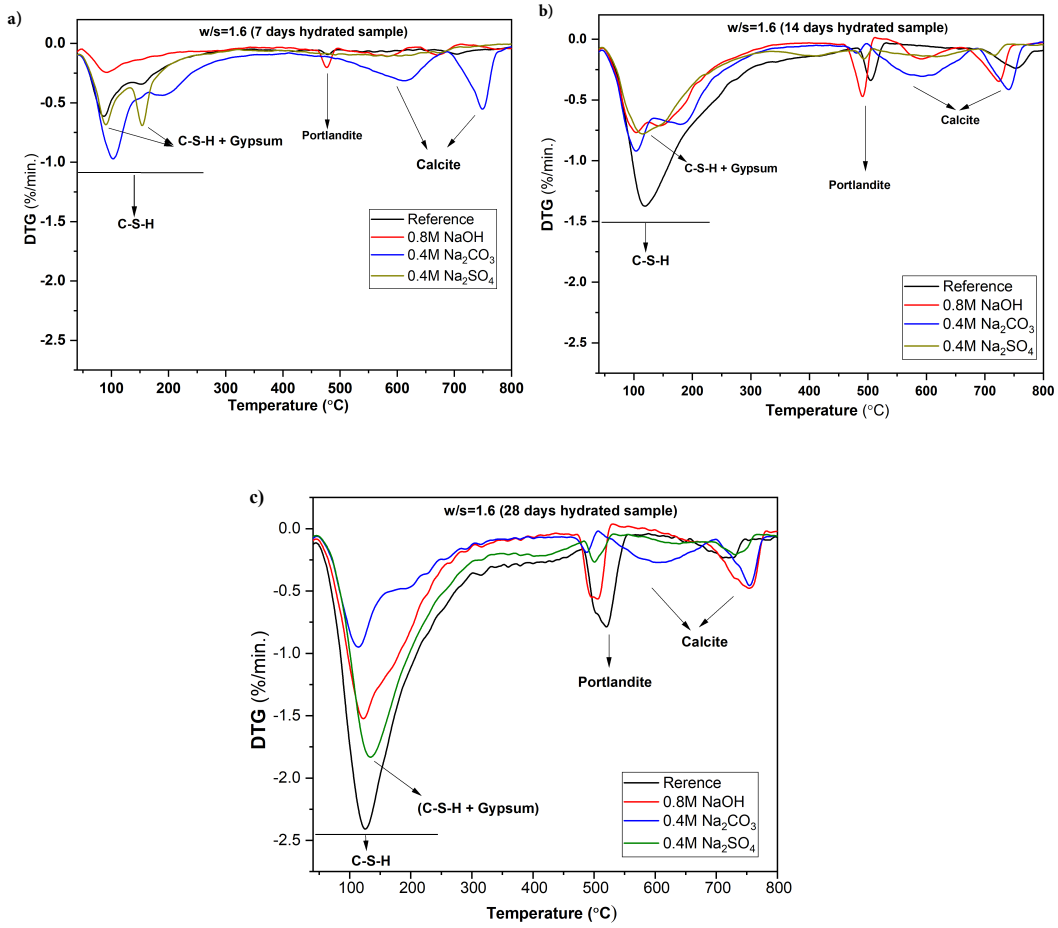

Figure 6.2: Differential thermal gravimetric (DTG) analysis of chemically activated C_2S at curing age of a) 7 b) 14 and c) 28 days with 1.6 w/s ratio.

To understand a correlation between portlandite formation and C-S-H gel-bound water, the $Ca(OH)_2$ as well as $CaCO_3$ wt.% amount in the hydrated sample is calculated using the tangential method as expressed by [60, 192]:

$$m_{measured} = weightloss(TGA) \cdot \frac{m_{mineral}}{m_{volatile}} \tag{6.4}$$

Moreover, the differences in total bound water were calculated by converting the sample wt. % into portlandite and calcite anhydrous mass by Eq. 6.5.

$$m_{anhydrous} = \frac{m_{measured}}{1 - evaporable\,water} \tag{6.5}$$

As the sample has undergone carbonation, the carbonate is recalculated to the equivalent amount of anhydrous portlandite using Eq. 6.6 under the assumption that the

calcite in all samples originates from the carbonation of portlandite. Factor 1.35 refers to the molar mass ratio of $CaCO_3$ (100.09 g/mol) and $Ca(OH)_2$ (74.09 g/mol) [193].

$$m_{\text{anhydrous Portlandite equiv.}} = \frac{1.35 \cdot m_{\text{measured calcite}} + m_{\text{measured portlandite}}}{1 - m_{\text{measured calcite}} + 1.35 \cdot m_{\text{measured calcite}}} \tag{6.6}$$

Weight loss (TGA) = Portlandite (T = 450-540 °C), Calcite (T = 550-800 °C)
$M_{mineral}$ = (Portlandite = 74 g/mol), (Calcite = 100 g/mol)
$M_{volatile}$ = (Water = 18 g/mol), (Calcite = 44 g/mol)
Evaporable water (wt. %) = TGA weight loss (100- (residual mass + portlandite + calcite)

The comparison between C-S-H gel water and the formation of equivalent dry portlandite amount helped to understand the formation of hydration products as shown in Figure 6.3 (a, b). In the reference sample, a clear increase in the C-S-H bound water and portlandite is observed over time. In the 0.8M NaOH sample, a higher amount of calcium hydroxide (1.1-4.0 wt. %, 7-14 days hydrated sample) was observed as compared to the reference (0.3-2.1 wt. %, 7-14 days hydrated sample) sample while significantly lower (61%) C-S-H bound water indicates the lower reactivity of C_2S contrary to previous study [168]. These results indicate the earlier precipitation of portlandite in 0.8M NaOH sample compared to the reference would lead to the slow dissolution of C_2S. A serious decrease in the dissolution of C_2S is reported in the presence of a high initial concentration of portlandite [155]. However, if a very high supersaturation with respect to portlandite could be maintained, the portlandite and C-S-H nucleation can happen without the need for high dissolution [194]. That is usually observed at high concentrations of NaOH/KOH activated C_2S reaction [168] but low concentration delays the hydration as observed in 0.8M NaOH sample. Furthermore, the hydroxyl ions-rich solution promotes the precipitation of calcium hydroxide leading to a possible decrease in the Ca/Si ratio due to less calcium available for incorporation in C-S-H as the solubility of calcium hydroxide decreases at high pH.

In the 0.4M Na_2CO_3 sample, the amount of equiv. calcium hydroxide and C-S-H bound water remain constant once it is precipitated. After 14 days, a slightly lower mass loss for the gel water can be attributed to the enriching of C-S-H with Q^2-type silicate chains (Table 6.3). In the 0.4M Na_2SO_4 sample, the calculation of C-S-H volatiles was difficult because the gel water weight loss overlaps with the bound water of gypsum (100-200 °C). So, the C-S-H gel amount is high because it also contains gypsum water for crystallization.

C_2S hydration reaction products are confirmed via QXRD as shown in Figure 6.4 (see Figure B.4 (b, c, d) in appendix Bfor new hydration product peak assignment of the hydrated sample) and normalize to the portlandite ($m_{measured}$) mass from TG analysis. The presence of β-C_2S hydration by-products such as portlandite, calcite, and gypsum are observed for 28 days. In the 0.4M Na_2SO_4 sample, gypsum is observed only in 7 days hydrated sample while at a later stage (14 and 28 days), only portlandite is visible. The pH of the 0.4M Na_2SO_4 sample was found to be in the range of 12.5-13.0 measured at random moments between 5 and 12 days. The dissolution of gypsum increases at pH 12-13 [195] explaining why, no gypsum crystal is observed at later stages (14 and 28 days cured samples). The degree of hydration (DOH) is calculated by using:

$$\text{DOH}(\%)t_x = \frac{mXRD_{\beta C_2S}t_0 - mXRD_{\beta C_2S}t_x(1 - evaporable\,water)}{mXRD_{\beta C_2S}t_0} \tag{6.7}$$

As the mass increases β-C_2S partially consists of evaporable water and is also corrected from the TGA mass loss.

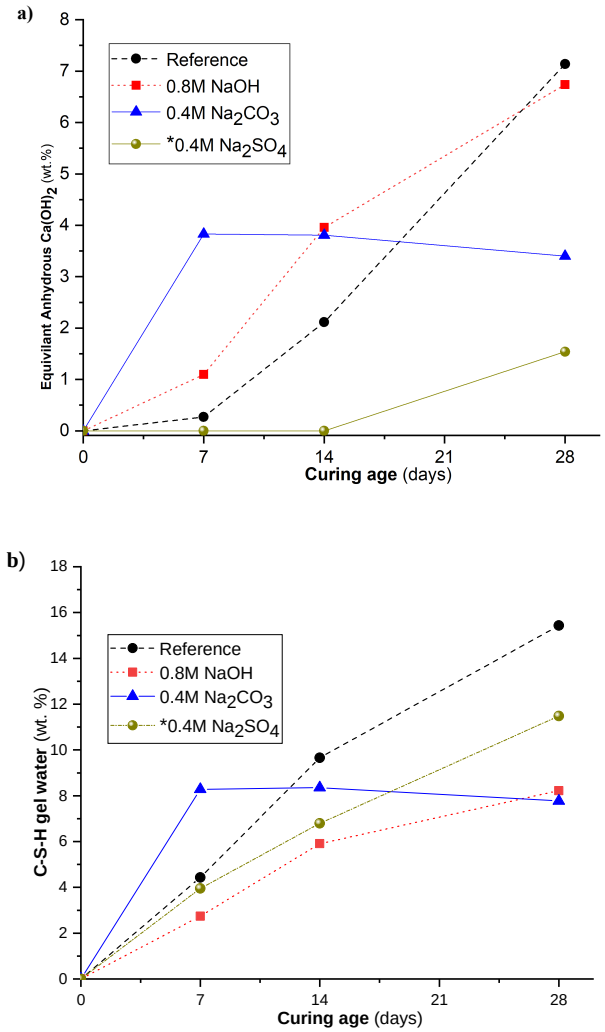

Figure 6.3: Calculation of chemically bound water over time of chemically activated C_2S a) equivalent anhydrous portlandite (wt. %) via Eq. 6.6. b) calcium silicate hydrate (C-S-H) gel water (wt. %) or evaporable water (Eq. 6.5). *It is not possible to differentiate between weight loss event of gypsum and C-S-H in 0.4M Na_2SO_4 sample (Fig. 6.2). Because the C-S-H volatiles coincides with the gypsum water of crystallization.).

At 7 days of hydration, the DOH increased by 60% for 0.4M Na_2CO_3 compared reference sample. So, the carbonate is the only suitable hydration medium to accelerate the early stage β-C_2S. In the 0.4M Na_2SO_4 sample, the highest DOH (223%) increase was observed at curing age between 14 and 28 days. The increase in hydration can be attributed to the dissolution of calcium sulphate at high pH (12-13) and promotes C-S-H precipitation leading to an increase in C_2S dissolution. As NaOH is described as an alkali activator but the present result argues that hydration in 0.8M NaOH lowers the β-C_2S reactivity at every age [167]. Overall, the reference sample exhibited a continuous increase and reaches 67% until 28 days as shown in Figure 6.5. At 28 days of hydration,

the addition of various anions lowered the degree of hydration. For 0.8M NaOH, 0.4M Na_2CO_3, and 0.4M Na_2SO_4 samples, a decrease of 54%, 54%, and 30%, respectively, in hydration degree was measured.

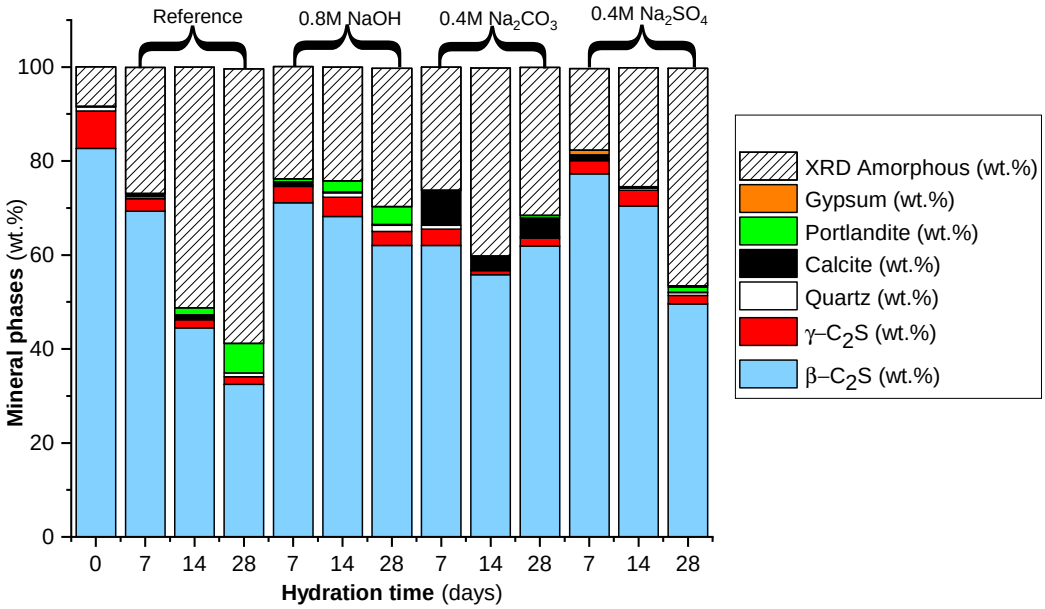

Figure 6.4: Quantitative X-ray diffraction (QXRD) of chemically activated β-C_2S at curing ages of 7, 14, and 28 days.

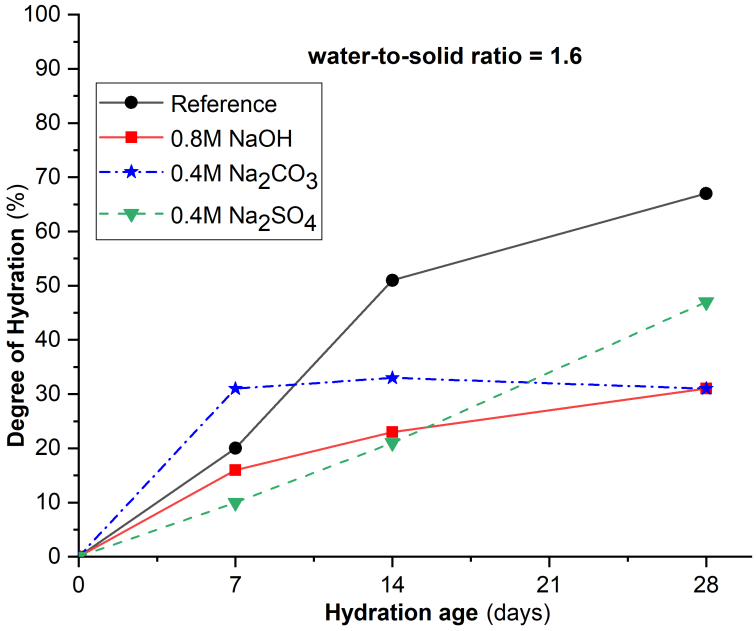

Figure 6.5: Degree of hydration (DOH) of chemically activated β-C_2S calculated via QXRD and TGA over 28 days.

The morphology of the hydration product under varying anions has been presented in Figure 6.6. The reference sample exhibited a densely interconnected structure in the early

stage (7 days) which changes into well distributed wider needle-like structure upon the later stage curing (Figure 6.6 (a, b)) [194]. In the case of carbonate anion-rich hydration medium, the C-S-H structure exhibited the crumbled foil structure alongside rhombohedral agglomerated calcite crystal (Figure 6.6 (c, d)). For the 0.8M NaOH sample, a fibrous morphology of the C-S-H was observed alongside the hexagonal crystal of portlandite (Figure 6.6 (e)). A dense aggregated network with possible gypsum crystal was observed in the sulphate-activated sample (Figure 6.6 (f)). The varying morphology of C-S-H is dependent on the Ca/Si ratio and type of activator [178, 196].

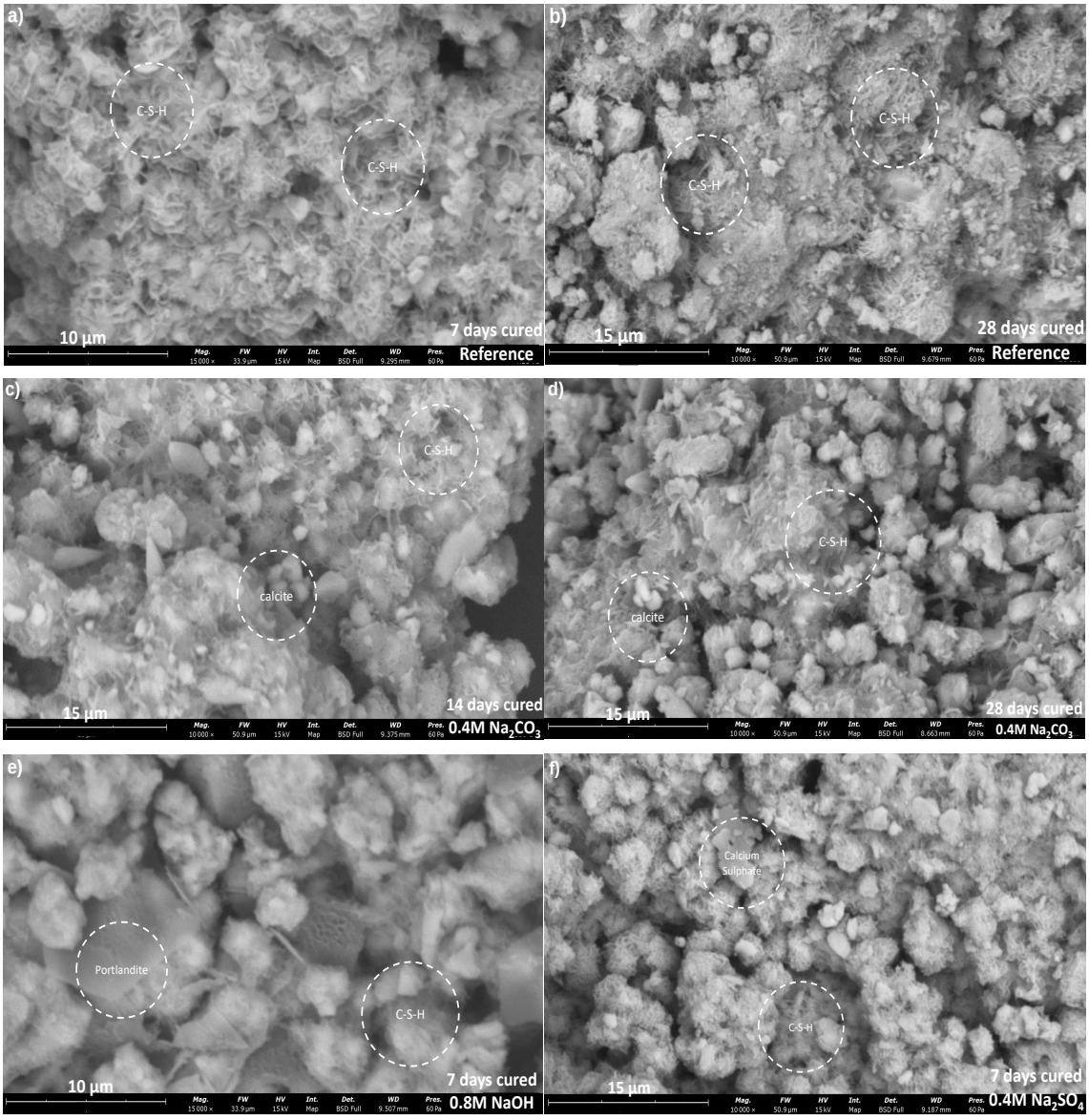

Figure 6.6: Scanning electron microscopy (SEM) micrographs of chemically activated β-C_2S a) 7 b) 28 days cured reference sample c) 0.4M Na_2CO_3 14 and d) 28 days cured sample f) 0.8M NaOH g) 0.4M Na_2SO_4.

By comparing all the anion's behaviour in C_2S activation, it is observed that the 0.4M Na_2CO_3 sample exhibited high hydration activity at an early stage (7 days) and

undergoes an apparent dormant period that lasts for 28 days of curing. On the contrary, a slow and continuous β-C_2S hydration process is observed in the reference sample which attains a high reaction degree at a later stage (14-28 days). In presence of sulphate anions, pH seems to play an important role in the dissolution-precipitation of gypsum, calcite, and portlandite respectively. Moreover, the hydroxyl-rich medium exhibited the early precipitation of portlandite seriously decreases the β-C_2S hydration reaction over time. To understand the two different β-C_2S hydration behaviour in water and sodium carbonate at an early stage, in-situ pH and conductivity are measured. The conductivity of the solution is taken as a measure of ions concentration and mobility in a solution at a given temperature. As the concentration of hydroxyl ions and ionic strength of hydration mediums play an important role in the C_2S reactivity.

6.3.3 *In-situ pH and conductivity measurement*

The evolution of hydroxyl ion concentration and ionic conductivity was measured for 5 days as shown in Figure 6.7. It is worth mentioning here that the same temperature condition such as 20 ± 2 °C as well as 1.6 water to solid ratio was chosen to have comparable results with calorimetric data. In the reference sample, a continuous increase in pH and conductivity is observed till 60 h observed indicating the continuous dissolution of C_2S. After 60 h, the pH attains a plateau, but the conductivity still increases which can be attributed to the high activity phase of precipitation of the hydration product (Figure 6.7 (a)). In the case of the 0.4M Na_2CO_3 sample, a clear increase in the hydroxyl ion concentration and conductivity was observed around 15 h which can be dominantly attributed to the dissolution. After 15 h an acceleration period of precipitation-dissolution last for a further 6 h followed by a clear decrease in the ionic concentration in the solution. However, the concentration of hydroxyl ions remains high (pH = 13.1), and ionic mobility around 40 h attains its plateau indicating the solution attaining the equilibrium (Figure 6.7 (b)). So, the proposed chemical reaction can be written as follow:

$$Ca_2SiO_{4(s)} + 2\,H_2O \rightleftharpoons 2\,Ca^{2+} + 4\,OH^- + H_4SiO_4 \tag{6.8}$$

$$Ca_2(OH)_{2(aq)} + {CO_3}^{2-}{}_{(aq)} \longrightarrow CaCO_{3(s)} + 2\,OH^-_{(aq)} \tag{6.9}$$

A basic dissolution medium does not enhance the dissolution of dicalcium silicate. A high pH (13) leads to a negative surface charge that would further limit the solubility (Eqs. (6.2) (6.3)). The high negative surface charge attracts strongly the Ca^{2+} or Na^+ ions. Moreover, the precipitation of $CaCO_3$ increases at high pH. The simultaneous precipitation of C-S-H and calcium carbonate deprives the solution of transportable cations between the solid surface and the solution leading to a longer dynamic equilibrium state for 0.4M Na_2CO_3 from 2 to 28 days at high pH (13). The term dynamic equilibrium rather than steady-state equilibrium is used because no net change in the hydration degree till 28 days was observed. Moreover, the simultaneous precipitation of calcium carbonate leads to lesser calcium ions available to get incorporated in C-S-H hydration product.

If the lack of transportable cations is the leading cause for the longer equilibrium period at high pH and relatively lower Ca/Si ratio, then any solid surface site that has a high

affinity for the Ca^{2+} would speed up the dissolution-precipitation reaction. To test the hypothesis, the 3 wt. % $CaCO_3$ is provided as a nucleation site for the Ca^{2+} ions.

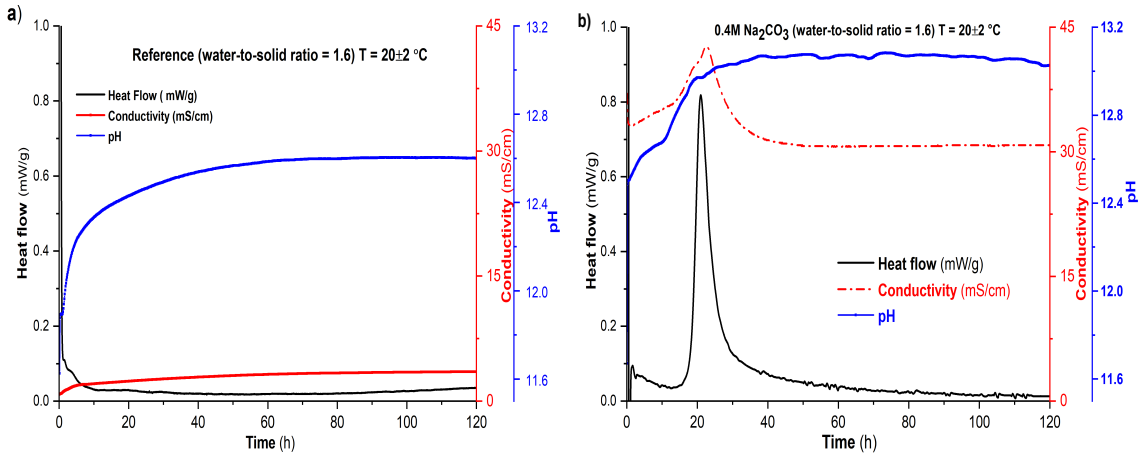

Figure 6.7: In-situ pH, conductivity, and isothermal calorimetric analysis at 20 °C of a) reference b) 0.4M Na_2CO_3 sample.

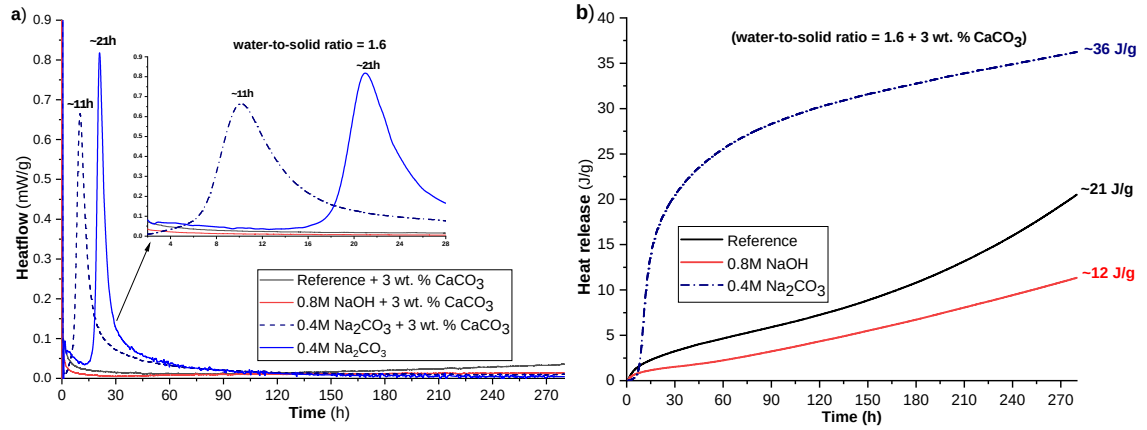

Figure 6.8: Exothermic heat curve of chemically activated β-C_2S in the presence of 3 wt. % $CaCO_3$ a) normalized heat flow b) cumulative heat of hydration.

6.3.4 *Effect of $CaCO_3$ as a nucleation site for Ca^{2+} ions*

The exothermic heat of the reaction supplied with 3 wt. % $CaCO_3$ has been presented in Figure 6.8. In the 0.4M Na_2CO_3 sample, the presence of solid calcium carbonate shortens the induction period from 15 to 3 h. Consequently, the time for the heat of hydration peak maxima reduces from 22 to 11 h and the system early reaches into dynamic equilibrium state (Figure 6.8 (a)). But overall, the addition of calcium carbonate did not exhibit any change in the cumulative heat release (36 J/g) (Figure 6.8 (b)). These findings indicate that the lack of transportable cations between a solid surface and solution leads to a dormant period from 2 to 28 days making β-C_2S dissolution highly discontinuous as compared to a reference, 0.4M Na_2SO_4, 0.8M NaOH. In the case of the reference and 0.8M NaOH sample, the provision of calcium carbonate as an inert material seriously delayed the hydration

reaction. The delay in the reaction can be attributed to the relatively earlier precipitation of calcium ions delaying the C-S-H formation and precipitation.

Overall, the C_2S reactivity in the presence of anions such as CO_2^{2-}, SO_2^{2-} and OH^- etc. can be broadly divided into three different cases: C_2S dissolution-precipitation reaction (case I), simultaneous precipitation of C-S-H and carbonates (case II): An early precipitation of reaction byproducts such as portlandite, gypsum, etc. (case III).

Case I: The standard C_2S reaction in the reference sample exhibited a dissolution equilibrium followed by precipitation of C-S-H. The important point to mention here is that the C-S-H precipitates earlier than the portlandite. That's why, the least amount of equivalent anhydrous portlandite (0.3 wt. %) is observed after 7 days of hydration (Figure 6.3). Moreover, the changes in the w/s ratio markedly shift the dissolution equilibrium which emphasizes the importance of local ion concentration at the C_2S-grain surface interface that predominantly plays an important role in C_2S reactivity [155, 197].

Case II: In the case of 0.4M Na_2CO_3, simultaneous precipitation of C-S-H and calcite leaves the solution enriched with hydroxyl ions. Due to the high hydroxyl ion concentration in the solution, the silicate surface got deprotonated and become negatively charged. The negatively charged surface not only restricts the C_2S dissolution but also hinders the diffusion of cations between the solid surface and the solution in this case.

Case III: In the case of 0.8M NaOH, early precipitation of portlandite (equiv. anhydrous portlandite 1.1 wt. % which is 366 times more than the reference sample) seriously delays the C-S-H precipitation. The same is observed for the 0.4M Na_2SO_4 sample at an early stage (7 days). But the calcium sulphate (gypsum) is more soluble at high pH than portlandite. So, the dissolution of dissolution over time saturates the solution to promote C-S-H precipitation. Therefore, the highest DOH (223%) increase was observed in the 0.4M Na_2SO_4 sample between the age of 14 and 28 days.

6.4 CONCLUSIONS

The effect of fixed moles of (0.8M) Na^+ cations balanced by either OH^-, SO_4^{2-} or CO_3^{2-} anions on β-C_2S hydration was investigated at ambient temperature. The important findings are as follows.

β-C_2S reactivity is highly dependent on the water-to-solid ratio. The increase in w/s ratio from 0.5 to 1.6 significantly increases C_2S dissolution leading to a 47 and 100% increase in cumulative hydration heat (14 days) respectively, in reference as well as 0.4M Na_2CO_3. But in 0.8M NaOH, the change in w/s ratio did not alter the cumulative hydration degree indicating the slowing of C_2S dissolution.

β-C_2S hydration reaction proceeds over time by dissolution equilibrium, C-S-H/portlandite precipitation, and silicate chain polymerization as a slow and continuous process. The β-C_2S reactivity exhibited a continuous increase in hydration degree (DOH) and reaches the highest 67% at 28 days hydrated reference sample.

At 7 days, the carbonate-activated β-C_2S exhibited a 55% higher DOH than the reference. But at later ages (7-28 days), no further hydration activity was observed except for the polymerization of silicate chains (enrichment with Q^2 (C-S-H) type units). The apparent dormant period is attributed to the simultaneous precipitation of C-S-H and calcium carbonate depriving the solution of transportable cations between the solid

surface and hydration medium at high pH (13.1). The idea is further confirmed by the addition of 3 wt. % calcium carbonate as nucleation site that further reduced the induction period from 22 to 11 h without changing the overall cumulative heat of hydration.

The β-C_2S hydration of sulphate-rich ions is more dependent on the pH. At first, gypsum was found to be the only hydration product alongside C-S-H at 7 days. As the C_2S dissolution increases so does the pH of the hydration medium, the gypsum started to dissolve and portlandite started precipitating at later stages. At curing age between 14 and 28 days, the highest DOH (223%) was observed which is attributed to the dissolution of calcium sulphate dissolution, and the promotion of C-S-H precipitation.

0.8M NaOH activated β-C_2S exhibited no significant increase in hydration degree at any stage compared to the reference sample leading to the lowest DOH (31%) after 28 days. This behaviour is attributed to the early precipitation of portlandite and the high pH of the solution leading to the slow dissolution of β-C_2S.

7

REACTIVITY OF AIR GRANULATED BASIC OXYGEN FURNACE SLAG AND ITS IMMOBILIZATION OF HEAVY METALS

ABSTRACT

Air granulation of basic oxygen furnace slag can improve its hydraulic potential to enhance recycling potential. The hydration behavior of the slag has been investigated via isothermal calorimetry, QXRD, and TG/DTG analysis. The air granulated slag exhibited improved early-age hydration and led to the formation of C-S-H, hydrogarnet, and hydrotalcite phases. The slag reactivity is controlled by the dissolution of SiO_2 and Fe_2O_3 bearing phases as observed by SEM-EDX-based PARC analysis and the hydration degree reaches up to 41% after 28 days curing. The hydrated slag features an improved immobilization of V and Cr as confirmed by ICP analysis.

Major part of this chapter is summarized elsewhere: M.J. Ahmed, K. Schollbach, S.R. van der Laan, H.J.H. Brouwers, Reactivity of air granulated basic oxygen furnance steel slag and its immobilization of heay metals (manuscript submitted).

7.1 INTRODUCTION

Chapter 3 explained the effect of air granulations on the mineralogical composition of BOF slag and concluded that the fast cooling of the slag did not generate a significant amorphous content. Instead, It impacted crystallite size and mineralogical composition [198, 199]. The air granulation appears to suppress free lime formation, leading to a higher content of β-C_2S compared to standard cooled BOF slag, and generated perovskite in addition to brownmillerite. Additionally, a higher Cr and V leaching (300%, and 640%, respectively, above the permissible legislative limit) was observed indicating that air-granulated BOF slag exhibited a higher degree of dissolution of Cr and V bearing phases than standard cooled one [198]. Usually, the reaction products of the air granulated BOF slag are calcium silicate hydrate (C-S-H), hydrogarnets, and hydrotalcite that tend to immobilize heavy metals especially potentially hazardous oxidation state V (V) and Cr (VI) in the hydration matrix [152]. Before applying this material, it is important to see if air granulated BOF slag can immobilize the heavy metals in the hydration matrix. Moreover, the high Cr and V leaching connotates for the high hydraulic activity in the air granulated BOF slag. Therefore, this chapter intends to follow up on this observation and investigate the hydraulic reactivity of air granulated BOF slag with water to determine if air granulation is a viable option to make the slag more reactive. This includes an investigation of the leaching behavior because previous investigations on standard cooled BOF slag have shown that the hydration products of BOF slag tend to immobilize the Cr and V [160]. To the author's best knowledge, no systematic study about this topic exists.

This study is the continuation of Chapter 3 about the characterization of the air-granulation of BOF slag [198] using the same air-granulated slag. The two size fractions from 4-2- and 2-1-mm air granulated BOF slag were chosen as they yield 90% of air granulation of the BOF slag. Early age hydration is investigated via isothermal calorimetry with a fixed water-to-solid (w/s) ratio while the later ages of 7-, 14-, and 28-days hydrated sample via QXRD (quantitative X-ray diffraction) and TG (thermal gravimetric analysis). Furthermore, the microstructure of the 28-day hydrate sample has been analyzed through large area phase mapping using SEM-EDS using phase recognition and characterization (PARC) analysis. Moreover, the leaching of heavy metals (V and Cr specifically) in a 28-day hydrated slag sample has been quantified via ICP-OES and correlated with the degree of hydration.

7.2 MATERIALS

Air granulated BOF slag is taken from regular production at Tata Steel Europe in Ijmuiden. The most granules were in the range of 4-2 (47.5 wt. %) and 2-1 mm (39 wt. %) as chosen for the detailed hydration studies.

7.3 METHODS

Two BOF slag fractions were ground for 40 minutes at 300 rpm to get fine particles via a planetary ball mill (Pulverisette 5, Fritsch). The PSD and SSA are presented in Figure 7.1.

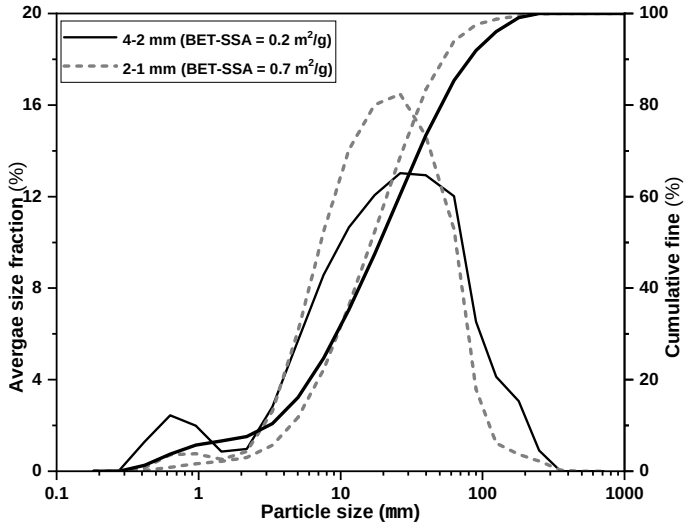

Figure 7.1: The PSD (particle size distribution) of 4-2- and 2-1-mm fraction of air granulated BOF slag. In the inset, the specific surface area (SSA) obtained via the BET method is given.

The 7-, 14-, and 28-day hydrated air granulated BOF slag samples were prepared to employ a 0.35 w/s ratio. The hydration of cured (7, 14, and 28 days old) samples was stopped via the solvent exchange (Isopropanol, Diethyl ether) method. The detailed characterization methods are explained in Chapter 2.

7.4 RESULTS AND DISCUSSIONS

7.4.1 *Early age hydration*

The early age (1-4 days) hydration behavior of 4-2 mm and 2-1 mm fractions of air granulated BOF slag as well as standard cooled BOF slag has been investigated via isothermal calorimetry as shown in Figure 7.2. The heat flow is normalized by the mass of the sample.

The 2-1 mm (0.7 m^2/g) fraction showed slightly higher heat of hydration (2.2 mW/g, 67 J/g) than the 4-2 mm fraction (0.2 m^2/g) (2.0 mW/g, 64 J/g) due to high specific surface area (SSA). The obtained exothermic curve of the 2-1 mm fraction is directly comparable with the standard cooled BOF slag since both have a very similar specific surface area (0.7 m^2/g). The 2-1 mm fraction exhibited 2.7 times higher heat release than the standard cooled BOF slag, a clear indicator that air granulation increased the reactivity of the slag (Figure 7.2 (a)).

The main exothermic event in both air-granulated BOF slag samples can be attributed to the reactivity of calcium aluminoferrite phase such as brownmillerite that can be observed clearly in the 4-2 mm sample (Figure 7.2 (a)) [200, 201]. It appeared that the 4-2 mm fraction reacted earlier than the 2-1 mm sample which can be attributed to high percentage fines (D (10)) as shown in Figure 7.1, despite the overall lower SSA after grinding. The exothermic peak appears around 8-12 h and is caused by the precipitation of C-S-H (calcium silicate hydrate). The narrow heat flux peak persists for 10-12 h which is consistent with the previous literature [202–206].

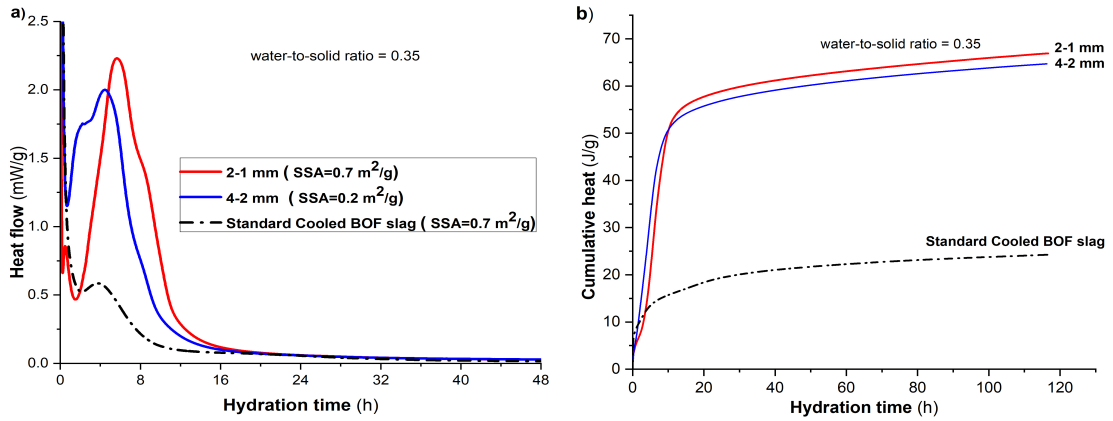

Figure 7.2: The exothermic heat curve of 2-1- and 4-2 mm fraction of air granulated BOF slag (a) heat of hydration and (b) cumulative heat of hydration.

7.4.2 *Later age reactivity of air granulated BOF slag*

The air granulated BOF slag was hydrated, and mineralogical composition change was determined after 7, 14, and 28 d for both fractions via QXRD as shown in Figure 7.3 (a, b). The detailed phase amounts with error in Table C.1, as well as the diffractogram with labeled peaks alongside Rietveld fit, can be found in Figure C.1, respectively. Upon hydration, the crystalline phases decrease with time while the XRD amorphous content increases. The new crystalline phases evolved such as portlandite, hydroandradite ($Ca_3Fe_2(SiO_4)_{3\text{-}x}(OH)_{4x}$), and sjoegrenite ($Mg_6Fe_2(CO_3)(OH)_{16}$) in both slags' fractions.

It is evident that portlandite is the byproduct of the C_2S phase's reaction as shown in Eq. 7.1.

$$Ca_2SiO_{4\,(s)} + 2\,H_2O \rightleftharpoons 2\,Ca^{2+} + H_4SiO_4 + 4\,OH^- \tag{7.1}$$

In both slag fractions, the α' as well as larnite crystalline content decreases (22.1 to 11.7 wt. %, 22-13.3 wt. % respectively) in 28 days hydrated slag. The decrease in crystalline content of brownmillerite (25.0-9.7 wt. %), Fe, Mg-wüstite (15.5-8.2 wt. %), perovskite (10.3-3.0 wt. %) and increase in XRD amorphous (7-41 wt. %) content in the slag indicates the dissolution of the slag phases over time (Table C.1, Figure C.1). The study indicates that the brownmillerite reaction will lead to the formation of hydrogarnet, Fe-hydroxides (amorphous), and portlandite (Figure C.1) [207]. So far, we have not considered the formation of amorphous Fe-hydroxides except amorphous C-S-H (from slag hydration). Whether Fe could be a substitute for Al in the structure of the hydration products is still under investigation, but a decrease in the Al/Fe ratio significantly decreases the brownmillerite hydration [208]. In the presence of iron oxide and silica-rich system due to the dissolution of dicalcium silicate phases alongside Fe, Mg-wustite, and perovskite, the brownmillerite favours the formation of Fe-katoite Ca3Fe2(OH)12) and hydroandradite ($Ca_3Fe_2(SiO_4)_{3\text{-}x}(OH)_{4x}$) as shown in Eqs. 7.2 and 7.3.

$$3\,Ca^{2+} + 2\,Fe(OH)_4{}^- + 4\,OH^- \longrightarrow Ca_3Fe_2(OH)_{12} \tag{7.2}$$

$$3\,Ca^{2+} + 2\,FeO^{2-} + xHSiO_3{}^{2-} + xOH^- \longrightarrow Ca_3Fe_2(SiO_4)_{3\text{-}X}(OH)_{4X} \tag{7.3}$$

The solubility product of hydroandradite decreases with increasing silica content in the solution leading to stabilization of the hydroandradite at room temperature [209–211]. The amount of crystalline Fe-katoite + hydroandradite reaches 5.9 (2-1 mm) and 5.1 wt.% (4-2 mm), respectively, after 28 days of hydration indicating the high silica and iron oxide dissolution over time. Less than 1 wt. % of the double-layer hydroxide sjoegrenite ($Mg_6Fe_2(CO_3)(OH)_{16}$) was detected likely due to poor crystallinity of the phase.

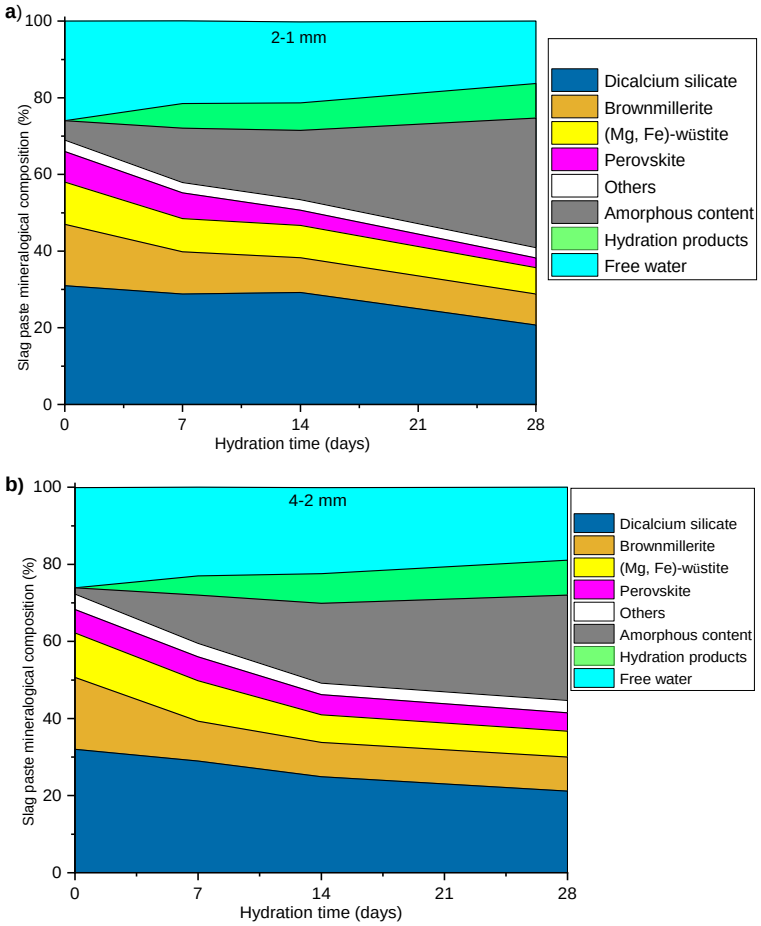

Figure 7.3: QXRD of a) 2-1- and b) 4-2-mm fraction of hydrated air granulated BOF slag cured for 7, 14, and 28 days. Free water value is taken from the initial water-to-solid ratio and bound water is calculated from the loss on ignition at 1000 °C.

To get more insight into the hydration product and XRD amorphous content, the TG/DTG thermogram of 7, 14, and 28 d hydrated slag fractions is shown in Figure 7.4 (a, b). The mass loss events below 60-200 °C can be assigned to the dehydration of C-S-H + Sjoegrenite. The next mass loss events from 260 to 400 °C can be attributed to the decomposition of silicious hydrogarnets [210, 212, 213]. It is important to mention here that the hydrotalcite phases start to decompose much earlier than the silicious hydrogarnet series (Figure 7.4). The decomposition steps include the removal of interlayer water, dihydroxylation of brucite-like layers, and decarbonation. The decarbonation steps depend on the bond length of Fe-OH and Mg-OH bond length in the case of the hydrotalcite layer double hydroxide solid solution series. The increase in bond length lowers the decarbonation temperature [214, 215]. The mass loss event

440-520 °C and 540 to 800 °C comprised of dehydration of portlandite as well as decarbonation of calcite respectively [95, 180].

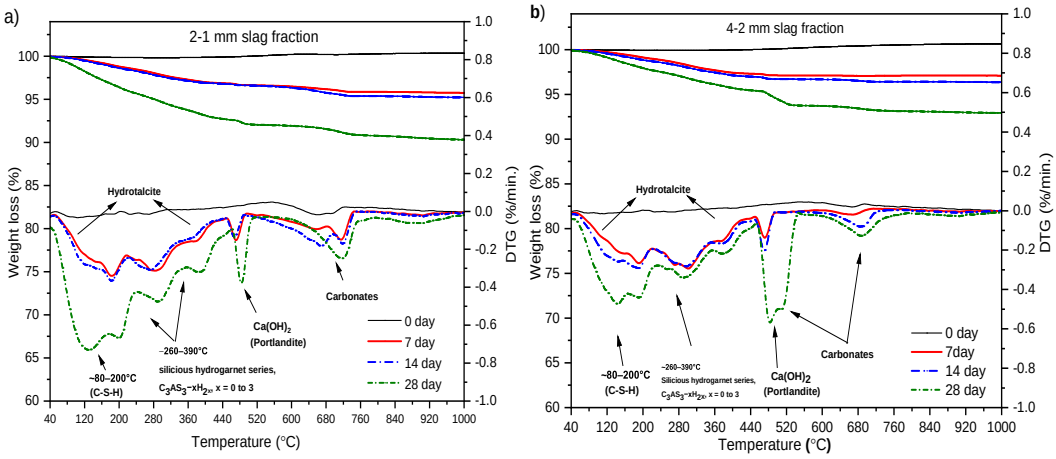

Figure 7.4: Thermal gravimetric analysis of hydrated air granulated BOF slag fractions a) 2-1 mm fraction and 1st derivative of thermal gravimetric analysis of 2-1 mm fractions b) 4-2 mm fractions and 1st derivative of thermal gravimetric analysis of 4-2 mm fraction.

The 2-1 mm fraction of air granulated BOF slag exhibited a higher degree of volatiles than the 4-2 mm fraction after 28 d hydrated samples. The enhanced reactivity of the 2-1 mm fraction can be attributed to the higher SSA (0.7 m^2/g) than the 4-2 mm (0.2 m^2/g) fraction. The QXRD and TGA are correlated to evaluate the degree of hydration (DOH) of both slag fractions. Firstly, the QXRD is rescaled considering the dilution effect and incorporation of bound water using Eq. 7.4.

$$W_{j,\text{rescaled,dilution corrected}} = W_{j,\text{Rietveld}}(1 - \text{Bound}\,water_{TG}) \tag{7.4}$$

The bound water is calculated from TGA. Then, the DOH is calculated by using the Eq. 7.5 and the results are presented in Figure 7.5.

$$\text{DOH}(t) = \frac{1 - W_{\text{anhydrous,dilution corrected}}(t)}{W_{\text{anhydrous(t=0)}}} \tag{7.5}$$

Wj = Weight of XRD phases (wt. %)
Bound-water$_{TG}$ = (mass loss $_{(104\text{-}1000\ °C)}$ - calcite)

The 2-1 mm slag fraction exhibited higher (18%) DOH than 4-2 mm (15%) after 7 days of hydration. A slight increase in DOH (18-21%) is observed from 7 to 14 days for 2-1 mm indicating the slag's slow reactivity at this time while the 4-2 mm slag fraction keeps reacting and reaches 27%. After 28 days of hydration, 2-1 mm fraction exhibited higher overall DOH (41%) than 4-2 mm (36%) can be attributed to the high SSA of 2-1 mm slag fraction. The DOH and TG bound water (mass loss) are significantly higher than standard cooled BOF slag which indicates the high reactivity of the slag [160].

To study the influence of air granulated hydration on the microstructure, the SEM-EDX-based large area phase mapping was carried out on 28 days of hydrated 2-1 and 4-2 mm air granulated slag fraction using PARC software as shown in Figure 7.6 (a,

b) (also see Figure C.2 (a, b) for 28 d hydrated 4-2 mm fraction) [26]. It is clear from the PARC image that the 2-1 mm slag fraction contained large crystals of C_2S and (Mg, Fe)O embedded in a fine-grained matrix. The fine-grained matrix or matrix phase is a mix of different mineral phases with a size below the EDX resolution of 1 µm [198]. Based on their composition they were divided into 3 parts: Matrix CS (Ca, Si rich), CF (Ca, Fe rich), and MF (Mg, Fe rich) (see reference [198] for further details).

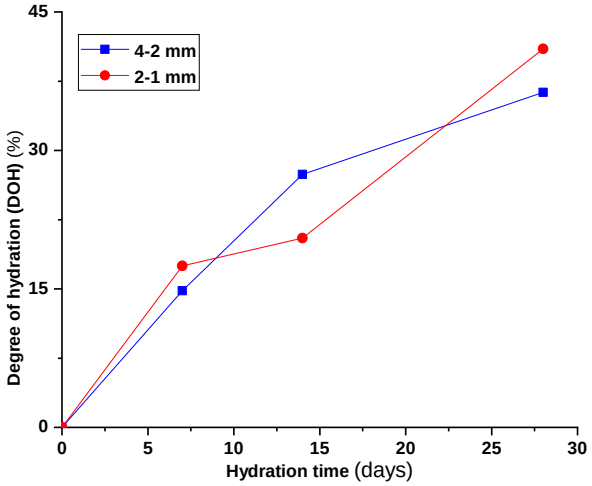

Figure 7.5: Degree of hydration (2-1-and-4-2 mm slag fractions) of hydrated air granulated BOF slag cured for 7, 14, and 28 days.

Contrary to XRD analysis, the C_2S polymorphs (α', β) cannot be differentiated as they have the same chemical composition. The C_2S phase also exhibited the presence of several minor ions such as P_2O_5, Cr_2O_3, V_2O_5, Fe_2O_3, TiO_2, etc. which tend to occupy more Si sites according to structure difference factor (D) calculations [216]. It is important to mention here that a significant amount of V_2O_5 and P_2O_5 are incorporated into the crystal structure of C_2S while the detection of Cr_2O_3 is erroneous due to a sum peak of Ca + Si = Cr in the EDS spectrum [7, 217]. However, electron probe micro-analyzer (EMPA) analysis revealed that the C_2S contains Cr_2O_3 < 0.05 wt. % [7]. The "hydration product" phase is a heterogeneous mix of the crystalline and amorphous hydration products detected with XRD and TG that cannot be differentiated with SI due to their size below the spatial resolution. The phase named "Portlandite" also contains calcium hydroxide and carbonate, as both are present according to TG and XRD, however, they are difficult to recognize with EDX. The hydrated sample matrix was divided into hydration products, C_2S phases, portlandite, wüstite, matrix CS (CaSi), CF (CaFe), and MF(MgFe) according to Ca/Si, Ca/Fe, and Mg/Fe, etc. composition by using a density plot as shown in Figure 7.6 (b) [7, 198, 218].

The area% of each phase and oxide composition of the hydrated 2-1 mm slag fraction is presented in Table 7.1. The hydration products take up 49 area% of the total. The ratios of calcium to silica and calcium to iron oxide in the hydration product are 2, and 3.4, respectively, indicating the dissolution of dicalcium silicate as well as iron oxide bearing brownmillerite phases.

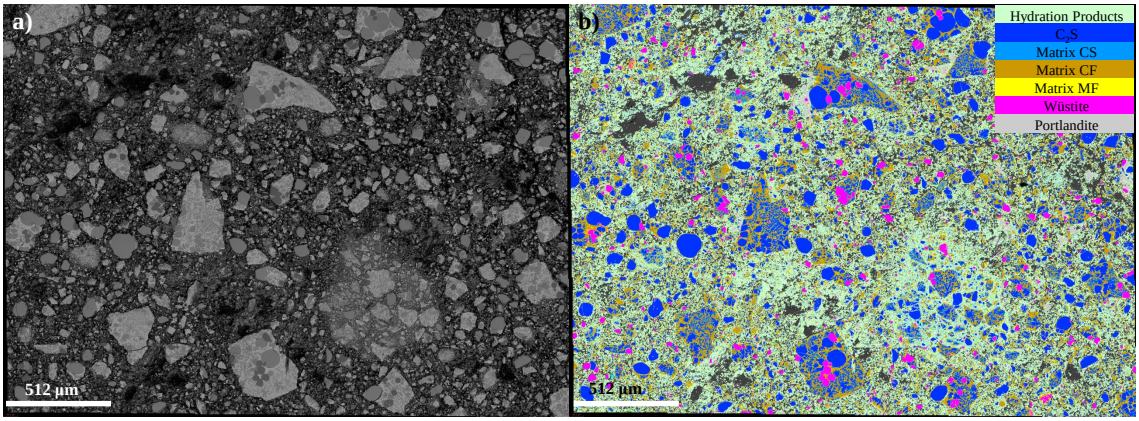

Figure 7.6: Microstructure analysis of 2-1 mm fraction of air granulated BOF slag after 28 days of hydration at 512 µm (one spectral image (SI) field consists of a data set of 512×384 data points) a) backscattered image (BSI) b) PARC phase map.

Table 7.1: Phases identified in 28 days hydrated 2-1 mm granulated slag in area % via PARC analysis.

2-1 mm slag	Phases Amount (Area%)	MgO	Al_2O_3	SiO_2	P_2O_5	CaO	TiO_2	V_2O_5	Cr_2O_3	MnO	Fe_2O_3
Hydration Products	48.8	5.7	1.8	23.5	1.9	46.8	1.4	0.7	0.5	2.9	13.9
C_2S	25.5	0.7	0.3	30.1	2.9	61.1	1.0	0.4	1.3	0.2	1.9
Matrix	21.3	6.3	3.1	7.4	0.6	36.2	2.5	0.8	0.3	6.7	35.6
Wüstite	2.8	67.2	0.0	1.6	0.0	2.2	0.1	0.2	0.4	8.2	20.0
Portlandite	1.4	0.3	0.2	1.2	0.3	94.5	0.7	0.0	0.1	0.5	1.7
Bulk PARC Composition		16.1	1.1	12.8	1.1	48.1	1.1	0.4	0.5	3.7	14.6

7.4.3 *Environmental behaviour of hydrated air granulated BOF slag*

The one batch leaching test was performed on the 28 days of hydrated slag of 2-1 mm and 4-2 mm air granulated BOF slag fractions as shown in Table 7.2 and compared to the leaching on the slag granulated BOF slag before the milling and hydration. The data for unhydrated slag was published previously and used for direct comparison [198]. One can argue that the direct comparison cannot be due to the dilution effect of the hydration of slag. As 2-1- and 4-2-mm slag has a low value of loss on ignition (LOI) (8 and 6 wt. % respectively), the dilution effect will not cause much change in elemental composition. The vanadium element leaching decreases from 11.03 to 1.3 mg/kg for the 2-1 mm fraction after 28 days of hydration and from 11.83 to 1.1 mg/kg for the 4-2 mm slag fraction. These vanadium emission (1.1 to 1.3 mg/kg) values are below the permissible (1.8 mg/kg) emission values. Cr emission decreases from 1.86 to 0.72 and from 1.75 to 1.01 mg/kg, respectively, in 2-1- and 4-2-mm slag fraction which is above the permissible emission

(0.63 mg/kg) values. The remaining heavy metals are below the legal limits of the Dutch soil quality decree.

Table 7.2: The heavy metals leaching values 2-1 mm and 4-2 mm of air granulated slag fraction.

Slag fractions	**Permissible limit**	**Unhydrated 2-1 mm**	**28 days hydrated 2-1 mm**	**Unhydrated 4-2 mm**	**28 days hydrated 4-2 mm**
	(mg/kg)	(mg/kg)	(mg/kg)	(mg/kg)	(mg/kg)
pH (20 ± 2 °C)		10.8	11.5	11.0	11.8
Antimony (Sb)	0.32	0.19	L.D.	0.19	L.D.
Arsenic (As)	0.9	0.22	L.D.	0.21	L.D.
Barium (Ba)	22	0.02	0.1	0.11	0.6
Chromium (Cr)	0.63	1.86	0.72	1.75	1.01
Vanadium (V)	1.8	11.03	1.3	11.83	1.1

*L.D.= below detection limit

The pH of the hydrated slag sample lies in the range of 11.5-11.8. The equilibrium formation of Ca-Si-H phases with C_2S dissolution would permit the high Ca^{2+} concentration in the leachate which limits the solubility of vanadium oxide [219]. From the PARC analysis of the 2-1- and 4-2-mm slag granules, it was concluded that the C_2S contributes more toward V leaching in the slag [198]. That's why, the V is immobilized in the hydration product phase upon C_2S reactivity as C-S-H actively takes V_2O_5 on the tetrahedral Si-site. All these factors contribute toward the immobilization of V in the BOF slag.

In the case of Cr leaching, the identifiable Cr complex is $CaCrO_4$ at pH 11.5-11.9 as shown in Eq. 7.6.

$$Ca^{2+} + {CrO_4}^{2-} \rightleftharpoons CaCrO_4 \tag{7.6}$$

The $CaCrO_4$ is soluble species in aqueous media, and the decrease in the Cr leaching can be attributed to the heavy metal immobilization potential of the hydration product particularly hydrogarnet and double layer hydroxide which can host large quantities of Cr^{6+} [220]. It is worth mentioning that the BOF slag contains Cr^{3+} in brownmillerite and wüstite -type phases [221, 222].

Consequently, the 28 days hydrated 2-1 mm slag sample shows a higher decrease (61%) in Cr-leaching than (42%) 4-2 mm slag sample due to high DOH (41%) value. In summary, the Cr and V can be immobilized in the slag matrix by enhancing slag hydration via increasing the reactivity of C_2S and brownmillerite phases. As compared to standard cooled BOF slag, the overall higher leaching of the air-granulated BOF slag is

probably due to a higher oxidation state of V and Cr since the air-granulated slag is more oxidized overall. However, further investigation would be required to confirm it.

7.5 CONCLUSIONS

The hydration of air granulated BOF slag fractions 2-1-and-4-2 mm as well as the immobilization behaviour of Cr and V, has been investigated. The air-granulated slag exhibited a significantly (2.7 times) higher reactivity than the standard cooled BOF slag. The hydration products consisted of C-S-H, a mix of Fe-katoite and hydroandradite, double-layer hydroxide (sjoegrenite), and portlandite (a byproduct of C-S-H). The formation of hydration products is controlled by the dissolution of C_2S and brownmillerite which are very similar to the reaction of standard cooled BOF slag. The calculated reaction degree shows that the 2-1 mm fraction exhibited higher DOH (41%) than the 4-2 mm (36%) fraction after 28 days of hydration. The high reactivity of 2-1 mm slag is attributed to higher SSA (0.7 m^2/g) than the 4-2mm (0.2 m^2/g) slag fraction.

The 2-1- and -4-2-mm slag fractions after 28 days of hydration immobilize up to 88% and 91% of vanadium respectively as compared to the unhydrated slag. The 28-day hydrated 2-1 mm slag fraction immobilizes Cr up to 61% due to high DOH (41%) while the hydrated 2-4 mm slag fraction decreases Cr leaching up to 42%. The decrease in the V and Cr leaching is largely attributed to immobilization in hydration products.

In summary, the current chapter provides detailed insight into the hydration of air granulated BOF slag. This study shows that the air granulation shows the promise of high reactivity at an early stage alongside immobilizing Cr and V in the hydration product which confirms the fitness of the material for sustainable building products. The efforts like mechano-chemical activation, and partial replacement with other industrial byproducts can enhance its recycling potential for the valorization of the steel slag which will be the next step of this study.

8

AIR GRANULATED BOF SLAG APPLICATION AS A BINDER: EFFECT ON STRENGTH, VOLUME STABILITY, HYDRATION STUDY, AND ENVIRONMENTAL RISK

ABSTRACT

This study evaluates the air granulated BOF slag potential as a cementitious material by substituting in OPC at replacement levels of 5, 20, 35, and 50%. The mechanical performance of the cement-slag composites is correlated with the hydration behaviour through thermal, mineralogical, and microstructural analysis. The findings show that the granulation improved the grindability, early-stage reactivity, and compressive strength till 28 days. The 5% slag can be substituted as a binder and 35% as an inert filler. The performance decline upon 20-50% replacements is attributed to the absence of brownmillerite reactivity of the slag in cementitious environment. Overall, the granulation did not improve the cement-slag composite performance significantly till 90 days. All the samples exhibited the leaching of heavy metals below the permissible limit of the Dutch soil quality decree.

Major part of this chapter is published elsewhere: M. Jawad Ahmed, W. Franco Santos, H.J.H. Brouwers, Air granulated basic Oxygen furnace (BOF) slag application as a binder: Effect on strength, volumetric stability, hydration study, and environmental risk, Constr. Build. Mater. 367 (2023) 130342.

8.1 INTRODUCTION

Climate change due to anthropogenic CO_2 emissions is a critical challenge of this century. Among the CO_2 emission sources, the cement industry contributes 7-8% of anthropogenic CO_2 emissions and 26% of the industrial carbon emissions globally [223, 224]. The worldwide cementitious material partners with the global cement and concrete association (GCCA), the International Energy Agency (IEA), and the Cement Sustainability Initiative (CSI) have set out several road maps aiming to be carbon neutral by 2050 [225–228]. In Europe, the two main construction sectors release 10% of total European CO_2 emissions. The cement industry produces 5% of CO_2 emissions while the same amount is contributed by the steel used in construction [229]. The UN Environment (2015) report "Eco-Efficient types of cement" identifies the two main routes that can promise CO_2 reduction in the relatively short term as mitigation for emissions. Route number one is to increase the clinker substitution by supplementary cementitious material (SCM). And the second one is the more efficient use of cement in the downstream products such as mortars, concrete, etc. [60].

The recycling and reuse of BOF slag carry many challenges [13, 14]. Several strategies have been reported to improve the BOF slag valorization, such as mineral modification, carbonation, weathering, mechanical and alkali activation as well as high-temperature curing [16–18, 230]. In particular, efforts are made to valorize BOF slag as fine aggregates for the development of geopolymer-based materials (high-end application) by mixing it with other waste streams such as fly ash, mine tailings, and blast furnace slag [19–24]. Moreover, the maximum 5% replacement as an alternative to blast furnace slag in cement production exhibited a promise for high-end application [6, 25]. As explained in Chapters 4 and 6, one strategy to enhance the slag reactivity is changing the cooling process from slow to relatively faster cooling by granulation to prevent crystallization. The studies have concluded that the fast cooling did not generate significant amorphous content but decreased the crystallite size and stabilized the reactive polymorphs of the slag phases that would contribute toward the high reactivity of BOF slag [231]. Nevertheless, some important questions need to be addressed systematically, such as to what extent air granulation enhances the hydration potential of BOF slag. Does air granulation exhibit more compatibility with OPC? Moreover, can the utilization of air granulated BOF slag as a filler improve the performance better than inert filler?

To address all the above questions and evaluate the possible fast cooling impact on the cementitious properties of the BOF slag, the air granulated BOF slags were applied as a replacement for OPC in mortar. To the author's best knowledge, there is no direct information reported about the air granulated BOF slag application as a replacement for cement. Furthermore, the hydration study of the cement-slag pastes is investigated for a better understanding of the possible cement-slag reaction.

This chapter investigates the potential of air granulated BOF slag as an OPC replacement in the mortar and compares it to quartz powder. It was added with the same degree of replacement to compare the performance of the material with an inert material. The workability, mechanical performance, dimension stability, and environmental risk of 5, 20, 35, and 50% replacement clusters of OPC with slag as well as quartz powder were analysed over time. In addition to that, the thermal, mineralogical, and microstructure analysis of cement-slag paste samples of the mortars were evaluated to understand the

hydration behaviour for the novel binder application. Finally, the correlation between the chemically bound water of cement-slag pastes and the strength development of mortars as well as the potential leaching of heavy metals were investigated.

8.2 MATERIALS

Air granulated BOF slag taken from regular production at Tata Steel Europe in Ijmuiden (see Chapter 2 for details). Moreover, quartz powder (QP) was used as an inert material, and for the type of ordinary Portland cement (OPC) selected as a reference binder (REF), CEM-I 42.5N (ENCI Heidelberg cement) was chosen. The sample labelling is shown in Table 8.1.

Table 8.1: The density of the used materials.

Material	**Abbreviations**	**Density (g/cm^3)**
CEM I 42.5 N	REF	3.1
Quartz powder	QP	2.6
Air-granulated BOF slag	GSS	3.6

8.3 METHODS AND CHARACTERIZATION

8.3.1 *Particle size distribution*

The slag distribution was designed and milled to have a similar size as a controlled parameter. The PSD and SSA have been presented in Figure 8.1.

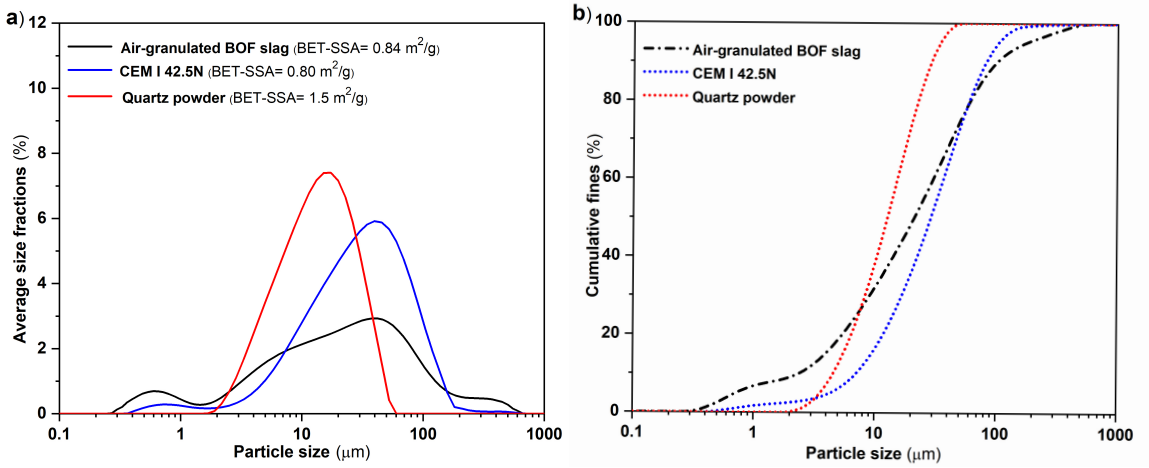

Figure 8.1: The PSD (particle size distribution) of CEM I 42.5 N (SSA=0.80 m²/g), quartz powder (SSA=1.5 m²/g), and air granulated BOF slag (SSA=0.84 m²/g) (a) average size fraction (%) (b) cumulative fine (%). The mentioned SSA is obtained via the BET method.

8.3.2 *Oxide composition*

The oxide composition of the raw material has been presented in Table 8.2. The GSS samples contain a high amount of Fe_2O_2 (27 wt. %) and MgO (8 wt. %) than CEM I 42.5 N sample Fe_2O_2(4 wt. %). The GSS exhibited a mass gain (negative value of a loss on ignition) due to the conversion of ferrous oxide into ferric oxide.

Table 8.2: Oxide composition of GSS, CEM I, and QP in wt. %.

Raw Material	MgO	Al_2O_3	SiO_2	P_2O_5	SO_3	CaO	TiO_2	V_2O_5	Cr_2O_3	MnO	Fe_2O_3	Others	*LOI
GSS	7.3	1.3	12.5	1.2		44.6	1.3	0.7	0.3	3.9	26.8		-0.02
CEM I 42.5N		4.2	17.7		3.1	64.6					3.3	3.2	3.9
QP		1.5	97.5								0.9		0.01

*LOI= loss on ignition

8.3.3 *Mineralogy of raw materials*

The peak assignment of the raw material is shown in Figure 8.2 and a detailed quantitative analysis is presented in Table 8.3. The mineral phases of all the raw materials have been presented in Table 8.3. The GSS exhibited almost the same mineralogical phases as standard cooled BOF slag [191]. The air-granulation of the BOF slag leads to the formation of a high amount of α'-C_2S (22.0 wt. %). Moreover, the iron-rich perovskite phase was observed only in GSS, which formed due to the breakdown of brownmillerite due to quick cooling. Air granulation of the slag also suppresses the formation of free lime [198]. The CEM I sample contains a high amount of hatrurite (tricalcium silicate 60 wt. %) which is responsible for the early age hydration activity of the cement [128]. The BOF slag sample contains a high amount of larnite + α'-C_2S (dicalcium silicate 45 wt. %) which contributes to the later age strength of the cement [43, 138]. In this regard, the replacement of the cement with BOF slag could contribute toward the synergy of the hydration reaction.

Table 8.3: QXRD of the GSS, CEM I 42.5 N in (wt. %).

Mineral Phases	Hatrurite	Larnite	α'-C_2S	Brownmillerite	Fe (Mg)-Wüstite +Magnetite	Perovskite	XRD amorphous	Others
CEM I 42.5 N	59.6	5.71	2.11	11.6			14.1	6.7
GSS		16.9	22.0	25.7	17.6	6.4	10.1	1.3

8.3.4 *Mortars study*

8.3.4.1 *Mix design*

For the mortars mix design, a reference (REF) of 100% of OPC (CEM I 42.5 N) was adopted, and replacements of 5, 20, 35, and 50% were done with GSS and QP to evaluate the effect of replacing cement by GSS and to compare its performance with an inert material QP as shown in Table 8.4. The replacement percentages were chosen to start from 5%, to include

in this study the possibility of using BOF slag as a minor additional constituent (MAC) as well.

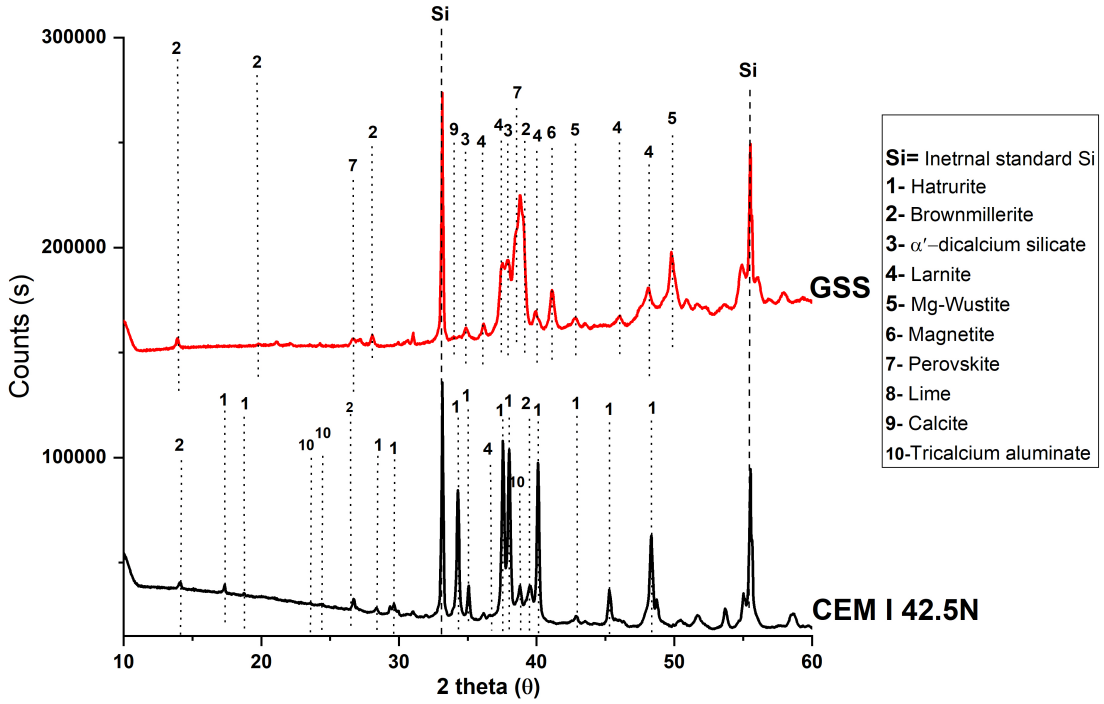

Figure 8.2: X-ray diffraction (XRD) analysis of CEM I 42.5 N and GSS samples with labelled peaks.

Table 8.4: Mix design proportions of the mortars (vol. %).

MIX ID	CEM I 42.5 N	GSS	QP	Standard Sand	Water/binder	OPC Replacement by volume	Superplasticizer (% of total binder)
REF	0.22	-	-	0.78	1.2	0%	0.25
GSS05	0.21	0.01	-	0.78	1.2	5%	0.07
GSS20	0.17	0.04	-	0.78	1.2	20%	0.07
GSS35	0.14	0.08	-	0.78	1.2	36%	0.07
GSS50	0.11	0.11	-	0.78	1.2	51%	0.07
QP05	0.21	-	0.01	0.78	1.2	5%	0.10
QP20	0.17	-	0.04	0.78	1.2	20%	0.10
QP35	0.14	-	0.08	0.78	1.2	36%	0.10
QP50	0.11	-	0.11	0.78	1.2	51%	0.13

The mixes were designed from a starting reference (REF) with a standard sand/binder = 3 ratio using a water-to-binder (w/b) ratio of 0.4 by mass. Those ratios were kept constant for the design of all the other mixes in volume. Samples were prepared according to EN 196-1, composed of mass (25% of binder and 75% of standard sand). The value of w/b = 0.4 was chosen due to the low demand for BOF slag. The fresh

samples were cast in plastic moulds of 160 x 40 x 40 mm covered with a plastic film for the first 24h, then demoulded and cured at a temperature of 20 °C until their testing age.

8.3.5 *Leaching analysis*

One batch leaching test was performed on raw material and 28 days mortar sample according to EN-12457 using deionized water with a liquid-to-solid ratio of 10.

Table 8.5: One batch leaching (NEN: 1245-7) analysis of raw materials.

Sample		**CEM I 42.5 N**	**Air-granulated BOF Slag**	**Quartz Powder**
	pH	13.1	12.4	9.8
Element*	Legal limit	mg/kg	mg/kg	mg/kg
Sb	0.32	0.04	0.04	0.03
As	0.19	0.02	0.05	0.03
Ba	22	5.5	0.4	0.09
Cr	0.63	0.5	0.4	0.06
Mo	1	0.05	0.08	0.02
V	1.8	0.003	0.4	0.0
Zn	4.5	0.007	0.04	0.002
Fe		0.1	0.001	2.2

*Cu, Co, Hg, Ni, Se, Cd, Pb, and Sn were below the detection limit

The mortar sample is crushed into a powder for good insight into the leaching behaviour of slag. The leaching of raw material has been presented in Table 8.5. All the raw materials exhibited the leaching of heavy metals below the legal limits of the Dutch soil quality decree.

8.4 RESULTS AND DISCUSSION

8.4.1 *Physio-mechanical behaviour of cement-slag mortars*

8.4.1.1 *Workability*

The spread flow values of the fresh mortars for each mix design are plotted in Figure 8.3. The flowability of the REF was adjusted with 1.4 g of superplasticizer to achieve 120 mm average diameter. The substitution of OPC by the BOF slags did not increase the fresh mortar diameter. In comparison to the spread-flow value of 120 mm presented by the REF mix, the values of GSS05, GSS20, GSS35, and GSS50 samples decreased to 107, 105, 100, and 100 mm respectively. The decreasing trend in fresh mixes in the specific present case can be attributed to a practical optimization point to avoid later bleeding and segregation. When compared to the literature [201, 232, 233], the fresh mortars with replacements of slag presented a relative decrease in the spread flow value. The

QP05 (100 cm), QP20 (100 cm), QP35 (100 cm), and QP50 (110 cm) also exhibited a relative decrease in fluidity due to a higher specific surface area (1.5 m^2/g) than REF (0.8 m^2/g). Usually, the higher fineness and specific surface area of QP than OPC increases the water demand of the mixture which leads to a decrease in flowability [234].

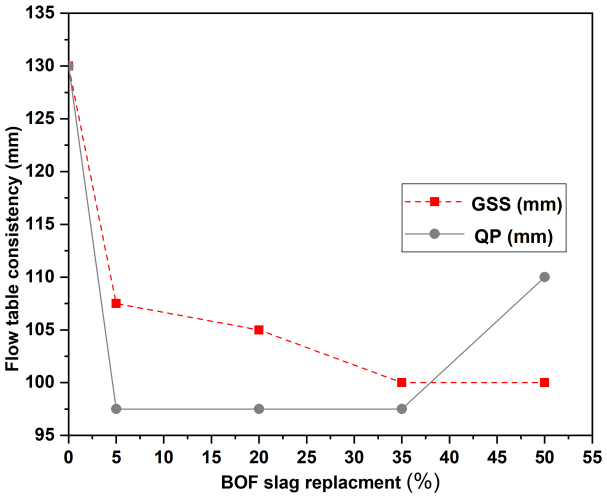

Figure 8.3: Determination of consistency of fresh mortar by flow table (diameter) for REF and the replacements of 5, 20, 35, and, 50% of GSS and QP.

8.4.1.2 *Mechanical performance*

Compressive strength development of the mortar specimens tested at ages 7,14, 28, and 91 days is presented in Figure 8.4. The 5% OPC replacement with BOF slag in GSS05 samples increased the 7-day compressive strength to 63 MPa. That is notably higher than the REF mix 56 MPa mechanical performance [6, 235]. At 28 days, the compressive strength of GSS05 reached 70 MPa showing a significant increase compared to the REF mix of 62 MPa. Upon further curing to 91 days, the GSS05 reached a plateau, and no further strength gain was observed. In comparison to the mechanical performance of the inert material (quartz powder), the 5% replacement cement-slag samples at all ages present a compressive strength considerably higher than QP05. With higher than 5% replacement, the compressive strength of all mixes starts decreasing with an inversely proportional relationship to the substitution in comparison with the reference mix. Moreover, the 35% exhibited a mechanical performance analogous to inert material even having 44-58% lower specific surface area than quartz powder (Figure 8.4) [16, 203, 236, 237].

8.4.1.3 *Drying shrinkage and drying mass loss*

To understand the mechanical properties, the length stabilization of all the mortar specimens was measured till 72 days when reached constant values as shown in Figure 8.5. Regardless of the mixture and replacement percentages, the length changes vary between 0 to 1 mm/m, and the observed values were close to the REF. The highest drying shrinkage value of 0.9 mm/m was observed for GSS50 at 23 days of curing and posing no harm to the volume stability of mortars [238]. In general, most mortar

specimens reached 95% drying shrinkage by 28 days. Moreover, the GSS05 and GSS20 exhibited high-length stabilization after 37 days similar to the REF mortar specimen.

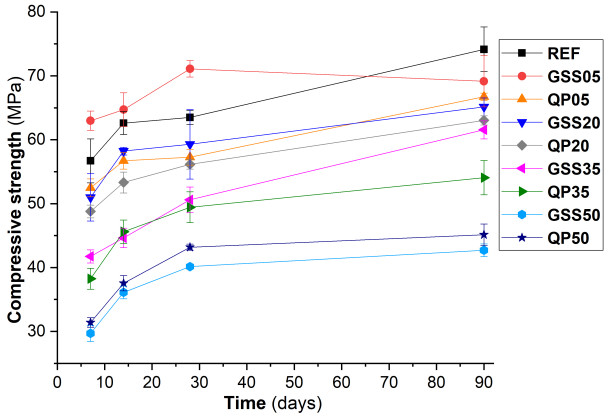

Figure 8.4: Compressive strength of mortar specimen of REF, 5, 20, 35, and, 50% of GSS as well as QP mixes.

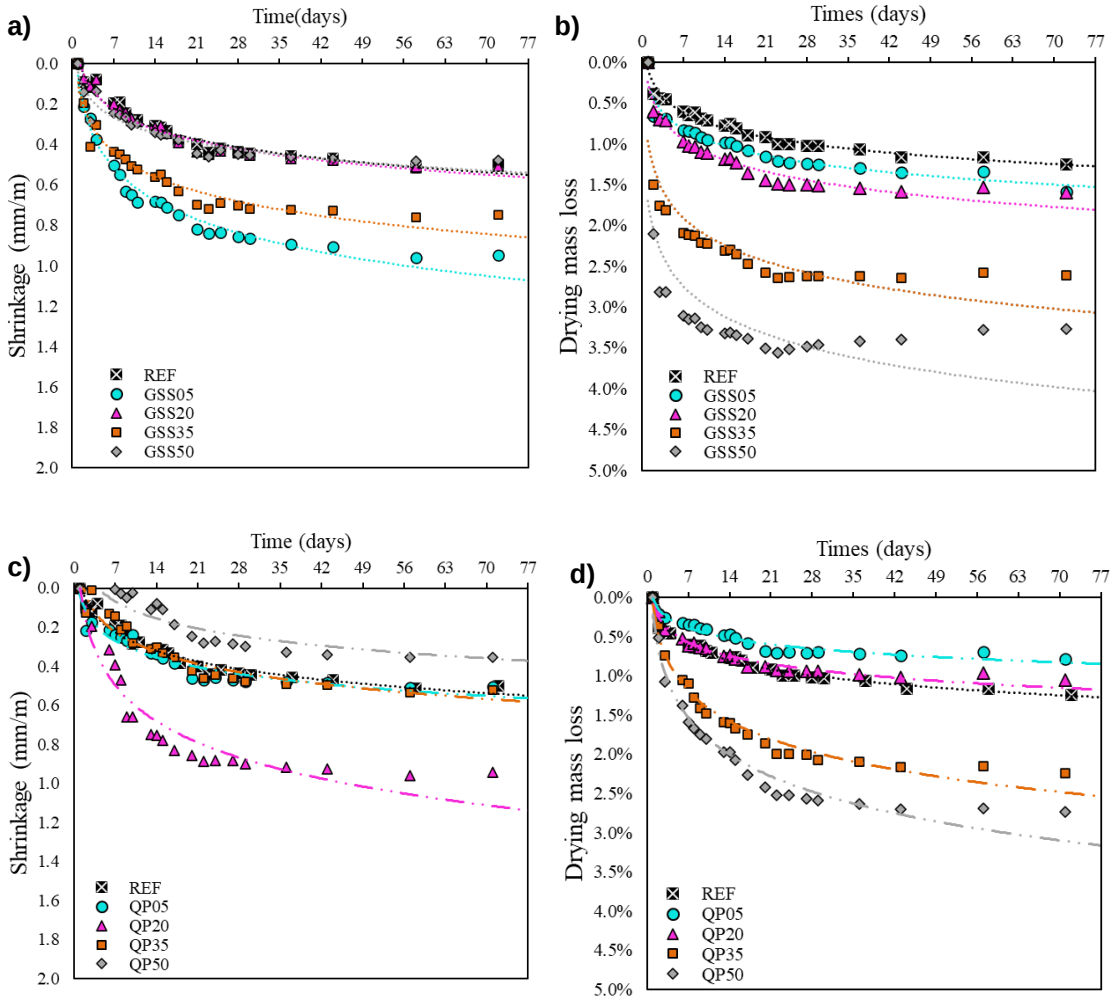

Figure 8.5: Drying shrinkage of mortar specimens of 5, 20, 35, and, 50% replacement by (a) GSS, (c) QP in comparison to the REF sample. Mass change of mortar specimens of 5, 20, 35, and, 50% replacement by (b) GSS, (d) QP, in comparison to the REF sample.

8.4.2 *Reactivity of cement-slag pastes and its correlation with mechanical performance*

8.4.2.1 *Early age hydration studies*

The early age hydration behaviour of cement-slag paste has been investigated via isothermal calorimetry as shown in Figure 8.6. The exothermic heat of hydration is normalized with the mass of the sample. The SSA among the samples REF (0.80 m^2/g) and GSS (0.84 m^2/g) are almost the same (Figure 8.6) [239]. So, the early-stage (0-72 h) reaction between air-granulated BOF slag and CEM I is directly comparable. A typical hydration process of OPC is comprised of five stages; rapid heat release period, dormant period, acceleration period, deceleration period, and steady period respectively which can be observed in the REF sample as shown in Figure 8.6 (a, b) [204].

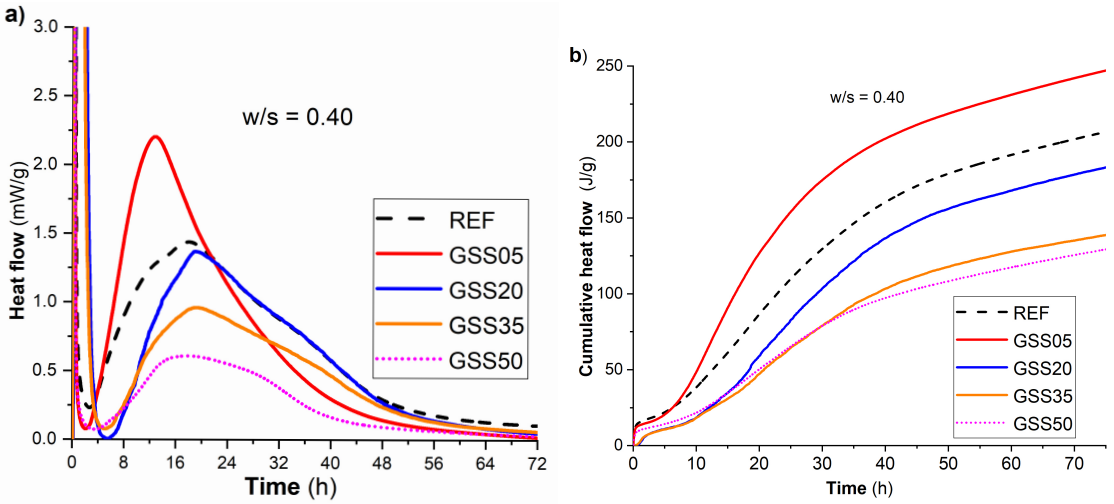

Figure 8.6: The exothermic heat curve of cement-slag with reference to cement (a) heat flow of cement-GSS clusters (b) cumulative heat flow of cement-GSS clusters.

The first exothermic peak in 1-2 h can be attributed to the partial dissolution of the cement. Therefore, the cement hydration enters the dormant period after the first exothermic peak of dissolution[206]. The second exothermic peak around 3-7 h can be attributed to the reactivity of the calcium aluminate (AFm) phases [200, 201]. The hydration products such as C-S-H and $Ca(OH)_2$ precipitate only when the concentration of Ca^{2+} in the solution reaches a saturation state [205]. The apex point of the exothermic peak appears around 18 h and is caused by the precipitation of C-S-H (calcium silicate hydrate) and CH (portlandite). Then, the deacceleration heat flux persists for 20-40 h which is consistent with the previous literature [203, 238]. The 5% replacement of cement with the air-granulated slag expedites the precipitation of C-S-H phases that occurred earlier 13 h indicating the clear synergy between the slag and cement in the GSS05 sample. In addition to that, the cumulative heat release of the GSS05 sample reaches 246 J/g as compared to the CEM I sample at 207 J/g (Figure 8.6 (b)). A further increase in cement replacement with the air-granulated slag in GSS20, GSS35, and GSS50 samples decreases the rate of hydration incrementally than in the REF sample which indicates that the hydration is primarily dominated by the hatrurite (Ca_3SiO_5-alite) reactivity.

For a better understanding of the enrichment of cement phases with the slag and mineral phase's reaction at an early age, a ternary composition diagram has been presented in Figure 8.7. To make the composition diagram, the value of the mineral composition is taken from the QXRD of the raw material and normalized to 100% (Table 8.3). It indicated that the addition of 5% slag in cement does not alter the composition of cement significantly. Substitution of the cement with slag enriches the cement-slag composite with brownmillerite, dicalcium silicate, and RO (Mg-wüstite phases) while decreasing the amount of hatrurite. It is concluded that the early-stage (48-72 h) hydration of the cement-slag composite is dominated by the reaction of tricalcium silicate (Figure 8.6). The composition diagram pointed out that the replacement of cement with slag leads to a new composition. The new phase composition would enhance the chances of a decrease in reactivity due to the enrichment of slow-reacting phases such as dicalcium silicate, Fe, Mg-wüstite, and a decreasing amount of hatrurite. The possible hydration synergy between cement and BOF slag at an early age can only be achieved if the brownmillerite from the slag significantly contributes to the hydration reaction alongside the hatrurite phase. Unfortunately, that is not the case with the BOF slag substitution in cement as shown in Figure 8.6. A few studies explained the slag retardation effect on the early age hydration of cement which has been attributed to low alkali content, slow depletion of gypsum, and reduction in the formation of ettringite [203, 240]. However, the ternary composition diagram provides a new perspective to understand the possible slag activation efforts as a cementitious binder. Moreover, the hydration of brownmillerite is highly dependent on the Al/Fe ratio in the solid solution and the amount of added sulfate alongside the presence of possible minor ions [213, 241]. Without this knowledge, the cement-slag composite reactivity at the solution level cannot be well explained.

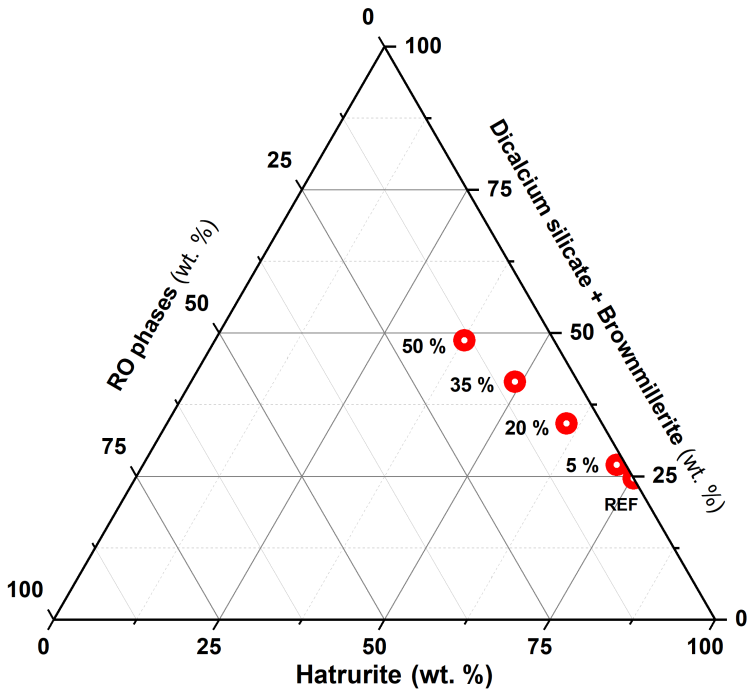

Figure 8.7: The mineralogical composition of the cement-slag composite changing with the increase of cement replacement by BOF slag.

8.4.2.2 *Characterization of hydration products*

Differential thermogravimetric analysis (DTG) was used to determine the dominant hydration phases. The curves for the cement-slag pastes after 7, 28, and 90 days are shown in Figure 8.8 (a, b, c) (thermal mass loss events can be found in Figure D.1 in appendix D). The mass loss events have revealed that GSS05 and REF samples exhibited higher mass loss at 40-200 °C (dehydration of calcium silicate hydrate and ettringite, AFm), 340-400 °C (dehydration of double layer hydrotalcite), 430-510 °C (dehydroxylation of calcium hydroxide), and 550-800 °C (decarbonation of calcium carbonate) than GSS (20-50%) cement-slag paste [242].

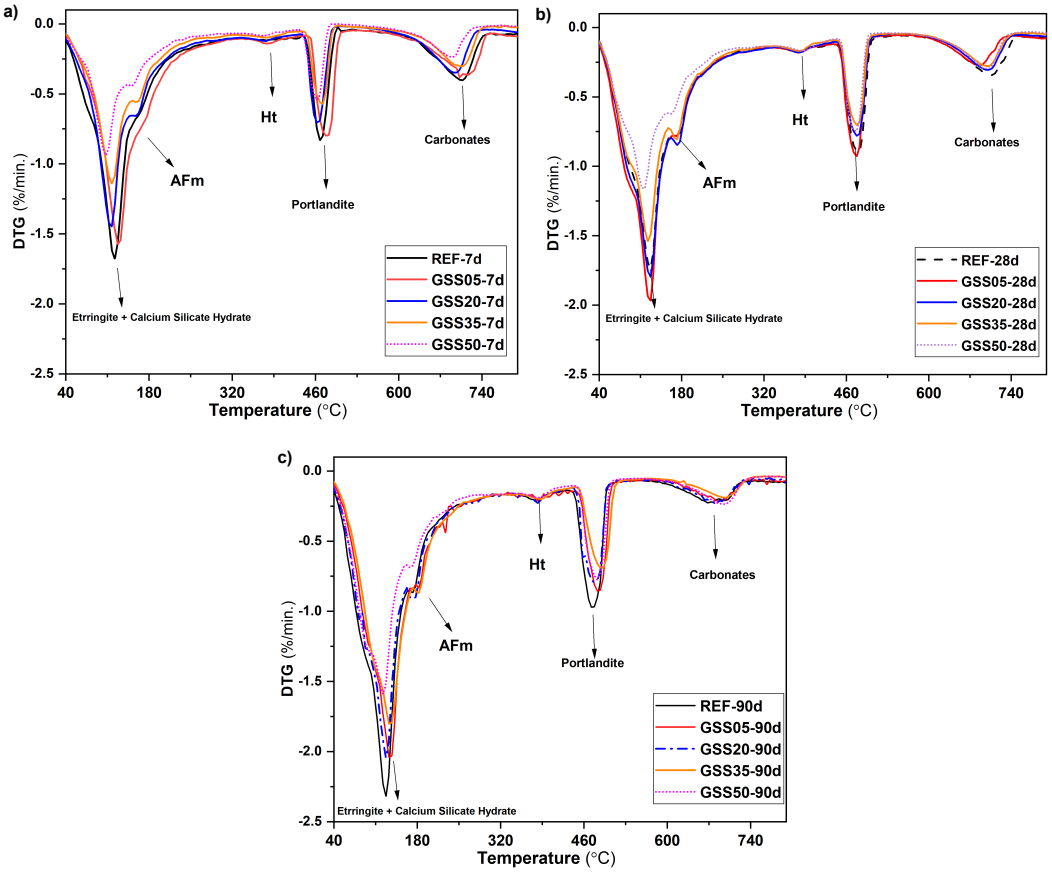

Figure 8.8: DTG analysis of cement-slag pastes sample with 5, 20, 35, and 50 % replacement of cement with BOF slag in comparison of REF, cured for (a) GSS-7 days (b) GSS-28 days (c) GSS-90 days. The mass loss event is assigned as Ettringite + Calcium silicate hydrate, AFm (C_4A-C hydrate), Ht (hydrotalcite), Portlandite (calcium hydroxide), and calcite (calcium carbonate).

The mass loss events indicated that the cement-slag paste hydration reaction is dominated by the hydration of tricalcium silicate and dicalcium silicate. The assigned mass loss events in the thermal analysis of cement-slag paste are further confirmed by analyzing the X-ray diffraction pattern of 90 days of cured cement-slag paste as shown in Figure 8.9. The crystalline hydration phases such as ettringite, tetra calcium aluminate monocarbonate hydrate (C_4A-monocarbonate hydrate), as well as hydration products of C_3S and C_2S such as calcium silicate hydrate, portlandite, and calcite (formed upon

carbonation of portlandite), was observed. Moreover, a double-layer hydrotalcite, especially pyroaurite, and Zn-rich hydrotalcite was observed in the 90 days of hydrated air-granulated cement-slag paste composite. The type of hydration products is further complemented by microstructure analysis of 28 days cured past sample as shown in Figure 8.10. The SEM-BS (backscattered images) of 28 days cured 100% cement sample exhibited the well-intercalated hydration phases of C-S-H, ettringite, portlandite, and calcite (Figure 8.10 (a, b)) [230, 243]. The addition of 5% BOF slag substitution in cement exhibited dense hydration that was significantly distributed all over cement-slag composite grains. Upon 50% slag replacement, a clear decrease in homogenous hydration product distribution with unreacted slag particles is observed in the cement-slag composite (Figure 8.10 (c, d)).

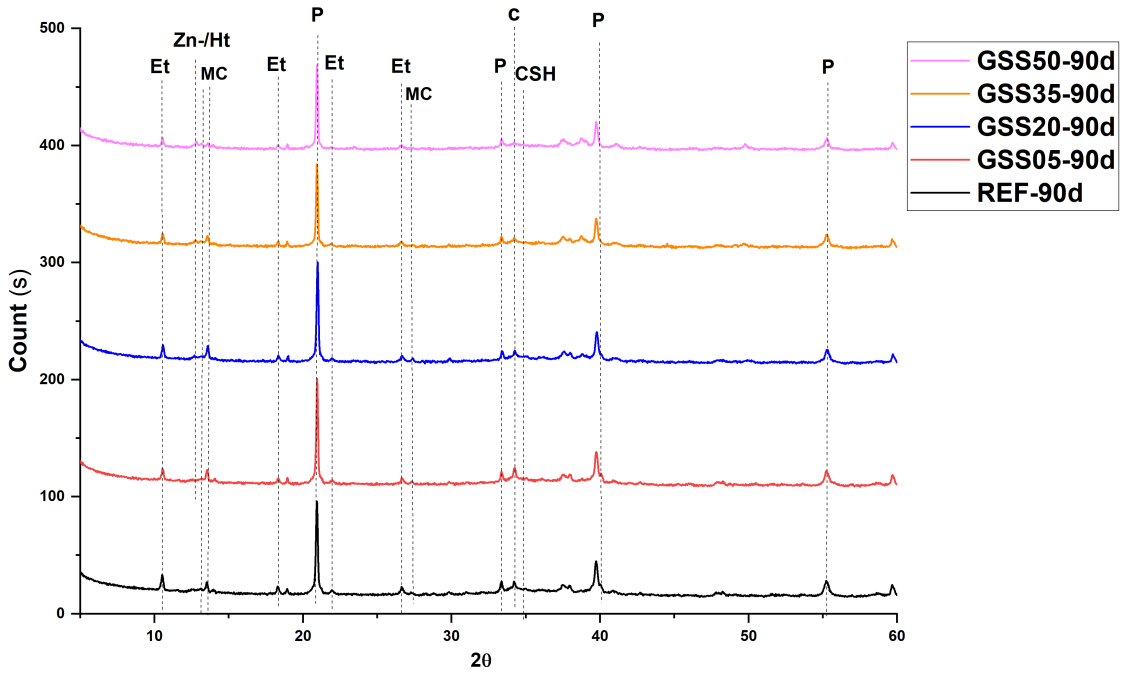

Figure 8.9: XRD analysis of 91 days cured paste sample a) REF, GSS (05, 20, 35, 50). The peak of hydration products is labelled as Et = ettringite, MC = C4A-monocarbonate hydrate, Ht = hydrotalcite, Zn-/Ht = Zn-hydrotalcite, P = Portlandite, C = calcite.)

The bound water due to cement-slag hydration decreases incrementally upon the incremental replacement of cement with the slag as compressive strength drops in the mortar sample (Figure 8.4). Moreover, the cement-slag composite lacks brownmillerite reactivity even till 90 days of curing (Figure 8.8 and Figure 8.9). The observation is further confirmed due to the lack of mass loss event at 260-390 °C usually attributed to Fe-siliceous hydrogarnet formation upon the reactivity of brownmillerite. A typical hydrated BOF steel slag usually contains Fe-siliceous hydrogarnet (hydroandradite) and Fe-katoite alongside calcium silicate hydrate due to brownmillerite hydration [7]. Because the formation of Al-siliceous hydrogarnet (hydrogrossular) is hindered kinetically at room temperature [244]. The formation of hydrogarnets is usually restricted under a cementitious system. In addition to that, a significant amount of up to 50% aluminium in hydrated slag blended-cement is incorporated in C-A-S-H while uptake of

Fe (III) is negligible as compared to aluminium [213, 244, 245]. All these factors can contribute to inhibiting the brownmillerite reaction.

By juxtaposing the early-stage hydration as well as the cement-slag composition diagram (Figures 8.6 & 8.7), the microstructure as well as diffraction pattern of hydration products and DTG analysis of cement-slag paste cured for 7, 28, and 90 days (Figures 8.8 & 8.10), it is concluded that the enrichment of cement with slag phases inhibits the reactivity of the BOF slag brownmillerite and restricts the formation of Fe-siliceous hydrogarnet till 90 days. Moreover, the GSS contains dicalcium silicate alongside brownmillerite that usually reacts slowly till 28 days leading to a delay in cement-slag reactivity at a higher replacement than 5% [43].

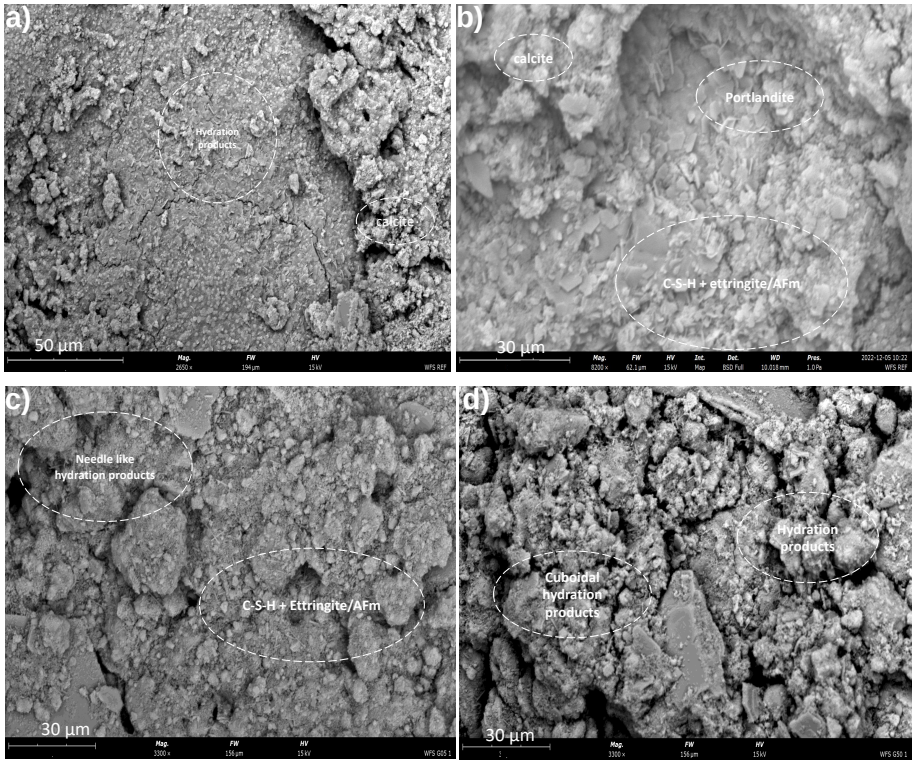

Figure 8.10: SEM analysis of 28 days cured cement-slag paste (a) REF (50 µm) sample (b) REF (30 µm) sample (c) GSS05 (30 µm) (e) GSS50 (30 µm).

8.4.3 *Correlation of bound water with mechanical performance*

Considering the importance of cement-slag reactivity on strength development in mortar, chemical-bound water is calculated from cement-slag paste samples and plotted against the mortar's compressive strength as shown in Figure 8.11. Even having the two independent studies (mortar and paste), the compressive strength of all the mortar replacement clusters is directly proportional to the chemical-bound water of the cement-slag paste which indicates the importance of cement-slag reactivity for mixed design applications. The value of bound water in GSS05 increases from 20 to 21% between 28 and 90 days respectively which explains the insignificant change of mortar strength from 28 to 91 days. While the reference sample bound water increases from 19

to 23% between 28 and 90 days which explains a higher increase in mortar strength from 28 to 90 days. Overall, no significant differences in mechanical performance, as well as hydration activity of the air-granulated as compared to standard cooled BOF slag are observed except the former reacts faster than the latter [191]. In addition to that, the air-granulation BOF slag can save grinding costs and improve the grindability of BOF steel slag.

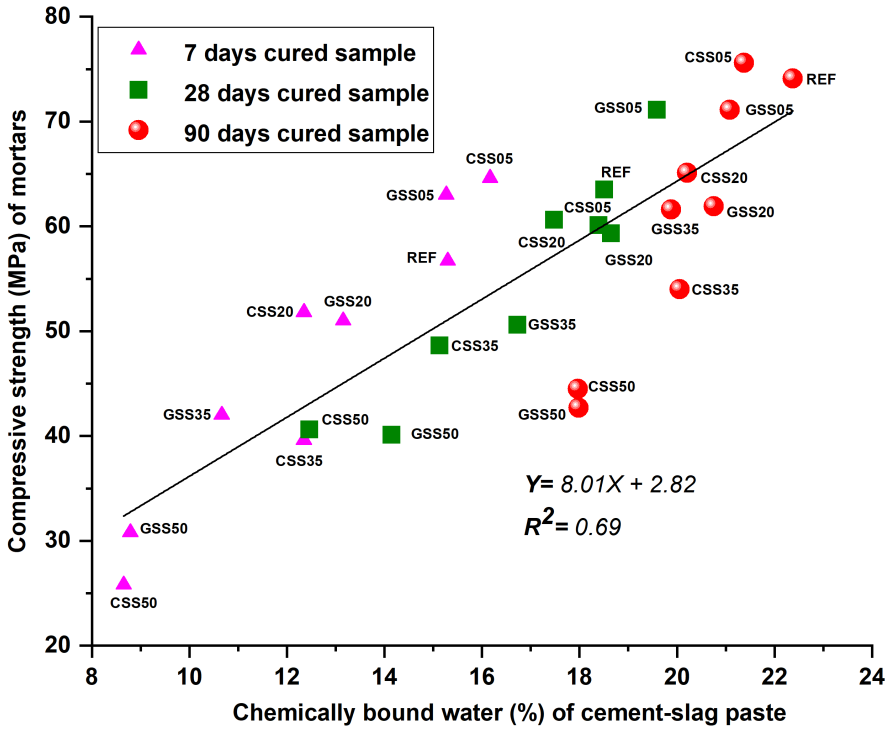

Figure 8.11: The correlation between the chemically bound water of cement-slag pastes and the strength development of mortar samples cured for 7, 28, and 90 days.

8.4.4 *Environmental impact*

The one batch leaching test was performed on the 28 days cured mortar sample as shown in Table 8.6 (see Table D.1 in appendix D for QP (5-50%) mortar specimen leaching). All raw material exhibits heavy metal leaching below the permissible limits (Table 8.5). The replacement of cement with BOF slag decreases the V leaching significantly as compared to raw material (0.4 mg/kg for GSS). While the Cr leaching increases in the GSS sample. The $Ca_3(VO_4)_2$ and $CaCrO_4$ are the dominant chemical species at pH >12. Usually, calcium vanadate is insoluble, and calcium chromate is soluble > 20 g/L at room temperature which indicates that Cr is immobilized by the hydration products [138, 159]. Moreover, the barium leaching increases in mortar samples as compared to raw material (5.5 mg/kg CEM I) that is released from the cement. Usually, BOF slag exhibits the problem of heavy metal leaching particularly V and Cr [124, 127]. Moreover, ordinary Portland cement also contains leachable chromium oxide [115]. The leaching of aliovalent heavy metals (V and Cr) is highly dependent on the oxidation state. In BOF slag, V exhibits V (III, IV, V) oxidation state while Cr is present as (II, III) as well as in cement.

However, it is established that the leached Cr and V contain the potentially hazardous oxidation state (VI) and (V) respectively [37, 135]. Overall, the leaching values exhibited that the BOF slag is a suitable candidate to mix with OPC.

Table 8.6: One batch leaching (NEN: 1245-7) analysis of 28 days cured mortar sample.

Sample		**REF**	**GSS50**	**GSS35**	**GSS20**	**GSS05**
pH		12.9	12.3	12.6	12.7	12.9
Element*	Legal limit	mg/kg	mg/kg	mg/kg	mg/kg	mg/kg
Si		0.17	0.01	0.01	0.02	0.02
Al		0.14	0.03	0.03	0.01	0.01
Ba	22	10.3	10.2	11.4	9.2	11.8
Cr	0.63	0.2	0.5	0.3	0.2	0.19
Mo	1	0.05	0.07	0.06	0.02	0.01
V	1.8	0.002	0.001	0	0.001	0.001
Zn	4.5	0.004	0.03	0.02	0.03	0.02

*Fe, Sb, As, Cu, Co, Hg, Ni, Se, Cd, Pb and Sn were below the detection limit

8.5 CONCLUSIONS AND IMPLICATIONS

The study aimed to demonstrate that air granulation of BOF steel slag can be considered a viable solution for slag valorisation as a binder as well as filler replacement in mortar application. For this purpose, cement is replaced by 5-50% air granulated and compared to inert material (quartz powder). Moreover, a detailed study of the cement-slag pastes is investigated to understand the correlation between the cement-slag reactivity and the mechanical performance of the novel binder. The main conclusions are as follows:

Air granulated BOF slag having a 5% replacement in OPC exhibited higher compressive strength than the reference as well as 5% quartz powder. The substitutions of 20% and 35% of BOF slag resulted in the same strength as the quartz powder. Overall, 5% slag can be substituted in OPC as a binder and 35% as an inert filler. All 28 days cured cement-slag mortar samples exhibited the Cr and vanadium leaching below permissible limit according to the Dutch soil quality decree.

The addition of the slag does not affect the mortars' stability, since the length variations were below 1mm/m. All samples replacing 5 and 20% do not show considerably higher drying mass loss in comparison with the REF. In replacements of 35 and 50%, not only slags but quartz powder also, show a higher percentage of the mortars drying mass loss 2-3.5%, an effect of the capillary water evaporation. The high drying mass loss in 35 and 50% clusters indicated that the water to solid can be lowered to get better mechanical performance.

Cement-slag composite study revealed that the degree of hydration is crucial to understanding the mechanical performance of novel binders. The enrichment of the cement with the 5% air-granulated BOF slag increases the early-stage hydration reaction by lowering the precipitation peak maxima from 18 to 13 h in the early stage (0-72 h).

The incremental addition of more than 5% slag cement delays the hydration reaction of hatrurite at an early stage. At later stages (1-90 days), the decrease in reactivity can be attributed to the slow reaction of C_2S, and the absence of brownmillerite reactivity in a cementitious environment inhibiting the formation of Fe-containing siliceous hydrogarnet. A correlation between the strength development of cement-slag mortar and chemical-bound water calculated from cement-slag pastes indicated that the compressive strength development is directly proportional to the degree of cement-slag reactivity at different ages.

The air granulated BOF slag exhibited better hydration activity and mechanical performance for up to 28 days. Overall, the air granulation of BOF slag did not affect the cement-slag composite performance significantly till 90 days. Moreover, the air-granulated slag exhibited a good grindability that can reduce the cost of energy-intensive grinding steps of jaw crushing which can enhance the economic viability of BOF recycling.

In summary, the current study provides a comprehensive understanding of air granulated BOF slag potential as a binder and filler in building material applications. This study shows that air granulation shows the promise of grindability, workability, volume stability, better early-age mechanical performance, and environmentally safe building products. This knowledge can be used to valorize BOF slag by mechano-chemical, alkaline activation, and partial replacement with industrial by-products. The objective of this study was to explore air granulation as a crucial step for the valorization of BOF slag.

9

UTILIZATION OF AIR GRANULATED BASIC OXYGEN FURNACE SLAG AS A BINDER IN BELITE CALCIUM SULFOALUMINATE CEMENT: A SUSTAINABLE ALTERNATIVE

ABSTRACT

Basic oxygen furnace (BOF) slag impacts negatively the OPC performance when replacement levels exceed 5%. This necessitates the exploration of alternative applications for BOF slag. At the same time, a high-volume slag utilization is desired to benefit slag recycling as supplementary cementitious materials. Therefore, this study aims to optimize the air granulated BOF slag substitution potential in belite calcium sulfoaluminate cement (BCSA) by investigating the hydration products in standard mortar. Especially, the reactivity of BCSA-slag binder is correlated with workability, and mechanical performance alongside volumetric stability by thermal, mineralogical, and microstructure analysis. As a result, the 10-30 vol. % cement replacement delays the final setting time by inhibiting the ettringite formation leading to a decrease in mechanical performance till 28 days. At later ages (28-180), the 30-50 vol. % substitution exhibited the synergy of mechanical performance, which is attributed to the reactivity of slag with BCSA by forming hydrogarnet, C-S-H, and strätlingite like hydration products. Moreover, all BCSA-slag mortars exhibited heavy metals' leaching and drying shrinkage below the permissible limit indicating the fitness of the material for building products. The BCSA-slag binder promises a high replacement volume for efficient air granulated BOF slag recycling.

Major part of this chapter is summarized elsewhere: M.J. Ahmed, S. Durand, M. Antoun, F. Gauvin, S. Amziane, H.J.H. Brouwers, Utilization of air granulated basic oxygen furnace slag as a binder in belite calcium sulfoaluminate cement: a sustainable alternative (manuscript submitted).

9.1 INTRODUCTION

Belite calcium sulfoaluminate cements (BCSA) has 30% lower associated CO_2 emission than conventional Portland cement. BCSA requires a lower kiln firing temperature of 1250 °C leading to a less amount of NO_x emissions and better grindability as compared to Portland cement clinker. However, the limited availability of raw materials as well as low demand for these types of cement makes the product expensive and can only be utilized for special applications. Several parameters need to be considered for appropriate mix design, for instance, 1) early hydration kinetics and volume stability due to the amount of calcium sulfate 2) the early setting need to be controlled with admixtures 3) the effect of altering these parameters on the later age concrete performance and durability [44, 240, 246, 247]. Therefore, a significant amount of industrial side streams such as blast furnace slag, silica fumes, waste glass, and fly ash, etc. have been added alongside calcium sulfoaluminate cement in concrete to study the more efficient use of the building materials [248, 249].

Basic oxygen furnace (BOF) slag is the tremendously available byproduct of steel making process [250]. In Europe, approximately 10 Mio.t/year of BOF slag is produced, and approximately 23% directly stacked piles leading to occupy the land resources [251]. As explained in the Chapter 8, our study showed [191] that the air granulation of BOF slag did not improve the reactivity significantly except for the grindability. Moreover, only a low percentage of up to 5% by volume can be replaced as a binder in OPC [191, 252] which demands alternative building products. An efficient building product is desired in which slag can be recycled in a high volume as SCM.

In this regard, a few studies have reported that the steel slag addition in calcium sulfoaluminate cement (CSA) as SCM brings many benefits of improved workability and performance [253–255]. However, strength loss of CSA-based cement is reported at later ages which are attributed to the ettringite decomposition [256]. The BOF slag contains dicalcium silicate and brownmillerite as main reactive phases which would enrich the hydration matrix with calcium silicate hydrate, ettringite, hydrotalcite, etc. [160]. These newly formed hydration products could provide later-age stability besides enhancing the immobilization potential of heavy metals [257]. The role of BOF slag as a binder is well understood in OPC but the effect of BOF slag on the BCSA cement hydration, workability, mechanical performance, shrinkage as well as environmental risks requires a systematic understanding [203]. To the author's best knowledge, there is no information available about a BCSA- (air granulated) BOF slag based novel binder. Therefore, this study aims to understand the effect of air granulated BOF slag substitution in BCSA cement. For this purpose, the replacement of 10, 20, 30, 40, and 50% BCSA cement by the slag in mortars is chosen to optimize the substitutional potential. The effect on workability, mechanical performance, and drying shrinkage over time is studied through thermal, mineralogical, and microstructural analysis. Moreover, the potential leaching of heavy metals especially V and Cr is evaluated by ICP-OES to assess the environmental risk.

9.2 MATERIALS

Air granulated BOF slag taken from regular production at Tata Steel Europe in Ijmuiden. The air granulation process of BOF slag has been studied elsewhere in detail [198]. The 4-1 mm fraction that accounts for 90% of total air granulation yield is milled and used for the study. Belite calcium sulfoaluminate cement (BCSA) cement is supplied by Vicat cement.

9.3 METHODS AND CHARACTERIZATION

A representative slag sample was chosen by using a static sample splitter. The PSD and SSA are presented in Figure 9.1. The BCSA cement contains a higher amount of Al_2O_3 (15.3 wt. %) as compared to the slag which is considered to be an important elemental oxide for the mineral modifier to improve the reactivity of the BOF slag as shown in Table 9.1 [258].

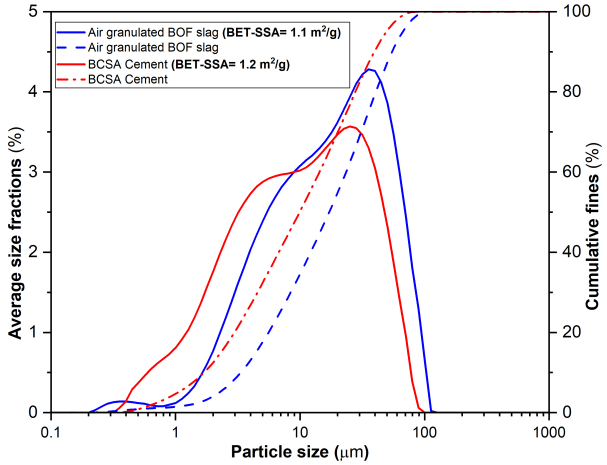

Figure 9.1: The PSD (particle size distribution) of the raw material. In the inset, specific surface area (SSA) is obtained via the BET method.

Table 9.1: Oxide composition of air granulated BOF slag and BCSA Cement (wt. %).

Material	MgO	Al_2O_3	SiO_2	SO_3	P_2O_5	CaO	TiO_2	V_2O_5	Cr_2O_3	MnO	Fe_2O_3	*LOI
BCSA Cement	0.7	15.3	8.0	13.5	-	50.6	1.1	-	0.1	0.1	10.6	4.04
Air-granulated BOF slag	7.3	1.3	12.5	-	1.2	44.6	1.3	0.7	0.3	3.9	26.8	-0.02

*LOI= loss on ignition

The BCSA contains mineral phases ye'elimite, larnite/belite, α'-dicalcium silicate (C_2S), anhydrite, tricalcium aluminate, brownmillerite, calcite etc. with traces of Mg and Fe-wüstite phases as shown in Figure 9.2. The air granulated BOF slag exhibited a high amount of α'-C_2S (high-temperature modification) alongside larnite, brownmillerite, perovskite, and Mg, Fe- wüstite with traces of calcite. The BCSA cement contains a significant amount of ye'elimite alongside anhydrite and tricalcium aluminate which is responsible for early-age reactivity leading to high early strength while the air

granulated BOF slag contains a high amount of the C_2S (α'-modification, larnite) and brownmillerite that would contribute to the later age strength of the BSCA-slag clusters [198, 240].

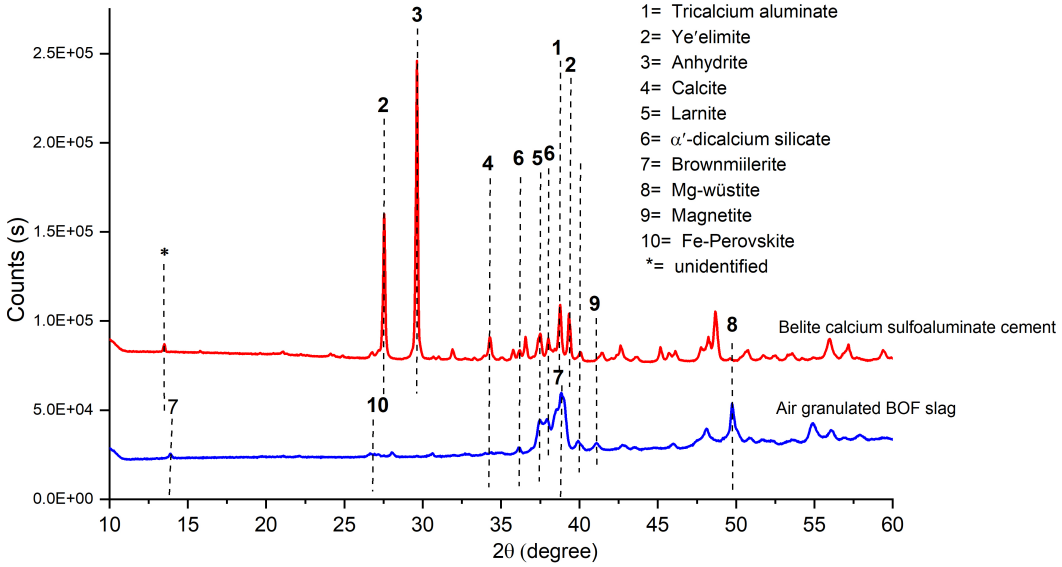

Figure 9.2: X-ray diffraction pattern of BCSA and air granulated BOF slag with labelled peaks.

9.3.1 *Mix design of BCSA-slag mortar*

The mortar mix design was adopted according to EN 196-1 standard with an effective water-to-binder ratio (w/b) of 0.5. The mortar sample is composed of 25% binder and 75% standard sand by volume as shown in Table 9.2. The 100% BCSA sample was chosen as a reference and replacements by volume of 10, 20, 30, 40, and 50% BOF slag was made to optimize the effective substitution in BCSA. The fresh sample was cast in plastic molds of 160 × 40 × 40 mm covered with a thin plastic film for 24 h, then demolded and cured at room temperature until their testing age.

Table 9.2: Mix design proportions of the BCSA-slag mortars (vol. %).

MIX ID	BCSA Cement	Air granulated BOF slag	Standard Sand	water/binder	BCSA Replacement (%)	Superplasticizer (% of total binder)
REF	0.25	0	0.75	0.5	0	0.24
10% BOF	0.22	0.03	0.75	0.5	10	0.19
20% BOF	0.2	0.06	0.74	0.5	20	0.17
30% BOF	0.17	0.09	0.74	0.5	30	0.14
40% BOF	0.15	0.12	0.73	0.5	40	0.10
50% BOF	0.12	0.15	0.73	0.5	50	0.00

9.4 RESULTS AND DISCUSSION

9.4.1 *Workability and its correlation with early age hydration*

The spread flow of fresh mortar with different BCSA-slag compositions was adjusted in a way to attain approximate consistent flowability as presented in Figure 9.3. For this purpose, the mixture with 50% slag was chosen as the starting point since it presents the highest flowability due to the low water demand of the BOF slag [239, 259]. The remaining BCSA-slag (0-40%) composition was adjusted by the addition of a superplasticizer to achieve a consistent 20 ± 0.5 cm slump flow (Figure 9.3 (a)). The substitution of slag in BCSA improves not only the flowability but also delays the final setting time from 45 to 85 minutes for the 0-30% BOF slag replacement as shown in Figure 9.3 (b). The 30% slag addition in BCSA exhibited the highest delay in the setting time, and the further substitution (40 and 50%) did not further delay the setting time of the mixture. The improvement in the setting time of BCSA by substitution of the slag could help in diversifying its application [247, 260].

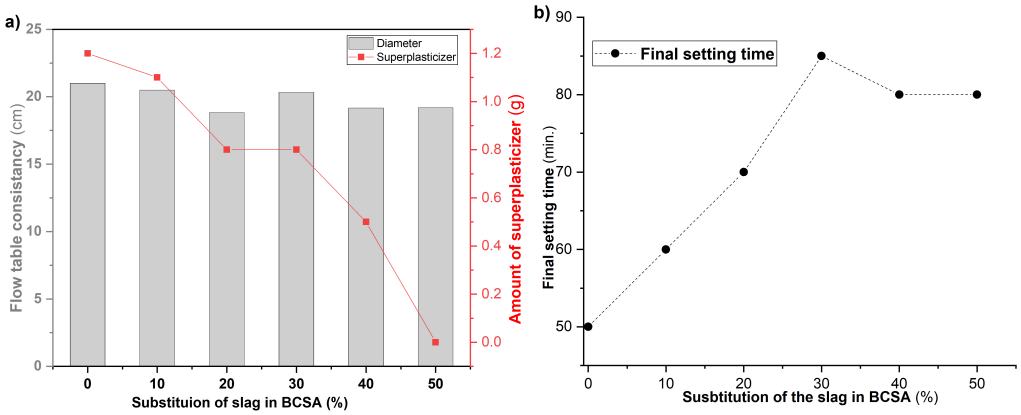

Figure 9.3: Workability of BCSA-slag mortar (a) consistency of flowability of fresh mortar determined by flow table (diameter) and amount of superplasticizer (b) final setting of fresh mortar determined by Vicat needle test.

BCSA-slag composite, a detailed thermal analysis was performed on the BCSA-slag paste with the same composition as used for mortar alongside the same water-to-binder (0.5) ratio. The 7-day heat of hydration is determined by isothermal calorimetry as shown in Figure 9.4 (a, b). The first main exothermic heat of hydration maxima appears around 3 h in BCSA as well as 0-50% substitution of the slag sample. Peak 1 is attributed to the precipitation of tricalcium sulfoaluminate hydrate ($C_6A\bar{S}_3H_{32}$, ettringite, AFt) due to a rapid reaction of ye'elimite ($C_4A_3\bar{S}$) with water in the presence of adequate amount of gypsum ($C\bar{S}H_2$) (9.1) [255]:

$$C_4A_3\bar{S} + C\bar{S}H_2 + 34\,H \longrightarrow C_6A\,\bar{S}_3\,H_{32} + 2\,AH_3 \tag{9.1}$$

As the amount of sulfate decreases in the solution, the peak 2 maxima appear around 6 h due to calcium monosulfoaluminate hydrate ($C_4A\bar{S}H_{12}$, AFm) precipitation upon depletion of gypsum (9.2) [246]:

$$C_4A_3\bar{S} + C\bar{S}H_2 + 18\,H \longrightarrow C_4A\bar{S}H_{12} + 2\,AH_3 \tag{9.2}$$

After the 14 h activity, BCSA cement, and the slag replacement clusters undergo a dormant period apparently, and no further exothermic hydration activity was observed.

The 10% slag substitution in BCSA decreases the formation of AF_t while promoting the formation of AFm phases compared to the BCSA sample due to the less gypsum available in the solution (Figure 9.4 (a)). The further increase from 10-50% slag substitution decreases the formation of AF_t as well as AF_m phases. The cumulative heat release exhibited a significant downward trend upon 20-50% slag substitution in BCSA from 200 to 130 J/g until 7 days (Figure 9.4 (b)).

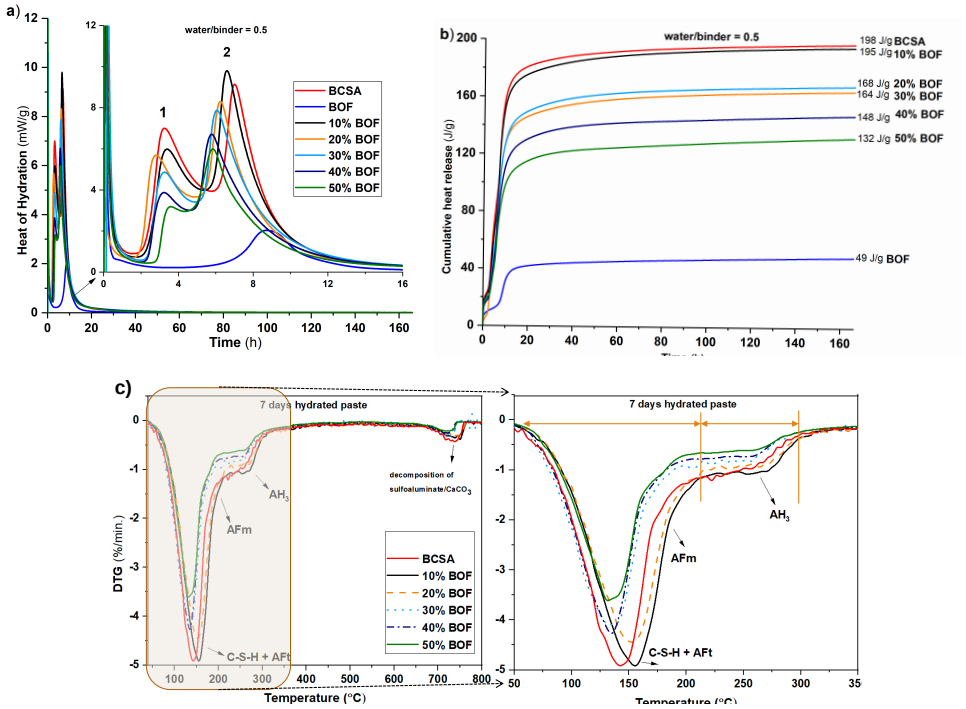

Figure 9.4: Thermal analysis BCSA-slag pastes sample with 0-50% BOF slag substitution in BCSA cement (a) heat of hydration (b) cumulative heat of hydration (c) DTG analysis of 7 days cured sample (in the inset, the zoomed version of important mass loss events).

The type of hydration products in 7-day-old BCSA-slag pastes is further confirmed by derivative thermogravimetry (DTG) as shown in Figure 9.4 (c) (see Figure E.1 for percentage mass loss). The overlapping peaks <215 °C can be attributed largely to the dehydration of ettringite (AF_t), monosulfoaluminate hydrate (AFm) alongside a small amount of C-S-H type phase. The mass loss event 220-300 °C is attributed to the decomposition of amorphous aluminum hydroxide (AH_3). The mass loss event around 700-800 °C occurs due to the decarbonation of calcium carbonate as well as the decomposition of sulfoaluminates [178, 249, 261]. The mass loss events confirmed that the 10-50% slag substitution in BCSA significantly decreases the amount of chemical-bound water leading to a negative effect on early hydration reaction.

It is clear from the thermal analysis that the 10-50% substitution of slag delays the setting time by inhibiting the early reactivity of BCSA (Figures 9.3 & 9.4). It is important

to mention here that the addition of slag does not delay the hydration reaction of BCSA but decreases the degree of hydration. Moreover, the early-stage (7 days) BCSA-slag composite reactivity is dominated by the BCSA reactivity, and the BOF slag contributes as a dilution effect [249]. This shows that it is necessary to investigate the long-term BCSA-slag cured sample to observe the possible synergy of chemical interaction.

9.4.2 *Mechanical performance and correlation with BCSA-slag hydration*

Mechanical performance of the mortar specimens tested at ages 1,3, 7, 28, 90, and 180 days has been shown in Figure 9.5 (also see Figure E.2 for percentage flexural and compressive strength performance with respect to REF sample respectively).

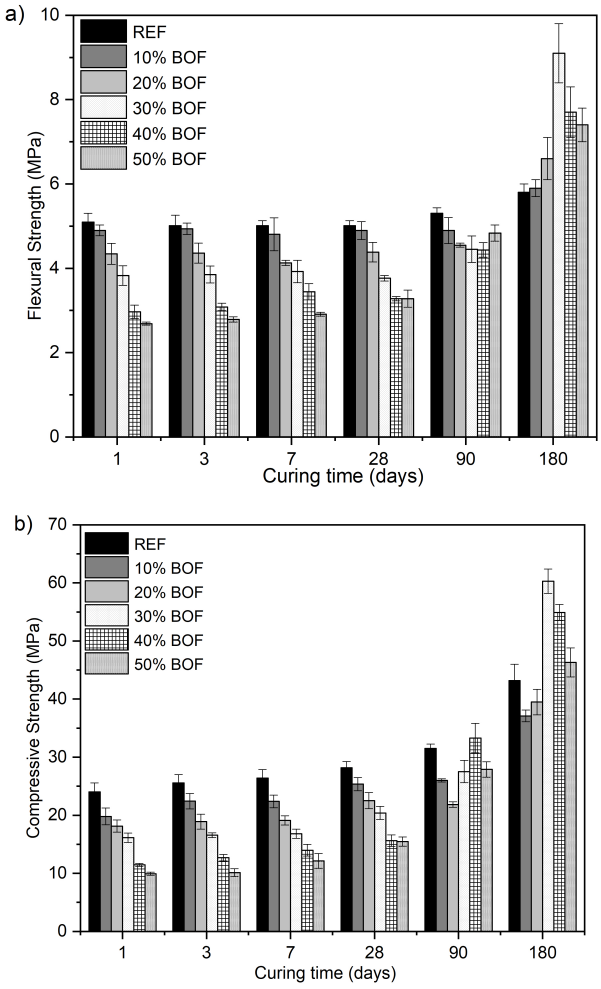

Figure 9.5: Mechanical performance of BSCA-slag mortar specimens containing 0-50% substitution of air granulated BOF slag (a) flexural and (b) compressive strength.

The BCSA replacement with BOF slag exhibited a decrease in flexural strength till 28 days. At 90 days, 20-50% BOF slag samples exhibited an improvement in flexural strength. Upon curing for 180 days, all BOF slag replacement samples attained higher

flexural strength than 100% BCSA (REF) cement. The 30% slag replacement in BCSA cement provides the best flexural resistance after 6 months of curing (Figure 9.5 (a)).

When 10% of BCSA cement was replaced by the BOF slag in 10% BOF, a slight decrease up to 11% in the compressive strength was observed till 28 days as compared to REF specimens (Figure 9.5 (b)). The decrease in the compressive strength becomes more pronounced 18% at 90 and 180 days of curing of the mortar sample. A clear decrease from 25 to 46% in the compressive strength of 20-50% BOF samples as compared to the BCSA specimen was observed at 28 days. At 90 days, the 30-50% BOF slag sample exhibited a clear increase in compression resistance, and the 40% BOF sample reached 33 MPa similar to the REF (32 MPa) sample. At 180 days, the compressive strength of 30-50% BOF samples reaches 60, 55, and 46 MPa, respectively, as compared to REF 43 MPa (Figure 9.5 (b)). The flexural strength of the 30% BOF sample reaches 9.1 MPa with the highest compressive strength of 60.3 MPa at 180 days Figure 9.5 (a, b).

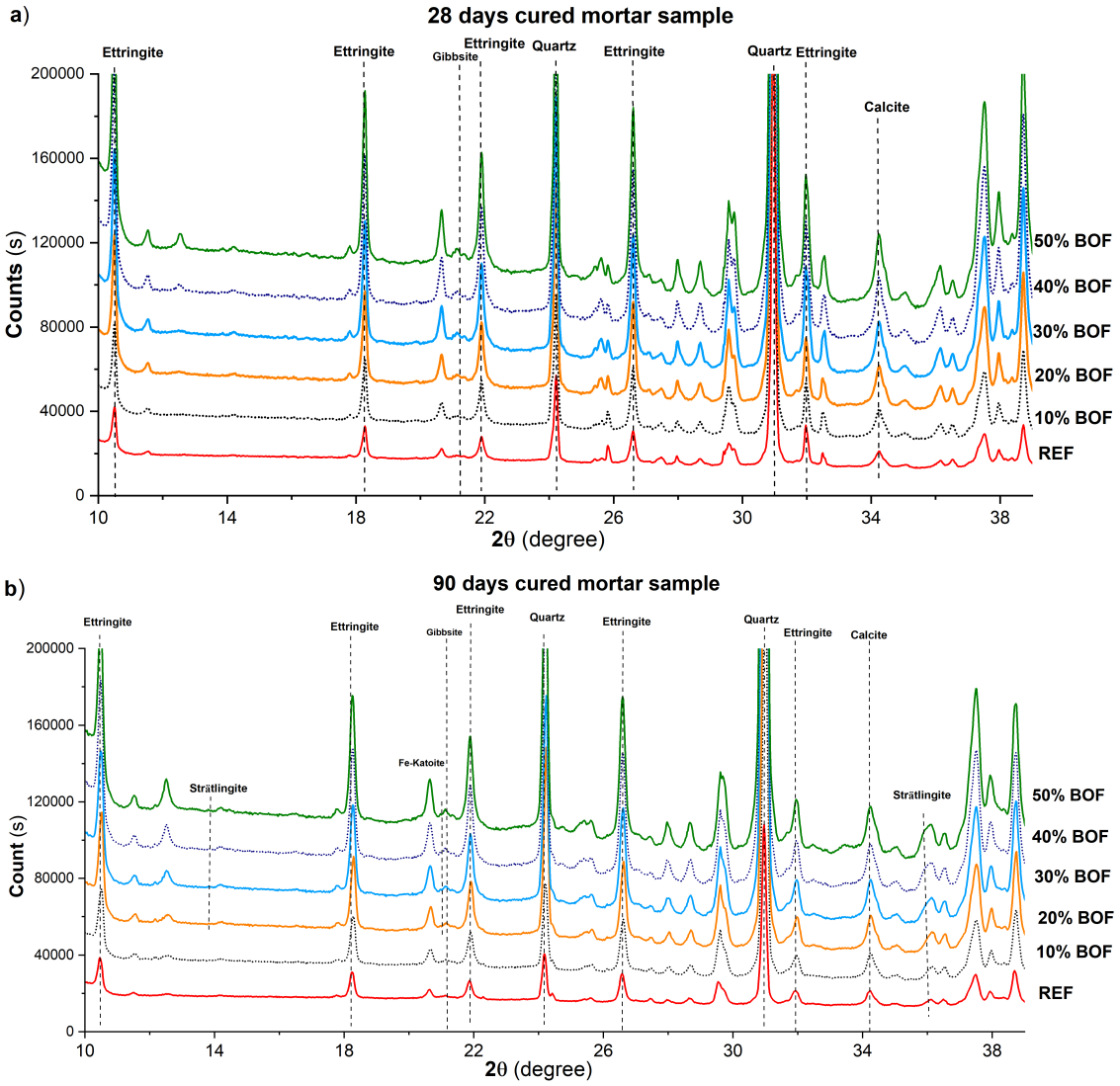

Figure 9.6: The labelled peak diffractogram of BCSA-slag mortar specimens containing 0-50% substitution of air granulated BOF slag (a) 28 days cured mortar sample (b) 90 days cured mortar sample.

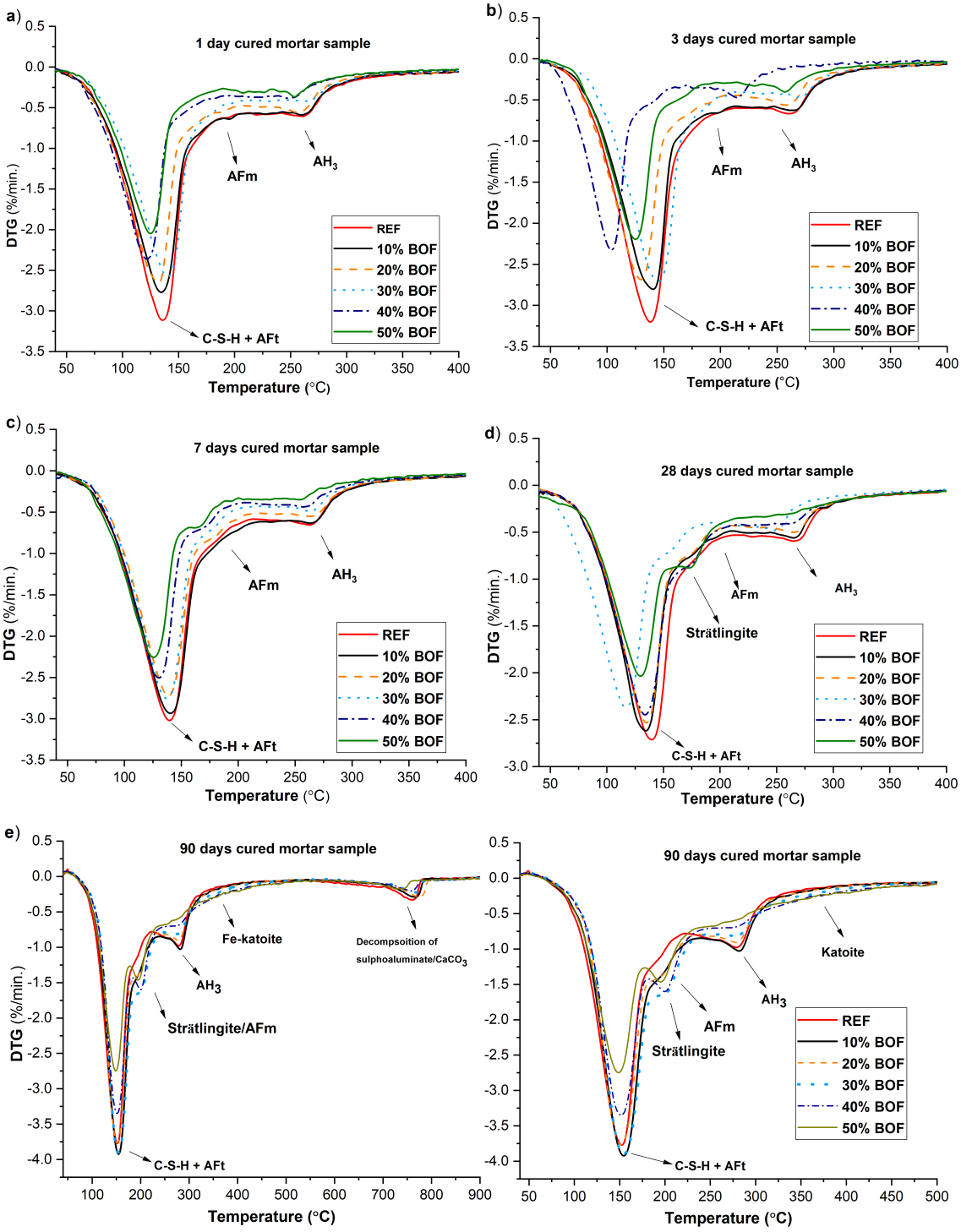

Figure 9.7: Derivative thermogravimetry (DTG) of BSCA-slag mortar specimens containing 0-50% substitution of air granulated BOF slag (a) 1 (b) 3 (c) 7 (d) 28 and (e) 90 days cured mortar samples.

To get insight into the mechanical performance, the hydration products BCSA-mortar specimens were analyzed by XRD as well as thermal gravimetric analysis. The diffraction pattern of the BSCA-slag specimens has been shown in Figure 9.6 (a, b). At 28 days, the

crystalline hydration products were dominated by ettringite, and calcite alongside the gibbsite. At 90 days, more crystalline hydration products such as strätlingite and Fe-katoite alongside the main hydration products of BCSA cement were observed. The labelled peak of strätlingite and Fe-katoite can also be assigned to the layered double hydroxide (LDH) like compounds containing CO_3^{2-}, OH^-, and Cl^- ions [262]. Moreover, the diffraction analysis was performed on the mortar sample that requires mechanical grinding and contains large amount of quartz peaks making smaller amount of hydration products difficult to detect. Therefore, the hydration products are further confirmed through DTG as shown in Figure 9.7 (also see Figure E.1 in appendix D for percentage mass loss). The 1, 3, and 7 days cured mortar samples exhibited the mass loss event around 60-220 °C corresponding to the thermal dehydration of the AFt, AFm as well as C-S-H partially. While the mass loss event 230-300 °C attributed to the dehydration of gibbsite (AH_3) (Figure 9.7). At 28 days, a new mass loss event centered 175 °C which corresponds to the dehydration of strätlingite (C_2ASH_8) as evident in the 40 and 50% BOF samples (Figure 9.7 (d)) [263].

Upon further curing till 90 days, a new mass loss event 300-420 °C associated with the dehydration of katoite (hydrogarnet) alongside strätlingite (C_2ASH_8) was observable in 20, 30, 40, and 50% BOF samples (Figure 9.7 (e)) [264]. The presence of katoite and strätlingite was not observed in REF, 10% BOF samples. The C_2S tends to form strätlingite under an alumina-rich environment (9.3) [249]:

$$C_2S + AH_3 + 5\,H \longrightarrow C_2ASH_8 \tag{9.3}$$

Moreover, the katoite hydrogarnet is the product of the brownmillerite reaction.

It is clear from the hydration product of BCSA-slag mortar clusters that the brownmillerite alongside C_2S also contributes toward reactivity in 30-50% BOF samples leading to improved compressive and flexural strength at 90 days (Figure 9.5). While these phases did not show significant reactivity in BCSA cement, 10 and 20% BOF samples till 90 days of curing. Among all these samples, the 30% slag replacement cluster is recommended for the best performance at a later age (28-180 days).

9.4.3 *Microstructure Analysis*

The SEM-BS (backscattered images) of 7 and 28-day cured BSCA-slag specimens have been presented in Figure 9.8. The rod-like crystals of AFt covered with colloidal and spherical AH_3 gel structures form a skeleton during the hydration of BCSA leading to the high strength of the BCSA sample (Figure 9.8 (a)). Upon 28 days of curing of REF mortar specimen, the hydration products such as AFt and amorphous intergrown colloidal AH_3 structure seem well distributed all over the mortar matrix, thereby providing high strength from an early age (1-28 days) hydration (Figure 9.8 (b)). The morphology of AH_3 precipitated particles depends on the gypsum ($C\bar{S}H_2$) concentration in the hydration media [265] .

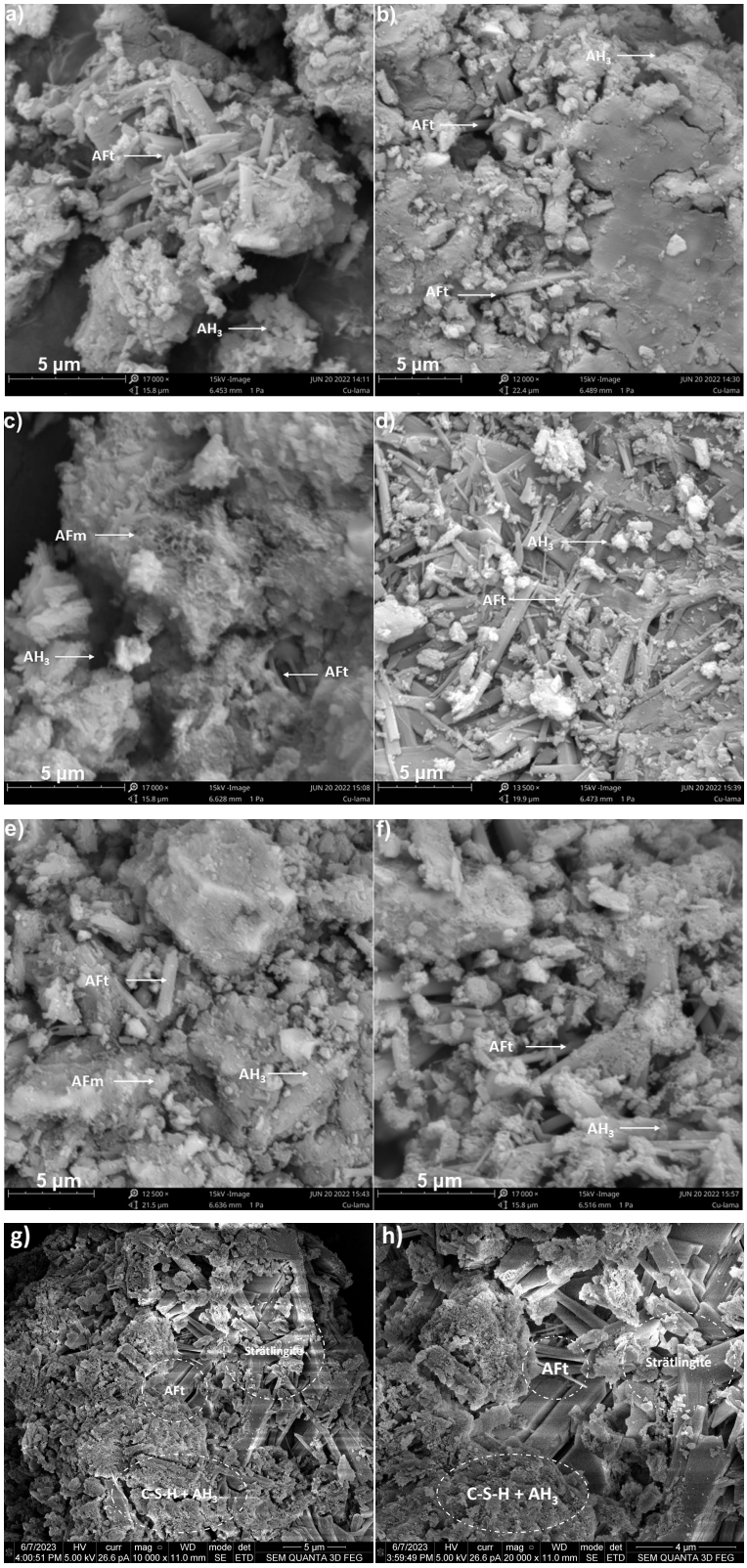

Figure 9.8: SEM analysis of BSCA-slag specimens (a) 7 days cured BCSA paste sample (b) 28 days cured REF sample (c) 7 days cured 10% BOF paste sample (d) 28 days cured 10% BOF mortar sample (e) 7 days cured 50% BOF paste sample (f) 28 days cured 50% BOF mortar sample (g, h) 90 days cured 50% BOF mortar sample

Upon 10% BOF slag replacement in BCSA, the irregular lamellar morphology AFm (less distinctive) intercalated with distinctive AFt observed with dominant colloidal AH_3 morphology (Figure 9.8 (c)). As the hydration progressed to 28 days, the 10% BOF mortar matrix contained a uniform distribution of AFt phases (Figure 9.8 (d)). A further 50% BOF slag in BCSA, a clear decrease in the AFt formation alongside a distinctive decrease in the formation of amorphous AH_3 formation (Figure 9.8 (e, f)). The decrease in the formation of AFt and amorphous AH_3 colloidal network reduces the binding between hydration products and the BCSA-slag matrix. Thereby, a decrease in mechanical performance slag substituted mortar is observed upon curing till 28 days (Figure 9.5).

It is worth noticing that the formation of amorphous phases such as gibbsite (AH_3) contributes significantly to the mechanical stability of BCSA-slag binder. The 90-day cured mortar sample of 40% BOF sample showed a laminar particle of strȧtlingite alongside katoite well intergrown with the AFt, C-S-H, and gibbsite phases (Figure 9.8 (g, h)) [191]. That is why, the 30-50% BOF replacement exhibited better mechanical performance at 90 days due to equilibrium gibbsite and CSH-C_2ASH_8 formation which enhances the binding capacity of BCSA-slag composite. So, the presence of an adequate amount of amorphous matrix is a prerequisite for the good mechanical resistance of BCSA-slag mortars.

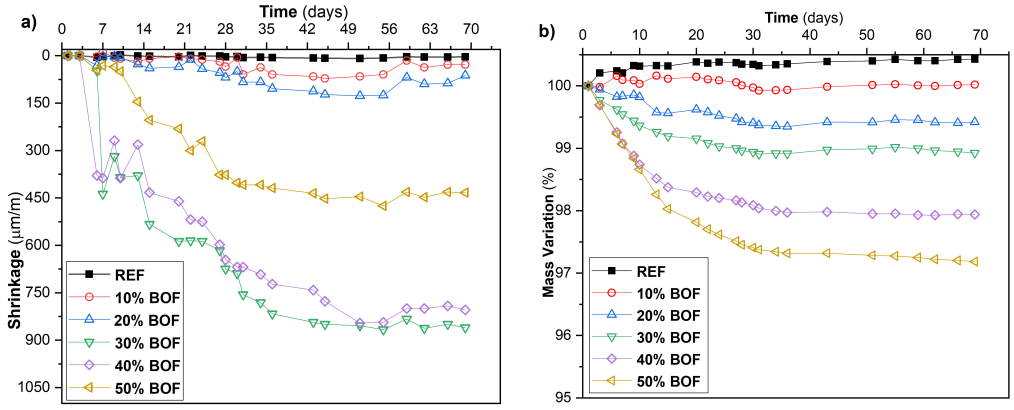

Figure 9.9: BSCA-slag mortar specimens containing 0-50% substitution of air granulated BOF slag (a) length variation (b) mass variation.

9.4.4 *Drying shrinkage and drying mass loss*

The drying shrinkage tests were carried out to confirm the volumetric stability of BCSA due to the addition of air granulated BOF slag over 72 days as shown in Figure 9.9 (a). The permissible limit for shrinkage on BCSA mortar should not exceed 750 µm at 28 days according to BCSA cement technical data sheet. In this regard, the highest length variation value found was 675 µm at 28 days which is below the technical requirement of the cement. The absence of shrinkage is one of the advantages of the BCSA compared to OPC [266]. The drying mass stability of the BCSA-slag mortar was measured as shown in Figure 9.9 (b). The slag replacement in BCSA cement consistently increases the mass loss till 28 days. As explained in Section 9.4.1, the addition of slag contributes to a dilution effect till 28 days. Afterwards, the dicalcium silicate and brownmillerite phases also contribute toward the hydration reaction leading to the stabilization of water loss from the BCSA-slag mortar specimens. A high drying mass loss of 3% in 50% BOF slag replacement is observed.

Considering the compressive strength and hydration product analysis, the water-to-solid ratio can be lowered to achieve good mechanical performance due to improved particle packing. Moreover, it shows lesser drying shrinkage than 30-40% slag replacement mixes. In this way, the 50% slag can be substituted in BCSA cement.

9.4.5 *Environmental Impact*

The leaching of BOF slag and BCSA cement (raw materials) as well as 28 days cured mortar sample has been presented in Table 9.3. The BCSA cement exhibited significantly higher Cr (2.3 ppm) leaching than the permissible limit (0.63 ppm).

The air granulated BOF slag also releases slightly higher Cr (0.64) than the permissible limit. On the other hand, V leaching of the slag is below the permissible limit of the Dutch soil quality decree [60]. Upon 28 days of curing, the REF mortar specimen Cr leaching reduced to 0.59 ppm which gradually decreased with every 10% BOF slag replacement (Table 9.3). In the case of V leaching, the slag replacement increased the leaching up to 1 ppm except for 50% BOF replacement. The variation of heavy metals leaching can be explained in terms of pH, mineral source, immobilization potential of hydration products, and kinetic equilibrium between varying oxides of chromate and vanadate.

Table 9.3: One batch leaching (NEN: 1245-7) analysis of raw material and 28 days cured mortar sample.

Sample	legal limits	BOF slag	BCSA cement	REF	10% BOF	20% BOF	30% BOF	40% BOF	50% BOF
pH		12.6	11.9	11.9	11.9	11.9	12.1	12.1	12.2
Elements									
Al (ppm)	-	7.5	282.1	242.2	123	145.1	245.3	215.1	142.5
Ba (ppm)	22	1.2	0.5	0.1	0.3	0.1	0.1	0.1	0.1
Cr (ppm)	0.63	0.64	2.3	0.6	0.48	0.43	0.39	0.31	0.29
Fe (ppm)	-	0.3	17.6	3.9	3.8	3.8	2.9	2.4	1.7
Si (ppm)	-	26.9	24.5	17.3	22.7	22.2	13.1	13.2	18
V (ppm)	1.8	0.4	0.1	0.0	0.7	0.9	1.2	1	0.4

*Sb, As, Cu, Co, Hg, Ni, Se, Cd, Pb, and Sn were below the detection limit

As explained above, the main hydration product of BCSA is AFt which tends to immobilize the CrO_4^{2-} in the molecular structure [267]. The replacement of BCSA with BOF slag decreases the Cr leaching partially due to the dilution effect of the slag as explained above. Moreover, the dominant chromate ion is CrO_4^{2-} at pH 11.9-12.6 which has very low solubility (K_{sp}= 5.1 × 10^{-6}). So, the Cr can also be immobilized partially by the formation of the low solubility complex. However, the BOF slag also contains a significant amount of leachable Cr (Table 9.3). It can be argued that the Cr leaching will be high at the curing age > 28 days upon hydration of slag phases. However, the hydration products such as katoite (hydrogarnet) that form at later stages can also host high quantities of Cr^{6+} alongside strätlingite, AFt, and AFm which would increase the

immobilization potential of hydration media [266, 267]. Regarding the air granulated BOF slag leaching, V^{5+} tends to occupy the Si-site in C_2S in BOF slag [159]. So, the dissolution of C_2S also increases the chances of V release in the leachate. $Ca_3(VO_4)_2$ ($logK_{sp}$ = -17.97) is the dominant precipitate at pH = 11.9-12.6 that is insoluble at room temperature [124]. The equilibrium formation of C-S-H phases with C_2S dissolution would permit the high Ca^{2+} concentration in the leachate which limits the solubility of $Ca_3(VO_4)_2$ [55]. Moreover, C-S-H can also actively uptake some parts of V_2O_5 on tetrahedral Si-sites. As explained above in Section 9.4.2, C_2S actively takes part in hydration reaction at curing age > 28 days in 30-50% BOF samples. So, the BCSA-composite provides a way to avoid leaching in the novel binder.

9.5 CONCLUSION AND SUMMARY

In this study, the standard mortar specimens with 0, 10, 20, 30, 40, and 50% air granulated BOF slag as for BCSA were investigated for the workability, mechanical performance, drying mass, and length variation as well as immobilization of heavy metals in relations with the degree of hydration and type of hydration products. The main hydration products are ettringite, monosulphoaluminate hydrate, and aluminum hydroxide with C-S-H phase partially for all the ages in BCSA-slag specimens (1, 3, 7, 28, 90, and 180 days). However, the 30-50% replacement with BOF also exhibited the presence of strätlingite and katoite alongside the major hydration products at 90 days due to dicalcium silicate and brownmillerite reactivity. At an early age (1- 28 days), the 10-50% slag acts as a dilution effect which decreases the degree of hydration of BCSA-slag mortar leading to a delay in final setting time on one hand. However, it causes a loss in mechanical performance at an early age. At 180 days, the 30-50% BOF replacement clusters showed better mechanical performance than 100% BCSA cement (5.8 MPa flexural and 43.2 MPa compressive strength). Among all the replacement clusters, the 30% BOF slag replacement cluster provides the highest flexural and compressive strength of 9.1 and 60.3 MPa, respectively. The better mechanical of 30-50% slag mortars can be attributed to the formation of equilibrium gibbsite and CSH-C_2ASH_8 semi-crystalline amorphous matrix together with katoite, ettringite, calcium monosulfoaluminate hydrate which enhances the binding capacity between BSCA-slag specimens. The drying shrinkage of all BCSA-slag specimens does not exceed the permissible limit of 750 μm/m at 28 days. Moreover, a high drying mass loss of 3% in 50% BOF slag replacement indicates that the water-to-solid ratio can be lowered to get good mechanical performance. In this way, the BOF substitution potential can be improved up to 50% as SCM. All BCSA-slag mortar specimens exhibited the Cr and V leaching below the permissible limit according to the Dutch soil quality decree.

OUTLOOK

This study provides a basis for the valorization of air granulated BOF slag in BCSA cement where a high replacement of 30-50% can be warranted. This study shows that air granulated slag provides a lot of stability and variability in setting time to belite calcium sulfoaluminate cement which could help diversify its application in concrete. The mechanical and chemical activation of the slag approaches can be employed successfully

to improve the mechanical performance of the new BCSA-slag binder. The air granulated BOF slag as an ideal match for the BCSA substitution was the main aim of this study.

COMMERCIAL INTEREST

In Europe, research has focused on the "Belite-Ye'elimite-Ferrite" (BYF) clinkers containing belite as major content alongside ferrite (C_4AF), and ye'elimite content below 35% [60]. Therefore, the manufacturers require much smaller amounts of the most expensive aliminium-rich raw materials than conventional calcium sulfoaluminate cement. The BOF slag is a good source of belite and ferrite phases which can be used alongside BYF clinker. BYF clinkers (e.g., "Aether" or "Ternocem") have the potential to replace Portland cement clinker as well as Portland-slag cement in many applications with a CO_2 saving of 20% per unit of clinker in the cement approximately. Using 30-50% BOF slag as a kiln feed or in mortar application would help mitigate the challenge of high raw material costs to the commercialisation of BYF technology. Moreover, it would also help to achieve the sustainability goals set by the Netherlands.

10 CONCLUSIONS AND RECOMMENDATIONS

10.1 SUMMARY OF CONCLUSIONS AND RECOMMENDATIONS

Environmental challenges, such as climate change and resource depletion have put a spotlight on the need for a low-carbon, resource-efficient, and closed-loop economy for sustainable development. The main challenge lies in the utilization of industrial residues to get zero-waste flow sheets [223, 224, 268]. The steel industry is no exception to these crises. In 2016, the total steel production was reported to be 1666.2 Mt of crude steel with a worldwide average growth of 5% approximately per annum for the last decade [269]. In 2018, the basic Oxygen steel-making process produced over 70% of the crude steel globally, generating 90-150 kg of basic Oxygen furnace (BOF) slag for every tonne of crude steel [270]. As explained in Chapter 1, a small portion is recycled while a high percentage is stockpiled occupying land resources as the same problem faced by TATA Steel Netherlands.

To achieve the sustainability goal set by the Netherlands, the recycling of BOF slag gained much attention in terms of supplementary cementitious materials (SCMs) in building materials. Because the first choice of SCMs such as granulated blast furnace slag (GBFS) and fly ashes (FA) sources of adequate quality are limited in Europe and unlikely to increase [229]. Applying BOF slag as cementitious material will not only diminish the landfilled/land occupation but also reduce the need for natural resources. To achieve the efficient recycling of BOF slag as a binder (high-end application), there is a need to improve BOF slag reactivity as well as leaching especially Cr and V from the slag. BOF is a complicated material mineralogically. So, the effort to improve the slag reactivity via air granulation (a relatively faster cooling than standard cooling) requires a systematic understanding of the cooling speed on chemical and mineralogical composition, speciation of heavy metals (Cr and V), leaching behaviour of BOF slag is a pre-requisite.

This project aims to develop an understanding of the effect of air granulation on the BOF slag, leaching, reactivity and leaching behaviour of slag. BOF slag reactivity as well as Cr and V speciation is further investigated by ex-situ mimicking of the C_2S slag phase which accounts for 35-45 wt. % of the whole slag. Moreover, the mineralogy reactivity and application of air granulated BOF slag as a binder in different types of cement (OPC and BCSA) is investigated to utilize slag as SCM. The work of this research can be divided primarily dealing with **1)** Air granulation, Cr and V doped C_2S, leaching mechanism **2)** Hydration of C_2S and air granulated BOF **3)** Application of BOF slag as a binder for high-end building products. The main conclusions and recommendations for further research are as follows:

10.2 AIR GRANULATION, CHROMIUM AND VANADIUM DOPED DICALCIUM SILICATE, LEACHING MECHANISM

The section (Chapters 3-5) deals with the effect of cooling speed on the mineralogy of BOF slag and leaching behaviour quantitatively. Moreover, the synthesis of C_2S via varying sol-gel routs and stabilization of high temperature (α', β, and γ) concerning crystallite size and essay-amorphous polymorphs quantitatively. Chapter 5 especially deals with the ex-situ mimicking of slag C_2S doped with Cr and V on Si-site under varying calcination conditions, the impact on the stability of C_2S polymorphs' as well as reactivity and leaching behaviour quantitively. The following main conclusion is drawn from this section.

10.2.1 *Mineralogy of air granulated BOF slag and its leaching behaviour*

BOF slag is a by-product of steelmaking that is produced in large quantities worldwide. It currently has few applications, because the presence of free lime often prevents its use as aggregate, while the low reactivity makes it undesirable as a cement replacement. Air granulation may help to improve the reactivity of converter slag and enable recycling as a cement replacement. For this reason, converter slag was air granulated and separated into different fractions (0.5-0.25 mm, 1-0.5 mm, 2-1 mm, 4-2 mm) to study the influence of size and therefore cooling speed on its mineralogy. The results showed that the main minerals in air granulated BOF slag are the same as in industrially cooled slag, but that additional perovskite is formed. All fractions contained large phenocrysts of C_2S and (Mg, Fe)O surrounded by a dense matrix containing the other minerals. The three largest fractions are very similar to each other in chemical composition and microstructure, while the smallest fraction (0.5-0.25 mm) contains a higher content of (Mg, Fe)O even though the starting composition was the same. The leaching of chromium and vanadium is significantly increased compared to standard cooled BOF slag.

10.2.2 *C_2S synthesis via different sol-gel methods*

The predominant phase in converter steel slags is dicalcium silicate, comprising 35-45% of the slag. In this study, the synthesis of dicalcium silicate (C_2S) via sol-gel (acid-catalyzed) process including the aqueous route, non-aqueous route, and the Pechini method is reported. The composition of C_2S (α', β, and γ) polymorphs, by-products, and amorphous content is established by employing QXRD (quantitative X-ray diffraction) studies. The attention has been focused on comprehending the number of crystalline polymorphs, amorphous as well as residual and complementary forming phases. Intermediate dried gels have been investigated via thermal analysis to monitor changes in the gel structures and precursors at low temperatures. The synthetic parameters including calcination time and temperature, Ca/Si molar ratio and mode of cooling have been optimized to get pure β-C_2S with low amorphous content. The dependency of $\beta \rightarrow \gamma$ C_2S polymorphic transformation on mean crystallite size (D_{cryst}) is studied. Overall, the Pechini method exhibits the most promising results for the purity and tuning of β-C_2S polymorph. Moreover, the non-aqueous and aqueous routes require calcining the dried gel at a temperature higher than 1200 °C due to the presence of CaO precursors as

$CaCO_3$. The theoretical calculations of amorphous content have revealed that the change in the stoichiometry from 2.0 to 1.7 Ca/Si ratio is not a viable solution to improve the C_2S product yield.

10.2.3 *Ex-situ mimicking of C_2S slag phase*

C_2S is known to incorporate potentially hazardous metals (Cr and V) in a belite-rich clinker or slag system. The effect of the electrovalence nature of V and Cr on C_2S polymorphs' (α', β, γ) stability under oxidizing and reducing (20% CO/80% CO_2) conditions, as well as their reactivity, are systematically investigated via analyzing quantitative XPS, QXRD, bonding system, and microstructure as well as phase composition. It is shown that C_2S can incorporate Cr (VI) and V(V) consequently leading to the stabilization of α', β-C_2S. Instead, Cr (II, III) and V < (V) tend not to substitute in C_2S. For reactive polymorphs (α', β-C2S) with stability due to Cr (VI) and V(V) incorporation, the early age (48-72 h) C_2S reactivity is controlled by the specific surface area. Moreover, one batch leaching test revealed that the V (V) leaching is inversely proportional to aqueous Ca^{2+} ion at pH > 12 while Cr leaching is sensitive to its oxidation state, and dissolution of C_2S. Even though C_2S can incorporate Cr (VI) and V (V) ions, the final leaching is governed by the immobilization potential of C-S-H gel, types of calcium chromate and vanadate complexes as well as pH of the medium.

10.3 HYDRATION RATE OF DICALCIUM SILICATE OF AND AIR GRANULATED BOF SLAG

The second section (Chapters 6-7) deals with the hydration rate of β-C_2S under varying anions (OH^-, SO_4^{2-}, and CO_3^{2-}) qualitatively and quantitively. The main idea is to understand the possible strategies to understand the chemical activation of larnite/belite in slag. Furthermore, the in-depth hydration of BOF slag is studied to understand its hydration products and their tendency to immobilize heavy metals. The following main conclusion is drawn from this section.

10.3.1 *Hydration rate of β-C_2S with various sodium salts*

The effect of fixed (0.8M) Na^+ balanced by either OH^-, SO_4^{2-}, and CO_3^{2-} anions on β-dicalcium silicate reactivity is investigated. The exothermic reaction of varying water-to-solid ratios and chemical activation is monitored. Subsequently, the hydration products are characterized via FTIR, TG/DTG, QXRD, and SEM analysis. The findings showed that the carbonate ions expedited the reactivity up to 55% at 1-7 days due to the simultaneous precipitation of calcium silicate hydrate (C-S-H) and calcite. At 7-28 days, the lack of transportable cations between the solid surface and solution impeded further hydration, as confirmed by in-situ pH and conductivity measurements. The sulphate ions accelerated the reactivity only upon calcium sulphate dissolution at high pH. The hydroxide ions decelerated the hydration due to the earlier precipitation of portlandite than C-S-H. Overall, the β-C_2S reaction with water exhibited the highest hydration degree (67%) after 28 days of hydration.

10.3.2 *Hydration of air granulated BOF slag*

This study is the continuation of Chapter 3. For the first time, the hydration behaviour of air granulated basic oxygen furnace slag has been investigated. The hydration of BOF slag has been analyzed via isothermal calorimetry, QXRD, and TG/DTG. The air granulated slag exhibited higher early-age (4 days) hydration than standard-cooled BOF slag. The hydration of the slag leads to the formation of hydration products such as C-S-H, hydrogarnet and hydrotalcite. Moreover, the slag degree of hydration (DOH) reaches up to 41% after 28 days of curing. The formation of slag hydration products is controlled by the dissolution of SiO_2 and Fe_2O_3 bearing phases such as larnite and brownmillerite phases as confirmed by SEM-EDX-based PARC analysis. The hydrated slag tends to immobilize heavy metals such as V and Cr into the hydration product phase confirmed by ICP analysis. The percentage immobilization of V and Cr increases with increasing DOH.

10.4 APPLICATION OF BOF SLAG AS A CEMENTITIOUS MATERIAL

This section (Chapters 8-9) deals with the application of air granulated BOF slag as a cement replacement in ordinary Portland cement and belite calcium sulfoaluminate cement (BCSA) qualitatively and quantitively. The granulation of the BOF slag exhibited good promise of hydration activity than standard cooled slag as explained in Chapter 7. It is worth mentioning here that air granulated slag used for the cement replacement is the new batch of production. The following main conclusion is drawn from this section.

10.4.1 *Air granulated BOF slag replacement in OPC*

This study demonstrates the air granulated BOF slag potential as a cementitious material by substituting in OPC at replacement levels of 5, 20, 35 and 50%. The mechanical performance of the cement-slag composites is correlated with the hydration behaviour through thermal, mineralogical, and microstructural analysis. The findings show that the granulation improved the grindability, reactivity, and compressive strength till 28 days. The 5% slag replacement exhibited the synergy of mechanical performance while 35% performs better than quartz (an inert filler). The performance decline upon 20-50% replacements is attributed to the absence of brownmillerite reactivity of the slag. Overall, the granulation did not improve the cement-slag composite performance significantly till 90 days.

10.4.2 *Air granulated BOF slag substitution in BCSA*

Basic oxygen furnace (BOF) slag impacts negatively the OPC performance when replacement levels exceed 5%. This necessitates the exploration of alternative applications for BOF slag. At the same time, a high-volume slag utilization is desired to benefit slag recycling as supplementary cementitious materials. Therefore, this study aims to optimize the air granulated BOF slag substitution potential in belite calcium sulfoaluminate cement (BCSA) by investigating the hydration products in standard mortar. Especially, the reactivity of BCSA-slag binder is correlated with workability, and

mechanical performance alongside volumetric stability by thermal, mineralogical, and microstructure analysis. As a result, the 10-30% slag replacement delays the final setting time by inhibiting the ettringite formation leading to a decrease in mechanical performance till 28 days. At later ages (28-180), the 30-50% substitution exhibited the synergy of mechanical performance, which is attributed to the reactivity of slag with BCSA by forming hydrogarnet, C-S-H, and strätlingite like hydration products. Moreover, all BCSA-slag mortars exhibited heavy metals' leaching and drying shrinkage below the permissible limit indicating the fitness of the material for building products. The BCSA-slag binder promises a high replacement volume for efficient air granulated BOF slag recycling.

10.5 RECOMMENDATIONS FOR FUTURE WORK

This thesis systematically investigated the mineralogical, hydration and leaching behaviour of air granulated BOF slag. The investigation of air granulated BOF slag encompasses the fundamental understanding of the speciation of Cr and V in C_2S, activation strategies, leaching mechanisms and application as a cementitious material. This knowledge was successfully exploited to design upgrade recycling of air granulated BOF slag in BCSA. However, the following research aspects require further research.

- The mineralogy and hydration of air granulated BOF slag have been investigated and explained. The acquired results showed that the formation of slag hydration products such as C-S-H, Fe-hydrogarnets, hydrotalcite etc. is controlled by the dissolution of C_2S and Fe-bearing phases of slag. This information can be used to make a kinetic dissolution model of the slag. By using this model, the slag-admixture chemical reaction can be better exploited.

- The application of air granulated slag as a binder in the standard mortar was investigated in detail. The 5% slag substitution shows the synergy of mechanical performance and hydration activity. The decrease in mechanical performance has been attributed to the absence of slag phase reactivity under a cementitious environment. These results do not align with the first batch of granulation. So, the variability of the batch performance needs to be controlled for reproducible results. Moreover, the addition of a third component such as ye'elimite-based cement or granulated blast furnace slag would be the next step for the study.

- The role of C_2S in relation to potentially toxic elements (Cr and V) was investigated and explained. The oxidation state-based incorporation of Cr and V in C_2S under well-defined calcination conditions, the impact on the stability of C_2S polymorphs' as well as reactivity and leaching behaviour were studied to understand the complex nature of slag C_2S. The acquired result can further be complemented by XANES analysis of air granulated BOF slag. This would provide the true oxidation of Cr and V in the slag which can further validate the findings and confirm the leaching mechanism. Moreover, the reactivity of brownmillerite is also dependent on the Fe/Al ratio. Therefore, a synthesis of brownmillerite with varying Al/Fe ratios will help to understand the slag reactivity.

- For application purposes, the air granulated BOF slag was substituted in BCSA from 0-50%. A detailed hydration and mechanical performance study was conducted. The result showed that the addition of slag not only delays the setting time but fulfills the low drying shrinkage demand of BCSA. The 30-50% air granulated BOF slag can be substituted in BCSA cement. This study makes a good case for the application of BOF slag as SCM in BCSA. The BOF slag is a good source of belite and ferrite phases which can be used alongside "Belite-Ye'elimite-Ferrite" (BYF) clinker. BYF clinkers (e.g., "Aether" or "Ternocem") have the potential to replace Portland cement clinker as well as Portland-slag cement in many applications with a CO_2 saving of 20% per unit of clinker in the cement approximately. Using 30-50% BOF slag as a kiln feed or in mortar application would help mitigate the challenge of high raw material costs to commercialisation of BYF technology. Moreover, it would also help to achieve the sustainability goals set by the Netherlands. Further studies on the durability aspects of BCSA-slag novel binders can help with the valorization of the slag.

APPENDIX: THE MINERALOGY OF AIR GRANULATED BASIC OXYGEN FURNACE SLAG

A

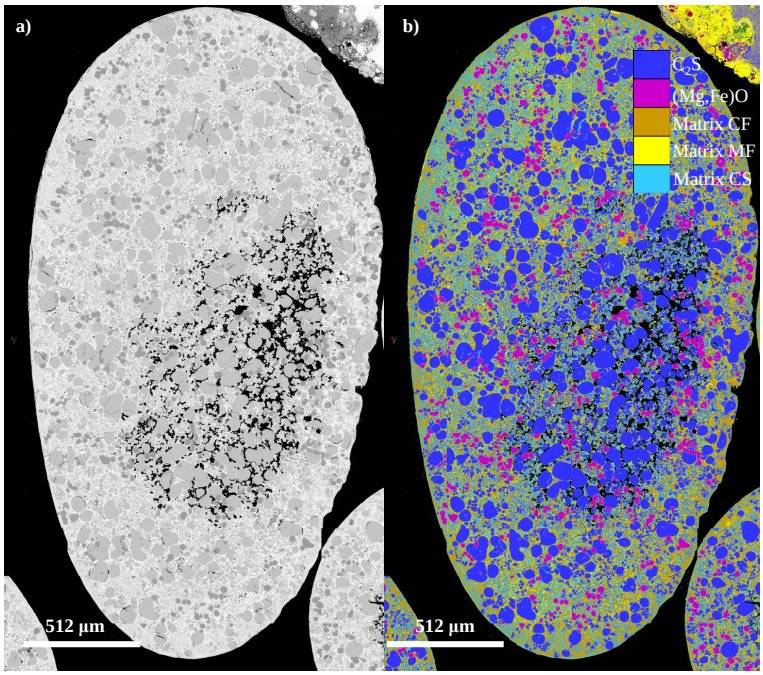

Figure A.1: Air granulated BOF slag 2-1 mm a) SEM greyscale image b) Phase map.

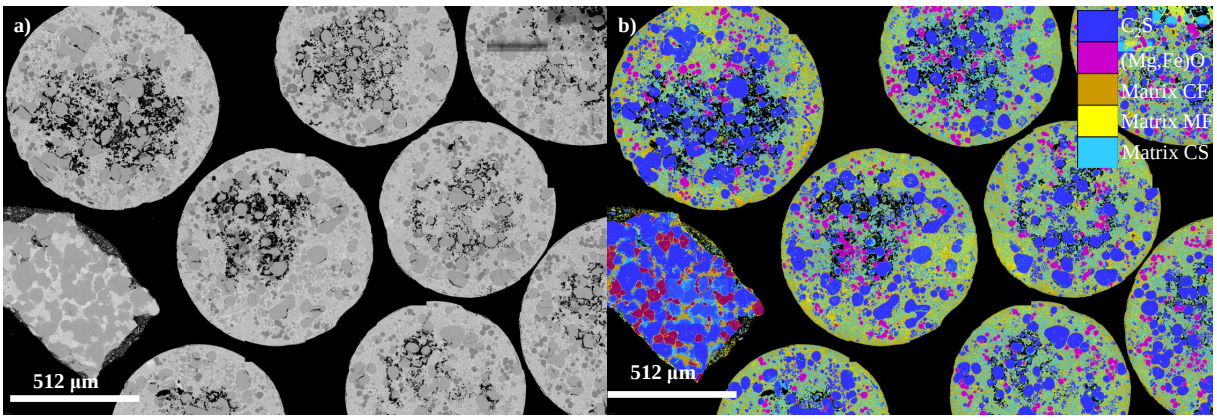

Figure A.2: Air granulated BOF slag 1-0.5 mm, lower right corner shows grain of industrially cooled BOF slag a) SEM greyscale image b) Phase map.

Table A.1: Mineralogical composition of BOF slag. P-primary slag phase, A-Alteration product, N-natural contamination, M–milling contamination, I-industrial contamination. Stdev. = Standard deviation as calculated by TOPAS

Phase	Type	>4 mm	Stdev.	2-4 mm	Stdev.	1-2 mm	Stdev.	0.5-1mm	Stdev.	0.5-0.25 mm	Stdev.	<0.25 mm	Stdev.
Larnite	P	22.9	0.5	21	0.5	18.9	0.5	13.9	0.5	6.2	0.5	2.7	0.3
α'-C_2S	P	16.5	1	20.9	0.9	21.4	0.9	26.4	1	19	1.2		
Mg-Wüstite	P	17.1	1.5	14.8	1.1	15	0.9	14.8	0.8	10.2	0.3	5.9	0.2
Srebrodolskite	P	23.9	0.4	24.1	0.3	21.4	0.3	20.8	0.3	12.6	0.4	10.3	0.3
Perovskite	P	6.6	0.3	7.6	0.2	10	0.2	12.5	0.2	8.4	0.2	1.7	0.1
Magnetite	P	1.9	0.2	2.5	0.1	2	0.1	2.8	0.1	6.6	0.2	10.3	0.2
Pseudobrookite	P			0.3	0.1	0.3	0.1	0.3	0.1	0.1	0.1	0.5	0.1
Lime	P	0.1	0.1	0.1	0.1			0.1	0.1				
Protoenstatite	P	1.2	0.2	1.2	0.1	0.7	0.2						
Naquite	P	0.9	0.1	0.7	0.1	0.5	0.1	0.6	0.1	0.3	0.1		
Hematite	I									2.1	0.1	1.9	0.1
Titanite	P									0.5	0.1		
Rutile	P			0.4	0.1	0.4	0.1	0.5	0.1			0.2	0.1
Quartz	N	0.1	0.04							8.9	0.1	13.3	0.1
Vaterite	A	1	0.2	1.1	0.2	0.8	0.2	1	0.2	0.7	0.2		
Calcite	A							0.3	0.1	4	0.1	17.9	0.2
Lepidocrocite	A									2.8	0.9		
Corundum	M	3.3	0.2	2.9	0.2	1.7	0.2	3	0.2	5.6	0.2	0.8	0.2
Graphite	I	0.9	0.1	0.3	0.1	0.2	0.05						
Moissanite 2H	I											0.3	0.1
Albite	N											1.1	0.3
Clinoenstatite	I											2.1	0.3
Amorphous		3.5	2.2	2	1.7	6.8	1.5	3	1.7	12.1	1.8	31	0.9

B

APPENDIX: VANADIUM AND CHROMIUM SUBSTITUTION IN DICALCIUM SILICATE UNDER OXIDIZING AND REDUCING CONDITIONS

Table B.1: ICSD data code and chemical formulas of crystal structures.

Mineral Phases	**Chemical formula**	**Crystal system/Notation**	**ICSD**
Dicalcium silicate	Ca_2SiO_4	Orthorhombic/α´	81097
Dicalcium silicate	Ca_2SiO_4	Monoclinic/β	81096
Dicalcium silicate	Ca_2SiO_4	Orthorhombic/γ	81095
Wollastonite	$CaSiO_3$	Triclinic, 1-A	23567
Wollastonite	$CaSiO_3$	Monoclinic, 2-M	201538
Pseudowollastonite	$CaSiO_3$	Triclinic, 4-A	26553
Lime	CaO	Cubic	60199
Calcium aluminum oxide	$Ca_2Al_2O_5$	Orthorhombic	89708
Grossular	$Ca_3Al_2(SiO_4)_3$	Cubic	31082
Cristobalite	SiO_2	Cubic	44269
Quartz low	SiO_2	Trigonal	41446
Calcium chromosilicate	$Ca_5(Cr_{1.824}Si_{1.176}O_{12})$	Orthorhombic	71958
Calcium chromium phyllo-decaoxotetrasilicate	$CaCr(Si_4O_{10})$	Tetragonal	30872
Calcium divanadium oxide	CaV_2O_4	Orthorhombic	1008146
Vanadium oxide	V_5O_9	Triclinic	1008536
Hypo-vanadate	CaV_4O_9	Tetragonal	2106845
Chromium oxide	Cr_2O_3	Tetragonal	202836

Table B.2: Quantitative XPS analysis of Cr and V doped C_2S (elemental analysis (atomic %)).

Sample	Ca 2p	Si 2p	O 1s	C 1s	Cr $2p_{3/2}$	V $2p_{3/2}$	N 1s
Cr5-O	13.9	7.6	45.4	32.8	0.4	0.0	0.0
Cr10-O	14.5	7.5	48.5	29.1	0.5	0.0	0.0
Cr15-O	13.7	8.1	43.0	34.5	0.8	0.0	0.0
Cr6R	16.3	8.1	47.7	27.6	0.4	0.0	0.0
Cr10R	14.9	8.3	45.2	30.8	0.7	0.0	0.0
Cr15R	13.5	7.9	49.2	24.0	0.8	0.0	4.7
V5-O	12.9	10.4	43.4	32.5	0.0	0.8	0.0
V10-O	15.0	10.6	43.6	29.6	0.0	1.2	0.0
V15-O	14.2	10.5	42.9	31.2	0.0	1.2	0.0
V6R	14.9	9.2	45.3	30.0	0.0	0.6	0.0
V10R	15.9	9.1	44.6	29.6	0.0	0.9	0.0
V15R	16.3	8.8	45.2	28.5	0.0	1.2	0.0

Table B.3: The $\delta_{Ca2p\text{-}Si2p}$ binding energy values of the sample calculated from Ca 2p and Si 2p value (XPS spectroscopy).

Sample	Ca 2p (eV)	Si 2p (eV)	$\delta_{Ca2p\text{-}Si\ 2p}$
Cr5-O	346.9	101.1	245.8
Cr10-O	347.0	101.2	245.8
Cr15-O	346.9	101.1	245.8
Cr5R	347.0	101.3	245.7
Cr10R	346.9	101.1	245.8
Cr15R	346.8	101.1	245.8
V5-O	346.8	101.0	245.8
V10-O	346.9	101.1	245.8
V15-O	346.9	101.1	245.8
V5R	347.0	101.2	245.8
V10R	347.1	101.6	245.5
V15R	346.9	101.2	245.6

Table B.4: QXRD of the Cr doped C_2S synthesized via the sol-gel process under oxidizing for leached residues.

Temperature [°C]	**1200**	**1200**	**1200**	**1200**	**1200**	**1200**
Calcination time [h]	8	8	8	8	8	8
Sample (wt. %)	Cr5-O	Cr5-O leached	Cr10-O	Cr10-O leached	Cr15-O	Cr15-O leached
α′-C_2S	5.3 ± 0.2	3.6 ± 0.3	23.1 ± 0.3	17.0 ± 0.4	43.3 ± 0.6	26.3 ± 0.7
β-C_2S	87.8 ± 0.3	73.9 ± 0.5	46.9 ± 0.4	37.6 ± 0.6	24.5 ± 0.6	16.6 ± 0.6
Lime	1.2 ± 0.06	0.00	0.7 ± 0.08	0.0	0.6 ± 0.1	0.00
Quartz	0.6 ± 0.09	0.7 ± 0.2	0.4 ± 0.04	0.3 ± 0.09	0.5 ± 0.07	0.4 ± 0.07
Cristobalite	0.5 ± 0.08	1.0 ± 0.1	0.3 ± 0.1	0.3 ± 0.08	0.3 ± 0.08	0.1 ± 0.1
$CaCr_{1.824}Si_{1.176}O_{12}$					2.3 ± 0.4	2.3 ± 0.6
Calcite	0.7 ± 0.1	1.7 ± 0.2	0.8 ± 0.1	1.6 ± 0.2	1.5 ± 0.2	2.1 ± 0.2
$CaCrSi_4O_{10}$			0.7 ± 0.2	0.6 ± 0.3	0.2 ± 0.4	0.1 ± 0.7
Cr_2O_3	0.3 ± 0.06	0.1 ± 0.06	0.7 ± 0.1	0.4 ± 0.1	1.3 ± 0.2	0.8 ± 0.2
Portlandite		1.0 ± 0.2		1.6 ± 0.1		0.8 ±0.2
Grossular	0.1 ± 0.09	0.05 ± 0.09				
XRD amorphous	3.5 ± 1.5	18.1 ± 2.1	26.4 ± 1.2	40.6 ± 2.3	25.6 ± 2.1	50.6 ± 2.3

Table B.5: Leaching of elements from Cr and V doped dicalcium silciate

Sample	**Ca**	**Si**	**Cr**	**Sample**	**Ca**	**Si**	**V**
	(mg/kg)	**(mg/kg)**	**(mg/kg)**		**(mg/kg)**	**(mg/kg)**	**(mg/kg)**
Cr5-O	11520.6	2.8	561.9	V5-O	10579.1	2.05	0.51
Cr10-O	10943.3	1.69	592	V10-O	8662.6	2.74	8.40
Cr15-O	10986.1	1.3	603.6	V15-O	10263.9	2.3	4.26
Cr2R	2228.7	2.9	1.7	V2R	1797.1	0.76	0.01
Cr4R	1397.4	0.3	1.8	V6R	147.4	0.39	0.05
Cr6R	197.9	0.5	1.9	V8R	5574.5	0.65	0.02
Cr8R	227.5	0.5	2.3	V10R	2913.4	0.36	0.01
Cr10R	8104	2.7	1.9	V15R	8647.2	1.34	0.02
Cr15R	8601.6	0.4	3.5				

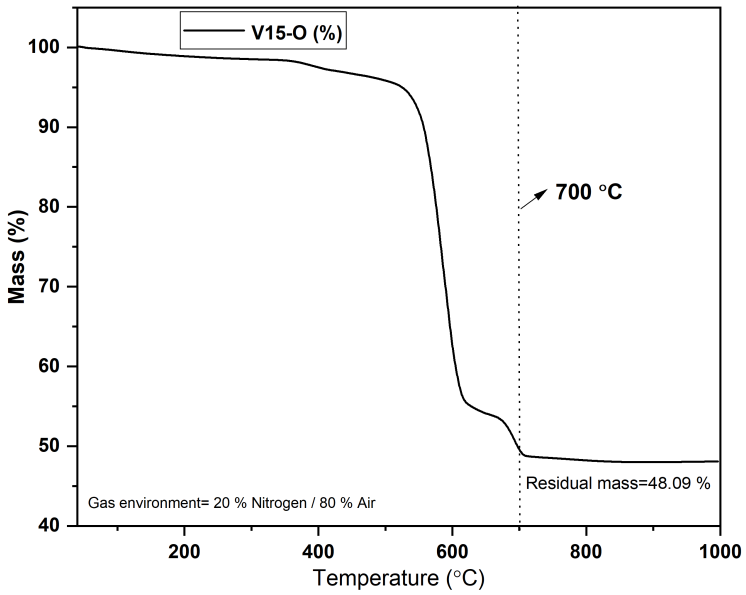

Figure B.1: Thermal gravimetric analysis of V15-O.

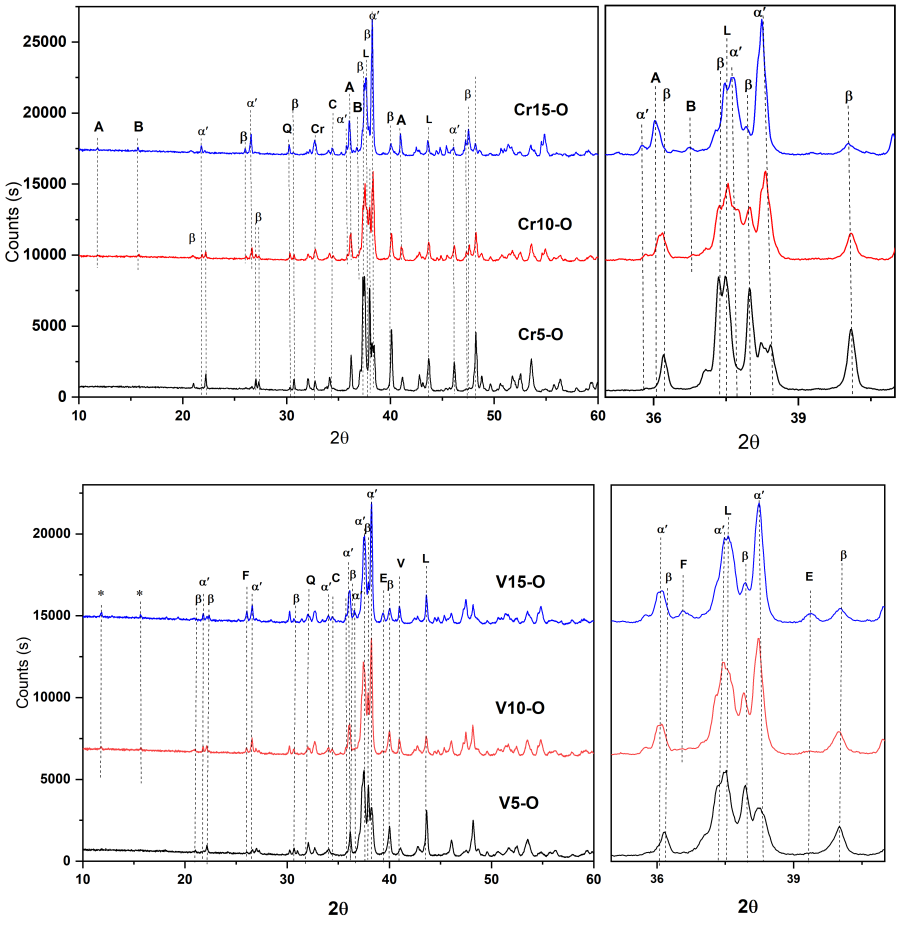

Figure B.2: XRD of (a) Cr doped C_2S (b) V doped C_2S under oxidizing conditions.

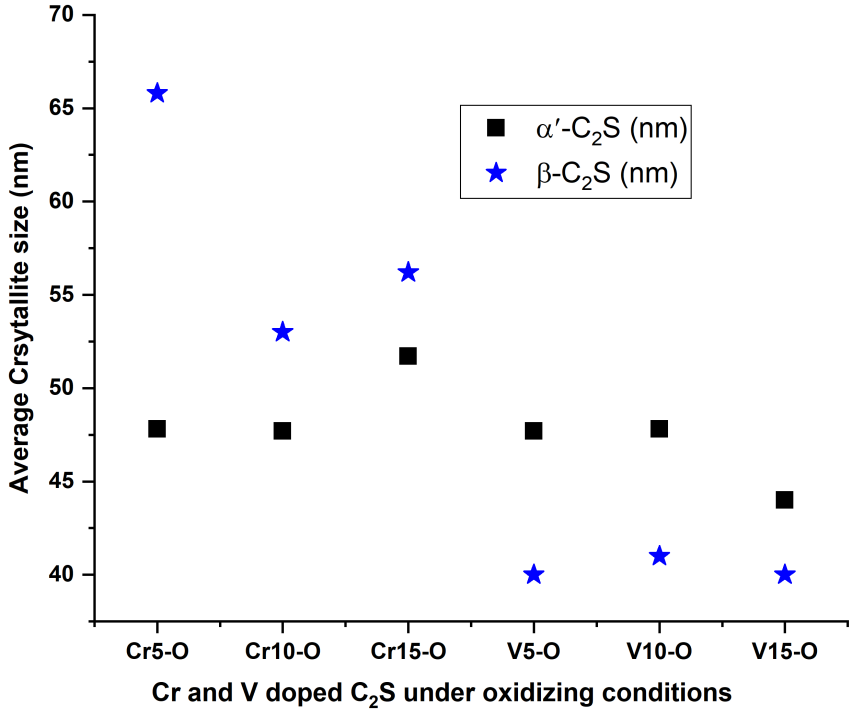

Figure B.3: Average crystallite size of α'/β-C_2S in Cr and V doped CβS under oxidizing condition.

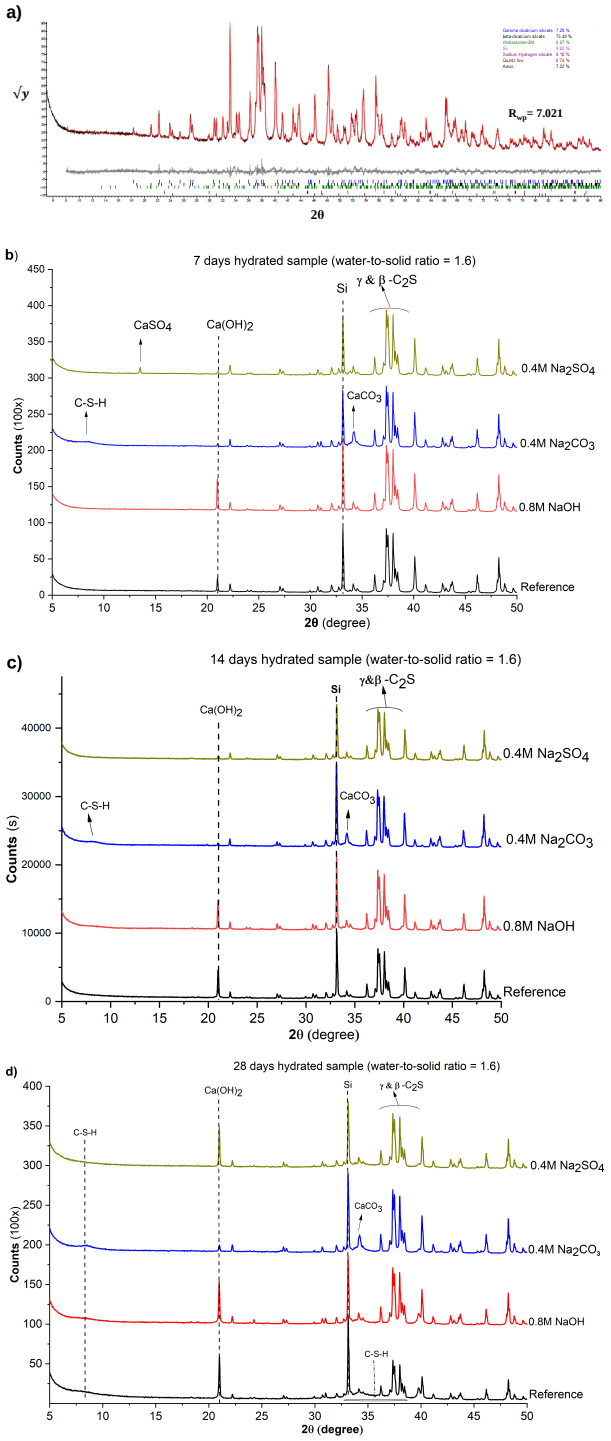

Figure B.4: X-ray diffractogram with labelled peaks a) synthesized C_2S b) 7 c) 14 and d) 28 days hydrated samples.

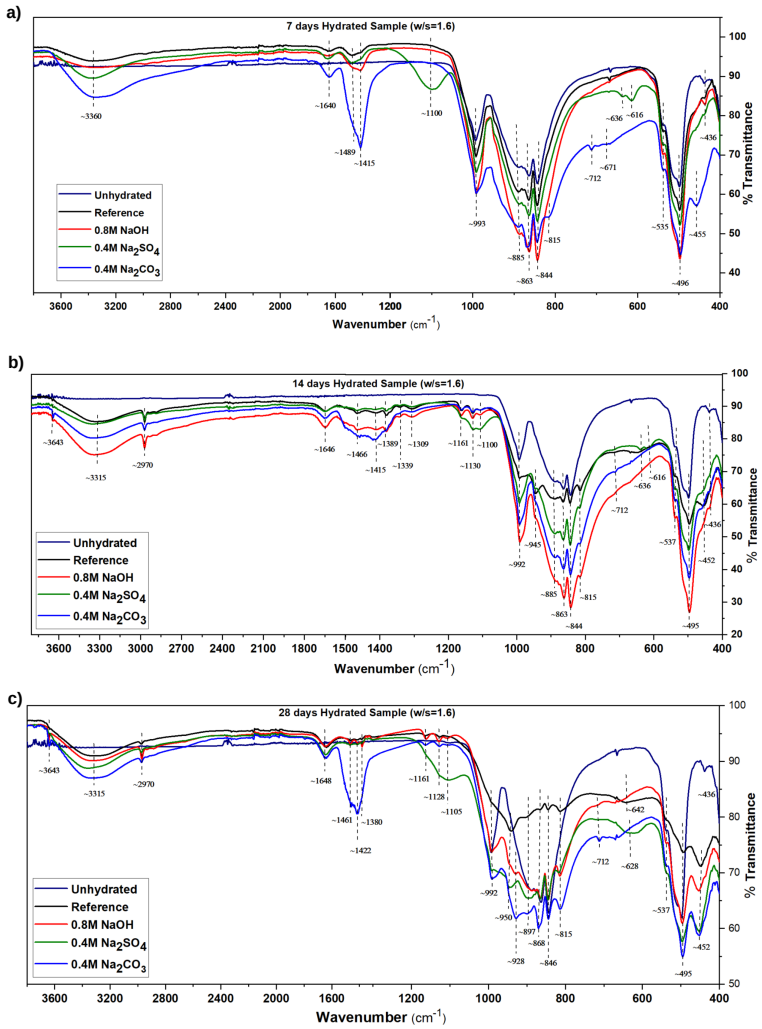

Figure B.5: FTIR fingerprint region with labelled peaks a)7 b)14 and c)28 days hydrated samples.

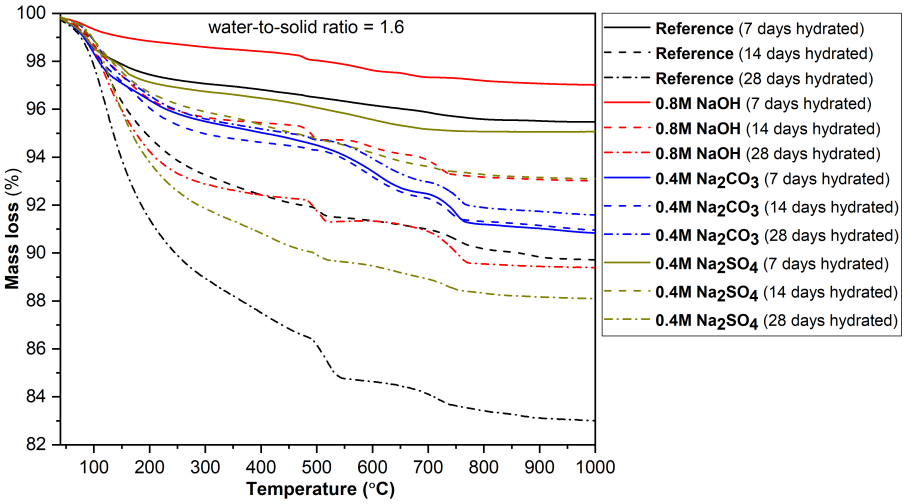

Figure B.6: Mass loss events of chemically activated C_2S.

C

APPENDIX: REACTIVITY OF AIR GRANULATED BASIC OXYGEN FURNACE SLAG

Table C.1: QXRD of the hydrated 2-1 mm and 4-2 mm fractions of air granulated BOF slag with error values.

Slag Fractions		**2-1 mm**	**2-1 mm**	**2-1 mm**	**2-1 mm**	**4-2 mm**	**4-2 mm**	**4-2 mm**	**4-2 mm**
Hydration Period (days)		0	7	14	28	0	7	14	28
Mineral phases	Chemical Formula	(wt. %)	(wt. %)	(wt. %)	(wt. %)	(wt. %)	(wt. %)	(wt.%)	(wt. %)
α´-C_2S	α´-Ca_2SiO_4	22 ± 0.9	19.7 ± 0.9	19.0 ± 0.7	11.2 ± 0.9	21.9 ± 0.9	16.7 ± 0.8	15.2 ± 0.8	11.7 ± 0.9
β-C_2S (Larnite)	β-Ca_2SiO_4	19.4 ± 0.5	18.0 ± 0.7	18.0 ± 0.5	13.3 ± 0.6	22 ± 0.5	21.0 ± 0.6	16.9 ± 0.6	13.7± 0.6
Brownmillerite	$Ca_4Fe_2Al_2O_{10}$	22 ± 0.3	14.0 ± 0.6	11.5 ± 0.4	9.7 ± 0.5	25.2 ± 0.3	13.4 ± 0.4	11.4 ± 0.5	10.8 ± 0.6
(Fe, Mg)-Wuestite	(Fe,Mg)O	15.4 ± 0.9	11.3 ± 0.6	10.6 ± 0.4	8.2 ± 0.4	15.5 ± 0.2	13.7 ± 0.5	9.3 ± 0.4	8.3 ± 0.6
Perovskite	$Ca(Ti,Fe)O_3$	10.3 ± 0.2	8.5 ± 0.4	5.1 ± 0.3	3.0 ± 0.2	7.9 ± 0.2	8.0 ± 0.4	6.7 ±0.4	5.9 ± 0.6
Magnetite +others	Fe_3O_4	4.0 ± 0.1	3.4 ± 0.3	3.4 ± 0.3	3.2 ± 0.3	5.4 ± 0.1	4.0 ± 0.3	3.9 ± 0.3	4.0 ± 0.3
Portlandite	$Ca(OH)_2$		1.1 ± 0.1	1.3 ± 0.1	2.7± 0.1		1.1 ± 0.1	1.6 ± 0.5	2.7 ± 0.1
Hydroandradite + Katoite	$Ca_3Fe_2(SiO_4)_{3-x}(OH)_{4x}$ + $Ca_3Fe_2(OH)_{12}$		4.2 ± 0.4	5.7 ± 0.3	5.9 ± 0.5		2.9 ± 0.6	5.1 ± 0.6	5.1 ± 0.6
Calcite	$CaCO_3$		0.2 ± 0.1	0.2 ± 0.1	0.8 ± 0.2		0.6 ± 0.3	0.2 ± 0.1	0.7 ± 0.3
Sjoegrenite /pyroaurite	$Mg_6Fe_2(CO_3)(OH)_{16}$		0.9 ± 0.2	0.4 ± 0.2	0.4 ± 0.2		0.9 ± 0.2	0.6 ± 0.5	0.4 ± 0.3
Amorphous		7.0 ± 1.5	18.1 ± 1.8	23.3 ±1.3	40.4 ± 1.3	2.1 ± 1.8	16.2 ± 1.7	26.5± 1.6	33.7± 1.7

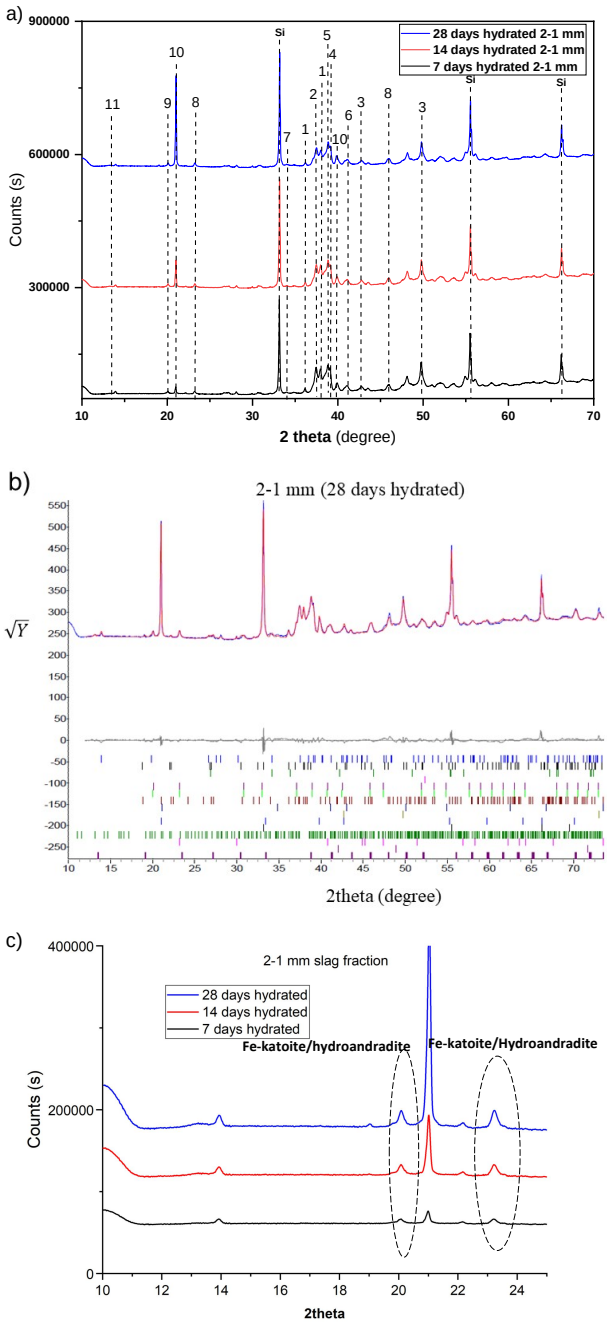

Figure C.1: XRD of 7, 14- and -28 days hydrated air granulated BOF slag 2-1 mm fractions (a) The peaks of hydrated slag assigned such as Si= Si (internal standard) 10 wt. %, 1= α'-C_2S, 2= β-C_2S (Larnite), 3= (Fe, Mg)-Wüstite, 4= Srebrodolskite, 5= Perovskite, 6= Magnetite, 7= Calcite, 8= Hydroandradite, 9= Fe-katoite, 10= Portlandite, 11= Pyroaurite/sjoegrenite . (b) The Rietveld fit of 28 days 1-2 mm hydrated air granulated BOF slag fraction (Rwp= 2.068). (c) XRD of 7, 14- and -28 days hydrated air granulated BOF slag 2-1 mm fractions with labeled hydroandradite and Fe-katoite peaks.

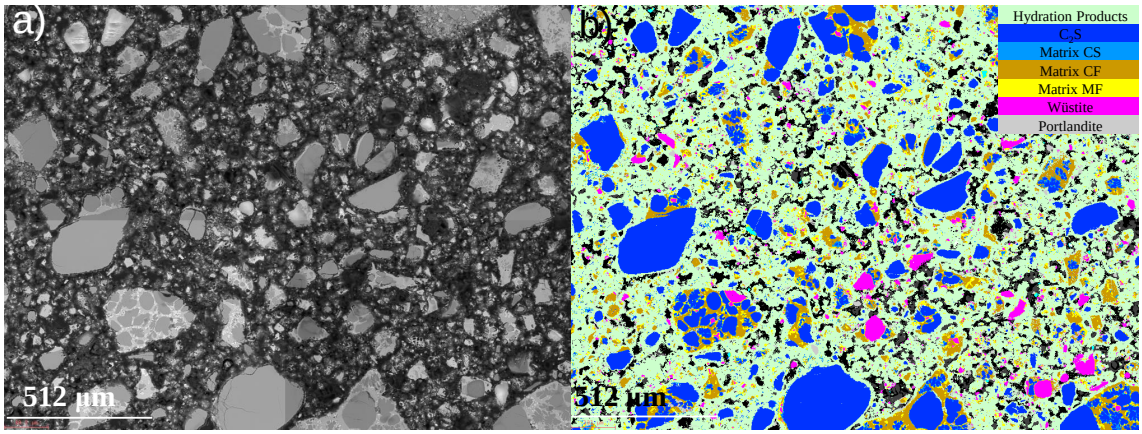

Figure C.2: Microstructure analysis of 4-2 mm fraction of air granulated BOF slag after 28 days of hydration at 512 µm a) backscattered image (BSI) b) PARC phase map.

D

APPENDIX: AIR GRANULATED BOF SLAG APPLICATION AS A BINDER

Table D.1: One batch leaching (NEN: 1245-7) analysis of 28 days cured mortar sample with varying replacement of quartz powder.

Sample		**REF**	**QP50**	**QP35**	**QP15**	**QP05**
	pH	12.9	12.1	12.4	12.4	12.8
Element*	Legal limit	mg/kg	mg/kg	mg/kg	mg/kg	mg/kg
Si		0.17	0.1	0.9	0.2	0.5
Al		0.14	1.1	0.2	0.3	0.08
Ba	22	10.3	13.6	14.2	12.0	12.8
Cr	0.63	0.2	0.5	0.4	0.4	0.1
Mo	1	0.05	0.09	0.07	0.06	0.02
V	1.8	0.002	0.00	0.001	0	0.001
Zn	4.5	0.004	0.04	0.03	0.02	0.03

*Cu, Co, Hg, Ni, Se, Cd, Pb and Sn were below the detection limit.

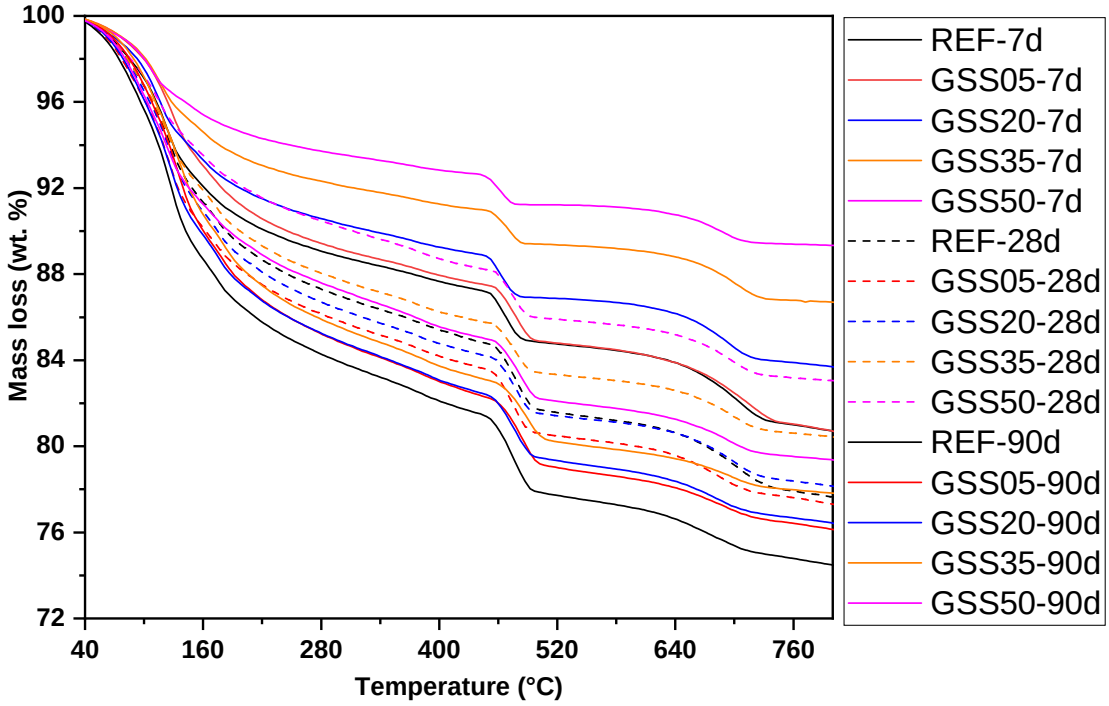

Figure D.1: TGA analysis of 7, 28 and 90 days cured GSS (5, 20, 35, 50) paste samples.

E

APPENDIX: UTILIZATION OF AIR GRANULATED BASIC OXYGEN FURNACE SLAG AS A BINDER IN BELITE CALCIUM SULFOALUMINATE CEMENT

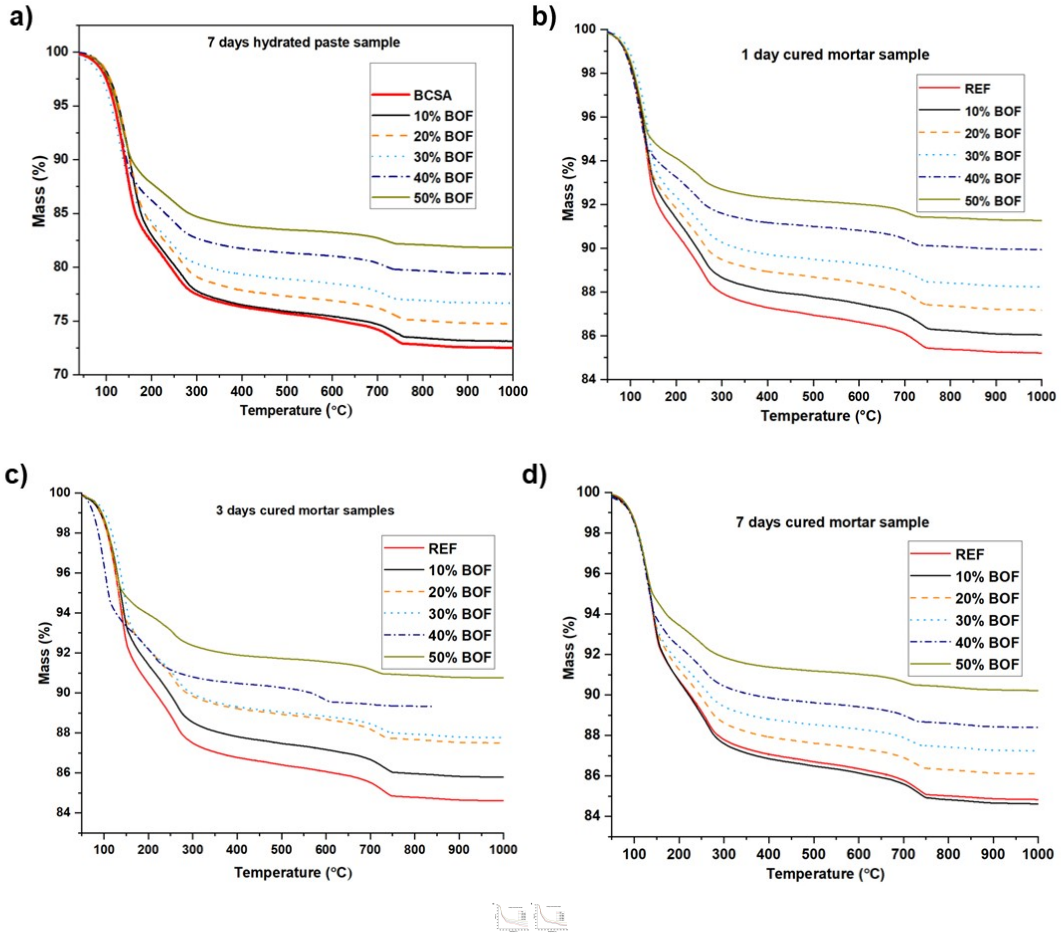

Figure E.1: Thermogravimetric analysis of BSCA-slag paste and mortar specimens, respectively, containing 0-50 % substitution of air granulated BOF slag (a) 7 (b) 1 (c) 3 (d) 7 (e) 28 (f) 90 days cured mortar samples.

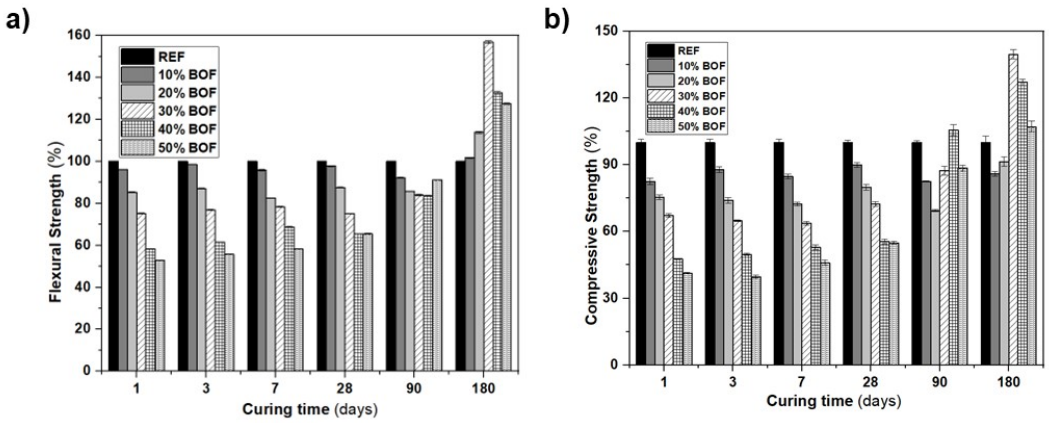

Figure E.2: Percentage mechanical performance of BSCA-slag mortar specimens containing 0-50% substitution of air granulated BOF slag (a) flexural strength (b) compressive strength.

LIST OF PUBLICATIONS

Peer-Reviewed Journal Publications

1. K. Schollbach, **M. Jawad Ahmed**, S.R. van der Laan, The mineralogy of air granulated converter slag, Int. J. Ceram. Eng. Sci. 3 (2021) 21–36.

2. **M. Jawad Ahmed**, K. Schollbach, S.R. van der Laan, M. Florea, H.J.H. Brouwers, A quantitative analysis of dicalcium silicate synthesized via different sol-gel methods, Mater. Des. 213 (2022) 110329.

3. **M. Jawad Ahmed**, R. Cuijpers, K. Schollbach, S.R. van der Laan, M. Van Wijngaarden-Kroft, T. Verhoeven, H.J.H. Brouwers, V and Cr substitution in dicalcium silicate under oxidizing and reducing conditions – Synthesis, reactivity, and leaching behavior studies, J. Hazard. Mater. 442 (2023) 130032.

4. **M. Jawad Ahmed**, K. Lambrechts, X. Ling, K. Schollbach, H.J.H. Brouwers, Effect of hydroxide, carbonate, and sulphate anions on the β-dicalcium silicate hydration rate, Cem. Concr. Res. 173 (2023) 107302.

5. **M. Jawad Ahmed**, W. Franco Santos, H.J.H. Brouwers, Air granulated basic Oxygen furnace (BOF) slag application as a binder: Effect on strength, volumetric stability, hydration study, and environmental risk, Constr. Build. Mater. 367 (2023) 130342.

6. **M. Jawad Ahmed**, S. Durand, M. Antoun, F. Gauvin, S. Amziane, H.J.H. Brouwers, Utilization of air granulated basic oxygen furnace slag as a binder in belite calcium sulfoaluminate cement: a sustainable alternative, (submitted).

7. **M. Jawad Ahmed**, K. Schollbach, S.R. van der Laan, H.J.H. Brouwers, Reactivity of air granulated basic oxygen furnace slag and its immobilization of heavy metals, (submitted).

8. **M. Jawad Ahmed**, K. Schollbach, S.R. van der Laan, H.J.H. Brouwers, 25 months alkali-activated air granulated basic Oxygen furnace slag and its immobilization of heavy metals, (in preparation).

Conference Proceedings

1. **M. Jawad Ahmed**, K. Schollbach, M.V.A. Florea, S. van der Laan, and H.J.H. Brouwers "Characterization of air granulated converter slag and its leaching", The 2nd International Conference of Sustainable Building Materials, 12-15 August 2019, Eindhoven, the Netherlands.

2. **M. Jawad Ahmed**, R. Cuijpers, K. Schollbach, S. van der Laan, and H.J.H. Brouwers "V and Cr substitution in dicalcium silicate under oxidizing and reducing conditions-synthesis, reactivity and leaching behaviour studies", 4th International Conference

on the Chemistry of Construction Materials - ICCCM 2022 Karlsruhe, September 26 - 28, Germany.

BIBLIOGRAPHY

[1] S. Eloneva, S. Teir, J. Salminen, C.-J. Fogelholm, and R. Zevenhoven. "Steel Converter Slag as a Raw Material for Precipitation of Pure Calcium Carbonate." In: *Industrial & Engineering Chemistry Research* 47.18 (2008), pp. 7104–7111. DOI: 10.1021/ie8004034.

[2] T. S. Naidu, C. M. Sheridan, and L. D. van Dyk. "Basic oxygen furnace slag: Review of current and potential uses." In: *Minerals Engineering* 149 (2020). DOI: 10.1016/J.MINENG.2020.106234.

[3] A. Öhman, E. Karakaya, and F. Urban. "Enabling the transition to a fossil-free steel sector: The conditions for technology transfer for hydrogen-based steelmaking in Europe." In: *Energy Research & Social Science* 84 (2022), p. 102384. DOI: 10.1016/J.ERSS.2021.102384.

[4] G. Lopez, J. Farfan, and C. Breyer. "Trends in the global steel industry: Evolutionary projections and defossilisation pathways through power-to-steel." In: *Journal of Cleaner Production* 375 (2022), p. 134182. DOI: 10.1016/J.JCLEPRO.2022.134182.

[5] H. Jalkanen and L. Holappa. "Converter Steelmaking." In: *Treatise on Process Metallurgy* 3 (2014), pp. 223–270. DOI: 10.1016/B978-0-08-096988-6.00014-6.

[6] S. Z. Carvalho, F. Vernilli, B. Almeida, M. Demarco, and S. N. Silva. "The recycling effect of BOF slag in the portland cement properties." In: *Resources, Conservation and Recycling* 127 (2017), pp. 216–220. DOI: 10.1016/J.RESCONREC.2017.08.021.

[7] A. M. Kaja, K. Schollbach, S. Melzer, S. R. van der Laan, H. J. Brouwers, and Q. Yu. "Hydration of potassium citrate-activated BOF slag." In: *Cement and Concrete Research* 140 (2021), p. 106291. DOI: 10.1016/j.cemconres.2020.106291.

[8] *Statistics 2018*. URL: https://www.euroslag.com/research-library-downloads/downloads/ (visited on 07/27/2023).

[9] *Slag recycling - recovery*. URL: https://www.recovery-worldwide.com/en/artikel/slag-recycling{_}3528047.html (visited on 06/21/2022).

[10] Y. Jiang, T. C. Ling, C. Shi, and S. Y. Pan. "Characteristics of steel slags and their use in cement and concrete—A review." In: *Resources, Conservation and Recycling* 136 (2018), pp. 187–197. ISSN: 0921-3449. DOI: 10.1016/J.RESCONREC.2018.04.023.

[11] L. De Windt, P. Chaurand, and J. Rose. "Kinetics of steel slag leaching: Batch tests and modeling." In: *Waste Management* 31.2 (2011), pp. 225–235. DOI: 10.1016/J.WASMAN.2010.05.018.

[12] A. Said, H. P. Mattila, M. Järvinen, and R. Zevenhoven. "Production of precipitated calcium carbonate (PCC) from steelmaking slag for fixation of CO2." In: *Applied Energy* 112 (2013), pp. 765–771. DOI: 10.1016/J.APENERGY.2012.12.042.

[13] A Todorut and T Heput. "Broadening of Raw Materials in the Steel Industry , by Recycling and Recovery Wastes." In: 6.11 (2012), pp. 1035–1041.

[14] "Recycling and environmental issues of metallurgical slags and salt fluxes." In: ().

[15] L. Kriskova, Y. Pontikes, F. Zhang, Ö. Cizer, P. T. Jones, K. Van Balen, and B. Blanpain. "Influence of mechanical and chemical activation on the hydraulic properties of gamma dicalcium silicate." In: *Cement and Concrete Research* (2014). DOI: 10.1016/j.cemconres.2013.10.004.

[16] P. E. Tsakiridis, G. D. Papadimitriou, S. Tsivilis, and C. Koroneos. "Utilization of steel slag for Portland cement clinker production." In: *Journal of Hazardous Materials* 152.2 (2008), pp. 805–811. DOI: 10.1016/J.JHAZMAT.2007.07.093.

[17] Y. Li and W. B. Dai. "Modifying hot slag and converting it into value-added materials: A review." In: *Journal of Cleaner Production* 175 (2018), pp. 176–189. DOI: 10.1016/J.JCLEPRO.2017.11.171.

[18] S. Eloneva. "Reduction of CO2 emissions by mineral carbonation: steelmaking slags and raw material with a pure calcium carbonate end product." PhD thesis. 2010. ISBN: 9789526034560.

[19] M. Bodor, R. M. Santos, G. Cristea, M. Salman, Ö. Cizer, R. I. Iacobescu, Y. W. Chiang, K. Van Balen, M. Vlad, and T. Van Gerven. "Laboratory investigation of carbonated BOF slag used as partial replacement of natural aggregate in cement mortars." In: *Cement and Concrete Composites* 65 (2016), pp. 55–66. DOI: 10.1016/J.CEMCONCOMP.2015.10.002.

[20] M. Bodor, R. M. Santos, G. Cristea, M. Salman, Cizer, R. I. Iacobescu, Y. W. Chiang, K. Van Balen, M. Vlad, and T. Van Gerven. "Utilization of carbonated BOF slag as partial replacement of aggregate in cement mortars." In: *5th International Conference on Accelerated Carbonation for Environmental and Material Engineering 2015* (2015), pp. 11–20.

[21] T. Mashifana and N. Sithole. "Utilization of fly ash: basic oxygen furnace slag as a raw material in geopolymerization." In: *IOP Conference Series: Materials Science and Engineering* 652.1 (2019), p. 012060. DOI: 10.1088/1757-899X/652/1/012060.

[22] N. T. Sithole, F. Okonta, and F. Ntuli. "Development of Lightweight Construction Blocks by Alkaline Activation of Bof Slag." In: *Journal of Solid Waste Technology and Management* 45.2 (2019), pp. 175–185. ISSN: 10881697. DOI: 10.5276/JSWTM/2019.175.

[23] N. T. Sithole, F. Okonta, and F. Ntuli. "Mechanical Properties and Structure of Fly Ash Modified Basic Oxygen Furnace Slag Based Geopolymer Masonry Blocks." In: *Journal of Solid Waste Technology and Management* 46.3 (2020), pp. 372–383. DOI: 10.5276/JSWTM/2020.372.

[24] S. Sandybay, C. S. Shon, A. Tukaziban, D. Syzdykov, I. Orynbassarov, D. Zhang, and J. R. Kim. "Blended Basic Oxygen Furnace (BOF) Slag with Ground Granulated Blast Furnace Slag (GGBFS) as a Pozzolanic Material." In: *Materials Science Forum* 1053 (2022), pp. 331–337. DOI: 10.4028/P-Q7N2CU.

[25] F. Saly, L. Guo, R. Ma, C. Gu, and W. Sun. "Properties of Steel Slag and Stainless Steel Slag as Cement Replacement Materials: A Comparative Study." In: *Journal of Wuhan University of Technology-Mater. Sci. Ed. 2018 33:6* 33.6 (2018), pp. 1444–1451. DOI: 10.1007/S11595-018-1989-3.

[26] C. van Hoek, J. Small, and S. van der Laan. "Large-Area Phase Mapping Using PhAse Recognition and Characterization (PARC) Software." In: *Microscopy Today* 24.5 (2016), pp. 12–21. DOI: 10.1017/S1551929516000572.

[27] T. Gao, T. Dai, L. Shen, and L. Jiang. "Benefits of using steel slag in cement clinker production for environmental conservation and economic revenue generation." In: *Journal of Cleaner Production* 282 (2021), p. 124538. DOI: 10.1016/J.JCLEPRO.2020.124538.

[28] T. H. Lu, Y. L. Chen, P. H. Shih, and J. E. Chang. "Use of basic oxygen furnace slag fines in the production of cementitious mortars and the effects on mortar expansion." In: *Construction and Building Materials* 167 (2018), pp. 768–774. DOI: 10.1016/j.conbuildmat.2018.02.102.

[29] H. Yi, G. Xu, H. Cheng, J. Wang, Y. Wan, and H. Chen. "An Overview of Utilization of Steel Slag." In: *Procedia Environmental Sciences* 16 (2012), pp. 791–801. DOI: 10.1016/j.proenv.2012.10.108.

[30] J. Guo, Y. Bao, and M. Wang. *Steel slag in China: Treatment, recycling, and management*. 2018. DOI: 10.1016/j.wasman.2018.04.045.

[31] T. Takahashi and K. Yabuta. "New applications for iron and steelmaking slag." In: *NKK Technical Review* (2002).

[32] G. Liu, K. Schollbach, S. van der Laan, P. Tang, M. V. Florea, and H. J. Brouwers. "Recycling and utilization of high volume converter steel slag into CO2 activated mortars – The role of slag particle size." In: *Resources, Conservation and Recycling* 160 (2020), p. 104883. DOI: 10.1016/J.RESCONREC.2020.104883.

[33] J. Wan, H. Du, F. Gao, S. Wang, M. Gao, B. Liu, and Y. Zhang. "Direct Leaching of Vanadium from Vanadium-bearing Steel Slag Using NaOH Solutions: A Case Study." In: *Mineral Processing and Extractive Metallurgy Review* 00.00 (2020), pp. 1–11. DOI: 10.1080/08827508.2020.1762182.

[34] A. van Zomeren, S. R. van der Laan, H. B. Kobesen, W. J. Huijgen, and R. N. Comans. "Changes in mineralogical and leaching properties of converter steel slag resulting from accelerated carbonation at low CO 2 pressure." In: *Waste Management* 31.11 (2011), pp. 2236–2244. ISSN: 0956053X. DOI: 10.1016/j.wasman.2011.05.022.

[35] J. Waligora, D. Bulteel, P. Degrugilliers, D. Damidot, J. L. Potdevin, and M. Measson. "Chemical and mineralogical characterizations of LD converter steel slags: A multi-analytical techniques approach." In: *Materials Characterization* 61.1 (2010), pp. 39–48. DOI: 10.1016/J.MATCHAR.2009.10.004.

[36] L. V. Fisher and A. R. Barron. "The recycling and reuse of steelmaking slags — A review." In: *Resources, Conservation and Recycling* 146.April (2019), pp. 244–255. DOI: 10.1016/j.resconrec.2019.03.010.

[37] P. Chaurand, J. Rose, V. Briois, M. Salome, O. Proux, V. Nassif, L. Olivi, J. Susini, J. L. Hazemann, and J. Y. Bottero. "New methodological approach for the vanadium K-edge X-ray absorption near-edge structure interpretation: Application to the speciation of vanadium in oxide phases from steel slag." In: *Journal of Physical Chemistry B* 111.19 (2007), pp. 5101–5110. DOI: 10.1021/JP063186I/ASSET/IMAGES/LARGE/JP063186IF00008.JPEG.

[38] I. Iwasaki, E. Fregeau-Wu, and T. Fujita. "Removal of Phosphorus from Steelmaking Slags: A Literature Survey." In: *Mineral Procesing and Extractive Metallurgy Review* 12.1 (1993), pp. 19–36. DOI: 10.1080/08827509308935251.

[39] M. Gautier, J. Poirier, F. Bodénan, G. Franceschini, and E. Véron. "Basic oxygen furnace (BOF) slag cooling: Laboratory characteristics and prediction calculations." In: *International Journal of Mineral Processing* 123 (2013), pp. 94–101. ISSN: 03017516. DOI: 10.1016/j.minpro.2013.05.002.

[40] F Engström, D Adolfsson, Q Yang, C Samuelsson, and B Björkman. "Crystallization behaviour of some steelmaking slags." In: *Steel Research International* 81.5 (2010), pp. 362–371. ISSN: 16113683. DOI: 10.1002/srin.200900154.

[41] M. A. Aranda. "Recent studies of cements and concretes by synchrotron radiation crystallographic and cognate methods." In: *Crystallography Reviews* 22.3 (2016), pp. 150–196. ISSN: 0889-311X. DOI: 10.1080/0889311X.2015.1070260.

[42] X. Liu, W. Lin, B. Chen, F. Zhang, P. Zhao, A. Parsons, C. Rau, and I. Robinson. "Coherent diffraction study of calcite crystallization during the hydration of tricalcium silicate." In: *Materials & Design* 157 (2018), pp. 251–257. ISSN: 02641275. DOI: 10.1016/j.matdes.2018.07.031.

[43] A. Cuesta, A. Ayuela, and M. A. Aranda. "Belite cements and their activation." In: *Cement and Concrete Research* 140 (2021), p. 106319. ISSN: 00088846. DOI: 10.1016/j.cemconres.2020.106319.

[44] H. M. Ludwig and W. Zhang. "Research review of cement clinker chemistry." In: *Cement and Concrete Research* 78 (2015), pp. 24–37. ISSN: 0008-8846. DOI: 10.1016/J.CEMCONRES.2015.05.018.

[45] J. Skibsted and R. Snellings. *Reactivity of supplementary cementitious materials (SCMs) in cement blends*. 2019. DOI: 10.1016/j.cemconres.2019.105799.

[46] A. Santamaría, A. Orbe, M. Losañez, M. Skaf, V. Ortega-Lopez, and J. J. González. "Self-compacting concrete incorporating electric arc-furnace steelmaking slag as aggregate." In: *Materials & Design* 115 (2017), pp. 179–193. ISSN: 02641275. DOI: 10.1016/j.matdes.2016.11.048.

[47] T. Staněk and P. Sulovský. "Active low-energy belite cement." In: *Cement and Concrete Research* 68 (2015), pp. 203–210. ISSN: 00088846. DOI: 10.1016/j.cemconres.2014.11.004.

[48] P. Guo, B. Wang, M. Bauchy, and G. Sant. "Misfit Stresses Caused by Atomic Size Mismatch: The Origin of Doping-Induced Destabilization of Dicalcium Silicate." In: *Crystal Growth and Design* 16.6 (2016), pp. 3124–3132. ISSN: 15287505. DOI: 10.1021/ACS.CGD.5B01740/ASSET/IMAGES/LARGE/CG-2015-017403_0008.JPEG.

[49] Y.-M. Kim and S.-H. Hong. "Influence of Minor Ions on the Stability and Hydration Rates of β-Dicalcium Silicate." In: *Journal of the American Ceramic Society* 87.5 (2004), pp. 900–905. ISSN: 00027820. DOI: 10.1111/j.1551-2916.2004.00900.x.

[50] L. Nicoleau, A. Nonat, and D. Perrey. "The di- and tricalcium silicate dissolutions." In: *Cement and Concrete Research* (2013). ISSN: 00088846. DOI: 10.1016/j.cemconres.2013.01.017.

[51] A. Wesselsky and O. M. Jensen. "Synthesis of pure Portland cement phases." In: *Cement and Concrete Research* (2009). ISSN: 14390108. DOI: 10.1007/s11368-012-0598-6.

[52] N. El Fami, H. Ez-zaki, A. Diouri, O. Sassi, and A. Boukhari. "Improvement of hydraulic and mechanical properties of dicalcium silicate by alkaline activation." In: *Construction and Building Materials* 247 (2020), p. 118589. ISSN: 09500618. DOI: 10.1016/j.conbuildmat.2020.118589.

[53] A. J. Cuberos, Á. G. De la Torre, M. C. Martín-Sedeño, L. Moreno-Real, M. Merlini, L. M. Ordónez, and M. A. Aranda. "Phase development in conventional and active belite cement pastes by Rietveld analysis and chemical constraints." In: *Cement and Concrete Research* 39.10 (2009), pp. 833–842. ISSN: 00088846. DOI: 10.1016/j.cemconres.2009.06.017.

[54] P. Chaurand, J. Rose, V. Briois, L. Olivi, J. L. Hazemann, O. Proux, J. Domas, and J. Y. Bottero. "Environmental impacts of steel slag reused in road construction: A crystallographic and molecular (XANES) approach." In: *Journal of Hazardous Materials* 139.3 (2007), pp. 537–542. ISSN: 0304-3894. DOI: 10.1016/J.JHAZMAT.2006.02.060.

[55] S. Neuhold et al. "Investigation of Possible Leaching Control Mechanisms for Chromium and Vanadium in Electric Arc Furnace (EAF) Slags Using Combined Experimental and Modeling Approaches." In: *Minerals* 9 (), p. 525. ISSN: 2075-163X. DOI: 10.3390/min9090525.

[56] M. Suzuki, N. Umesaki, T. Okajima, and T. Tanaka. "Formation and Local Structure Analysis of High-Valence Chromium Ion in Dicalcium Silicate." In: *Journal of the American Ceramic Society* 99.9 (2016), pp. 3151–3158. ISSN: 1551-2916. DOI: 10.1111/JACE.14337.

[57] X. Wu, L. Li, and Y. Dong. "Enrichment and crystallization of vanadium in factory steel slag." In: *Metallurgist* 55.5-6 (2011), pp. 401–409. ISSN: 00260894. DOI: 10.1007/S11015-011-9444-0/FIGURES/7.

[58] D. I. Stewart, A. W. Bray, G. Udoma, A. J. Hobson, W. M. Mayes, M. Rogerson, and I. T. Burke. "Hydration of dicalcium silicate and diffusion through neo-formed calcium-silicate-hydrates at weathered surfaces control the long-term leaching behaviour of basic oxygen furnace (BOF) steelmaking slag." In: *Environmental Science and Pollution Research* 25.10 (2018), pp. 9861–9872. ISSN: 0944-1344. DOI: 10.1007/s11356-018-1260-7.

[59] M. Jawad Ahmed, K. Schollbach, S. van der Laan, M. Florea, and H. J. Brouwers. "A quantitative analysis of dicalcium silicate synthesized via different sol-gel methods." In: *Materials & Design* 213 (2022), p. 110329. ISSN: 0264-1275. DOI: 10.1016/J.MATDES.2021.110329.

[60] K. Scrivener, R. Snellings, and B. Lothenbach. *A Practical Guide to Microstructural Analysis of Cementitious Materials*. Ed. by K. Scrivener, R. Snellings, and B. Lothenbach. CRC Press, 2018. ISBN: 9781351228497. DOI: 10.1201/b19074.

[61] Q. Alam, K. Schollbach, C. van Hoek, S. van der Laan, T. de Wolf, and H. Brouwers. "In-depth mineralogical quantification of MSWI bottom ash phases and their association with potentially toxic elements." In: *Waste Management* 87 (2019), pp. 1–12. ISSN: 0956053X. DOI: 10.1016/j.wasman.2019.01.031.

[62] C. A. Schneider, W. S. Rasband, and K. W. Eliceiri. "NIH Image to ImageJ: 25 years of image analysis." In: *Nature Methods 2012 9:7* 9.7 (2012), pp. 671–675. ISSN: 1548-7105. DOI: 10.1038/nmeth.2089.

[63] European Commission. *Circular Economy Action Plan: The European Green Deal*. 2020.

[64] H. Zhang, H. Wang, X. Zhu, Y. J. Qiu, K. Li, R. Chen, and Q. Liao. "A review of waste heat recovery technologies towards molten slag in steel industry." In: *Applied Energy* 112 (2013), pp. 956–966. ISSN: 0306-2619. DOI: 10.1016/J.APENERGY.2013.02.019.

[65] S. K. Tripathy, J. Dasu, Y. R. Murthy, G. Kapure, A. R. Pal, and L. O. Filippov. "Utilisation perspective on water quenched and air-cooled blast furnace slags." In: *Journal of Cleaner Production* 262 (2020), p. 121354. DOI: 10.1016/J.JCLEPRO.2020.121354.

[66] L. S. Ökvist. "High Temperature Properties of BOF Slag and its Behaviour in the Blast Furnace." In: *steel research international* 75.12 (2004), pp. 792–799. ISSN: 1869-344X. DOI: 10.1002/SRIN.200405844.

[67] H. F. W. Taylor. *Cement chemistry. 2nd ed.* 1997. ISBN: 012683900X. DOI: 10.1016/S0958-9465(98)00023-7.

[68] M.-w. Choi and S.-M. Jung. "Crystallization behavior of melted BOF slag during non-isothermal constant cooling process." In: *Journal of Non-Crystalline Solids* 468 (2017), pp. 105–112. ISSN: 0022-3093. DOI: https://doi.org/10.1016/j.jnoncrysol.2017.04.042.

[69] M. Gautier, J. Poirier, F. Bodénan, G. Franceschini, and E. Véron. "Basic oxygen furnace (BOF) slag cooling: Laboratory characteristics and prediction calculations." In: *International Journal of Mineral Processing* 123 (2013), pp. 94–101. ISSN: 03017516. DOI: 10.1016/j.minpro.2013.05.002.

[70] M. Tossavainen, F. Engstrom, Q. Yang, N. Menad, M. Lidstrom Larsson, and B. Bjorkman. "Characteristics of steel slag under different cooling conditions." In: *Waste Management* 27.10 (2007), pp. 1335–1344. ISSN: 0956053X. DOI: 10.1016/j.wasman.2006.08.002.

[71] J. Waligora, D. Bulteel, P. Degrugilliers, D. Damidot, J. Potdevin, and M. Measson. "Chemical and mineralogical characterizations of LD converter steel slags: A multi-analytical techniques approach." In: *Materials Characterization* 61.1 (2010), pp. 39–48. DOI: 10.1016/j.matchar.2009.10.004.

[72] P. Rejmak, J. S. Dolado, M. A. G. Aranda, and A. Ayuela. "First-Principles Calculations on Polymorphs of Dicalcium Silicate—Belite, a Main Component of Portland Cement." In: *The Journal of Physical Chemistry C* 123.11 (2019), pp. 6768–6777. ISSN: 1932-7447. DOI: 10.1021/acs.jpcc.8b10045.

[73] C. Duée, C. Bourgel, E. Véron, M. Allix, F. Fayon, F. Bodénan, and J. Poirier. "Phosphorus speciation in dicalcium silicate phases: Application to the basic oxygen furnace (BOF) slag." In: *Cement and Concrete Research* 73 (2015), pp. 207–214. ISSN: 00088846. DOI: 10.1016/j.cemconres.2015.03.012.

[74] E. V. Antipov, A. M. Abakumov, and S. Y. Istomin. "Target-Aimed Synthesis of Anion-Deficient Perovskites." In: *Inorganic Chemistry* 47.19 (2008), pp. 8543–8552. ISSN: 0020-1669. DOI: 10.1021/ic800791s.

[75] V. D. Eisenhüttenleute et al. *Slag atlas*. Verlag Stahleisen, 1995. ISBN: 3-514-00457-9.

[76] G. Troemel, K. Koch, W. Fix, and N. Grosskurth. "Der Einfluss des magnesiumoxyds auf die Gleichgewichte im System Fe-CaO- FeO- SiO2 und die Schwefelverteilung bei 1600 C." In: *Arch Eisenhuettenw* (1969).

[77] F. Bodénan, M. Gautier, N. Rafai, J. Poirier, P. Piantone, G. Franceschini, I. Moulin, P. Chaurand, and J. Rose. "Phosphorus speciation in dicalcium silicate polymorphs of basic oxygen furnace (BOF) slag - Preliminary results." In: *Environnement, Ingénierie & Développement* N°57 - Jan.57 (2010), pp. 1–5. ISSN: 2778-844X. DOI: 10.4267/dechets-sciences-techniques.3142.

[78] X. Li, X. Shen, M. Tang, and X. Li. "Stability of Tricalcium Silicate and Other Primary Phases in Portland Cement Clinker." In: *Industrial & Engineering Chemistry Research* 53.5 (2014), pp. 1954–1964. DOI: 10.1021/ie4034076.

[79] L. Mohammed, H. G. Gomaa, D. Ragab, and J. Zhu. "Magnetic nanoparticles for environmental and biomedical applications: A review." In: *Particuology* 30 (2017), pp. 1–14. ISSN: 16742001. DOI: 10.1016/j.partic.2016.06.001. arXiv: NIHMS150003.

[80] A. Chatterjee. "High belite cements—Present status and future technological options: Part I." In: *Cement and Concrete Research* 26.8 (1996), pp. 1213–1225. ISSN: 00088846. DOI: 10.1016/0008-8846(96)00099-3.

[81] Z. Gou and J. Chang. "Synthesis and in vitro bioactivity of dicalcium silicate powders." In: *Journal of the European Ceramic Society* 24.1 (2004), pp. 93–99. ISSN: 09552219. DOI: 10.1016/S0955-2219(03)00320-0.

[82] O. Shtepenko, C. Hills, A. Brough, and M. Thomas. "The effect of carbon dioxide on β-dicalcium silicate and Portland cement." In: *Chemical Engineering Journal* 118.1-2 (2006), pp. 107–118. ISSN: 13858947. DOI: 10.1016/j.cej.2006.02.005.

[83] M. Upendra Rao, C. Hanumantharayappa, K. Ramesh, and D. Haranath. "Effect of alkali charge compensator on luminescent properties in Eu3+ doped β-dicalcium silicate." In: *Optik* 178 (2019), pp. 1255–1263. ISSN: 00304026. DOI: 10.1016/j.ijleo.2018.10.015.

[84] M. C. Gather, A. Köhnen, and K. Meerholz. "White Organic Light-Emitting Diodes." In: *Advanced Materials* 23.2 (2011), pp. 233–248. ISSN: 1521-4095. DOI: 10.1002/ADMA.201002636.

[85] F. Rodrigues. "Synthesis of chemically and structurally modified dicalcium silicate." In: *Cement and Concrete Research* 33.6 (2003), pp. 823–827. ISSN: 00088846. DOI: 10.1016/S0008-8846(02)01065-7.

[86] L. L. Hench and J. K. West. "The Sol-Gel Process." In: *Chemical Reviews* 90.1 (1990), pp. 33–72. ISSN: 15206890. DOI: 10.1021/CR00099A003/ASSET/CR00099A003.FP.PNG_V03.

[87] D. Stephan and P. Wilhelm. "Synthesis of Pure Cementitious Phases by Sol-Gel Process as Precursor." In: *Zeitschrift für anorganische und allgemeine Chemie* 630.10 (2004), pp. 1477–1483. ISSN: 0044-2313. DOI: 10.1002/zaac.200400090.

[88] A. C. Tas. "Chemical Preparation of the Binary Compounds in the Calcia-Alumina System by Self-Propagating Combustion Synthesis." In: *Journal of the American Ceramic Society* 81.11 (2005), pp. 2853–2863. ISSN: 00027820. DOI: 10.1111/j.1151-2916.1998.tb02706.x.

[89] J. C. Restrepo, A. Chavarriaga, O. J. Restrepo, and J. I. Tobón. "Synthesis of Hydraulically Active Calcium Silicates Produced by Combustion Methods." In: *MRS Proceedings* 1768 (2015), imrc2014–6d–008. ISSN: 0272-9172. DOI: 10.1557/opl.2015.321.

[90] X.-H. Huang and J. Chang. "Low-temperature synthesis of nanocrystalline β-dicalcium silicate with high specific surface area." In: *Journal of Nanoparticle Research* 9.6 (2007), pp. 1195–1200. ISSN: 1388-0764. DOI: 10.1007/s11051-006-9202-6.

[91] M. Georgescu, J. Tipan, A. Badanoiu, D. Crisan, and I. Dragan. "Highly reactive dicalcium silicate synthesised by hydrothermal processing." In: *Cement and Concrete Composites* 22.5 (2000), pp. 315–319. DOI: 10.1016/S0958-9465(00)00017-2.

[92] S. E. Pratsinis. "Flame aerosol synthesis of ceramic powders." In: *Progress in Energy and Combustion Science* 24.3 (1998), pp. 197–219. ISSN: 03601285. DOI: 10.1016/S0360-1285(97)00028-2.

[93] Y. Tan, Y. Liu, Z. Zhang, M. Hofmann, and L. Grover. "Comparing Three Methods for the Synthesis of Pure Beta-Dicalcium Silicate." In: *2010 4th International Conference on Bioinformatics and Biomedical Engineering*. IEEE, 2010, pp. 1–4. ISBN: 978-1-4244-4712-1. DOI: 10.1109/ICBBE.2010.5515290.

[94] A. Meiszterics, L. Rosta, H. Peterlik, J. Rohonczy, S. Kubuki, P. Henits, and K. Sinkó. "Structural Characterization of Gel-Derived Calcium Silicate Systems." In: *The Journal of Physical Chemistry A* 114.38 (2010), pp. 10403–10411. ISSN: 1089-5639. DOI: 10.1021/jp1053502.

[95] J. J. Thomas, S. Ghazizadeh, and E. Masoero. "Kinetic mechanisms and activation energies for hydration of standard and highly reactive forms of β-dicalcium silicate (C2S)." In: *Cement and Concrete Research* 100 (2017), pp. 322–328. ISSN: 00088846. DOI: 10.1016/j.cemconres.2017.06.001.

[96] L. Dimesso. "Pechini Processes: An Alternate Approach of the Sol–Gel Method, Preparation, Properties, and Applications." In: *Handbook of Sol-Gel Science and Technology*. Cham: Springer International Publishing, 2016, pp. 1–22. DOI: 10.1007/978-3-319-19454-7_123-1.

[97] R. Chrysafi, T. Perraki, and G. Kakali. "Sol–gel preparation of 2CaO·SiO2." In: *Journal of the European Ceramic Society* 27.2-3 (2007), pp. 1707–1710. ISSN: 09552219. DOI: 10.1016/j.jeurceramsoc.2006.05.004.

[98] Y. El Khessaimi, Y. El Hafiane, and A. Smith. "Ye'elimite synthesis by chemical routes." In: *Journal of the European Ceramic Society* 39.4 (2019), pp. 1683–1695. ISSN: 09552219. DOI: 10.1016/j.jeurceramsoc.2018.10.025.

[99] X. Lu, S. Wang, S. Liu, P. Du, Z. Ye, X. Geng, and X. Cheng. "Phase Identification of γ- and β-Ca 2 SiO 4 via the Rear-Earth Fluorescence Probe." In: *The Journal of Physical Chemistry C* 123.22 (2019), pp. 13877–13884. ISSN: 1932-7447. DOI: 10.1021/acs.jpcc.9b02262.

[100] J. Li, G. Geng, W. Zhang, Y.-S. Yu, D. A. Shapiro, and P. J. M. Monteiro. "The Hydration of β- and α H -Dicalcium Silicates: An X-ray Spectromicroscopic Study." In: *ACS Sustainable Chemistry & Engineering* 7.2 (2019), pp. 2316–2326. ISSN: 2168-0485. DOI: 10.1021/acssuschemeng.8b05060.

[101] S. N. Ghosh, P. B. Rao, A. K. Paul, and K. Raina. *The chemistry of dicalcium silicate mineral*. 1979. DOI: 10.1007/BF00569274.

[102] S.-H. Hong and J. F. Young. "Hydration Kinetics and Phase Stability of Dicalcium Silicate Synthesized by the Pechini Process." In: *Journal of the American Ceramic Society* 82.7 (1999), pp. 1681–1686. ISSN: 00027820. DOI: 10.1111/j.1151-2916.1999.tb01986.x.

[103] I. Nettleship, J. L. Shull, and W. M. Kriven. "Chemical preparation and phase stability of Ca2SiO4 and Sr2SiO4 powders." In: *Journal of the European Ceramic Society* 11.4 (1993), pp. 291–298. ISSN: 09552219. DOI: 10.1016/0955-2219(93)90028-P.

[104] Q. Sun, J. W. Gustin, F.-c. Tian, S. J. Sidow, B. E. Bergeron, J.-z. Ma, and F. R. Tay. "Effects of pre-mixed hydraulic calcium silicate putties on osteogenic differentiation of human dental pulp stem cells in vitro." In: *Journal of Dentistry* 108 (2021), p. 103653. ISSN: 03005712. DOI: 10.1016/j.jdent.2021.103653.

[105] C. J. Chan, W. M. Kriven, and J. F. Young. "Physical Stabilization of the beta gamma Transformation in Dicalcium Silicate." In: *Journal of the American Ceramic Society* 75.6 (1992), pp. 1621–1627. ISSN: 0002-7820. DOI: 10.1111/j.1151-2916.1992.tb04234.x.

[106] G. Laudisio and F. Branda. "Sol–gel synthesis and crystallisation of 3CaO·2SiO2 glassy powders." In: *Thermochimica Acta* 370.1-2 (2001), pp. 119–124. ISSN: 00406031. DOI: 10.1016/S0040-6031(00)00786-3.

[107] S. Saidani, A. Smith, Y. El Hafiane, and L. Ben Tahar. "Re-examination of the β→γ transformation of Ca2SiO4." In: *Journal of the European Ceramic Society* 38.14 (2018), pp. 4756–4767. ISSN: 09552219. DOI: 10.1016/j.jeurceramsoc.2018.06.011.

[108] S.-H. Hong and J. F. Young. "Hydration Kinetics and Phase Stability of Dicalcium Silicate Synthesized by the Pechini Process." In: *Journal of the American Ceramic Society* 82.7 (1999), pp. 1681–1686. ISSN: 00027820. DOI: 10.1111/j.1151-2916.1999.tb01986.x.

[109] F. Puertas and F. Triviño. "Examinations by infra-red spectroscopy for the polymorphs of dicalcium silicate." In: *Cement and Concrete Research* 15.1 (1985), pp. 127–133. ISSN: 00088846. DOI: 10.1016/0008-8846(85)90017-1.

[110] A. Meiszterics, L. Rosta, H. Peterlik, J. Rohonczy, S. Kubuki, P. Henits, and K. Sinko. "Structural Characterization of Gel-Derived Calcium Silicate Systems." In: *The Journal of Physical Chemistry A* 114.38 (2010), pp. 10403–10411. ISSN: 1089-5639. DOI: 10.1021/jp1053502.

[111] Q. T. Phung, N. Maes, and S. Seetharam. "Pitfalls in the use and interpretation of TGA and MIP techniques for Ca-leached cementitious materials." In: *Materials & Design* 182 (2019), p. 108041. ISSN: 02641275. DOI: 10.1016/j.matdes.2019.108041.

[112] C. Barbé, D. Cassidy, G. Triani, B. Latella, D. Mitchell, K. Finnie, J. Bartlett, J. Woolfrey, and G. Collins. "Sol–gel bonding of silicon wafers." In: *Thin Solid Films* 488.1-2 (2005), pp. 160–166. ISSN: 00406090. DOI: 10.1016/j.tsf.2005.04.109.

[113] E. Benhelal, G. Zahedi, E. Shamsaei, and A. Bahadori. "Global strategies and potentials to curb CO2 emissions in cement industry." In: 51 (2013), pp. 142–161. ISSN: 09596526. DOI: 10.1016/j.jclepro.2012.10.049.

[114] J. Zhu, K. Yang, Y. Chen, G. Fan, L. Zhang, B. Guo, X. Guan, and R. Zhao. "Revealing the substitution preference of zinc in ordinary Portland cement clinker phases: A study from experiments and DFT calculations." In: *Journal of Hazardous Materials* 409 (2021), p. 124504. ISSN: 03043894. DOI: 10.1016/j.jhazmat.2020.124504.

[115] C.-K. Lin, J.-N. Chen, and C.-C. Lin. "An NMR and XRD study of solidification/stabilization of chromium with Portland cement and β-C2S." In: *Journal of Hazardous Materials* 48.1-3 (1996), pp. 137–147. ISSN: 03043894. DOI: 10.1016/0304-3894(95)00154-9.

[116] O. Omotoso, D. Ivey, and R. Mikula. "Characterization of chromium doped tricalcium silicate using SEM/EDS, XRD and FTIR." In: *Journal of Hazardous Materials* 42.1 (1995), pp. 87–102. ISSN: 03043894. DOI: 10.1016/0304-3894(95)00012-J.

[117] J. S. Romano and F. A. Rodrigues. "Cements obtained from rice hull: Encapsulation of heavy metals." In: *Journal of Hazardous Materials* 154.1-3 (2008), pp. 1075–1080. ISSN: 03043894. DOI: 10.1016/j.jhazmat.2007.11.051.

[118] C. L. Goh and S. L. Gan. "Change in cement manufacturing process, a cause for decline in chromate allergy?" In: *Contact Dermatitis* 34.1 (1996), pp. 51–54. ISSN: 01051873. DOI: 10.1111/j.1600-0536.1996.tb02112.x.

[119] F. Pang, C. Wei, Z. Zhang, W. Wang, and Z. Wang. "The migration and immobilization for heavy metal chromium ions in the hydration products of calcium sulfoaluminate cement and their leaching behavior." In: *Journal of Cleaner Production* 365 (2022), p. 132778. ISSN: 09596526. DOI: 10.1016/j.jclepro.2022.132778.

[120] M. A. Silva, L. Mater, M. M. Souza-Sierra, A. X. Corrêa, R. Sperb, and C. M. Radetski. "Small hazardous waste generators in developing countries: use of stabilization/solidification process as an economic tool for metal wastewater treatment and appropriate sludge disposal." In: *Journal of Hazardous Materials* 147.3 (2007), pp. 986–990. ISSN: 03043894. DOI: 10.1016/j.jhazmat.2007.01.128.

[121] L. Pérez-Villarejo, S. Martínez-Martínez, B. Carrasco-Hurtado, D. Eliche-Quesada, C. Ureña-Nieto, and P. Sánchez-Soto. "Valorization and inertization of galvanic sludge waste in clay bricks." In: *Applied Clay Science* 105-106 (2015), pp. 89–99. ISSN: 01691317. DOI: 10.1016/j.clay.2014.12.022.

[122] Y.-L. Chen, P.-H. Shih, L.-C. Chiang, Y.-K. Chang, H.-C. Lu, and J.-E. Chang. "The influence of heavy metals on the polymorphs of dicalcium silicate in the belite-rich clinkers produced from electroplating sludge." In: *Journal of Hazardous Materials* 170.1 (2009), pp. 443–448. ISSN: 03043894. DOI: 10.1016/j.jhazmat.2009.04.076.

[123] A. Kaja, A. Delsing, S. van der Laan, H. Brouwers, and Q. Yu. "Effects of carbonation on the retention of heavy metals in chemically activated BOF slag pastes." In: *Cement and Concrete Research* 148 (2021), p. 106534. ISSN: 00088846. DOI: 10.1016/j.cemconres.2021.106534.

[124] J. Spooren, E. Kim, L. Horckmans, K. Broos, P. Nielsen, and M. Quaghebeur. "In-situ chromium and vanadium recovery of landfilled ferrochromium and stainless steel slags." In: *Chemical Engineering Journal* 303 (2016), pp. 359–368. ISSN: 13858947. DOI: 10.1016/j.cej.2016.05.128.

[125] Q. Alam, K. Schollbach, M. Rijnders, C. van Hoek, S. van der Laan, and H. Brouwers. "The immobilization of potentially toxic elements due to incineration and weathering of bottom ash fines." In: *Journal of Hazardous Materials* 379 (2019), p. 120798. ISSN: 03043894. DOI: 10.1016/j.jhazmat.2019.120798.

[126] M. A. Aranda. *Recent studies of cements and concretes by synchrotron radiation crystallographic and cognate methods*. 2016. DOI: 10.1080/0889311X.2015.1070260.

[127] A. van Zomeren, S. R. van der Laan, H. B. Kobesen, W. J. Huijgen, and R. N. Comans. "Changes in mineralogical and leaching properties of converter steel slag resulting from accelerated carbonation at low CO2 pressure." In: *Waste Management* 31.11 (2011), pp. 2236–2244. DOI: 10.1016/j.wasman.2011.05.022.

[128] A. Wesselsky and O. M. Jensen. "Synthesis of pure Portland cement phases." In: *Cement and Concrete Research* 39.11 (2009), pp. 973–980. ISSN: 0008-8846. DOI: 10.1016/J.CEMCONRES.2009.07.013.

[129] D. V. Lopatin and V. M. Chizhikova. "Crystal-chemical stabilization of dicalcium silicate." In: *Steel in Translation* 37.3 (2007), pp. 191–195. ISSN: 0967-0912. DOI: 10.3103/S0967091207030035.

[130] L. Black, A. Stumm, K. Garbev, P. Stemmermann, K. R. Hallam, and G. C. Allen. "X-ray photoelectron spectroscopy of the cement clinker phases tricalcium silicate and β-dicalcium silicate." In: *Cement and Concrete Research* 33.10 (2003), pp. 1561–1565. ISSN: 00088846. DOI: 10.1016/S0008-8846(03)00097-8.

[131] G.-C. Lai, T. Nojiri, and K.-i. Nakano. "Studies of the stability of β-Ca2SiO4 doped by minor ions." In: *Cement and Concrete Research* 22.5 (1992), pp. 743–754. ISSN: 00088846. DOI: 10.1016/0008-8846(92)90097-F.

[132] J. Maycock and M. McCarty. "Crystal lattice defects in di-calcium silicate." In: *Cement and Concrete Research* 3.6 (1973), pp. 701–713. ISSN: 00088846. DOI: 10.1016/0008-8846(73)90005-7.

[133] L. S. Wu, Y. Zhou, and Y. C. Dong. "Precipitation Behavior of V-Enrichment Mineral in Steelmaking Slag Bearing Vanadium Modified by SiO₂." In: *Applied Mechanics and Materials* 295-298 (2013), pp. 1729–1734. ISSN: 1662-7482. DOI: 10.4028/www.scientific.net/AMM.295-298.1729.

[134] M TREZZA and A SCIAN. "Waste with chrome in the Portland cement clinker production." In: *Journal of Hazardous Materials* 147.1-2 (2007), pp. 188–196. ISSN: 03043894. DOI: 10.1016/j.jhazmat.2006.12.082.

[135] Y.-L. Chen, Y.-C. Lai, C.-J. Lin, Y.-K. Chang, and M.-S. Ko. "Controlling sintering atmosphere to reduce the hazardous characteristics of low-energy cement produced with chromium compounds." In: *Journal of Cleaner Production* 43 (2013), pp. 45–51. ISSN: 09596526. DOI: 10.1016/j.jclepro.2012.12.027.

[136] P. Fierens and J. Tirlocq. "Nature and concentration effect of stabilizing elements of beta-dicalcium silicate on its hydration rate." In: *Cement and Concrete Research* 13.2 (1983), pp. 267–276. ISSN: 0008-8846. DOI: 10.1016/0008-8846(83)90110-2.

[137] R. Parkash, S. Mehta, S. Dixit, S. Singh, S. Ahluwalia, and J. Sharma. "Effect of chromium addition on the kinetics of hydration of dicalcium silicate phase." In: *Advances in Cement Research* 22.2 (2010), pp. 81–89. ISSN: 0951-7197. DOI: 10.1680/adcr.2010.22.2.81.

[138] M. Jawad Ahmed, K. Schollbach, S. van der Laan, M. Florea, and H. Brouwers. "A quantitative analysis of dicalcium silicate synthesized via different sol-gel methods." In: *Materials & Design* 213 (2022), p. 110329. ISSN: 02641275. DOI: 10.1016/j.matdes.2021.110329.

[139] A. Elhoweris, I. Galan, and F. P. Glasser. "Stabilisation of α dicalcium silicate in calcium sulfoaluminate clinker." In: *Advances in Cement Research* 32.3 (2020), pp. 112–124. ISSN: 0951-7197. DOI: 10.1680/jadcr.18.00050.

[140] K. T. Adendorff, J. P. R. Villiers, and G. J. Kruger. "Crystal Structures of Ca5Cr3O12 and Ca5Cr2SiO12, the Chromium Analogs of Silicocarnotite." In: *Journal of the American Ceramic Society* 75.6 (1992), pp. 1416–1422. ISSN: 0002-7820. DOI: 10.1111/j.1151-2916.1992.tb04203.x.

[141] L. Black, A. Stumm, K. Garbev, P. Stemmermann, K. R. Hallam, and G. C. Allen. "X-ray photoelectron spectroscopy of the cement clinker phases tricalcium silicate and β-dicalcium silicate." In: *Cement and Concrete Research* 33.10 (2003), pp. 1561–1565. ISSN: 00088846. DOI: 10.1016/S0008-8846(03)00097-8.

[142] L. Black, K. Garbev, P. Stemmermann, K. R. Hallam, and G. C. Allen. "Characterisation of crystalline C-S-H phases by X-ray photoelectron spectroscopy." In: *Cement and Concrete Research* 33.6 (2003), pp. 899–911. ISSN: 00088846. DOI: 10.1016/S0008-8846(02)01089-X.

[143] X. Li, C. He, Y. Bai, B. Ma, G. Wang, and H. Tan. "Stabilization/solidification on chromium (III) wastes by C3A and C3A hydrated matrix." In: *Journal of Hazardous Materials* 268 (2014), pp. 61–67. ISSN: 03043894. DOI: 10.1016/j.jhazmat.2014.01.002.

[144] A. Basak, L. Ramrakhiani, S. Ghosh, R. Sen, and A. K. Mandal. "Preparation of chromium doped phosphate glass adopting microwave irradiation and comparative analysis of properties with conventional glass." In: *Journal of Non-Crystalline Solids* 500 (2018), pp. 11–17. ISSN: 00223093. DOI: 10.1016/j.jnoncrysol.2018.04.014.

[145] A APTE, V TARE, and P BOSE. "Extent of oxidation of Cr(III) to Cr(VI) under various conditions pertaining to natural environment." In: *Journal of Hazardous Materials* 128.2-3 (2006), pp. 164–174. ISSN: 03043894. DOI: 10.1016/j.jhazmat.2005.07.057.

[146] A. Ghose, S. Chopra, and J. F. Young. "Microstructural characterization of doped dicalcium silicate polymorphs." In: *Journal of Materials Science* 18.10 (1983), pp. 2905–2914. ISSN: 0022-2461. DOI: 10.1007/BF00700771.

[147] G. Silversmit, D. Depla, H. Poelman, G. B. Marin, and R. De Gryse. "Determination of the V2p XPS binding energies for different vanadium oxidation states (V5+ to V0+)." In: *Journal of Electron Spectroscopy and Related Phenomena* 135.2-3 (2004), pp. 167–175. ISSN: 03682048. DOI: 10.1016/j.elspec.2004.03.004.

[148] R Zimmermann, R Claessen, F Reinert, P Steiner, and S Hüfner. "Strong hybridization in vanadium oxides: evidence from photoemission and absorption spectroscopy." In: *Journal of Physics: Condensed Matter* 10.25 (1998), pp. 5697–5716. ISSN: 0953-8984. DOI: 10.1088/0953-8984/10/25/018.

[149] A. Kumar, F. Rahman, and A. Khan. "Fabrication and characterization of VO2 nanoparticles: A simple and low-cost combustion method." In: *AIP Conference Proceedings*. Vol. 2369. 1. AIP Publishing LLCAIP Publishing, 2021, p. 020019. ISBN: 9780735441217. DOI: 10.1063/5.0060865.

[150] L. D. Frederickson and D. M. Hausen. "Infrared Spectra-Structure Correlation Study of Vanadium-Oxygen Compounds." In: *Analytical Chemistry* 35.7 (1963), pp. 818–827. ISSN: 0003-2700. DOI: 10.1021/ac60200a018.

[151] A. A. El-Moneim, H. A. Hashem, A. El-Namrouty, and A. Atef. "Effect of V2O5 on structural and elastic properties of alkali silicate SiO2–Na2O–NaF glasses." In: *Journal of Non-Crystalline Solids* 580 (2022), p. 121389. ISSN: 00223093. DOI: 10.1016/j.jnoncrysol.2021.121389.

[152] H. Miyata, K. Fujii, T. Ono, Y. Kubokawa, T. Ohno, and F. Hatayama. "Fourier-transform infrared investigation of structures of vanadium oxide on various supports." In: *Journal of the Chemical Society, Faraday Transactions 1: Physical Chemistry in Condensed Phases* 83.3 (1987), p. 675. ISSN: 0300-9599. DOI: 10.1039/f19878300675.

[153] S. Saidani, A. Smith, Y. El Hafiane, and L. Ben Tahar. "Role of dopants (B, P and S) on the stabilization of β-Ca2SiO4." In: *Journal of the European Ceramic Society* 41.1 (2021), pp. 880–891. ISSN: 09552219. DOI: 10.1016/j.jeurceramsoc.2020.07.037.

[154] M. Georgescu, J. Tipan, A. Badanoiu, D. Crisan, and I. Dragan. "Highly reactive dicalcium silicate synthesised by hydrothermal processing." In: *Cement and Concrete Composites* 22.5 (2000), pp. 315–319. DOI: 10.1016/S0958-9465(00)00017-2.

[155] L. Nicoleau, A. Nonat, and D. Perrey. "The di- and tricalcium silicate dissolutions." In: *Cement and Concrete Research* 47 (2013), pp. 14–30. ISSN: 0008-8846. DOI: 10.1016/J.CEMCONRES.2013.01.017.

[156] H. El-Didamony, A. Sharara, I. Helmy, and S. El-Aleem. "Hydration characteristics of β-C2S in the presence of some accelerators." In: *Cement and Concrete Research* 26.8 (1996), pp. 1179–1187. ISSN: 00088846. DOI: 10.1016/0008-8846(96)00103-2.

[157] R. Parkash, S. K. Mehta, S. Dixit, S. Singh, S. C. Ahluwalia, and J. M. Sharma. "Effect of chromium addition on the kinetics of hydration of dicalcium silicate phase." In: *http://dx.doi.org/10.1680/adcr.2010.22.2.81* 22.2 (2015), pp. 81–89. ISSN: 09517197. DOI: 10.1680/ADCR.2010.22.2.81.

[158] A. S. Brand, J. M. Gorham, and J. W. Bullard. "Dissolution rate spectra of β-dicalcium silicate in water of varying activity." In: *Cement and Concrete Research* 118 (2019), pp. 69–83. ISSN: 00088846. DOI: 10.1016/j.cemconres.2019.02.014.

[159] A. J. Hobson, D. I. Stewart, A. W. Bray, R. J. G. Mortimer, W. M. Mayes, M. Rogerson, and I. T. Burke. "Mechanism of Vanadium Leaching during Surface Weathering of Basic Oxygen Furnace Steel Slag Blocks: A Microfocus X-ray Absorption Spectroscopy and Electron Microscopy Study." In: *Environmental Science & Technology* 51.14 (2017), pp. 7823–7830. ISSN: 0013-936X. DOI: 10.1021/acs.est.7b00874.

[160] W. F. Santos, K. Schollbach, S. Melzer, S. van der Laan, and H. Brouwers. "Quantitative analysis and phase assemblage of basic oxygen furnace slag hydration." In: *Journal of Hazardous Materials* 450 (2023), p. 131029. ISSN: 03043894. DOI: 10.1016/j.jhazmat.2023.131029.

[161] E. Gartner and H. Hirao. "A review of alternative approaches to the reduction of CO2 emissions associated with the manufacture of the binder phase in concrete." In: *Cement and Concrete Research* 78 (2015), pp. 126–142. ISSN: 0008-8846. DOI: 10.1016/J.CEMCONRES.2015.04.012.

[162] M. Ben Haha, F. Winnefeld, and A. Pisch. "Advances in understanding ye'elimite-rich cements." In: *Cement and Concrete Research* 123 (2019), p. 105778. ISSN: 00088846. DOI: 10.1016/j.cemconres.2019.105778.

[163] T. Staněk and P. Sulovský. "Active low-energy belite cement." In: *Cement and Concrete Research* 68 (2015), pp. 203–210. ISSN: 0008-8846. DOI: 10.1016/J.CEMCONRES.2014.11.004.

[164] A. Bouregba, H. Ez-zaki, A. Diouri, and O. Sassi. "Dicalcium silicate hydration behavior in the presence of Na2CO3 and water glass." In: *Asian Journal of Civil Engineering* 20.6 (2019), pp. 857–867. ISSN: 1563-0854. DOI: 10.1007/s42107-019-00150-0.

[165] A. Cuesta, E. R. Losilla, M. A. Aranda, J. Sanz, and Á. G. De La Torre. "Reactive belite stabilization mechanisms by boron-bearing dopants." In: *Cement and Concrete Research* 42.4 (2012), pp. 598–606. ISSN: 0008-8846. DOI: 10.1016/J.CEMCONRES.2012.01.006.

[166] T Stanek, P Sulovský, and D Vsianský. "Active Belite Clinker doped with SO3." In: *13th International Congress on the Chemistry of Cement*. 2011, pp. 1–7.

[167] H. El-Didamony, A. M. Sharara, I. M. Helmy, and S. Abd El-Aleem. "Hydration characteristics of β-C2S in the presence of some accelerators." In: *Cement and Concrete Research* 26.8 (1996), pp. 1179–1187. ISSN: 0008-8846. DOI: 10.1016/0008-8846(96)00103-2.

[168] M. J. Sánchez-Herrero, A. Fernández-Jiménez, and Á. Palomo. "Alkaline Hydration Of C 2 S and C 3 S." In: *Journal of the American Ceramic Society* 99.2 (2016). Ed. by L. Klein, pp. 604–611. ISSN: 0002-7820. DOI: 10.1111/jace.13985.

[169] I. García Lodeiro, A. Fernández-Jimenez, A. Palomo, and D. Macphee. "Effect on fresh C-S-H gels of the simultaneous addition of alkali and aluminium." In: *Cement and Concrete Research* 40.1 (2010), pp. 27–32. ISSN: 00088846. DOI: 10.1016/j.cemconres.2009.08.004.

[170] T. Kim, M. F. Alnahhal, Q. D. Nguyen, P. Panchmatia, A. Hajimohammadi, and A. Castel. "Initial sequence for alkali-silica reaction: Transport barrier and spatial distribution of reaction products." In: *Cement and Concrete Composites* 104 (2019), p. 103378. ISSN: 09589465. DOI: 10.1016/j.cemconcomp.2019.103378.

[171] Y. Yan, S.-Y. Yang, G. D. Miron, I. E. Collings, E. L'Hôpital, J. Skibsted, F. Winnefeld, K. Scrivener, and B. Lothenbach. "Effect of alkali hydroxide on calcium silicate hydrate (C-S-H)." In: *Cement and Concrete Research* 151 (2022), p. 106636. ISSN: 00088846. DOI: 10.1016/j.cemconres.2021.106636.

[172] C. K. Park. "Effects of Alkalies on Hydration of β-Dicalcium Silicate and Its Resultant Hydrates." In: *Journal of the Ceramic Society of Japan* 108.1254 (2000), pp. 113–117. ISSN: 0914-5400. DOI: 10.2109/JCERSJ.108.1254_113.

[173] L. Nicoleau and M. A. Bertolim. "Analytical Model for the Alite (C3S) Dissolution Topography." In: *Journal of the American Ceramic Society* 99.3 (2016), pp. 773–786. ISSN: 1551-2916. DOI: 10.1111/JACE.13647.

[174] I. García Lodeiro, D. Macphee, A. Palomo, and A. Fernández-Jiménez. "Effect of alkalis on fresh C–S–H gels. FTIR analysis." In: *Cement and Concrete Research* 39.3 (2009), pp. 147–153. ISSN: 00088846. DOI: 10.1016/j.cemconres.2009.01.003.

[175] W. Kunther, S. Ferreiro, and J. Skibsted. "Influence of the Ca/Si ratio on the compressive strength of cementitious calcium–silicate–hydrate binders." In: *Journal of Materials Chemistry A* 5.33 (2017), pp. 17401–17412. ISSN: 2050-7488. DOI: 10.1039/C7TA06104H.

[176] I. Richardson. "The nature of C-S-H in hardened cements." In: *Cement and Concrete Research* 29.8 (1999), pp. 1131–1147. ISSN: 00088846. DOI: 10.1016/S0008-8846(99)00168-4.

[177] M. Radwan, H. Abd El-Hamid, and A. Mohamed. "Influence of saline solution on hydration behavior of β-dicalcium silicate in comparison with biphasic calcium phosphate/hydroxyapatite bio-ceramics." In: *Materials Science and Engineering: C* 57 (2015), pp. 355–362. ISSN: 09284931. DOI: 10.1016/j.msec.2015.07.011.

[178] J. Zhang, W. Zhang, J. Ye, X. Ren, L. Liu, and W. Shen. "Influence of alkaline carbonates on the hydration characteristics of β-C2S." In: *Construction and Building Materials* 296 (2021), p. 123661. ISSN: 09500618. DOI: 10.1016/j.conbuildmat.2021.123661.

[179] K. Scrivener, A. Ouzia, P. Juilland, and A. Kunhi Mohamed. "Advances in understanding cement hydration mechanisms." In: *Cement and Concrete Research* 124 (2019), p. 105823. ISSN: 00088846. DOI: 10.1016/j.cemconres.2019.105823.

[180] E. Durgun, H. Manzano, R. J. M. Pellenq, and J. C. Grossman. "Understanding and Controlling the Reactivity of the Calcium Silicate phases from First Principles." In: *Chemistry of Materials* 24.7 (2012), pp. 1262–1267. ISSN: 0897-4756. DOI: 10.1021/cm203127m.

[181] K. L. Scrivener, P. Juilland, and P. J. Monteiro. "Advances in understanding hydration of Portland cement." In: *Cement and Concrete Research* 78 (2015), pp. 38–56. ISSN: 00088846. DOI: 10.1016/j.cemconres.2015.05.025.

[182] M. J. Sánchez-Herrero, A. Fernández-Jiménez, and A. Palomo. "C 3 S and C 2 S hydration in the presence of Na 2 CO 3 and Na 2 SO 4." In: *Journal of the American Ceramic Society* 100.7 (2017), pp. 3188–3198. ISSN: 0002-7820. DOI: 10.1111/jace.14855.

[183] E. Bernard, Y. Yan, and B. Lothenbach. "Effective cation exchange capacity of calcium silicate hydrates (C-S-H)." In: *Cement and Concrete Research* 143 (2021), p. 106393. ISSN: 00088846. DOI: 10.1016/j.cemconres.2021.106393.

[184] J. R. Rumble. *CRC Handbook of Chemistry and Physics*. Ed. by J. John R. Rumble, T. J. Bruno, and M. J. Doa. 102nd ed. Boca Raton: CRC Press/Taylor & Francis Group, 2021. ISBN: 9780367712600 0367712601.

[185] D. I. Stewart, A. W. Bray, G. Udoma, A. J. Hobson, W. M. Mayes, M. Rogerson, and I. T. Burke. "Hydration of dicalcium silicate and diffusion through neo-formed calcium-silicate-hydrates at weathered surfaces control the long-term leaching behaviour of basic oxygen furnace (BOF) steelmaking slag." In: *Environmental Science and Pollution Research* 25.10 (2018), pp. 9861–9872. ISSN: 16147499. DOI: 10.1007/S11356-018-1260-7/FIGURES/5.

[186] N. Mostafa, E. Kishar, and S. Abo-El-Enein. "FTIR study and cation exchange capacity of Fe3+- and Mg2+-substituted calcium silicate hydrates." In: *Journal of Alloys and Compounds* 473.1-2 (2009), pp. 538–542. ISSN: 09258388. DOI: 10.1016/j.jallcom.2008.06.029.

[187] E. John and D. Stephan. "Calcium silicate hydrate— in-situ development of the silicate structure followed by infrared spectroscopy." In: *Journal of the American Ceramic Society* 104.12 (2021), pp. 6611–6624. ISSN: 0002-7820. DOI: 10.1111/jace.18019.

[188] P. Yu, R. J. Kirkpatrick, B. Poe, P. F. McMillan, and X. Cong. "Structure of Calcium Silicate Hydrate (C-S-H): Near-, Mid-, and Far-Infrared Spectroscopy." In: *Journal of the American Ceramic Society* 82.3 (1999), pp. 742–748. ISSN: 0002-7820. DOI: 10.1111/j.1151-2916.1999.tb01826.x.

[189] F Reig. "FTIR quantitative analysis of calcium carbonate (calcite) and silica (quartz) mixtures using the constant ratio method. Application to geological samples." In: *Talanta* 58.4 (2002), pp. 811–821. ISSN: 00399140. DOI: 10.1016/S0039-9140(02)00372-7.

[190] P. Prasad. "Direct formation of the -CaSO4 phase in dehydration process of gypsum: In situ FTIR study." In: *American Mineralogist* 90.4 (2005), pp. 672–678. ISSN: 0003-004X. DOI: 10.2138/am.2005.1742.

[191] M. Jawad Ahmed, W. Franco Santos, and H. Brouwers. "Air granulated basic Oxygen furnace (BOF) slag application as a binder: Effect on strength, volumetric stability, hydration study, and environmental risk." In: *Construction and Building Materials* 367 (2023), p. 130342. ISSN: 09500618. DOI: 10.1016/j.conbuildmat.2023.130342.

[192] Y. A. Villagrán-Zaccardi, H. Egüez-Alava, K. De Buysser, E. Gruyaert, and N. De Belie. "Calibrated quantitative thermogravimetric analysis for the determination of portlandite and calcite content in hydrated cementitious systems." In: *Materials and Structures* 50.3 (2017), p. 179. ISSN: 1359-5997. DOI: 10.1617/s11527-017-1046-2.

[193] S. Steiner, B. Lothenbach, T. Proske, A. Borgschulte, and F. Winnefeld. "Effect of relative humidity on the carbonation rate of portlandite, calcium silicate hydrates and ettringite." In: *Cement and Concrete Research* 135 (2020), p. 106116. ISSN: 00088846. DOI: 10.1016/j.cemconres.2020.106116.

[194] J. W. Bullard, H. M. Jennings, R. A. Livingston, A. Nonat, G. W. Scherer, J. S. Schweitzer, K. L. Scrivener, and J. J. Thomas. "Mechanisms of cement hydration." In: *Cement and Concrete Research* 41.12 (2011), pp. 1208–1223. ISSN: 00088846. DOI: 10.1016/j.cemconres.2010.09.011.

[195] J. Shukla, V. P. Mohandas, and A. Kumar. "Effect of pH on the Solubility of CaSO 4 ·2H 2 O in Aqueous NaCl Solutions and Physicochemical Solution Properties at 35 °C." In: *Journal of Chemical & Engineering Data* 53.12 (2008), pp. 2797–2800. ISSN: 0021-9568. DOI: 10.1021/je800465f.

[196] W. Ashraf. "Microstructure of chemically activated gamma-dicalcium silicate paste." In: *Construction and Building Materials* 185 (2018), pp. 617–627. ISSN: 09500618. DOI: 10.1016/j.conbuildmat.2018.07.030.

[197] A. S. Brand, J. M. Gorham, and J. W. Bullard. "Dissolution rate spectra of β-dicalcium silicate in water of varying activity." In: *Cement and Concrete Research* 118 (2019), pp. 69–83. ISSN: 00088846. DOI: 10.1016/j.cemconres.2019.02.014.

[198] K. Schollbach, M. J. Ahmed, and S. R. van der Laan. "The mineralogy of air granulated converter slag." In: *International Journal of Ceramic Engineering & Science* 3.1 (2021), pp. 21–36. ISSN: 2578-3270. DOI: 10.1002/ces2.10074.

[199] N. Mostafa, S. El-Hemaly, E. Al-Wakeel, S. El-Korashy, and P. Brown. "Hydraulic activity of water-cooled slag and air-cooled slag at different temperatures." In: *Cement and Concrete Research* 31.3 (2001), pp. 475–484. ISSN: 00088846. DOI: 10.1016/S0008-8846(00)00462-2.

[200] T. Hertel, J. Neubauer, and F. Goetz-Neunhoeffer. "Study of hydration potential and kinetics of the ferrite phase in iron-rich CAC." In: *Cement and Concrete Research* 83 (2016), pp. 79–85. ISSN: 00088846. DOI: 10.1016/j.cemconres.2016.01.004.

[201] Q. Wang, P. Yan, and S. Han. "The influence of steel slag on the hydration of cement during the hydration process of complex binder." In: *Science China Technological Sciences* 54.2 (2011), pp. 388–394. ISSN: 1674-7321. DOI: 10.1007/s11431-010-4204-0.

[202] T. Zhang, Q. Yu, J. Wei, and J. Li. "Investigation on mechanical properties, durability and micro-structural development of steel slag blended cements." In: *Journal of Thermal Analysis and Calorimetry* 110.2 (2012), pp. 633–639. ISSN: 1388-6150. DOI: 10.1007/s10973-011-1853-6.

[203] S. Zhuang and Q. Wang. "Inhibition mechanisms of steel slag on the early-age hydration of cement." In: *Cement and Concrete Research* 140 (2021), p. 106283. ISSN: 00088846. DOI: 10.1016/j.cemconres.2020.106283.

[204] W. Nocuń-Wczelik. "Differential calorimetry as a tool in the studies of cement hydration kinetics with sulphate and nitrate solutions." In: *Journal of Thermal Analysis and Calorimetry* 130.1 (2017), pp. 249–259. ISSN: 1388-6150. DOI: 10.1007/s10973-017-6378-1.

[205] E Dubina, L Black, R Sieber, and J Plank. "Interaction of water vapour with anhydrous cement minerals." In: *Advances in Applied Ceramics* 109.5 (2010), pp. 260–268. ISSN: 1743-6753. DOI: 10.1179/174367509X12554402491029.

[206] J. Li, Q. Yu, J. Wei, and T. Zhang. "Structural characteristics and hydration kinetics of modified steel slag." In: *Cement and Concrete Research* 41.3 (2011), pp. 324–329. ISSN: 00088846. DOI: 10.1016/j.cemconres.2010.11.018.

[207] D. H. Moon and M. Wazne. "Impact of brownmillerite hydration on Cr(VI) sequestration in chromite ore processing residue." In: *Geosciences Journal* 15.3 (2011), pp. 287–296. ISSN: 1226-4806. DOI: 10.1007/s12303-011-0023-y.

[208] X. Huang, F. Wang, S. Hu, Y. Lu, M. Rao, and Y. Mu. "Brownmillerite hydration in the presence of gypsum: The effect of Al/Fe ratio and sulfate ions." In: *Journal of the American Ceramic Society* 102.9 (2019), pp. 5545–5554. ISSN: 0002-7820. DOI: 10.1111/jace.16384.

[209] E. L. Shock, D. C. Sassani, M. Willis, and D. A. Sverjensky. "Inorganic species in geologic fluids: Correlations among standard molal thermodynamic properties of aqueous ions and hydroxide complexes." In: *Geochimica et Cosmochimica Acta* 61.5 (1997), pp. 907–950. ISSN: 00167037. DOI: 10.1016/S0016-7037(96)00339-0.

[210] P. A. Terry. "Characterization of Cr ion exchange with hydrotalcite." In: *Chemosphere* 57.7 (2004), pp. 541–546. ISSN: 00456535. DOI: 10.1016/j.chemosphere.2004.08.006.

[211] D. Rogers and L. Aldridge. "Hydrates of calcium ferrites and calcium aluminoferrites." In: *Cement and Concrete Research* 7.4 (1977), pp. 399–409. ISSN: 00088846. DOI: 10.1016/0008-8846(77)90068-0.

[212] N. Noguchi, K. Siventhirarajah, T. Chabayashi, H. Kato, T. Nawa, and Y. Elakneswaran. "Hydration of ferrite-rich Portland cement: Evaluation of Fe-hydrates and Fe uptake in calcium-silicate-hydrates." In: *Construction and Building Materials* 288 (2021), p. 123142. ISSN: 09500618. DOI: 10.1016/j.conbuildmat.2021.123142.

[213] B. Dilnesa, E. Wieland, B. Lothenbach, R. Dähn, and K. Scrivener. "Fe-containing phases in hydrated cements." In: *Cement and Concrete Research* 58 (2014), pp. 45–55. ISSN: 00088846. DOI: 10.1016/j.cemconres.2013.12.012.

[214] K. Rozov, U. Berner, C. Taviot-Gueho, F. Leroux, G. Renaudin, D. Kulik, and L. Diamond. "Synthesis and characterization of the LDH hydrotalcite–pyroaurite solid-solution series." In: *Cement and Concrete Research* 40.8 (2010), pp. 1248–1254. ISSN: 00088846. DOI: 10.1016/j.cemconres.2009.08.031.

[215] G. Yu, Y. Zhou, R. Yang, M. Wang, L. Shen, Y. Li, N. Xue, X. Guo, W. Ding, and L. Peng. "Dehydration and Dehydroxylation of Layered Double Hydroxides: New Insights from Solid-State NMR and FT-IR Studies of Deuterated Samples." In: *The Journal of Physical Chemistry C* 119.22 (2015), pp. 12325–12334. ISSN: 1932-7447. DOI: 10.1021/acs.jpcc.5b01449.

[216] Z. Wensheng, R. Xuehong, and O. Shixi. " Development on Ion Substitution Effect on the Crystal Structure and Properties of Tricalcium Silicate." In: (). DOI: 10.14062/j.issn.0454-5648.2011.10.023.

[217] C. Liu, S. Huang, P. Wollants, B. Blanpain, and M. Guo. "Valorization of BOF Steel Slag by Reduction and Phase Modification: Metal Recovery and Slag Valorization." In: *Metallurgical and Materials Transactions B* 48.3 (2017), pp. 1602–1612. ISSN: 1073-5615. DOI: 10.1007/s11663-017-0966-0.

[218] J. Zepper, S. van der Laan, K. Schollbach, and H. Brouwers. "Reactivity of BOF slag under autoclaving conditions." In: *Construction and Building Materials* 364 (2023), p. 129957. ISSN: 09500618. DOI: 10.1016/j.conbuildmat.2022.129957.

[219] M. J. Ahmed, R. Cuijpers, K. Schollbach, S. Van Der Laan, M. Van Wijngaarden-Kroft, T. Verhoeven, and H. Brouwers. "V and Cr substitution in dicalcium silicate under oxidizing and reducing conditions – Synthesis, reactivity, and leaching behavior studies." In: *Journal of Hazardous Materials* 442 (2023), p. 130032. ISSN: 03043894. DOI: 10.1016/j.jhazmat.2022.130032.

[220] E. Rodrigues, O. Almeida, H. Brasil, D. Moraes, and M. dos Reis. "Adsorption of chromium (VI) on hydrotalcite-hydroxyapatite material doped with carbon nanotubes: Equilibrium, kinetic and thermodynamic study." In: *Applied Clay Science* 172 (2019), pp. 57–64. ISSN: 01691317. DOI: 10.1016/j.clay.2019.02.018.

[221] A.-M. Fällman. "Leaching of chromium and barium from steel slag in laboratory and field tests — a solubility controlled process?" In: *Waste Management* 20.2-3 (2000), pp. 149–154. ISSN: 0956053X. DOI: 10.1016/S0956-053X(99)00313-X.

[222] E. Kim, J. Spooren, K. Broos, L. Horckmans, M. Quaghebeur, and K. Vrancken. "Selective recovery of Cr from stainless steel slag by alkaline roasting followed by water leaching." In: *Hydrometallurgy* 158 (2015), pp. 139–148. ISSN: 0304386X. DOI: 10.1016/j.hydromet.2015.10.024.

[223] W. Shen, L. Cao, Q. Li, W. Zhang, G. Wang, and C. Li. "Quantifying CO2 emissions from China's cement industry." In: *Renewable and Sustainable Energy Reviews* 50 (2015), pp. 1004–1012. ISSN: 13640321. DOI: 10.1016/j.rser.2015.05.031.

[224] E. Benhelal, G. Zahedi, E. Shamsaei, and A. Bahadori. "Global strategies and potentials to curb CO2 emissions in cement industry." In: *Journal of Cleaner Production* 51 (2013), pp. 142–161. ISSN: 09596526. DOI: 10.1016/j.jclepro.2012.10.049.

[225] L. Chen, G. Msigwa, M. Yang, A. I. Osman, S. Fawzy, D. W. Rooney, and P.-S. Yap. "Strategies to achieve a carbon neutral society: a review." In: *Environmental Chemistry Letters* 20.4 (2022), pp. 2277–2310. ISSN: 1610-3653. DOI: 10.1007/s10311-022-01435-8.

[226] M. Schneider, M. Romer, M. Tschudin, and H. Bolio. "Sustainable cement production—present and future." In: *Cement and Concrete Research* 41.7 (2011), pp. 642–650. ISSN: 00088846. DOI: 10.1016/j.cemconres.2011.03.019.

[227] L. Rosa, V. Becattini, P. Gabrielli, A. Andreotti, and M. Mazzotti. "Carbon dioxide mineralization in recycled concrete aggregates can contribute immediately to carbon-neutrality." In: *Resources, Conservation and Recycling* 184 (2022), p. 106436. ISSN: 09213449. DOI: 10.1016/j.resconrec.2022.106436.

[228] F. Belaïd. "How does concrete and cement industry transformation contribute to mitigating climate change challenges?" In: *Resources, Conservation & Recycling Advances* 15 (2022), p. 200084. ISSN: 26673789. DOI: 10.1016/j.rcradv.2022.200084.

[229] A. Favier, C. De Wolf, K. Scrivener, and G. Habert. "A sustainable future for the European Cement and Concrete Industry." In: (). DOI: doi.org/10.3929/ethz-b-000301843.

[230] L. Kriskova, Y. Pontikes, F. Zhang, Ö. Cizer, P. T. Jones, K. Van Balen, and B. Blanpain. "Influence of mechanical and chemical activation on the hydraulic properties of gamma dicalcium silicate." In: *Cement and Concrete Research* 55 (2014), pp. 59–68. DOI: 10.1016/J.CEMCONRES.2013.10.004.

[231] D. Durinck, P. T. Jones, B. Blanpain, and P. Wollants. "Air-Cooling of Metallurgical Slags Containing Multivalent Oxides." In: *Journal of the American Ceramic Society* 91.10 (2008), pp. 3342–3348. ISSN: 0002-7820. DOI: 10.1111/j.1551-2916.2008.02597.x.

[232] B. Pang, Z. Zhou, and H. Xu. "Utilization of carbonated and granulated steel slag aggregate in concrete." In: *Construction and Building Materials* 84 (2015), pp. 454–467. ISSN: 09500618. DOI: 10.1016/j.conbuildmat.2015.03.008.

[233] D. Jiao, C. Shi, Q. Yuan, X. An, Y. Liu, and H. Li. "Effect of constituents on rheological properties of fresh concrete-A review." In: *Cement and Concrete Composites* 83 (2017), pp. 146–159. DOI: 10.1016/j.cemconcomp.2017.07.016.

[234] L. R. C. Tavares, J. F. T. Junior, L. M. Costa, A. C. da Silva Bezerra, P. R. Cetlin, and M. T. P. Aguilar. "Influence of quartz powder and silica fume on the performance of Portland cement." In: *Scientific Reports* 10.1 (2020), p. 21461. ISSN: 2045-2322. DOI: 10.1038/s41598-020-78567-w.

[235] S. Z. Carvalho, F Vernilli, B Almeida, M. D. Oliveira, and S. N. Silva. "Reducing environmental impacts : The use of basic oxygen furnace slag in portland cement." In: *Journal of Cleaner Production* 172 (2018), pp. 385–390. DOI: 10.1016/j.jclepro.2017.10.130.

[236] S. Kourounis, S. Tsivilis, P. Tsakiridis, G. Papadimitriou, and Z. Tsibouki. "Properties and hydration of blended cements with steelmaking slag." In: *Cement and Concrete Research* 37.6 (2007), pp. 815–822. ISSN: 00088846. DOI: 10.1016/j.cemconres.2007.03.008.

[237] Y. Wang and P. Suraneni. "Experimental methods to determine the feasibility of steel slags as supplementary cementitious materials." In: *Construction and Building Materials* 204 (2019), pp. 458–467. ISSN: 09500618. DOI: 10.1016/j.conbuildmat.2019.01.196.

[238] T. H. Lu, Y. L. Chen, P. H. Shih, and J. E. Chang. "Use of basic oxygen furnace slag fines in the production of cementitious mortars and the effects on mortar expansion." In: *Construction and Building Materials* 167 (2018), pp. 768–774. DOI: 10.1016/J.CONBUILDMAT.2018.02.102.

[239] S. Liu and L. Li. "Influence of fineness on the cementitious properties of steel slag." In: *Journal of Thermal Analysis and Calorimetry* 117.2 (2014), pp. 629–634. ISSN: 1388-6150. DOI: 10.1007/s10973-014-3789-0.

[240] L. Chen, H. Wang, K. Zheng, J. Zhou, F. He, and Q. Yuan. "The mechanism of basic oxygen furnace steel slag retarding early-age hydration of Portland cement and mitigating approach towards higher utilization rate." In: *Journal of Cleaner Production* 362 (2022), p. 132493. ISSN: 09596526. DOI: 10.1016/j.jclepro.2022.132493.

[241] G. Möschner, B. Lothenbach, F. Winnefeld, A. Ulrich, R. Figi, and R. Kretzschmar. "Solid solution between Al-ettringite and Fe-ettringite (Ca6[Al1xFex(OH)6]2(SO4)3·26H2O)." In: *Cement and Concrete Research* 39.6 (2009), pp. 482–489. ISSN: 00088846. DOI: 10.1016/j.cemconres.2009.03.001.

[242] T. Matschei, B. Lothenbach, and F. P. Glasser. "Thermodynamic properties of Portland cement hydrates in the system CaO–Al2O3–SiO2–CaSO4–CaCO3–H2O." In: *Cement and Concrete Research* 37.10 (2007), pp. 1379–1410. ISSN: 00088846. DOI: 10.1016/j.cemconres.2007.06.002.

[243] F. Han and Z. Zhang. "Properties of 5-year-old concrete containing steel slag powder." In: *Powder Technology* 334 (2018), pp. 27–35. ISSN: 00325910. DOI: 10.1016/j.powtec.2018.04.054.

[244] F. Deschner, B. Lothenbach, F. Winnefeld, and J. Neubauer. "Effect of temperature on the hydration of Portland cement blended with siliceous fly ash." In: *Cement and Concrete Research* 52 (2013), pp. 169–181. ISSN: 00088846. DOI: 10.1016/j.cemconres.2013.07.006.

[245] B. Z. Dilnesa. "Fe-containing Hydrates and their Fate during Cement Hydration." In: (2012). DOI: 10.5075/EPFL-THESIS-5262.

[246] C. W. Hargis, B. Lothenbach, C. J. Müller, and F. Winnefeld. "Carbonation of calcium sulfoaluminate mortars." In: *Cement and Concrete Composites* 80 (2017), pp. 123–134. ISSN: 09589465. DOI: 10.1016/j.cemconcomp.2017.03.003.

[247] A. Telesca, T. Matschei, and M. Marroccoli. "Study of Eco-Friendly Belite-Calcium Sulfoaluminate Cements Obtained from Special Wastes." In: *Applied Sciences* 10.23 (2020), p. 8650. ISSN: 2076-3417. DOI: 10.3390/app10238650.

[248] R. Iacobescu, Y. Pontikes, D. Koumpouri, and G. Angelopoulos. "Synthesis, characterization and properties of calcium ferroaluminate belite cements produced with electric arc furnace steel slag as raw material." In: *Cement and Concrete Composites* 44 (2013), pp. 1–8. ISSN: 09589465. DOI: 10.1016/j.cemconcomp.2013.08.002.

[249] L. Chi, Z. Wang, S. Lu, H. Wang, K. Liu, and W. Liu. "Early assessment of hydration and microstructure evolution of belite-calcium sulfoaluminate cement pastes by electrical impedance spectroscopy." In: *Electrochimica Acta* 389 (2021), p. 138699. ISSN: 00134686. DOI: 10.1016/j.electacta.2021.138699.

[250] J. Guo, Y. Bao, and M. Wang. "Steel slag in China: Treatment, recycling, and management." In: *Waste Management* 78 (2018), pp. 318–330. DOI: 10.1016/J.WASMAN.2018.04.045.

[251] *Slagreus – Reuse of slags from integrated steelmaking | BFI EN*. URL: https://www.bfi.de/en/projects/slagreus-reuse-of-slags-from-integrated-steelmaking/ (visited on 11/20/2022).

[252] H. Wulfert, H. M. Ludwig, and G. Wimmer. "A new process for production of cement clinker from steelmaking slags." In: *Cement International* (2017). ISSN: 16106199.

[253] P. Xue, A. Xu, D. He, Q. Yang, G. Liu, F. Engström, and B. Björkman. "Research on the sintering process and characteristics of belite sulphoaluminate cement produced by BOF slag." In: *Construction and Building Materials* 122 (2016), pp. 567–576. ISSN: 09500618. DOI: 10.1016/j.conbuildmat.2016.06.098.

[254] A. C. P. Martins, J. M. Franco de Carvalho, M. d. N. Duarte, G. E. S. de Lima, L. G. Pedroti, and R. A. F. Peixoto. "Influence of a LAS-based modifying admixture on cement-based composites containing steel slag powder." In: *Journal of Building Engineering* 53 (2022), p. 104517. ISSN: 23527102. DOI: 10.1016/j.jobe.2022.104517.

[255] Y. Liao, G. Jiang, K. Wang, S. Al Qunaynah, and W. Yuan. "Effect of steel slag on the hydration and strength development of calcium sulfoaluminate cement." In: *Construction and Building Materials* 265 (2020), p. 120301. ISSN: 09500618. DOI: 10.1016/j.conbuildmat.2020.120301.

[256] C. W. Hargis, A. Telesca, and P. J. Monteiro. "Calcium sulfoaluminate (Ye'elimite) hydration in the presence of gypsum, calcite, and vaterite." In: *Cement and Concrete Research* 65 (2014), pp. 15–20. ISSN: 00088846. DOI: 10.1016/j.cemconres.2014.07.004.

[257] S. Peysson, J. Péra, and M. Chabannet. "Immobilization of heavy metals by calcium sulfoaluminate cement." In: *Cement and Concrete Research* 35.12 (2005), pp. 2261–2270. ISSN: 00088846. DOI: 10.1016/j.cemconres.2005.03.015.

[258] C. Liu, S. Huang, B. Blanpain, and M. Guo. "Effect of Al2O3 Addition on Mineralogical Modification and Crystallization Kinetics of a High Basicity BOF Steel Slag." In: *Metallurgical and Materials Transactions B* 50.1 (2019), pp. 271–281. ISSN: 1073-5615. DOI: 10.1007/s11663-018-1465-7.

[259] S. Kourounis, S. Tsivilis, P. Tsakiridis, G. Papadimitriou, and Z. Tsibouki. "Properties and hydration of blended cements with steelmaking slag." In: *Cement and Concrete Research* 37.6 (2007), pp. 815–822. ISSN: 00088846. DOI: 10.1016/j.cemconres.2007.03.008.

[260] K. Quillin. "Performance of belite–sulfoaluminate cements." In: *Cement and Concrete Research* 31.9 (2001), pp. 1341–1349. ISSN: 00088846. DOI: 10.1016/S0008-8846(01)00543-9.

[261] J. Feng and J. Sun. "A comparison of the 10-year properties of converter steel slag activated by high temperature and an alkaline activator." In: *Construction and Building Materials* 234 (2020), p. 116948. ISSN: 09500618. DOI: 10.1016/j.conbuildmat.2019.116948.

[262] M. Borštnar, C. L. Lengauer, and S. Dolenec. "Quantitative in Situ X-ray Diffraction Analysis of Early Hydration of Belite-Calcium Sulfoaluminate Cement at Various Defined Temperatures." In: *Minerals* 11.3 (2021), p. 297. ISSN: 2075-163X. DOI: 10.3390/min11030297.

[263] F. Song, Z. Yu, F. Yang, Y. Lu, and Y. Liu. "Microstructure of amorphous aluminum hydroxide in belite-calcium sulfoaluminate cement." In: *Cement and Concrete Research* 71 (2015), pp. 1–6. ISSN: 00088846. DOI: 10.1016/j.cemconres.2015.01.013.

[264] I. Santacruz, Á. G. D. la Torre, G. Álvarez-Pinazo, A. Cabeza, A. Cuesta, J. Sanz, and M. A. G. Aranda. "Structure of stratlingite and effect of hydration methodology on microstructure." In: *Advances in Cement Research* 28.1 (2016), pp. 13–22. ISSN: 0951-7197. DOI: 10.1680/adcr.14.00104.

[265] D. Sirtoli, M. Wyrzykowski, P. Riva, and P. Lura. "Autogenous and drying shrinkage of mortars based on Portland and calcium sulfoaluminate cements." In: *Materials and Structures* 53.5 (2020), p. 126. ISSN: 1359-5997. DOI: 10.1617/s11527-020-01561-1.

[266] K. Piekkari, K. Ohenoja, V. Isteri, P. Tanskanen, and M. Illikainen. "Immobilization of heavy metals, selenate, and sulfate from a hazardous industrial side stream by using calcium sulfoaluminate-belite cement." In: *Journal of Cleaner Production* 258 (2020), p. 120560. ISSN: 09596526. DOI: 10.1016/j.jclepro.2020.120560.

[267] S. Peysson, J. Péra, and M. Chabannet. "Immobilization of heavy metals by calcium sulfoaluminate cement." In: *Cement and Concrete Research* 35.12 (2005), pp. 2261–2270. ISSN: 0008-8846. DOI: 10.1016/J.CEMCONRES.2005.03.015.

[268] H. Shen and E. Forssberg. "An overview of recovery of metals from slags." In: *Waste Management* 23.10 (2003), pp. 933–949. ISSN: 0956053X. DOI: 10.1016/S0956-053X(02)00164-2.

[269] T. S. Naidu, C. M. Sheridan, and L. D. van Dyk. "Basic oxygen furnace slag: Review of current and potential uses." In: *Minerals Engineering* 149 (2020), p. 106234. ISSN: 0892-6875. DOI: 10.1016/J.MINENG.2020.106234.

[270] X. Li, H. Huang, J. Xu, S. Ma, and X. Shen. "Statistical research on phase formation and modification of alite polymorphs in cement clinker with SO3and MgO." In: *Construction and Building Materials* (2012). ISSN: 09500618. DOI: 10.1016/j.conbuildmat.2012.07.099.

CURRICULUM VITAE

M. Jawad Ahmed was born in 1989 in Gujranwala, Pakistan. He obtained his bachelor of science degree (first division) in chemistry from the university of the Punjab, Pakistan in 2011. His bachelor thesis focused on the determination of heavy metals in industrial waste flora of Sialkot region, Pakistan. Afterward, he worked in different capacities as a chemistry teacher, lecturer, and headmaster alongside obtaining a diploma in teaching. In 2015, he got a fully funded scholarship from the international master's degree program for research chemists at the University of Eastern Finland, Joensuu, Finland. He graduated with a master of science degree in the field of inorganic chemistry from the University of Eastern Finland, Joensuu, Finland in 2017. His master's thesis was focused on the synthesis and characterization of d10 luminescent complexes built novel polyaromatic diphosphine ligands. From 2018 to 2023, he started a Ph.D. project in the Building Materials research group under the supervision of prof.dr.ir. H.J.H. Brouwers at the Eindhoven University of Technology, Eindhoven, the Netherlands. The results of this study are presented in this dissertation.

Bouwstenen is een publicatiereeks van de Faculteit Bouwkunde, Technische Universiteit Eindhoven. Zij presenteert resultaten van onderzoek en andere activiteiten op het vakgebied der Bouwkunde, uitgevoerd in het kader van deze Faculteit.

Bouwstenen en andere proefschriften van de TU/e zijn online beschikbaar via: https://research.tue.nl/

Reeds verschenen in de serie
Bouwstenen

nr 1
Elan: A Computer Model for Building Energy Design: Theory and Validation
Martin H. de Wit
H.H. Driessen
R.M.M. van der Velden

nr 2
Kwaliteit, Keuzevrijheid en Kosten: Evaluatie van Experiment Klarendal, Arnhem
J. Smeets
C. le Nobel
M. Broos
J. Frenken
A. v.d. Sanden

nr 3
Crooswijk: Van 'Bijzonder' naar 'Gewoon'
Vincent Smit
Kees Noort

nr 4
Staal in de Woningbouw
Edwin J.F. Delsing

nr 5
Mathematical Theory of Stressed Skin Action in Profiled Sheeting with Various Edge Conditions
Andre W.A.M.J. van den Bogaard

nr 6
Hoe Berekenbaar en Betrouwbaar is de Coëfficiënt k in x-ksigma en x-ks?
K.B. Lub
A.J. Bosch

nr 7
Het Typologisch Gereedschap: Een Verkennende Studie Omtrent Typologie en Omtrent de Aanpak van Typologisch Onderzoek
J.H. Luiten

nr 8
Informatievoorziening en Beheerprocessen
A. Nauta
Jos Smeets (red.)
Helga Fassbinder (projectleider)
Adrie Proveniers
J. v.d. Moosdijk

nr 9
Strukturering en Verwerking van Tijdgegevens voor de Uitvoering van Bouwwerken
ir. W.F. Schaefer
P.A. Erkelens

nr 10
Stedebouw en de Vorming van een Speciale Wetenschap
K. Doevendans

nr 11
Informatica en Ondersteuning van Ruimtelijke Besluitvorming
G.G. van der Meulen

nr 12
Staal in de Woningbouw, Korrosie-Bescherming van de Begane Grondvloer
Edwin J.F. Delsing

nr 13
Een Thermisch Model voor de Berekening van Staalplaatbetonvloeren onder Brandomstandigheden
A.F. Hamerlinck

nr 14
De Wijkgedachte in Nederland: Gemeenschapsstreven in een Stedebouwkundige Context
K. Doevendans
R. Stolzenburg

nr 15
Diaphragm Effect of Trapezoidally Profiled Steel Sheets: Experimental Research into the Influence of Force Application
Andre W.A.M.J. van den Bogaard

nr 16
Versterken met Spuit-Ferrocement: Het Mechanische Gedrag van met Spuit-Ferrocement Versterkte Gewapend Betonbalken
K.B. Lubir
M.C.G. van Wanroy

nr 17
De Tractaten van Jean Nicolas Louis Durand
G. van Zeyl

nr 18
Wonen onder een Plat Dak: Drie Opstellen over Enkele Vooronderstellingen van de Stedebouw
K. Doevendans

nr 19
Supporting Decision Making Processes: A Graphical and Interactive Analysis of Multivariate Data
W. Adams

nr 20
Self-Help Building Productivity: A Method for Improving House Building by Low-Income Groups Applied to Kenya 1990-2000
P. A. Erkelens

nr 21
De Verdeling van Woningen: Een Kwestie van Onderhandelen
Vincent Smit

nr 22
Flexibiliteit en Kosten in het Ontwerpproces: Een Besluitvormingondersteunend Model
M. Prins

nr 23
Spontane Nederzettingen Begeleid: Voorwaarden en Criteria in Sri Lanka
Po Hin Thung

nr 24
Fundamentals of the Design of Bamboo Structures
Oscar Arce-Villalobos

nr 25
Concepten van de Bouwkunde
M.F.Th. Bax (red.)
H.M.G.J. Trum (red.)

nr 26
Meaning of the Site
Xiaodong Li

nr 27
Het Woonmilieu op Begrip Gebracht: Een Speurtocht naar de Betekenis van het Begrip 'Woonmilieu'
Jaap Ketelaar

nr 28
Urban Environment in Developing Countries
editors: Peter A. Erkelens
George G. van der Meulen (red.)

nr 29
Stategische Plannen voor de Stad: Onderzoek en Planning in Drie Steden
prof.dr. H. Fassbinder (red.)
H. Rikhof (red.)

nr 30
Stedebouwkunde en Stadsbestuur
Piet Beekman

nr 31
De Architectuur van Djenné: Een Onderzoek naar de Historische Stad
P.C.M. Maas

nr 32
Conjoint Experiments and Retail Planning
Harmen Oppewal

nr 33
Strukturformen Indonesischer Bautechnik: Entwicklung Methodischer Grundlagen für eine 'Konstruktive Pattern Language' in Indonesien
Heinz Frick arch. SIA

nr 34
Styles of Architectural Designing: Empirical Research on Working Styles and Personality Dispositions
Anton P.M. van Bakel

nr 35
Conjoint Choice Models for Urban Tourism Planning and Marketing
Benedict Dellaert

nr 36
Stedelijke Planvorming als Co-Produktie
Helga Fassbinder (red.)

nr 37
Design Research in the Netherlands
editors: R.M. Oxman
M.F.Th. Bax
H.H. Achten

nr 38
Communication in the Building Industry
Bauke de Vries

nr 39
Optimaal Dimensioneren van Gelaste Plaatliggers
J.B.W. Stark
F. van Pelt
L.F.M. van Gorp
B.W.E.M. van Hove

nr 40
Huisvesting en Overwinning van Armoede
P.H. Thung
P. Beekman (red.)

nr 41
Urban Habitat: The Environment of Tomorrow
George G. van der Meulen
Peter A. Erkelens

nr 42
A Typology of Joints
John C.M. Olie

nr 43
Modeling Constraints-Based Choices for Leisure Mobility Planning
Marcus P. Stemerding

nr 44
Activity-Based Travel Demand Modeling
Dick Ettema

nr 45
Wind-Induced Pressure Fluctuations on Building Facades
Chris Geurts

nr 46
Generic Representations
Henri Achten

nr 47
Johann Santini Aichel: Architectuur en Ambiguiteit
Dirk De Meyer

nr 48
Concrete Behaviour in Multiaxial Compression
Erik van Geel

nr 49
Modelling Site Selection
Frank Witlox

nr 50
Ecolemma Model
Ferdinand Beetstra

nr 51
Conjoint Approaches to Developing Activity-Based Models
Donggen Wang

nr 52
On the Effectiveness of Ventilation
Ad Roos

nr 53
Conjoint Modeling Approaches for Residential Group preferences
Eric Molin

nr 54
Modelling Architectural Design Information by Features
Jos van Leeuwen

nr 55
A Spatial Decision Support System for the Planning of Retail and Service Facilities
Theo Arentze

nr 56
Integrated Lighting System Assistant
Ellie de Groot

nr 57
Ontwerpend Leren, Leren Ontwerpen
J.T. Boekholt

nr 58
Temporal Aspects of Theme Park Choice Behavior
Astrid Kemperman

nr 59
Ontwerp van een Geïndustrialiseerde Funderingswijze
Faas Moonen

nr 60
Merlin: A Decision Support System for Outdoor Leisure Planning
Manon van Middelkoop

nr 61
The Aura of Modernity
Jos Bosman

nr 62
Urban Form and Activity-Travel Patterns
Daniëlle Snellen

nr 63
Design Research in the Netherlands 2000
Henri Achten

nr 64
Computer Aided Dimensional Control in Building Construction
Rui Wu

nr 65
Beyond Sustainable Building
editors: Peter A. Erkelens
Sander de Jonge
August A.M. van Vliet
co-editor: Ruth J.G. Verhagen

nr 66
Das Globalrecyclingfähige Haus
Hans Löfflad

nr 67
Cool Schools for Hot Suburbs
René J. Dierkx

nr 68
A Bamboo Building Design Decision Support Tool
Fitri Mardjono

nr 69
Driving Rain on Building Envelopes
Fabien van Mook

nr 70
Heating Monumental Churches
Henk Schellen

nr 71
Van Woningverhuurder naar Aanbieder van Woongenot
Patrick Dogge

nr 72
Moisture Transfer Properties of Coated Gypsum
Emile Goossens

nr 73
Plybamboo Wall-Panels for Housing
Guillermo E. González-Beltrán

nr 74
The Future Site-Proceedings
Ger Maas
Frans van Gassel

nr 75
Radon transport in Autoclaved Aerated Concrete
Michel van der Pal

nr 76
The Reliability and Validity of Interactive Virtual Reality Computer Experiments
Amy Tan

nr 77
Measuring Housing Preferences Using Virtual Reality and Belief Networks
Maciej A. Orzechowski

nr 78
Computational Representations of Words and Associations in Architectural Design
Nicole Segers

nr 79
Measuring and Predicting Adaptation in Multidimensional Activity-Travel Patterns
Chang-Hyeon Joh

nr 80
Strategic Briefing
Fayez Al Hassan

nr 81
Well Being in Hospitals
Simona Di Cicco

nr 82
Solares Bauen: Implementierungs- und Umsetzungs-Aspekte in der Hochschulausbildung in Österreich
Gerhard Schuster

nr 83
Supporting Strategic Design of Workplace Environments with Case-Based Reasoning
Shauna Mallory-Hill

nr 84
ACCEL: A Tool for Supporting Concept Generation in the Early Design Phase
Maxim Ivashkov

nr 85
Brick-Mortar Interaction in Masonry under Compression
Ad Vermeltfoort

nr 86
Zelfredzaam Wonen
Guus van Vliet

nr 87
Een Ensemble met Grootstedelijke Allure
Jos Bosman
Hans Schippers

nr 88
On the Computation of Well-Structured Graphic Representations in Architectural Design
Henri Achten

nr 89
De Evolutie van een West-Afrikaanse Vernaculaire Architectuur
Wolf Schijns

nr 90
ROMBO Tactiek
Christoph Maria Ravesloot

nr 91
External Coupling between Building Energy Simulation and Computational Fluid Dynamics
Ery Djunaedy

nr 92
Design Research in the Netherlands 2005
editors: Henri Achten
Kees Dorst
Pieter Jan Stappers
Bauke de Vries

nr 93
Ein Modell zur Baulichen Transformation
Jalil H. Saber Zaimian

nr 94
Human Lighting Demands: Healthy Lighting in an Office Environment
Myriam Aries

nr 95
A Spatial Decision Support System for the Provision and Monitoring of Urban Greenspace
Claudia Pelizaro

nr 96
Leren Creëren
Adri Proveniers

nr 97
Simlandscape
Rob de Waard

nr 98
Design Team Communication
Ad den Otter

nr 99
Humaan-Ecologisch Georiënteerde Woningbouw
Juri Czabanowski

nr 100
Hambase
Martin de Wit

nr 101
Sound Transmission through Pipe Systems and into Building Structures
Susanne Bron-van der Jagt

nr 102
Het Bouwkundig Contrapunt
Jan Francis Boelen

nr 103
A Framework for a Multi-Agent Planning Support System
Dick Saarloos

nr 104
Bracing Steel Frames with Calcium Silicate Element Walls
Bright Mweene Ng'andu

nr 105
Naar een Nieuwe Houtskeletbouw
F.N.G. De Medts

nr 106 and 107
Niet gepubliceerd

nr 108
Geborgenheid
T.E.L. van Pinxteren

nr 109
Modelling Strategic Behaviour in Anticipation of Congestion
Qi Han

nr 110
Reflecties op het Woondomein
Fred Sanders

nr 111
On Assessment of Wind Comfort by Sand Erosion
Gábor Dezsö

nr 112
Bench Heating in Monumental Churches
Dionne Limpens-Neilen

nr 113
RE. Architecture
Ana Pereira Roders

nr 114
Toward Applicable Green Architecture
Usama El Fiky

nr 115
Knowledge Representation under Inherent Uncertainty in a Multi-Agent System for Land Use Planning
Liying Ma

nr 116
Integrated Heat Air and Moisture Modeling and Simulation
Jos van Schijndel

nr 117
Concrete Behaviour in Multiaxial Compression
J.P.W. Bongers

nr 118
The Image of the Urban Landscape
Ana Moya Pellitero

nr 119
The Self-Organizing City in Vietnam
Stephanie Geertman

nr 120
A Multi-Agent Planning Support System for Assessing Externalities of Urban Form Scenarios
Rachel Katoshevski-Cavari

nr 121
Den Schulbau Neu Denken, Fühlen und Wollen
Urs Christian Maurer-Dietrich

nr 122
Peter Eisenman Theories and Practices
Bernhard Kormoss

nr 123
User Simulation of Space Utilisation
Vincent Tabak

nr 125
In Search of a Complex System Model
Oswald Devisch

nr 126
Lighting at Work: Environmental Study of Direct Effects of Lighting Level and Spectrum on Psycho-Physiological Variables
Grazyna Górnicka

nr 127
Flanking Sound Transmission through Lightweight Framed Double Leaf Walls
Stefan Schoenwald

nr 128
Bounded Rationality and Spatio-Temporal Pedestrian Shopping Behavior
Wei Zhu

nr 129
Travel Information: Impact on Activity Travel Pattern
Zhongwei Sun

nr 130
Co-Simulation for Performance Prediction of Innovative Integrated Mechanical Energy Systems in Buildings
Marija Trčka

nr 131
Niet gepubliceerd

nr 132
Architectural Cue Model in Evacuation Simulation for Underground Space Design
Chengyu Sun

nr 133
Uncertainty and Sensitivity Analysis in Building Performance Simulation for Decision Support and Design Optimization
Christina Hopfe

nr 134
Facilitating Distributed Collaboration in the AEC/FM Sector Using Semantic Web Technologies
Jacob Beetz

nr 135
Circumferentially Adhesive Bonded Glass Panes for Bracing Steel Frame in Façades
Edwin Huveners

nr 136
Influence of Temperature on Concrete Beams Strengthened in Flexure with CFRP
Ernst-Lucas Klamer

nr 137
Sturen op Klantwaarde
Jos Smeets

nr 139
Lateral Behavior of Steel Frames with Discretely Connected Precast Concrete Infill Panels
Paul Teewen

nr 140
Integral Design Method in the Context of Sustainable Building Design
Perica Savanović

nr 141
Household Activity-Travel Behavior: Implementation of Within-Household Interactions
Renni Anggraini

nr 142
Design Research in the Netherlands 2010
Henri Achten

nr 143
Modelling Life Trajectories and Transport Mode Choice Using Bayesian Belief Networks
Marloes Verhoeven

nr 144
Assessing Construction Project Performance in Ghana
William Gyadu-Asiedu

nr 145
Empowering Seniors through Domotic Homes
Masi Mohammadi

nr 146
An Integral Design Concept for Ecological Self-Compacting Concrete
Martin Hunger

nr 147
Governing Multi-Actor Decision Processes in Dutch Industrial Area Redevelopment
Erik Blokhuis

nr 148
A Multifunctional Design Approach for Sustainable Concrete
Götz Hüsken

nr 149
Quality Monitoring in Infrastructural Design-Build Projects
Ruben Favié

nr 150
Assessment Matrix for Conservation of Valuable Timber Structures
Michael Abels

nr 151
Co-simulation of Building Energy Simulation and Computational Fluid Dynamics for Whole-Building Heat, Air and Moisture Engineering
Mohammad Mirsadeghi

nr 152
External Coupling of Building Energy Simulation and Building Element Heat, Air and Moisture Simulation
Daniel Cóstola

nr 153
Adaptive Decision Making In Multi-Stakeholder Retail Planning
Ingrid Janssen

nr 154
Landscape Generator
Kymo Slager

nr 155
Constraint Specification in Architecture
Remco Niemeijer

nr 156
A Need-Based Approach to Dynamic Activity Generation
Linda Nijland

nr 157
Modeling Office Firm Dynamics in an Agent-Based Micro Simulation Framework
Gustavo Garcia Manzato

nr 158
Lightweight Floor System for Vibration Comfort
Sander Zegers

nr 159
Aanpasbaarheid van de Draagstructuur
Roel Gijsbers

nr 160
'Village in the City' in Guangzhou, China
Yanliu Lin

nr 161
Climate Risk Assessment in Museums
Marco Martens

nr 162
Social Activity-Travel Patterns
Pauline van den Berg

nr 163
Sound Concentration Caused by Curved Surfaces
Martijn Vercammen

nr 164
Design of Environmentally Friendly Calcium Sulfate-Based Building Materials: Towards an Improved Indoor Air Quality
Qingliang Yu

nr 165
Beyond Uniform Thermal Comfort on the Effects of Non-Uniformity and Individual Physiology
Lisje Schellen

nr 166
Sustainable Residential Districts
Gaby Abdalla

nr 167
Towards a Performance Assessment Methodology using Computational Simulation for Air Distribution System Designs in Operating Rooms
Mônica do Amaral Melhado

nr 168
Strategic Decision Modeling in Brownfield Redevelopment
Brano Glumac

nr 169
Pamela: A Parking Analysis Model for Predicting Effects in Local Areas
Peter van der Waerden

nr 170
A Vision Driven Wayfinding Simulation-System Based on the Architectural Features Perceived in the Office Environment
Qunli Chen

nr 171
Measuring Mental Representations Underlying Activity-Travel Choices
Oliver Horeni

nr 172
Modelling the Effects of Social Networks on Activity and Travel Behaviour
Nicole Ronald

nr 173
Uncertainty Propagation and Sensitivity Analysis Techniques in Building Performance Simulation to Support Conceptual Building and System Design
Christian Struck

nr 174
Numerical Modeling of Micro-Scale Wind-Induced Pollutant Dispersion in the Built Environment
Pierre Gousseau

nr 175
Modeling Recreation Choices over the Family Lifecycle
Anna Beatriz Grigolon

nr 176
Experimental and Numerical Analysis of Mixing Ventilation at Laminar, Transitional and Turbulent Slot Reynolds Numbers
Twan van Hooff

nr 177
Collaborative Design Support: Workshops to Stimulate Interaction and Knowledge Exchange Between Practitioners
Emile M.C.J. Quanjel

nr 178
Future-Proof Platforms for Aging-in-Place
Michiel Brink

nr 179
Motivate: A Context-Aware Mobile Application for Physical Activity Promotion
Yuzhong Lin

nr 180
Experience the City: Analysis of Space-Time Behaviour and Spatial Learning
Anastasia Moiseeva

nr 181
Unbonded Post-Tensioned Shear Walls of Calcium Silicate Element Masonry
Lex van der Meer

nr 182
Construction and Demolition Waste Recycling into Innovative Building Materials for Sustainable Construction in Tanzania
Mwita M. Sabai

nr 183
Durability of Concrete with Emphasis on Chloride Migration
Przemysław Spiesz

nr 184
Computational Modeling of Urban Wind Flow and Natural Ventilation Potential of Buildings
Rubina Ramponi

nr 185
A Distributed Dynamic Simulation Mechanism for Buildings Automation and Control Systems
Azzedine Yahiaoui

nr 186
Modeling Cognitive Learning of Urban Networks in Daily Activity-Travel Behavior
Şehnaz Cenani Durmazoğlu

nr 187
Functionality and Adaptability of Design Solutions for Public Apartment Buildings in Ghana
Stephen Agyefi-Mensah

nr 188
A Construction Waste Generation Model for Developing Countries
Lilliana Abarca-Guerrero

nr 189
Synchronizing Networks: The Modeling of Supernetworks for Activity-Travel Behavior
Feixiong Liao

nr 190
Time and Money Allocation Decisions in Out-of-Home Leisure Activity Choices
Gamze Zeynep Dane

nr 191
How to Measure Added Value of CRE and Building Design
Rianne Appel-Meulenbroek

nr 192
Secondary Materials in Cement-Based Products: Treatment, Modeling and Environmental Interaction
Miruna Florea

nr 193
Concepts for the Robustness Improvement of Self-Compacting Concrete: Effects of Admixtures and Mixture Components on the Rheology and Early Hydration at Varying Temperatures
Wolfram Schmidt

nr 194
Modelling and Simulation of Virtual Natural Lighting Solutions in Buildings
Rizki A. Mangkuto

nr 195
Nano-Silica Production at Low Temperatures from the Dissolution of Olivine - Synthesis, Tailoring and Modelling
Alberto Lazaro Garcia

nr 196
Building Energy Simulation Based Assessment of Industrial Halls for Design Support
Bruno Lee

nr 197
Computational Performance Prediction of the Potential of Hybrid Adaptable Thermal Storage Concepts for Lightweight Low-Energy Houses
Pieter-Jan Hoes

nr 198
Application of Nano-Silica in Concrete
George Quercia Bianchi

nr 199
Dynamics of Social Networks and Activity Travel Behaviour
Fariya Sharmeen

nr 200
Building Structural Design Generation and Optimisation including Spatial Modification
Juan Manuel Davila Delgado

nr 201
Hydration and Thermal Decomposition of Cement/Calcium-Sulphate Based Materials
Ariën de Korte

nr 202
Republiek van Beelden:
De Politieke Werkingen van het Ontwerp in Regionale Planvorming
Bart de Zwart

nr 203
Effects of Energy Price Increases on Individual Activity-Travel Repertoires and Energy Consumption
Dujuan Yang

nr 204
Geometry and Ventilation:
Evaluation of the Leeward Sawtooth Roof Potential in the Natural Ventilation of Buildings
Jorge Isaac Perén Montero

nr 205
Computational Modelling of Evaporative Cooling as a Climate Change Adaptation Measure at the Spatial Scale of Buildings and Streets
Hamid Montazeri

nr 206
Local Buckling of Aluminium Beams in Fire Conditions
Ronald van der Meulen

nr 207
Historic Urban Landscapes:
Framing the Integration of Urban and Heritage Planning in Multilevel Governance
Loes Veldpaus

nr 208
Sustainable Transformation of the Cities:
Urban Design Pragmatics to Achieve a Sustainable City
Ernesto Antonio Zumelzu Scheel

nr 209
Development of Sustainable Protective Ultra-High Performance Fibre Reinforced Concrete (UHPFRC):
Design, Assessment and Modeling
Rui Yu

nr 210
Uncertainty in Modeling Activity-Travel Demand in Complex Uban Systems
Soora Rasouli

nr 211
Simulation-based Performance Assessment of Climate Adaptive Greenhouse Shells
Chul-sung Lee

nr 212
Green Cities:
Modelling the Spatial Transformation of the Urban Environment using Renewable Energy Technologies
Saleh Mohammadi

nr 213
A Bounded Rationality Model of Short and Long-Term Dynamics of Activity-Travel Behavior
Ifigeneia Psarra

nr 214
Effects of Pricing Strategies on Dynamic Repertoires of Activity-Travel Behaviour
Elaheh Khademi

nr 215
Handstorm Principles for Creative and Collaborative Working
Frans van Gassel

nr 216
Light Conditions in Nursing Homes: Visual Comfort and Visual Functioning of Residents
Marianne M. Sinoo

nr 217
Woonsporen: De Sociale en Ruimtelijke Biografie van een Stedelijk Bouwblok in de Amsterdamse Transvaalbuurt
Hüseyin Hüsnü Yegenoglu

nr 218
Studies on User Control in Ambient Intelligent Systems
Berent Willem Meerbeek

nr 219
Daily Livings in a Smart Home: Users' Living Preference Modeling of Smart Homes
Erfaneh Allameh

nr 220
Smart Home Design: Spatial Preference Modeling of Smart Homes
Mohammadali Heidari Jozam

nr 221
Wonen: Discoursen, Praktijken, Perspectieven
Jos Smeets

nr 222
Personal Control over Indoor Climate in Offices: Impact on Comfort, Health and Productivity
Atze Christiaan Boerstra

nr 223
Personalized Route Finding in Multimodal Transportation Networks
Jianwe Zhang

nr 224
The Design of an Adaptive Healing Room for Stroke Patients
Elke Daemen

nr 225
Experimental and Numerical Analysis of Climate Change Induced Risks to Historic Buildings and Collections
Zara Huijbregts

nr 226
Wind Flow Modeling in Urban Areas Through Experimental and Numerical Techniques
Alessio Ricci

nr 227
Clever Climate Control for Culture: Energy Efficient Indoor Climate Control Strategies for Museums Respecting Collection Preservation and Thermal Comfort of Visitors
Rick Kramer

nr 228
Fatigue Life Estimation of Metal Structures Based on Damage Modeling
Sarmediran Silitonga

nr 229
A multi-agents and occupancy based strategy for energy management and process control on the room-level
Timilehin Moses Labeodan

nr 230
Environmental assessment of Building Integrated Photovoltaics: Numerical and Experimental Carrying Capacity Based Approach
Michiel Ritzen

nr 231
Performance of Admixture and Secondary Minerals in Alkali Activated Concrete: Sustaining a Concrete Future
Arno Keulen

nr 232
World Heritage Cities and Sustainable Urban Development:
Bridging Global and Local Levels in Monitoring the Sustainable Urban Development of World Heritage Cities
Paloma C. Guzman Molina

nr 233
Stage Acoustics and Sound Exposure in Performance and Rehearsal Spaces for Orchestras:
Methods for Physical Measurements
Remy Wenmaekers

nr 234
Municipal Solid Waste Incineration (MSWI) Bottom Ash:
From Waste to Value Characterization, Treatments and Application
Pei Tang

nr 235
Large Eddy Simulations Applied to Wind Loading and Pollutant Dispersion
Mattia Ricci

nr 236
Alkali Activated Slag-Fly Ash Binders:
Design, Modeling and Application
Xu Gao

nr 237
Sodium Carbonate Activated Slag:
Reaction Analysis, Microstructural Modification & Engineering Application
Bo Yuan

nr 238
Shopping Behavior in Malls
Widiyani

nr 239
Smart Grid-Building Energy Interactions:
Demand Side Power Flexibility in Office Buildings
Kennedy Otieno Aduda

nr 240
Modeling Taxis Dynamic Behavior in Uncertain Urban Environments
Zheng Zhong

nr 241
Gap-Theoretical Analyses of Residential Satisfaction and Intention to Move
Wen Jiang

nr 242
Travel Satisfaction and Subjective Well-Being:
A Behavioral Modeling Perspective
Yanan Gao

nr 243
Building Energy Modelling to Support the Commissioning of Holistic Data Centre Operation
Vojtech Zavrel

nr 244
Regret-Based Travel Behavior Modeling:
An Extended Framework
Sunghoon Jang

nr 245
Towards Robust Low-Energy Houses:
A Computational Approach for Performance Robustness Assessment using Scenario Analysis
Rajesh Reddy Kotireddy

nr 246
Development of sustainable and functionalized inorganic binder-biofiber composites
Guillaume Doudart de la Grée

nr 247
A Multiscale Analysis of the Urban Heat Island Effect: From City Averaged Temperatures to the Energy Demand of Individual Buildings
Yasin Toparlar

nr 248
Design Method for Adaptive Daylight Systems for buildings covered by large (span) roofs
Florian Heinzelmann

nr 249
Hardening, high-temperature resistance and acid resistance of one-part geopolymers
Patrick Sturm

nr 250
Effects of the built environment on dynamic repertoires of activity-travel behaviour
Aida Pontes de Aquino

nr 251
Modeling for auralization of urban environments: Incorporation of directivity in sound propagation and analysis of a framework for auralizing a car pass-by
Fotis Georgiou

nr 252
Wind Loads on Heliostats and Photovoltaic Trackers
Andreas Pfahl

nr 253
Approaches for computational performance optimization of innovative adaptive façade concepts
Roel Loonen

nr 254
Multi-scale FEM-DEM Model for Granular Materials: Micro-scale boundary conditions, Statics, and Dynamics
Jiadun Liu

nr 255
Bending Moment - Shear Force Interaction of Rolled I-Shaped Steel Sections
Rianne Willie Adriana Dekker

nr 256
Paralympic tandem cycling and handcycling: Computational and wind tunnel analysis of aerodynamic performance
Paul Fionn Mannion

nr 257
Experimental characterization and numerical modelling of 3D printed concrete: Controlling structural behaviour in the fresh and hardened state
Robert Johannes Maria Wolfs

nr 258
Requirement checking in the building industry: Enabling modularized and extensible requirement checking systems based on semantic web technologies
Chi Zhang

nr 259
A Sustainable Industrial Site Redevelopment Planning Support System
Tong Wang

nr 260
Efficient storage and retrieval of detailed building models: Multi-disciplinary and long-term use of geometric and semantic construction information
Thomas Ferdinand Krijnen

nr 261
The users' value of business center concepts for knowledge sharing and networking behavior within and between organizations
Minou Weijs-Perrée

nr 262
Characterization and improvement of aerodynamic performance of vertical axis wind turbines using computational fluid dynamics (CFD)
Abdolrahim Rezaeiha

nr 263
In-situ characterization of the acoustic impedance of vegetated roofs
Chang Liu

nr 264
Occupancy-based lighting control: Developing an energy saving strategy that ensures office workers' comfort
Christel de Bakker

nr 265
Stakeholders-Oriented Spatial Decision Support System
Cahyono Susetyo

nr 266
Climate-induced damage in oak museum objects
Rianne Aleida Luimes

nr 267
Towards individual thermal comfort: Model predictive personalized control of heating systems
Katarina Katic

nr 268
Modelling and Measuring Quality of Urban Life: Housing, Neighborhood, Transport and Job
Lida Aminian

nr 269
Optimization of an aquifer thermal energy storage system through integrated modelling of aquifer, HVAC systems and building
Basar Bozkaya

nr 270
Numerical modeling for urban sound propagation: developments in wave-based and energy-based methods
Raúl Pagán Muñoz

nr 271
Lighting in multi-user office environments: improving employee wellbeing through personal control
Sanae van der Vleuten-Chraibi

nr 272
A strategy for fit-for-purpose occupant behavior modelling in building energy and comfort performance simulation
Isabella I. Gaetani dell'Aquila d'Aragona

nr 273
Een architectuurhistorische waardestelling van naoorlogse woonwijken in Nederland: Het voorbeeld van de Westelijke Tuinsteden in Amsterdam
Eleonore Henriette Marie Mens

nr 274
Job-Housing Co-Dependent Mobility Decisions in Life Trajectories
Jia Guo

nr 275
A user-oriented focus to create healthcare facilities: decision making on strategic values
Emilia Rosalia Catharina Maria Huisman

nr 276
Dynamics of plane impinging jets at moderate Reynolds numbers – with applications to air curtains
Adelya Khayrullina

nr 277
Valorization of Municipal Solid Waste Incineration Bottom Ash - Chemical Nature, Leachability and Treatments of Hazardous Elements
Qadeer Alam

nr 278
Treatments and valorization of MSWI bottom ash - application in cement-based materials
Veronica Caprai

nr 279
Personal lighting conditions of office workers - input for intelligent systems to optimize subjective alertness
Juliëtte van Duijnhoven

nr 280
Social influence effects in tourism travel: air trip itinerary and destination choices
Xiaofeng Pan

nr 281
Advancing Post-War Housing: Integrating Heritage Impact, Environmental Impact, Hygrothermal Risk and Costs in Renovation Design Decisions
Lisanne Claartje Havinga

nr 282
Impact resistant ultra-high performance fibre reinforced concrete: materials, components and properties
Peipeng Li

nr 283
Demand-driven Science Parks: The Perceived Benefits and Trade-offs of Tenant Firms with regard to Science Park Attributes
Wei Keat Benny Ng

nr 284
Raise the lantern; how light can help to maintain a healthy and safe hospital environment focusing on nurses
Maria Petronella Johanna Aarts

nr 285
Modelling Learning and Dynamic Route and Parking Choice Behaviour under Uncertainty
Elaine Cristina Schneider de Carvalho

nr 286
Identifying indoor local microclimates for safekeeping of cultural heritage
Karin Kompatscher

nr 287
Probabilistic modeling of fatigue resistance for welded and riveted bridge details. Resistance models and estimation of uncertainty.
Davide Leonetti

nr 288
Performance of Layered UHPFRC under Static and Dynamic Loads: Effects of steel fibers, coarse aggregates and layered structures
Yangyueye Cao

nr 289
Photocatalytic abatement of the nitrogen oxide pollution: synthesis, application and long-term evaluation of titania-silica composites
Yuri Hendrix

nr 290
Assessing knowledge adoption in post-disaster reconstruction: Understanding the impact of hazard-resistant construction knowledge on reconstruction processes of self-recovering communities in Nepal and the Philippines
Eefje Hendriks

nr 291
Locating electric vehicle charging stations: A multi-agent based dynamic simulation
Seheon Kim

nr 292
De invloed van Lean Management op de beheersing van het bouwproces
Wim van den Bouwhuijsen

nr 293
Neighborhood Environment and Physical Activity of Older Adults
Zhengying Liu

nr 294
Practical and continuous luminance distribution measurements for lighting quality
Thijs Willem Kruisselbrink

nr 295
Auditory Distraction in Open-Plan Study Environments in Higher Education
Pieternella Elizabeth Braat-Eggen

nr 296
Exploring the effect of the sound environment on nurses' task performance: an applied approach focusing on prospective memory
Jikke Reinten

nr 297
Design and performance of water resistant cementitious materials– Mechanisms, evaluation and applications
Zhengyao Qu

nr 298
Design Optimization of Seasonal Thermal Energy Storage Integrated District Heating and Cooling System: A Modeling and Simulation Approach
Luyi Xu

nr 299
Land use and transport: Integrated approaches for planning and management
Zhongqi Wang

nr 300
Multi-disciplinary optimization of building spatial designs: co-evolutionary design process simulations, evolutionary algorithms, hybrid approaches
Sjonnie Boonstra

nr 301
Modeling the spatial and temporal relation between urban land use, temperature, and energy demand
Hung-Chu Chen

nr 302
Seismic retrofitting of masonry walls with flexible deep mounted CFRP strips
Ömer Serhat Türkmen

nr 303
Coupled Aerostructural Shape and Topology Optimization of Horizontal-Axis Wind Turbine Rotor Blades
Zhijun Wang

nr 304
Valorization of Recycled Waste Glass and Converter Steel Slag as Ingredients for Building Materials: Hydration and Carbonation Studies
Gang Liu

nr 305
Low-Carbon City Development based on Land Use Planning
Gengzhe Wang

nr 306
Sustainable energy transition scenario analysis for buildings and neighborhoods - Data driven optimization
Shalika Saubhagya Wickramarachchi Walker

nr 307
In-between living and manufactured: an exploratory study on biobuilding components for building design
Berrak Kirbas Akyurek

nr 308
Development of alternative cementitious binders and functionalized materials: design, performance and durability
Anna Monika Kaja

nr 309
Development a morphological approach for interactive kinetic façade design: Improving multiple occupants' visual comfort
Seyed Morteza Hosseini

nr 310
PV in urban context: modeling and simulation strategies for analyzing the performance of shaded PV systems
Ádám Bognár

nr 311
Life Trajectory, Household Car Ownership Dynamics and Home Renewable Energy Equipment Adoption
Gaofeng Gu

nr 312
Impact of Street-Scale Built Environment on Walking/Cycling around Metro Stations
Yanan Liu

nr 313
Advances in Urban Traffic Network Equilibrium Models and Algorithms
Dong Wang

nr 314
Development of an uncertainty analysis framework for model-based consequential life cycle assessment: application to activity-based modelling and life cycle assessment of multimodal mobility
Paul Martin Baustert

nr 315
Variable stiffness and damping structural joints for semi-active vibration control
Qinyu Wang

nr 316
Understanding Carsharing-Facilitating Neighborhood Preferences
Juan Wang

nr 317
Dynamic alignment of Corporate Real Estate to business strategies: An empirical analysis using historical data and in-depth modelling of decision making
Howard Cooke

nr 318
Local People Matter: Towards participatory governance of cultural heritage in China
Ji Li

nr 319
Walkability and Walkable Healthy Neighborhoods
Bojing Liao

nr 320
Light directionality in design of healthy offices: exploration of two methods
Parisa Khademagha

nr 321
Room acoustic modeling with the time-domain discontinuous Galerkin method
Huiqing Wang

nr 322
Sustainable insulating lightweight materials for enhancing indoor building performance: miscanthus, aerogel and nano-silica
Yuxuan Chen

nr 323
Computational analysis of the impact of façade geometrical details on wind flow and pollutant dispersion
Xing Zheng

nr 324
Analysis of urban wind energy potential around high-rise buildings in close proximity using computational fluid dynamics
Yu-Hsuan Jang

nr 325
A new approach to automated energy performance and fault detection and diagnosis of HVAC systems: Development of the 4S3F method
Arie Taal

nr 326
Innovative Admixtures for Modifying Viscosity and Volume Change of Cement Composites
Hossein Karimi

nr 327
Towards houses with low grid dependency: A simulation-based design optimization approach
Zahra Mohammadi

nr 328
Activation of demand flexibility for heating systems in buildings: Real-life demonstration of optimal control for power-to-heat and thermal energy storage
Christian Finck

nr 329
A computational framework for analysis and optimisation of automated solar shading systems
Samuel B. de Vries

nr 330
Challenges and potential solutions for cultural heritage adaptive reuse: a comparative study employing the Historic Urban Landscape approach
Nadia Pintossi

nr 331
Shared control in office lighting systems
Tatiana Aleksandrovna Lashina

nr 332
Comfort in Urban Public Spaces
You Peng

nr 333
Numerical modelling of metal soap formation in historical oil paintings
Gerardus Johannes Anna Maria Eumelen

nr 334
A transdisciplinary decision-making approach to food-water-energy nexus: A guide towards sustainable development
Maryam Ghodsvali

nr 335
Numerical modelling of transient low-frequency sound propagation and vibration in buildings
Indra Sihar

nr 336
Characterization of impact sound from lightweight joist floors
Yi Qin

nr 337
Cities for Children: Supporting Children and Caregivers in Participatory Urban Planning
Özlemnur Ataol

nr 338
Engaging the unengaged: Exploring citizen participation in nature-based solutions in China
Li Dai

nr 339
Municipal Solid Waste Incineration Residues: analysis, treatments, and applications
Ekaterina Loginova

nr 340
Enhancing the Uptake of Nature-Based Solutions in Urban Settings: An Information Systems Approach
Shahryar Ershad Sarabi

nr 341
Work Schedule Arrangements in Two-Adult Households with Children
Bilin Han

nr 342
Increasing awareness of urban cultural heritage using digital technologies: empirical design and analysis of a new multi-media web platform
Benshuo Wang

nr 343
Mechanical and physical properties of fibre-cement composites using alternative natural fibres
Katerina Kochova

nr 344
Numerical and experimental investigation of urban microclimate in a real compact heterogeneous urban area
Nestoras Antoniou

nr 345
Examining in-class activities to facilitate academic achievement in higher education: A framework for optimal indoor environmental conditions
Henk W. Brink

nr 346
High-temperature resistant geopolymers: composition, microstructure and performance
Kinga Malgorzata Klima

nr 347
Individual and household decision-making in shared parking
Qianqian Yan

nr 348
In-situ formation of LDHs in Alkali activated binders
Tao Liu

nr 349
Condition assessment of concrete sewer pipes through an integrated experimental-numerical approach
Irene C. Scheperboer

nr 350
In situ PU-based characterization of sound absorbing materials for room acoustic modeling purposes
Baltazar Briere de La Hosseraye

nr 351
Uncertainty analysis and management in building energy data mining: A bottom-up approach considering the temporal and spatial aspect of data
Waqas Khan

nr 352
Personalized Heating Control Systems to improve thermal comfort and reduce energy consumption
Michal Veselý

nr 353
Restorative value of the urban greenscape: Urban residential streets as restorative environments
Robert P. van Dongen

nr 354
Urban ventilation and the compact Mediterranean city: numerical investigations of the dynamic relationships between density, morphology and wind flow
Olga Palusci

nr 355
Data science for buildings: a multi-scale approach bridging occupants to smart-city energy planning
Julien Leprince

nr 356
Class Association Rule Models for Predicting Transportation Mode Choice
Jiajia Zhang

nr 357
Acceptance and use of autonomous vehicles
Zhihui Tian

nr 358
Consumer Acceptance of Crowdshipping Services
Chenyu Wang

nr 359
Determinants of habitual participation in leisure-time physical activity and active travel in life trajectories
Xiaoyue Chen

nr 360
Analysis of Citizens' Motivation and Intention Using Modern Information Technology in Urban Planning Public Participation
Wenshu Li

nr 361
Linking smart and physical port cities. Port-city interface areas: from obsolete/isolated to smart environments
Mercè de Miguel Capdevila

nr 362
Assessment and improvement of indoor thermal comfort and energy demand of Chinese heritage apartment buildings under climate change
Muxi Lei

nr 363
Indoor airflow and heat transfer in a cross-ventilated generic building: wind tunnel experiments and computational fluid dynamics analyses
Katarina Kosutova

nr 364
A Robotic Construction Simulation Platform for Light-weight Prefabricated Structures. Lifetime prediction of vertical-axis wind turbines based on CFD simulations and high-cycle fatigue modeling
Aiyu Zhu

nr 365
Lifetime prediction of vertical-axis wind turbines based on CFD simulations and high-cycle fatigue modeling
Feiyu Geng

nr 366
Computational modeling of convective heat transfer at building surfaces
Samy Iousef

nr 367
Computational modeling of convective heat transfer at building surfaces
Vasaturo Raffaele

nr 368
Bouwen zonder scrupules. De Nederlandse bouwnijverheid tijdens de bezetting en de eerste jaren van wederopbouw (1940-1950)
Geert-Jan Mellink

nr 369
Factors Promoting a Positive Experienced Neighborhood Public Space--A Virtual Environment-based analysis
Yuwen Zhao

nr 370
Place quality making in high-speed railway station areas. Devising place quality indicators for urban design, beyond the transport-land use divide
Jinglun Du

nr 371
Sustainable Bio-based Adsorptive Concrete for Phosphorus Removal
Fan Wu

nr 372
The physical workplace as a resource for mental health
Lisanne Bergefurt

Basic oxygen furnace (BOF) slag is the byproduct of the steelmaking process. The main challenge lies in the utilization of industrial residues to get zero-waste flow sheets. In 2018, the basic oxygen steel-making process produced over ~70% of the crude steel globally, generating 90-150 kg of basic Oxygen furnace (BOF) slag for every tonne of crude steel. It is a complex material chemically and mineralogically. To achieve the efficient recycling of BOF slag as a partial replacement for cement, the cooling process of BOF slag is changed from standard cooling to air granulation. The air granulation of the BOF slag is investigated as an efficient way to modify material properties for the efficient recycling of the building materials. This dissertation aims to develop a systematic understanding of the effect of air granulation on the BOF slag mineralogy, reactivity, and leaching behaviour. Moreover, Cr and V speciation is further investigated by ex-situ mimicking of the dicalcium silicate, a slag phase that accounts for 35-45 wt. % of the whole slag. Moreover, the application of air granulated BOF slag as a binder in different types of cement (ordinary Portland cement and Belite calcium sulfoaluminate cement) is investigated to utilize slag as a supplementary cementitious material. The work of this research can be divided primarily dealing with 1) Air granulation, Cr and V doped dicalcium silicate, leaching mechanism (Chapters 3-5) 2) Hydration of dicalcium silicate and air granulated BOF (Chapters 6-7) 3) Application of BOF slag as a binder for high-end building products (Chapter 8-9).

DEPARTMENT OF THE BUILT ENVIRONMENT

TU/e EINDHOVEN UNIVERSITY OF TECHNOLOGY